Università degli Studi di Napoli Federico II

Dipartimento di Ingegneria Industriale

Dottorato di Ricerca in Ingegneria Industriale

XXXII Ciclo

A Deployable Aerobraking System for Atmospheric Re-entry

Coordinatore
Ch.mo Prof. Michele Grassi

Tutor
Ch.mo Prof. Raffaele Savino
Dott. Ing. Stefania Cantoni

Candidato
Ing. Alberto Fedele

Anno 2020

Abstract

PhD Thesis

A Deployable Aerobraking System for Atmospheric Re-entry

by Alberto FEDELE

Deployable aerobrakes for Earth re-entry capsules may offer many advantages in the near future, including the opportunity to recover on Earth payloads and samples from Space with reduced risks and costs with respect to conventional systems. Such capsules can be accommodated in the selected launcher in folded configuration (optimizing the available volume) and, when foreseen by the mission profile, the aerobrake can be deployed in order to increase the surface exposed to the hypersonic flow. Despite several proposed design and some experimental validation in the last years, a mechanically deployable heat shield capsule still has to demonstrate the capability to re-enter from a Low Earth Orbit Environment and to be successfully recovered. Maturing the deployable heat shield as a viable technology for entry, descent, and landing applications still require a considerable amount of analysis and testing.

This dissertation presents an overview of work performed in maturing a particular type of deployable heat shield, with a 45° sphere-cone geometry. The activities included the design and execution of a Plasma Wind Tunnel test to demonstrate the capability of the proposed capsule to survive the re-entry environment. A particular focus has been reserved to the study of the problem of dynamic stability. In particular aero-thermodynamic analysis have been conducted to characterize the dynamic response in the supersonic, transonic and subsonic regime by applying the forced-oscillation method through Computational Fluid Dynamics. The output of these analysis has been used in a six degree of freedom simulator to study the oscillating behavior during a re-entry trajectory. The last part of this work has been dedicated to study the controllability of these systems to reach the desired landing site in the case of re-entry from space, with the focus on landing dispersion minimization. In particular a means of controlling a mechanically deployable capsule during the re-entry phase using an aerodynamic control system and a new technological solution for re-entering and landing a capsule in a desired location from a low Earth orbit without the use of chemical propulsion have been proposed.

Acknowledgements

Although this manuscript bears my name as the author, it would not have come into existence had it not been for the contribution and support of several amazing people. First, I would like to thank my advisor, Raffaele Savino, for his valuable guidance and help throughout the execution of this research work and my tutor, Stefania Cantoni, for personally investing herself in nearly every aspect of this work and in my success as an engineering professional. I am also grateful to Camillo Richiello, Salvatore Borrelli and Michele Grassi for giving me the opportunity to grow professionally and humanely with this PhD experience. I would like to deeply thank Roberto Gardi and Paolo Vernillo and all the staff from the MIFE Team for the great work done together. Without their professionalism, inventive, high technical skills and preparation this work would never been possible. Many thanks to Giuseppe Pezzella, whose analysis and contribution have been important for this work, and to Marco Marini, for sparing time out of his busy schedule to help me with my research work. I also owe a great deal of thanks to Riccardo Bevilacqua, for the fruitful collaboration and the incredible experience to be part of the University of Florida family, and to Sanny Omar, whom provided a critical piece of software for the computational portion of this research and whom spent many hours working with me to ensure that the code was performing correctly. I am grateful to Stefano Mungiguerra, whom shared with me this adventure, and to Alessandro Zamprotta and Salvatore Carannante, I had the honor to supervise during their master thesis. On a more personal note, I would like to thank my family and my love for their unwavering affection, support, and understanding of my personal and professional goals throughout my academic and professional career.

Contents

List of Figures

List of Tables

List of Abbreviations

3DOF   Three Degrees of Freedom

6DOF   Six Degrees of Freedom

ADEPT   Adaptive Deployable Entry and Placement Technology

ASI   Italian Space Agency

AUSM   Advection Upstream Splitting Method

CFD   Computational Fluid Dynamics

CIRA   Italian Aerospace Research Centre

CoM   Centre of Mass

DSMC   Direct Simulation Monte Carlo

EFESTO   European Flexible hEat Shields: advanced Tps design and tests

for future in-Orbit demonstration

EI   Entry Interface

ESA   European Space Agency

EVA   Extra Vehicular Activities

FCW   Fully-Catalytic Wall

FD   Flight Demonstrator

FDS   Flux Difference Splitting

FEM   Finite Element Method

FM   Free Molecular

GD   Ground Demonstrator

HIAD   Hypersonic Inflatable Aerodynamic Decelerators

IRDT   Inflatable Re-entry and Descent Technology

IRENE   Italian RE-entry NacellE

IRVE   Inflatable Re-entry Vehicle Experiment

ISS   International Space Station

JAXA   Japan Aerospace Exploration Agency

LEO   Low Earth Orbit

MAAC   Membrane Aeroshell for Atmospheric entry Capsule

MISTRAL   Air-Launcheable MIcro-SaTellite with Reentry capability

MIT   Massachusetts Institute of Technology

NASA   National Aeronautics and Space Administration

NCW   Non-Catalytic Wall

NGS   Nose Gas Springs

NPC   Numerical Predictor Corrector

O-CMC   Oxide-Ceramic Matrix Composite

PID   Proportional-Integral-Derivative

PWT   Plasma Wind Tunnel

RANS   Reynolds Averaged Navier-Stokes

RCS	Reaction Control System
TPS	Thermal Protection System
TRL	Technology Readiness Level
UDF	User Defined Functions
UGS	Umbrella Gas Springs
UNINA	University of Naples "Federico II"
WFF	Wallops Flight Facility

List of Symbols

α	Angle of Attack	deg
α_m	Vertical De-orbit Burn Misalignment	deg
β	Sideslip Angle	deg
β_m	Horizontal De-orbit Burn Misalignment	deg
γ	Flight Path Angle	deg
ΔV	Change in Velocity	$\mathrm{m\,s^{-1}}$
Δt	Change in Time	s
θ	Longitude	deg
μ	Gravitational Parameter	$\mathrm{m^3\,s^{-2}}$
ρ	Air Density	$\mathrm{kg\,m^{-3}}$
σ	Bank Angle	deg
ϕ	Geodetic Latitude	deg
ϕ_G	Geocentric Latitude	deg
ψ	Heading Angle	deg
Ψ	Flap Definition Angle	deg
$\omega_\oplus$	Earth's Rotational Velocity	$\mathrm{rad\,s^{-1}}$

A	State Matrix	
B	Input Matrix	
BC	Ballistic Coefficient	$\mathrm{kg\,m^{-2}}$
C_D, C_L, C_Y	Drag, Lift and Cross-force coefficients	
D	Drag	N
g	Gravitational Acceleration	$\mathrm{m\,s^{-2}}$
h	Altitude	m
J_2	Gravity Perturbation	
L	Lift	N
m	Mass	kg
M	Mach Number	
r	Geocentric Altitude	m
q	Dynamic Pressure	Pa
$\dot{q}$	Stagnation Point Heat Flux	$\mathrm{kW\,m^{-2}}$
Q, R, N	LQR Weight Matrices	
$R_\oplus$	Earth Equatorial Radius	m
RN	Nose Radius	m
S_{ref}	Reference Surface	$\mathrm{m^2}$
x	State Vector	
Y	Cross-force	N
u	Input Vector	

V Velocity Magnitude $\mathrm{m\,s^{-1}}$

To my dear beloved

Part I

Introduction

Chapter 1

Introduction

1.1 Scope

Deployable aerobrakes for Earth re-entry capsules may offer many advantages in the near future, including the opportunity to recover on Earth payloads and samples from Space with reduced risks and costs with respect to conventional systems. Such capsules can be accommodated in the selected launcher in folded configuration (optimizing the available volume) and, when foreseen by the mission profile, the aerobrake can be deployed in order to increase the surface exposed to the hypersonic flow and therefore to reduce the ballistic parameter.

The ballistic parameter reduction offers as main advantage the opportunity to perform an aerodynamic de-orbit of the system without the need of a dedicated propulsive subsystem and an atmospheric re-entry with reduced aero-thermal and mechanical loads. It makes also possible the use of relatively lightweight and cheap thermal protection materials. Furthermore, the deployable surface can be modulated for the aerodynamic control of the de-orbit trajectory in order to correctly target the capsule towards the selected landing site.

Despite several proposed design and some experimental validation in the last years, a mechanically deployable heat shield capsule still has to demonstrate the

capability to re-enter from a Low Earth Orbit Environment and to be successfully recovered. Maturing the deployable heat shield as a viable technology for entry, descent, and landing applications will require a considerable amount of testing and analysis. Indeed, several problems must be solved prior of the use of this technology in a future space mission. First of all, any proposed design must demonstrate the ability to survive the re-entry environment in terms of mechanical loads and heat fluxes which characterized a space re-entry mission. Another problem that needs to be addressed is the capability to pass through the transonic regime without losing attitude control. Indeed, this particular geometry suffers dynamic instability in the transonic regime that could trigger a tumbling or an excessive oscillation that can be difficult to be recovered in the subsonic regime. This is a condition that needs to be avoid for the success of the mission. An addition open point is how to effectively control these capsules to reduce landing dispersion or to target a precise re-entry point on ground.

1.2 Summary of Contributions

During the PhD period, the candidate has been full involved in the design activity of a new mechanically deployable heat shield capsule for an ESA mission. The objective of this mission is to design and built a Flight Demonstrator and a Ground Demonstrator to prove, with a suborbital flight and with a Plasma Wind Tunnel (PWT) test campaign, the capability to survive to the re-entry environment. It is highlighted the importance of the design of the flight and ground demonstrators, which are unique prototypes of their kind for the demonstration of the concept of a mechanically deployed heat shield. As before mentioned, a concept of this kind has yet to be demonstrated.

In particular the activities included the design of the mission with a focus

on trajectory analysis; the population of an aerodynamic database for the characterization of the capsule; a contribution to the definition of the demonstrators architecture, with a specific focus on the assessment of the deployable mechanisms and the multi-layer thermal protection; and the design and execution of a Plasma Wind Tunnel test to demonstrate the capability of the proposed capsule to survive the re-entry environment.

A particular focus has been reserved to the study of the problem of dynamic stability. In particular aero-thermodynamic analysis have been conducted to characterize the dynamic response in the supersonic, transonic and subsonic regime of a capsule with a 45° sphere-cone geometry by applying the forced-oscillation method through Computational Fluid Dynamics. The output of these analysis have been used in a six degree of freedom simulator to study the oscillating behavior during a re-entry trajectory.

The last part of this work has been dedicated to the assessment of the controllability of these systems to reach the desired landing site in the case of re-entry from space, with the focus on landing dispersion minimization. In particular a means of controlling a mechanically deployable capsule during the re-entry phase using an aerodynamic control system has been proposed. The proposed system, consisting of eight aerodynamic flaps, is able to change the natural trim of the capsule through the flaps independent deflection, in order to produce enough lift and side force to ensure the capsule maneuverability during the re-entry trajectory. To conclude a new technological solution for re-entering and landing a capsule in a desired location from a low Earth orbit without the use of chemical propulsion has been studied and proposed in collaboration with University of Florida. Aerodynamic drag modulations, using the heat shield as a drag device, are utilized to guide the capsule to the desired re-entry location. A guidance and control algorithm have been proposed and tested through Monte Carlo analysis demonstrating that the landing in a desired recovery location is indeed feasible

using exclusively aerodynamic forces.

1.3   Thesis Overview

The dissertation is arranged as follows:

Chapter 1 identifies the thesis scope, introduces the original contribution of this work and gives a brief overview about the organization of this thesis.

Chapter 2 presents the literature review necessary in order to develop this work. It is divided in three sections: the first is an overview about deployable re-entry capsule, the second is an overview of the guidance and control algorithms used for re-entry capsule in general and in particular for these applications, while the third introduce the readers to the problematic of dynamic stability that affect this kind of system.

Chapter 3 introduces the re-entry reference mission and system with a particular focus on the critical elements that characterize the deployable heat shield concept analysed in this work.

Chapter 4 presents the flight mechanics tool used for the analysis in this thesis. It is divided in two section. The first describes an orbital simulator, while the second is focused on the description of a re-entry simulator.

Chapter 5 introduces the methodology and tool used for the aero-thermodynamic analysis. A specific section has been written to introduce the reader to the Plasma Wind Tunnel Facility used for the scope of this work.

Chapter 6 presents a means of controlling a mechanically deployable capsule during the re-entry phase using an aerodynamic control system based on the actuation of eight small flaps. Moreover, a new methodology for re-entering and landing a capsule in a desired location from a low Earth orbit without the use of chemical propulsion but only modulation of aerodynamic drag is proposed.

Chapter 7 presents the flight mechanics activities performed to design a demonstration mission for a capsule with a deployable heat shield.

Chapter 8 introduces the results obtained to populate an aerodynamic database and the analysis performed trough computational fluid dynamics to asses the aero-thermal loads during a re-entry from low Earth orbit.

Chapter 9 describes the activities performed to design and conduct a Plasma Wind Tunnel test, together with the analysis of the results obtained.

Chapter 10 presents the analysis conducted to characterize the dynamic response in supersonic, transonic and subsonic regime of a capsule with a $45°$ sphere-cone geometry and the analysis to study the oscillating behavior during a sub-orbital re-entry trajectory.

Chapter 11 presents the results of studies dedicated to assess the controllability and the performances of the control system and the methodologies proposed in Chapter 6. In particular several Monte Carlo analysis are presented to assess both guidance and control algorithms performances.

Finally, some conclusions are the subject of Chapter 12.

Part II

State of the Art and Mission

Chapter 2

Literature Review

2.1 Deployable System Overview

The first concept of a deployable heat shield was developed by three students of Professor Akin in an advanced space system design class at MIT in the fall of 1988 [1]. The concept, called ParaShield (because the deployable fabric framework should be used as both a heat shield and parachute), was based on the idea of reducing the ballistic coefficient to optimize the desired entry vehicle characteristics.

One demonstration vehicle based on the ParaShield concept, called Skidbladnir, was built by the University of Maryland and a launch was attempted on a suborbital flight in the 1989. Unfortunately, the launch failed due to a problem with the launch vehicle and the system was never tested in flight [2].

FIGURE 2.1: ParaShield Demonstrator [1]

Another concept of a mechanically deployable heat shield was studied in 1996 at the University of Bremen and called Brem-sat 2 [3]. It resembles an umbrella with heat resistant silicon fabric and twelve titanium arms. When folded it looked almost like a conventional satellite with solar panel attached to the arms and when deployed the same solar panel remained attached to the backside of the shield.

(a)   (b)
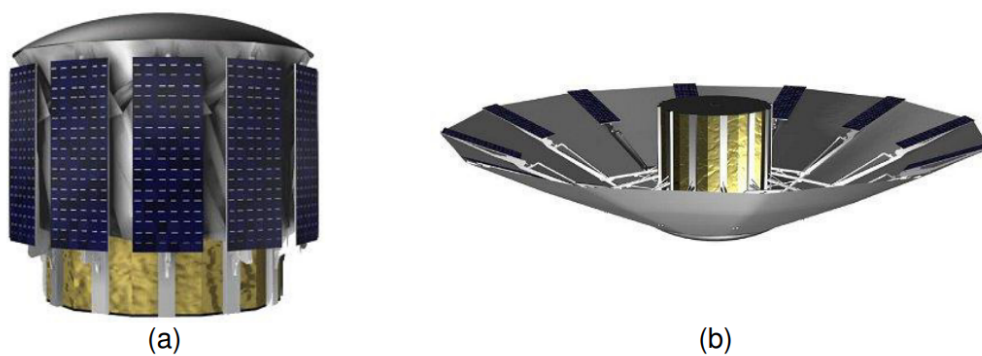
FIGURE 2.2: BREM-SAT 2 folded and deployed configurations [3]

These mechanical deployable concepts developed by American and European universities have, to date, never been tested. However, since 2000, some concept based on inflatable heat shields have been successfully tested within the ESA, NASA and JAXA programs.

In particular, the Inflatable Re-entry and Descent Technology (IRDT) technology was successfully tested in 2000 [4]. The IRDT re-entered the atmosphere after a 6-orbit flight into Space and was recovered successfully. The inflatable aero-braking shield consisted of different layers of multi-layer insulation and flexible ablative layers arranged on a flexible inflatable kernel. This kernel provided the form and stiffness of the inflatable shield. The shield was inflated by gas released through a pyro-valve from storage tanks onboard the spacecraft.
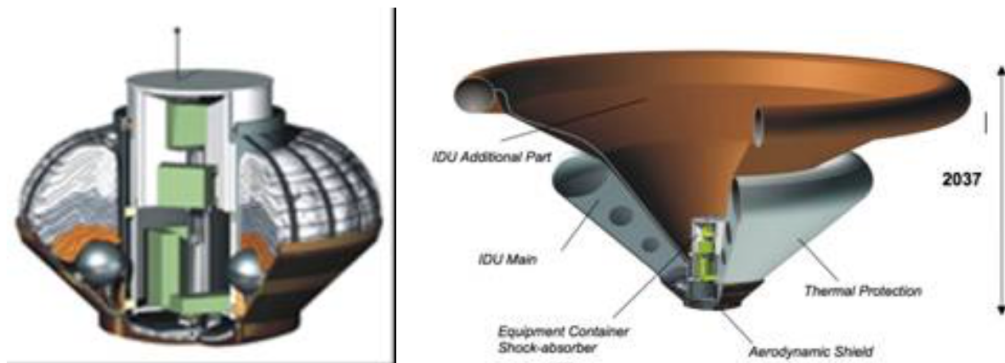
FIGURE 2.3: IRDT System in folded and deployed configuration [4]

The resulting re-entry configuration, which was inflated within seconds, performed aero-braking to subsonic speed while flying through the atmospheric layers. For braking to moderate landing velocities of about 10 m/s or less, a second inflatable aero-shield was supposed to be deployed to increase the cross-sectional area and serve as a type of parachute. Unfortunately during the reentry mission, the second device did not inflate properly which caused a harder impact than intended [5]. An additional demonstration mission planned in 2002 was not successful due to a failure in the launcher/payload interface of the Volna rocket used. The capsule of the last program mission launched in 2005 was not recovered due to an unexpected trajectory overshoot [6] [7] [8] [9] [10].

In the meantime in America, NASA started the Inflatable Re-entry Vehicle Experiment (IRVE) to demonstrate various aspects of inflatable technology during Earth re-entry through a sounding rocket campaign [11] [12]. The Inflatable Reentry Vehicle Experiment II (IRVE-II) launched on August 17, 2009 from Wallops Flight Facility on a Black Brant IX sounding rocket. It was the first successful sub-orbital test of an American-made deployable heat shield [13]. The flight was a complete success, with the re-entry vehicle separating cleanly from the launcher, reaching an apogee of 218km, inflating as planned, and demonstrating stable flight through re-entry and descent while on-board systems telemetered

video and flight performance data to the ground. The design of the IRVE system consists of a centerbody structure which houses the electronics and inflation subsystems as well as an inflatable aeroshell.
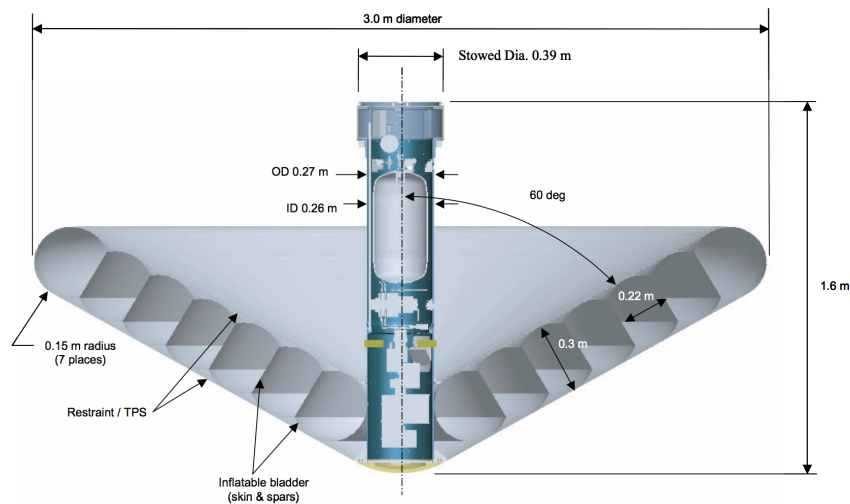
FIGURE 2.4: IRVE System in deployed configuration [13]

The IRVE-II mission [13] [14] was a reflight of the original IRVE design which was launched September 6, 2007 on a Terrier Orion sounding rocket. The IRVE launcher failed to release the reentry vehicle from the launch shroud, so the flight provided no data on the performance of the inflatable reentry vehicle. Thanks to the success of the IRVE-II mission, NASA started the Hypersonic Inflatable Aerodynamic Decelerators (HIAD) program which aimed to address three precise challenges relating to the use of inflatable heat shield technology on future NASA missions. These three challenges were surviving the heat pulse during atmospheric entry, demonstrating system performance at relevant scales, and demonstrating controllability in the atmosphere [15] [16] [17] [18] [19] [20] [21] [22] [23] [24] [25] [26] [27] [28] [29] [30] [31] [32] [33].

The Inflatable Reentry Vehicle Experiment 3 (IRVE-3) [34] [35] [36] was launched on July 23, 2012, from NASA Wallops Flight Facility (WFF) on a Black Brant XI suborbital sounding rocket with a mission objective of increasing the IRVE-II

peak heat flux by a factor of five to ten. It reached an apogee of 469 km and successfully performed its mission, demonstrating the survivability of a hypersonic inflatable aerodynamic decelerator (HIAD) in the reentry environment. Moreover, it demonstrated the possibility of steering the inflatable vehicle and controlling its descent as is done with rigid re-entry capsules. In fact, the IRVE-3 vehicle was equipped with a mechanism able to modulate the center of mass location during re-entry and therefore provide control of the magnitude and direction of the lift vector.

FIGURE 2.5: IRVE 3 during Assembly and Artistically view [34]

IRVE-3 inflated to the same general configuration as the earlier IRVE-II mission (3m diameter 60° cone). The primary difference was that the inflatable structure was redesigned to handle increased loads while reducing the thermal leak rate. The inflatable structure kept the stacked-toroid approach but added individual structural straps connecting the toroids to each other and to the centerbody. The thermal protection system (TPS) was upgraded from the layered Nextel fabric used on IRVE-II to a multi-layer system able to handle flight-relevant heating levels.

On August 7th in 2012, JAXA tested an inflatable heat shield called Membrane Aeroshell for Atmospheric-entry Capsule (MAAC) on a suborbital flight

(apogee 150 km). The MAAC consisted of a flexible membrane aeroshell deployed by an inflatable torus structure [37] [38] [39] [40] [41] [42] [43] [44]. The flight and reentry demonstration of a nano-satellite EGG (re-entry satellite with Gossamer aeroshell and GPS/iridium) in the low Earth orbit was initiated in January 2017 and successfully completed in May 2017. The EGG was designed to be burned out during atmospheric reentry from the viewpoint of ground safety against falling objects [45] [46].

Currently the European Union, in the framework of the H2020 program, is developing a large inflatable heat shield called EFESTO [47] with corresponding IAD diameters in the range of 4 and 10 m. The EFESTO is intended for small launcher upper stage recovery and for the safe landing of Mars robotic exploration missions.

In the last decade, the idea of a mechanically deployed heat shield returned under two projects. The first called ADEPT (Adaptive Deployable Entry and Placement Technology) is in development by NASA Ames, and the second IRENE (Italian Re-Entry NacellE) is in development by the Italian Aerospace Research Centre (CIRA). Unlike the inflatable heat shield concept, up to this date, a mechanically heat shield concept still has to demonstrate the capability to re-enter from a Low Earth Orbit Environment and to be successfully recovered.

ADEPT is a NASA technology development project to develop an entry system concept consisting of a series of deployable ribs and struts, connected with a flexible fabric skin which when deployed functions as a semi-rigid aeroshell entry system with a 70 degree sphere cone shape. In addition to acting as the aeroshell structural surface, the fabric skin serves as the primary component of the EDL thermal protection system (TPS). For the ADEPT deployable concept, woven carbon fabric is the primary drag-producing surface. The pure carbon fabric, with its high thermal conductivity, allows re-radiation from both the windward and leeward side of the fabric [48] [49] [50] [51] [52] [53] [54] [55] [56].

The downside of a novel design such as ADEPT is the limited experimental flight data pertaining to the vehicle's dynamics, during the design there were stability concerns for a 70 degree sphere cone vehicles that need addressing [57]. Consequently, NASA had commissioned a sounding rocket test (SR-1) of a scaled down geometry in order to acquire an initial assessment of the vehicle's free-flight behavior.
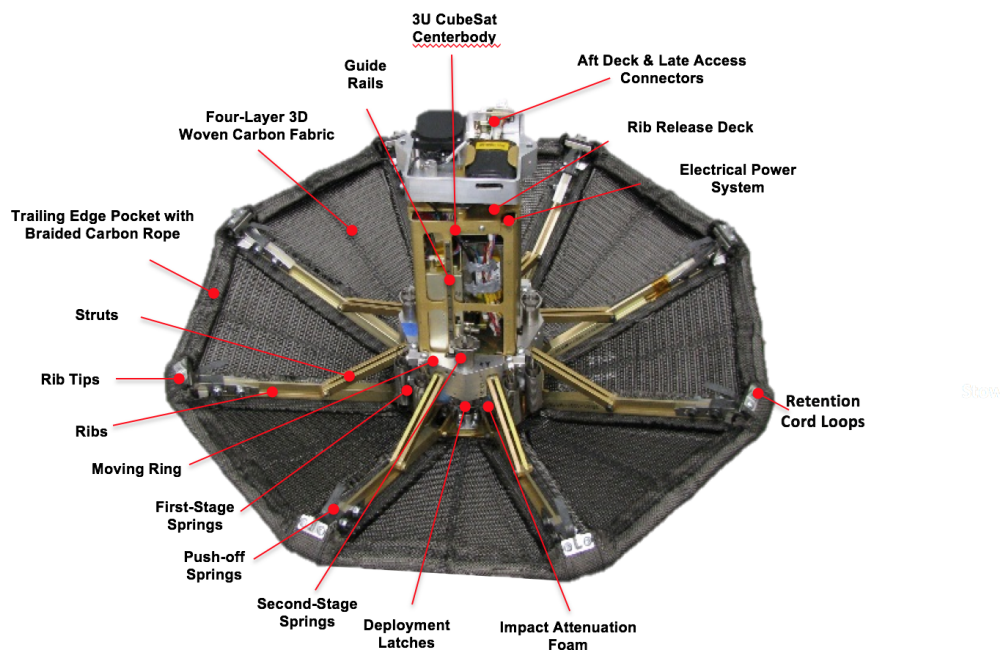
FIGURE 2.6: ADEPT demonstrator

ADEPT was launched on September 12th 2018 from White Sands Missile Range, New Mexico, on a SpaceLoft XL sub-orbital rocket manufactured by UP Aerospace and reached an apogee of 100 km [58] [59]. The sub-orbital mission demonstrate the capability of this system to achieves fully deployed configuration prior to reaching 80 km altitude on descent, but unfortunately, it suffer of some dynamic instability and started tumbling during the last phase of the re-entry trajectory.

The IRENE project started in 2011 when the Italian Space Agency founded a Feasibility study for a deployable re-entry system based on a 45 degree sphere cone heat shield to be developed by ALI (Aerospace Laboratory for Innovative components) and University of Naples Federico II [60] [61]. Consecutive studies have been focused on the development of a scaled down prototype of IRENE, named MINI-IRENE [62] [63] [64] [65] [66] [67] [68], for suborbital flight on MAXUS sounding rocket [69]. The current phase of the program that will bring the IRENE concept to flight is under the lead of the Italian Aerospace Research Centre (CIRA) and the European Space Agency (ESA). This phase involves the design and realization of a Flight Demonstrator (FD) for a suborbital flight on a VSB-30 rocket and the design and realization of a Ground Demonstrator (GD) for a Plasma Wind Tunnel (PWT) test campaign.
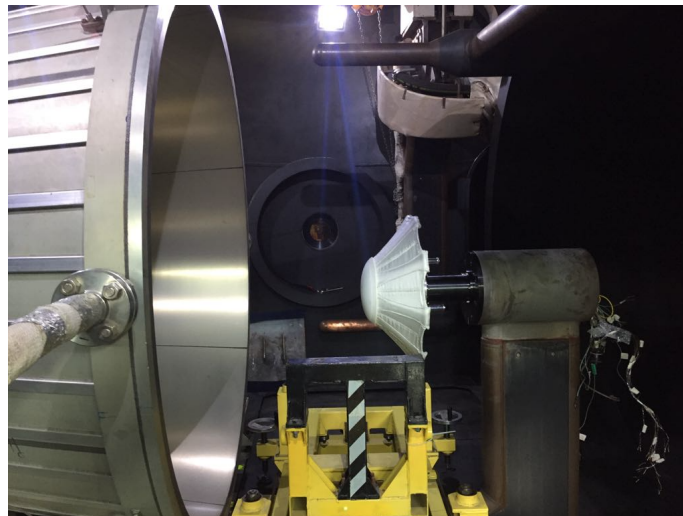
FIGURE 2.7: Mini-Irene Ground Demonstrator inside CIRA Plasma Wind Tunnel

The flight test shall be representative of the aero-mechanical environment during re-entry and will verify the dynamic stability behavior of the capsule during re-entry [66]. The GD shall test the material and of the mechanisms of the FD in order to achieve an overall TRL (Technology Readiness Level) equal to 6. The

goal of the GD is to replicate the LEO re-entry thermal environment to the extend possible. The FD capsule will be dropped by the payload stage of a VSB-30 Rocket and reach an apogee of 250km altitude. The VSB-30 sounding rocket flight is not sufficiently energetic for achieving significant heat fluxes on the TPS. Because of this, a PWT test is needed in order to achieve TRL 6 in a relevant environment. The Ground Demonstrator, that has already been tested in a Plasma Wind Tunnel Test campaign at CIRA [67], was representative not only of the materials, but also of the mechanisms of the flight model. Even if the thermal test environment was not exactly identical to the environment that would be experienced in flight, the analyses show that the aerodynamic environment encountered in the VSB-30 flight with an apogee of 250 km is very close to that of LEO entry [68]. The flight will thus prove the structural worthiness of the whole system and help determine the aerodynamic characteristics.

Another two Italian projects which could take advantage of the mechanical deployable heat shield concept are MISTRAL (Air-launcheable Micro-Satellite with Reentry Capability) and IPERDRONE.
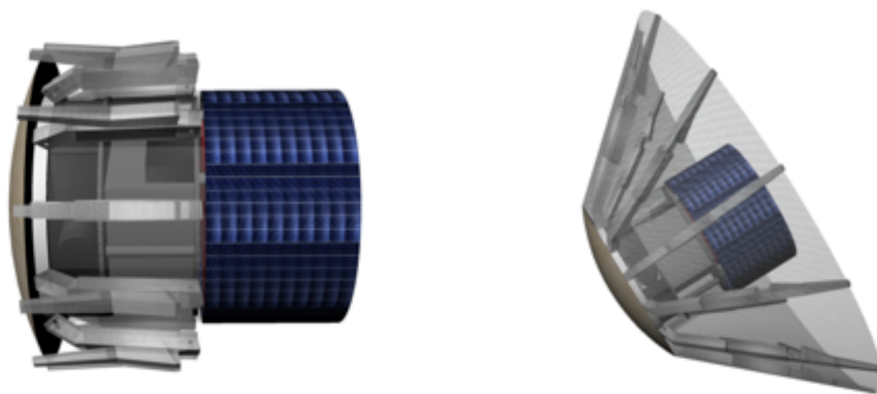
FIGURE 2.8: MISTRAL closed and deployed configurations [70]

The primary objective of the MISTRAL [70] [71] [72] [73] [74] [75] [76] [77] [78] project is to develop a 20-30 kg class spacecraft provided with a deployable,

flexible aero-brake able to return it to Earth in a designated recovery area. The mechanical heat shield concept presents some advantages compared to the inflatable heat shield including the possibility to modulate the frontal area of the shield to better control the drag during re-entry. The spacecraft is equipped with a payload compartment able to accommodate a variety of instruments to facilitate a number of potential missions ranging from radiation measurements to exobiology to atmospheric mapping to Earth observation. The Spacecraft does not have any propulsion system and therefore its operation could be considered extremely safe, opening the possibility for use on-board the ISS as "space mail" systems for the return of sample to Earth. The control of the satellite along its orbit is achieved through drag modulation by opening and closing the heat shield. The aero-brake system can be fully deployed and used to protect the satellite from the heavy thermal load during re-entry.

IPERDRONE [79] [80] is the name of the program funded by the Italian Space Agency (ASI) aimed at designing and developing a small spacecraft re-entry system able to perform in-orbit operations on the International Space Station (ISS) and/or other Space Systems, re-enter the atmosphere, and safely land on Earth bringing back unaltered scientific payloads/experiments.

IPERDRONE will consist of a series of missions characterized by incremental objectives with the goal of qualifying new technologies and mission architectures. The program includes the re-entry and retrieval of payloads on the ground. The first mission, named IPERDRONE.0, will demonstrate system capabilities such as proximity operations, inspections, and interaction with a target. The second mission, named IPERDRONE.1, will demonstrate the ability to bring a payload back to Earth. This mission will benefit from the many technologies demonstrated the IPERDRONE.0 mission. In particular, the challenge of controlled re-entry and payload recovery that will be demonstrated on the IPERDRONE.1 is made feasible by the key technologies demonstrated on IPERDRONE.0. The IRENE

deployable heat shield is one of the candidate re-entry technologies for flight on IPERDRONE.1 mission.

2.2   Re-entry Technique and Algorithm Overview

During 1961 and 1962, Jurij Alekseevič Gagarin and John Glenn re-entered Earth's atmosphere after orbiting the planet, following a ballistic trajectory, with the Vostok 1 and with the Mercury Spacecraft respectively. These first manned space missions were followed by more space missions which eventually led to the Moon landing.

NASA's Gemini Program, conducted during and after the Mercury Program between 1961 and 1966, had the objective of developing and testing new techniques such as Rendezvous and Extra Vehicular Activities (EVA) that would facilitate the Apollo program. One of the core objectives of the Gemini program was to develop a controlled re-entry capability for space capsules. The Gemini capsule was able to generate an average lift-to-drag ratio (L/D) of 0.9 by stabilizing at a non-zero angle of attack. Since the Gemini Spacecraft had a symmetrical body, a center of mass (CoM) offset from the center of pressure was used to trim the capsule. In order to give the desired vertical and lateral components of lift, the capsule was rolled during the re-entry according to the bank angle modulation logic shown in Figure 2.9.

This became a common technique used in future space missions in order to give re-entry capsules lifting and therefore control capabilities. In fact, if the lift-to-drag ratio is non-zero and a lift force acts in a direction perpendicular to the velocity vector, changing the vehicle orientation with respect to the airflow causes the lift vector direction to likewise change.

By changing the bank angle, the vertical component of lift in the vertical plane varies.
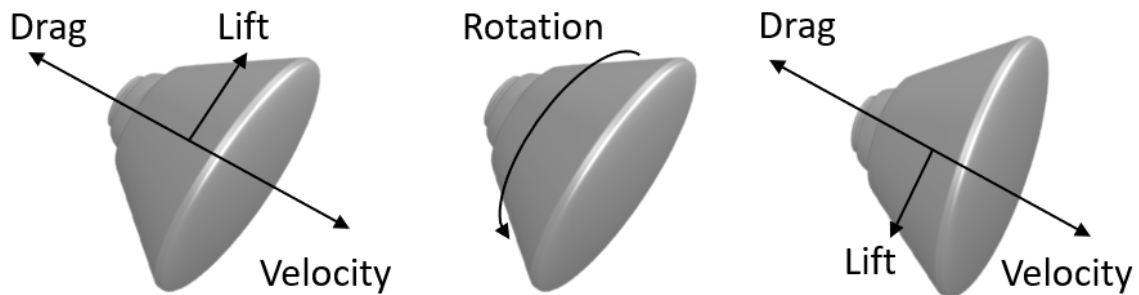
FIGURE 2.9: Bank Angle Modulation Logic [81]

As the total magnitude of lift remains constant, when the lift component in the vertical plane is reduced, the lift component in the horizontal plane increases. This lateral plane motion causes the vehicle's heading angle (defining where the vehicle is pointing in the horizontal plane) to change, causing it to turn. For this reason, the bank angle must occasionally be reversed from positive to negative to ensure no crossrange error accumulates. During the Gemini Program, two different guidance techniques were tested to control the capsule between 120 km and 25 km altitude, where parachutes were deployed:

1. Constant Bank Angle Technique

2. Zero Lift Range Prediction Technique

The constant bank angle technique uses a predefined bank angle and sign reversal logic in order to control the range along a computed trajectory to the target. The zero lift range prediction technique predicts terminal errors, immediately tries to eliminate them, and then follows a ballistic trajectory. While the constant bank technique is more sensitive to L/D uncertainties, the zero lift technique works even if there's no L/D value knowledge since it would steer the capsule toward the target independently from this information. A summary of Gemini Missions landing errors is presented in Table 2.1 [82].

TABLE 2.1: Gemini missions landing errors.
* indicates the presence of mission failures

Flight Mission	Guidance Technique	Landing Errors [km]
III	Zero Lift	110*
IV	\\	81.5*
V	Constant Bank	168.5*
VI	\\	13
VII	\\	12
VIII	Zero Lift	2
IX	\\	0.7
X	\\	6
XI	\\	4.8
XII	\\	4.8

The Russian Soyuz Capsule, which first flew in 1967 and is still the only operative spacecraft capable of carrying astronauts to the International Space Station (ISS) and back to Earth, works exploiting similar principles. The control system consists of a CoM offset and a roll control through a Reaction Control System (RCS). The Soyuz provides both nominal controlled re-entry and emergency ballistic re-entry (see Figure 2.10). While the landing accuracy for a controlled descent is on the order of 28 km, the capsule can fall up to 600 km short with respect to the targeted landing site [83].

For the Apollo program, a skip entry guidance algorithm was developed. The
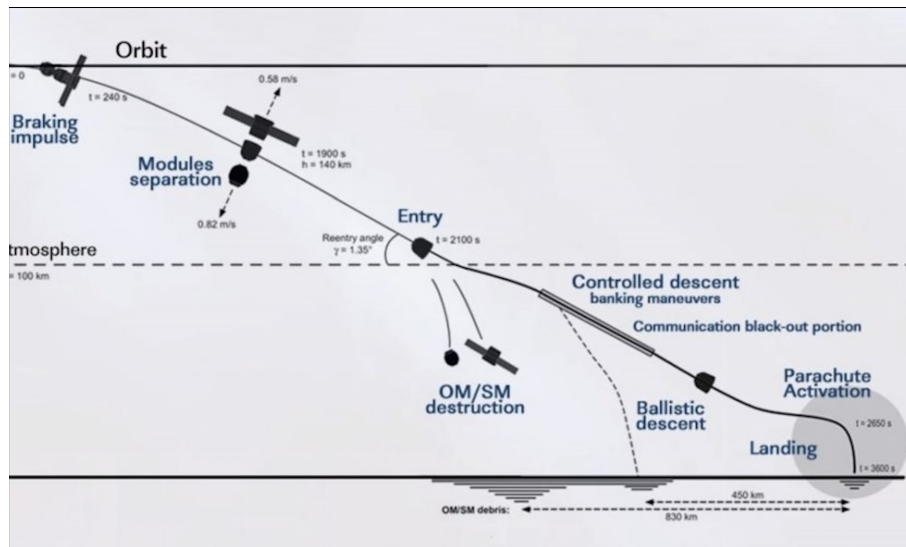
FIGURE 2.10: Soyuz re-entry phases

opportunity to perform this kind of re-entry led to augmented mission flexibility in terms of re-entry conditions and target locations. The control methodology was also robust to atmospheric and vehicle uncertainties [84] [85].

The Apollo Guidance scheme is divided in several components. The navigation module reads data from on-board sensors and propagates vehicle's state vector. Using this navigation data, the mode selector utilizes different components of the algorithm depending on the vehicle's flight conditions (Figure 2.11).

The first phase is the Initial Roll. An initial orientation, either lift up or lift down, is determined and set during a constant drag phase until an altitude rate threshold is passed.

The following phase is the Huntest. It is an optional phase and represent the analytical predictor-corrector component of the Apollo skip guidance. In this phase, a reference trajectory corresponding to a constant L/D value is computed iteratively such that the final miss distance is less than 46 km. When the true range-to-be-flown is equal to the target range or there is an undershoot, an L/D reference value to correct the trajectory is computed and utilized in the following
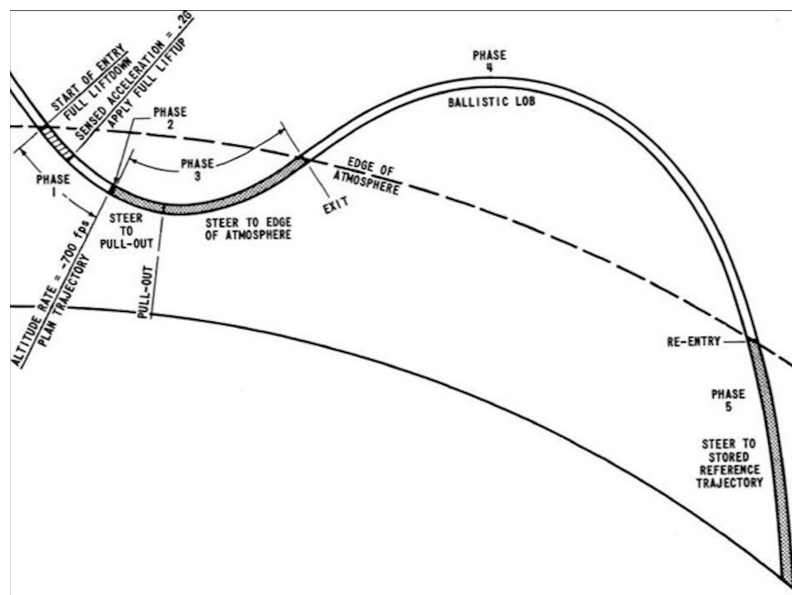
FIGURE 2.11: Apollo re-entry phases

phase.

The UpControl and Ballistic phases are optional phases too. An L/D command is produced such that the capsule performs a skip and is projected out of the atmosphere at a previously computed pull-out point. Until the atmospheric re-entry, the capsule is in the Ballistic phase, maintaining a zero degree bank angle. As soon as the spacecraft returns to the atmospheric environment, the final phase is activated.

The Final Phase involves the tracking of a pre-computed reference trajectory using a gain-scheduled PID controller. These kinds of algorithms are usually referred to as "Terminal Point Controllers". During this phase, if the target is passed, a full lift down is commanded. Pilot chutes are deployed at about 3 km altitude, pulling three main parachutes from their containers and leading the capsule to a splash-down landing.

During the final phase, the guidance algorithm uses a PID controller whose gains are the derivatives of range with respect to the:

- altitude rate, called next as $F2(V)$;

- drag, called next as $F1(V)$;

- L/D ratio, called next as $F3(V)$;

velocity V is the independent variable for all the three gains.

The expression to predict the final range is [86]:

$$s_{pred} = s_{ref}(V) + F2(V)[\dot{h} - \dot{h}_{ref}(V)] + F1(V)[D - D_{ref}(V)] \qquad (2.1)$$

where s is the range, V is the velocity, h is the altitude, D is the Drag, $()_{pred}$ refers to the predicted quantities and $()_{ref}$ to the reference values. The predicted range is used in order to compute the commanded L/D:

$$\frac{L}{D} = \left(\frac{L}{D}\right)_{ref} + 4\frac{s_{des} - s_{pred}}{F3(V)} \qquad (2.2)$$

Since for any bank angle other than 0 degrees or 180 degrees there is a horizontal component to the lift vector, a periodic bank reversal is required to prevent the accumulation of cross-range errors. A bank reversal is commanded whenever the cross range exceeds a specified threshold (see Figure 2.12).

The commanded bank angle is:

$$\sigma_c = K2 \arccos\left(\frac{L/D}{(L/D)_{max}}\right) + 2\pi K1 \qquad (2.3)$$

where $K1$ and $K2$ are indicators for switching the bank angle sign, and $(L/D)_{max}$ corresponds to the maximum achievable L/D value.

To date, the only operative manned re-entry capsule is the Russian Soyuz. While the U.S. aerospace company SpaceX is developing the reusable spacecraft "Crew Dragon" (or "Dragon 2"), based on the design of the original cargo spacecraft "Dragon", NASA and ESA are developing another crew vehicle called the "Orion"
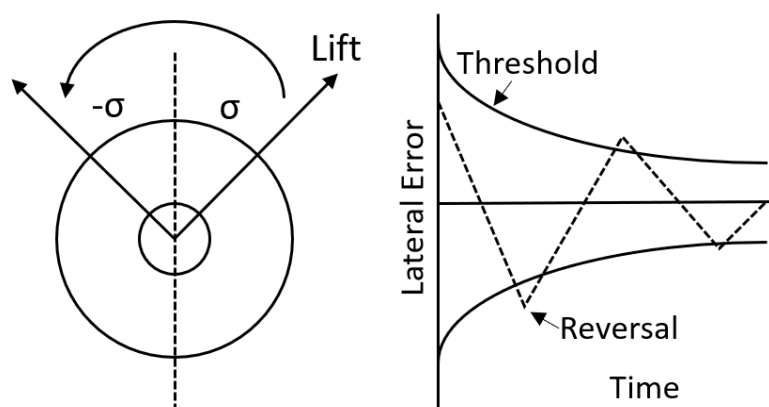
FIGURE 2.12: Bank Reversal Strategy

for LEO, Lunar and Mars missions. The Orion spacecraft presents itself as a scaled up and upgraded version of the Apollo command module. Two guidance algorithms have been developed for the Orion. The first is for a Lunar Return Skip Entry and the second is for an ISS/LEO Return Direct Entry. The latter has already been tested by NASA using a high-fidelity 6DOF simulator and achieved good results. Manual controls have been implemented and tested as well [87].

Starting from the Apollo guidance strategy, a numerical predictor-corrector (NPC) has been implemented in the algorithm since its analytical approximations led to low accuracy. The NPC addition greatly improves long-range accuracy for lunar return and brings minor improvements to LEO return performance.

For the LEO lifting atmospheric entry, Orion will use the PredGuid entry guidance algorithm [88].

After parameter initialization and a targeting routine which updates the vectors from vehicle to the target site (range-to-go and heading error) are run, the main phases of the guidance algorithm begin.

The first phase, referred to as Initial Roll, commands a constant attitude, based on current velocity and target direction, while the NPC minimizes the error at the transition with the following phase. The algorithm simulates a constant L/D trajectory to the final phase transition by numerically solving equations of motion

using a 4th order Runge-Kutta integration scheme with a 5Hz call rate. After this, an averaging algorithm performs a smooth transition, in terms of commanded bank angle, to the following phase.

The Final Phase is an Apollo-like reference-following terminal point control algorithm which guides the vehicle to the desired landing site by using a control law that utilizes a pre-derived influence coefficient stored on board and the errors with respect to a nominal trajectory. In addition, a g-limiter is used to control the acceleration experienced by the capsule. The limiter filters the commanded Bank Angle and is activated if the drag is more than half the load limit. If the limit is exceeded, a full lift up is commanded. During this phase, target landing site overflight is checked too. If the vehicle overflies the target, full lift down is commanded to reduce range error at the drogue deploy altitude.

During the Terminal Phase, which starts when the spacecraft velocity is 300 m/s, the remaining range error is minimized by pointing the vehicle directly at the target landing site. A simple guidance law with bank commands directly proportional to vehicle heading error is used for this phase. The Lateral Logic strategy used on Apollo is also utilized on the Orion.

Minimal literature exists regarding control techniques for capsules with deployable heat shields. The only flight experiment designed to test some control capability for this type of capsule was IRVE 3 [34]. As shown in Figure 2.13, the center body still houses the inflation system, but also contains a CoM offset mechanism.

The CoM offset mechanism allowed IRVE-3 to launch with its CoM on the axis of the launch vehicle, as required for launch stability, but re-enter with the CoM shifted to one side to produce a lift vector. Such a lift vector is typically used to steer a reentry vehicle toward a desired landing site, but IRVE-3 kept the vector fixed during reentry to measure the effect of the known lift vector on the trajectory. The CoM offset mechanism used a DC motor to laterally shift the
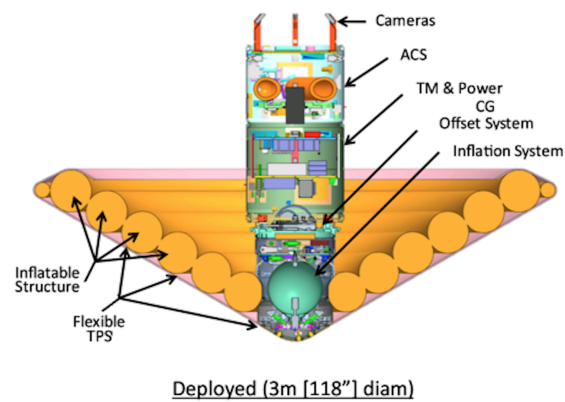
FIGURE 2.13: IRVE 3 CoM Offset System (CG in the figure) [34]

aft portion of the center body, about half the reentry vehicle mass, relative to the inflation system and the inflatable aeroshell. After the reentry experiment concluded, the CoM offset mechanism shifted the vehicle CoM four more times to provide data on the dynamic response of the vehicle trajectory to changes in the CoM location.

2.3   Dynamic Stability Problem Overview

Capsule stability can be defined as the property to maintain a specific attitude during the flight. There are two type of stability: static and dynamic stability. A capsule is statically stable when, as it is perturbed from its equilibrium position, the aerodynamic forces and moments acting on it tend initially to return it to the original position whereas it is statically unstable if it has the tendency to continue in the direction of the displacement. However, the capsule can also be neutrally stable if it has a tendency to neither return to the equilibrium nor to continue in the direction of the movement. An example of static stability principle is depicted in Figure 2.14.
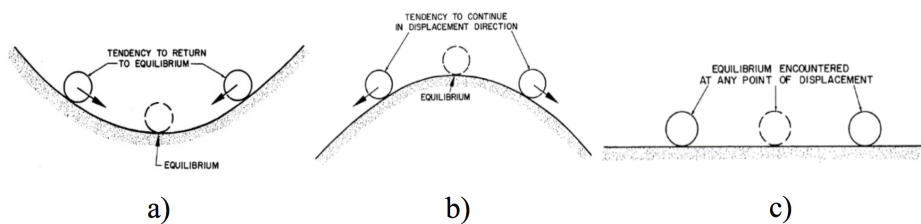
FIGURE 2.14: Static Stability Example: a) Statically Stable, b) Statically Unstable, c) Neutrally Stable

Dynamic stability is how an object responds over time to a disturbance that displaces it from a condition of equilibrium. The oscillations, due to dynamic stability, typically occur as the capsule tries to return to its original position or attitude. Even though the object may be statically stable, it could be dynamically stable, unstable or be characterized by a neutral dynamic stability as it is showed in Figure 2.15.

The capsule is dynamically stable when the oscillation, caused by a certain disturbance, dampens out over time, whereas it is dynamically unstable when the oscillations are amplified over time and it has neutral dynamic stability when oscillations never dampens out.
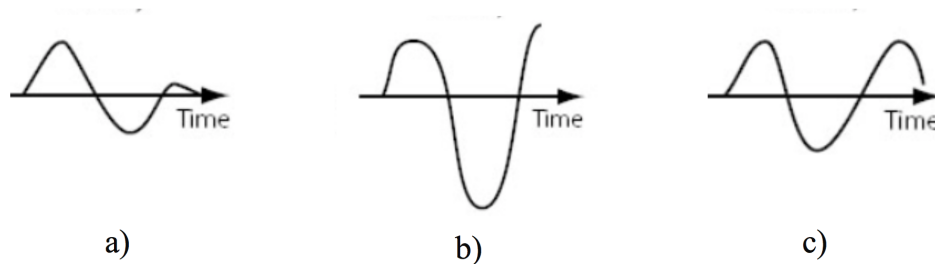
FIGURE 2.15: Dynamic Response Example: a) Positive Dynamic Stability, b) Negative dynamic stability, c) Neutral Dynamic Stability

Designing a capsule is a complex, multi-faceted problem. Every part of it contributes to the success of the project, starting from the TPS to the shape of the object, to the trajectory and so on. The dynamic behavior of the capsule is also an important issue that must be faced during the development of the re-entry capsules. In fact, the attitude of a capsule should be aligned along the velocity direction during the whole re-entry trajectory both to protect the payload and to ensure for example the deployment of a parachute. However, many capsules must maintain the attitude without any active control system and, therefore, only relying on their own aerodynamic stability. When the centre of mass of such vehicle is located forward of the centre of pressure, the capsule is statically stable in general, as it is demonstrated in [89] and [90].

On the contrary, dynamic stability is not granted, in particular in the transonic speed range, where it falls into self-excited pitching oscillation.

Most of the capsule geometries suffer dynamic instability in the transonic regime that could trigger a tumbling or an excessive oscillation that can be difficult to be recovered in the subsonic regime. Initial investigations into the phenomenon of dynamic stability as applied to blunt bodies began in the 1950s as the development of ballistic missile and space exploration technologies gained momentum. However, due the drastically different operational environments and geometries of entry vehicles, engineers lacked intuitive insight into the problem

at the early stages. The studies that have been made during the years highlighted the unpredictable nature of blunt body dynamic stability, its sensitivity to geometric and environmental variables, and the difficulties associated with determining the stability parameters analytically, numerically, or experimentally.

With the intuition gained from static stability experiments, one of the first trade studies regarding dynamic stability involved varying the location of the centre of gravity. In several studies has been demonstrated that the dynamic stability would benefit on the CoM axial motion toward the nose. For instance, Ericsson in [91] confirmed this behavior founding that the amplitude and angle of attack range of the instability region decreased as the CoM was moved axially toward the nose. Another example is found in [92] where experimental data on the stability of a sphere cone capsule with $45°$ semi aperture angle in both transonic and subsonic regime are shown. The transonic tests have been carried out on the same geometry with two different CoM locations, at $25°$ and $30°$ of diameter (Model L-25 and L-30 respectively). The paper shows that the capsule L-25 is always stable for AoA larger than $5°$ and that the L-30 is stable only at AoA larger than $17°$-$18°$, as it is showed in Figure 2.16.
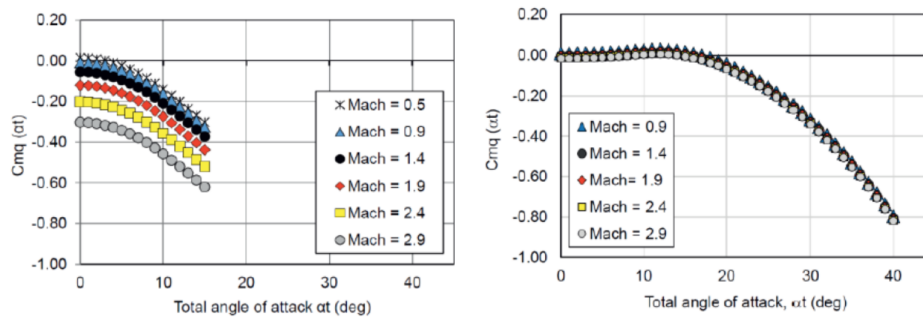
FIGURE 2.16: Cmq with respect to total angle of attack for the model L-25 (on the left) and model L-30 (on the right) for various Mach numbers

The presence of an aftbody greatly affects the resulting dynamic response of a body. This is clearly showed in [93] and [94], where $30°$ sphere cone and parabolic

shaped bodies at subsonic and supersonic conditions were tested, respectively. In fact, the presence of the aft-body decreases damping for all Mach numbers investigated, with the effect being more pronounced at lower Mach numbers for the parabolic body and consistent across all Mach numbers for the sphere cone with the small aft-body (top plot of Figure 2.17).
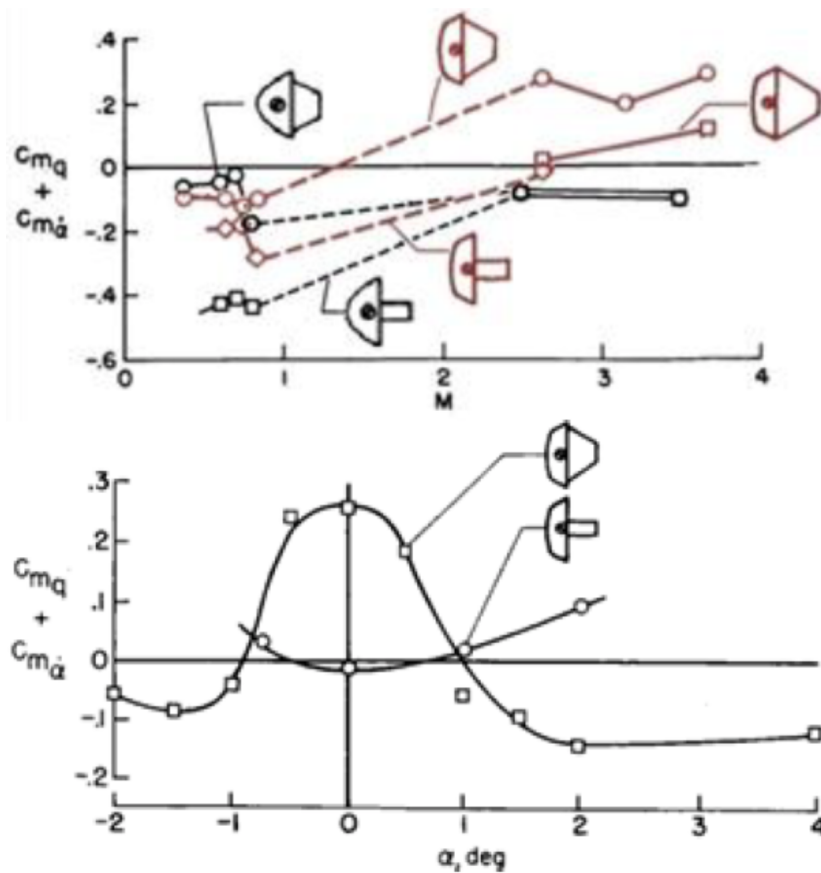
FIGURE 2.17: Effect of an aftbody on damping with Mach number (top) and angle of attack (bottom)

When the aft-body size was increased for the sphere cone at M = 2.5 the detrimental effects seem to be greatly reduced. Looking at the lower plot in Figure 2.17 the effect of angle of attack is demonstrated. Alone, the sphere cone forebody is approximately neutrally stable between -1° and 1° while the vehicle with the aft-body is highly unstable at these low angles of attack. As the incidence

angle increases, however, the vehicle with the aft-body becomes stable and the damping sum of the fore-body alone configuration drifts further positive and becomes unstable.

The effect of Mach number is dependent on the configuration being studied [95] [96] [97] [98]. In hypersonic, damping exhibited remains relatively constant with Mach number and is typically stable or neutrally stable. Between the hypersonic and subsonic regimes, the damping begins to decrease and the body generally becomes unstable, with a peak in the instability usually occurring between Mach 3 and Mach 1. As the vehicle approaches the transonic regime, a second instability spike is often found and then the damping increases again as the vehicle decelerates through subsonic speeds. While the effect of Mach number is clear, the effect of Reynolds number has been looked at thoroughly in the literature with inconclusive and contradictory observations. Negligible influence has been noted for various geometries over the decades.

Strouhal number (Sr, St, or k), also known as the "reduced frequency parameter," is a non-dimensional scaling parameter calculated using the relationship below:

$$k = \frac{2\pi f l}{V_\infty} \tag{2.4}$$

where $2\pi f = \omega$ is the angular velocity of the oscillatory motion (in rad/s), l is the characteristic length (diameter for blunt bodies) and V_∞ is the free stream flow velocity. Note that a factor of 2 in the denominator is occasionally used in the literature.

This scaling parameter captures the relative magnitude of the frequency content of a body oscillatory motion to the mean rate at which the free stream flow passes over the body. As the interactions of the resulting flow structure and the aft-body of a vehicle are critical to dynamic stability, matching of k during sub

scale testing of dynamic behavior is important for estimating limit cycle behavior and identifying any possible resonance frequencies that may be responsible for excitation of pitching oscillations. The effect of the reduced frequency parameter on dynamic stability value can be found in [99], where a correlation between k and the pitch damping sum ($Cm_q + Cm_\alpha$) of the BLDT configuration of the Viking capsule has been studied. As showed in Figure 2.18, increasing k leads to a better damping characteristic of the capsule.
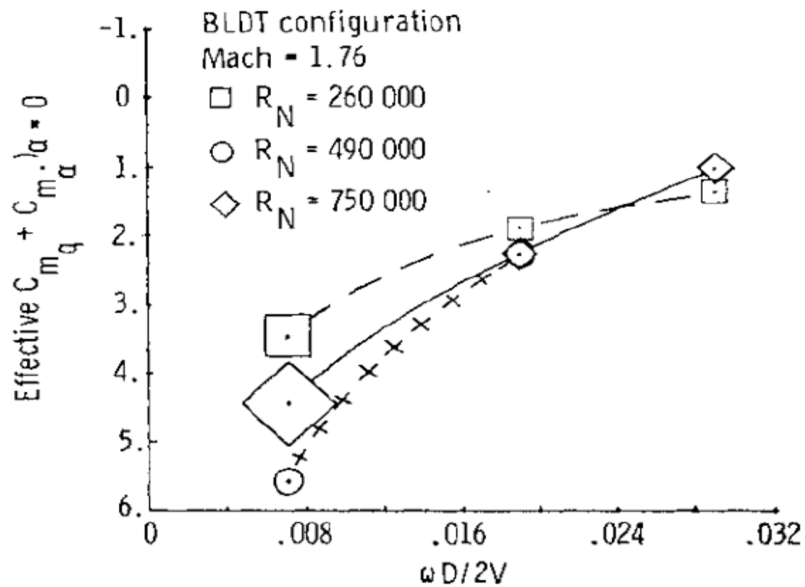
FIGURE 2.18: Effect of reduced frequency parameter on damping

Chapter 3

Mission and System Description

3.1 Reference Mission

3.1.1 Mission Objective

MINI Irene is the Flight Demonstrator of IRENE, a new-concept capsule with a variable geometry able to return payloads from the ISS to Earth and/or to perform short-duration, scientific missions in Low Earth Orbit (LEO) and/or to perform Earth Observation missions.
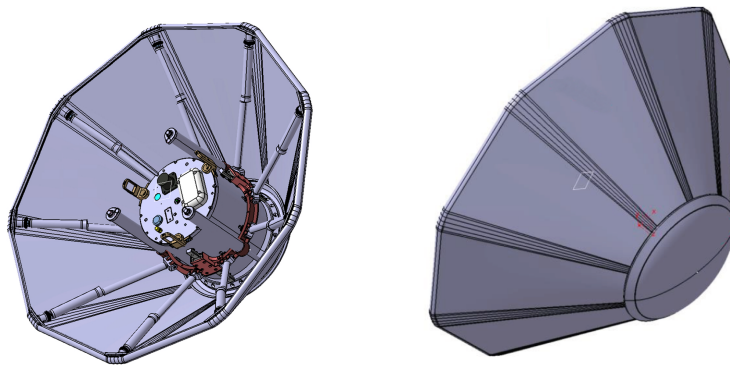
FIGURE 3.1: Mini Irene Capsule

Mini-Irene represents the technological demonstrator of IRENE whose innovative thermal protection system is characterized by a deployable, disposable

"umbrella-like" heat shield that allows relatively small dimensions at launch and a sufficient exposed surface area in re-entry conditions, reducing the ballistic coefficient and leading to acceptable heat fluxes, mechanical loads and final descent velocity. The Mini-Irene mission consists in performing a sub-orbital flight with this technological demonstrator exploiting a sounding rocket as a launcher. The Mini-Irene Capsule objective are:

- Survive the launch

- Separate from the rocket;

- Deploy the heat shield before the re-entry phase;

- Maintain aerodynamic stability and structural integrity during the flight;

- Acquire and store data during the flight (pressures, temperatures, accelerations, attitude);

- Endure (only the payload) the re-entry environmental conditions and the impact with the ground;

- Be localized after landing allowing the retrieval of the spacecraft and of the data collected in flight.

The Mini-Irene project also includes a Ground Demonstrator (GD) whose main purpose is the simulation on ground of severe conditions expected in flight and testing of the TPS performance under such conditions. The MINI-Irene ground demonstrator therefore is fully representative of the FD heat shield and is conceived to be tested in a Plasma Wind Tunnel. The FD shall have a heat shield of 76 cm of diameter in open configuration. The flight test shall be representative of the aero-mechanical part of the flight but not of the thermal part of a LEO re-entry. The GD shall be representative of the material and of the mechanisms of

the FD in order to achieve an overall TRL (Technology Readiness Level) equal to 6.

3.1.2 Mission Description

The capsule will be dropped by the payload stage of a VSB-30 Rocket (see Fig. 3.2 3.3), some seconds after the burn out of the second stage during the ascent, which occurs at 59 s from the lift off at an altitude close to 72.5 km.
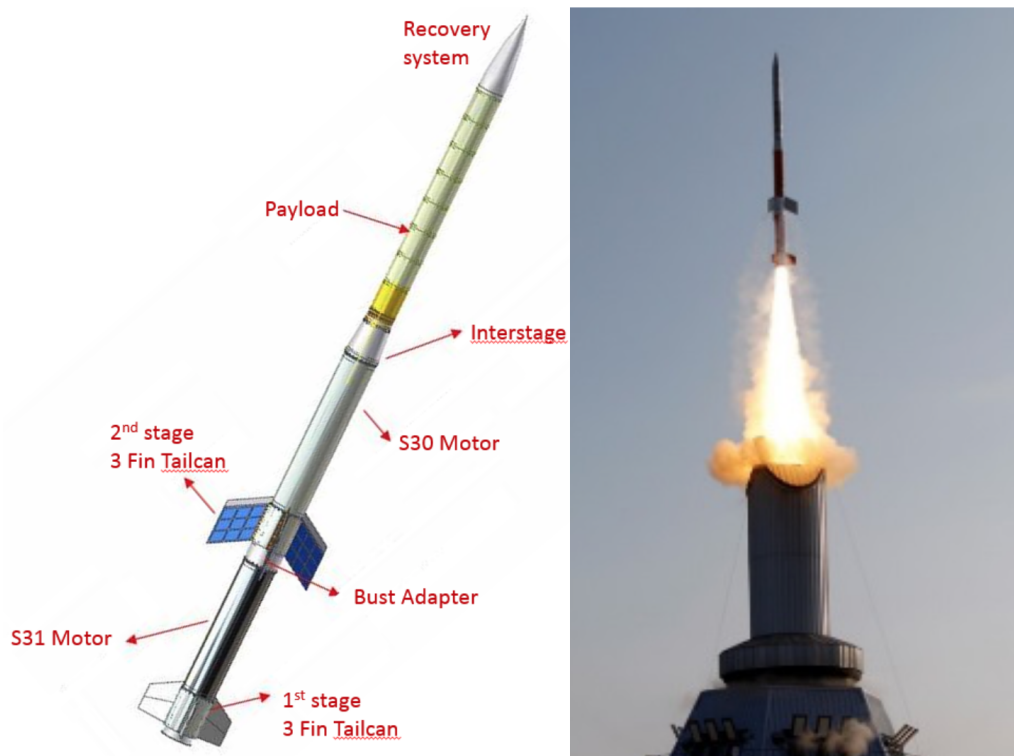
FIGURE 3.2: From left to right: The VSB30 Rocket; a launch from ESRANGE base

The flight would continue up to a 250 km altitude. The landing is scheduled 860 s after the separation from the Launcher.
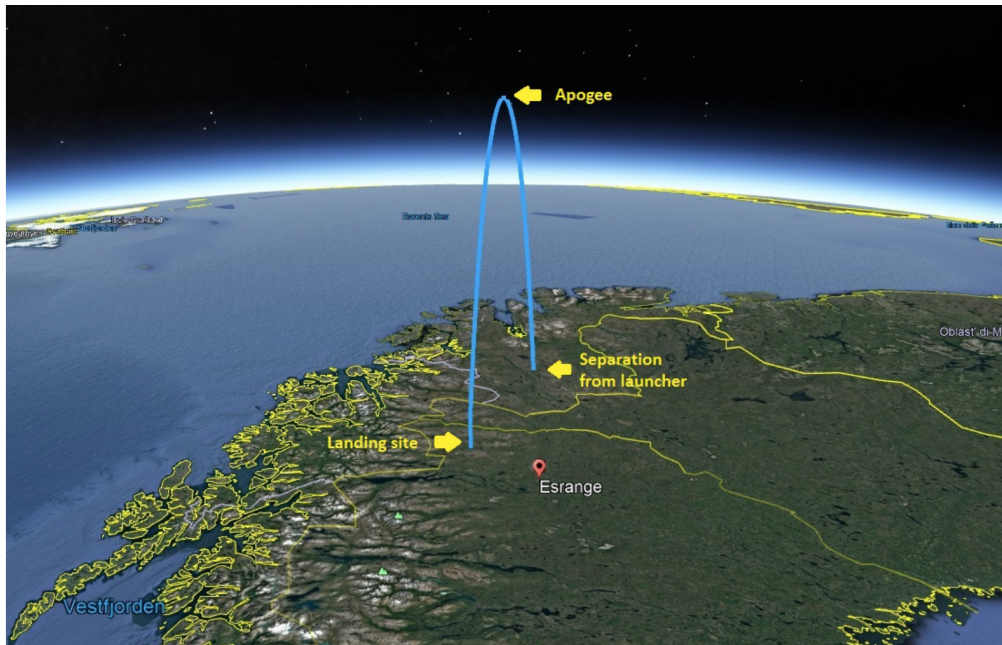
FIGURE 3.3: MIFE expected trajectory

The diagrams presented in Fig. 3.4 compare the dynamic pressure, the acceleration and the heat flux experienced by a capsule with the same mass and geometry in three different scenario: a LEO re-entry trajectory, on a MAXUS flight test and on a typical VSB-30 flight test (i.e. MAPHEUS).

The VSB-30 sounding rocket flight is not sufficiently energetic for achieving significant heat fluxes on the TPS. Because of this, a PWT test is needed in order to achieve TRL 6 in a relevant environment. The Ground Demonstrator that will be tested in PWT will be representative not only of the materials, but also of the mechanisms of the flight model. While the PWT test carried on in 2001 was a test on the materials, the current test is a test on the TPS and deployment mechanisms subsystem and shall be executed for matching as much is possible the real LEO re-entry thermal environment. Even if not representative of the thermal part of the flight, the analyses show that the aerodynamic environment encountered in the VSB-30 flight is very close to the LEO entry. The flight will then prove the
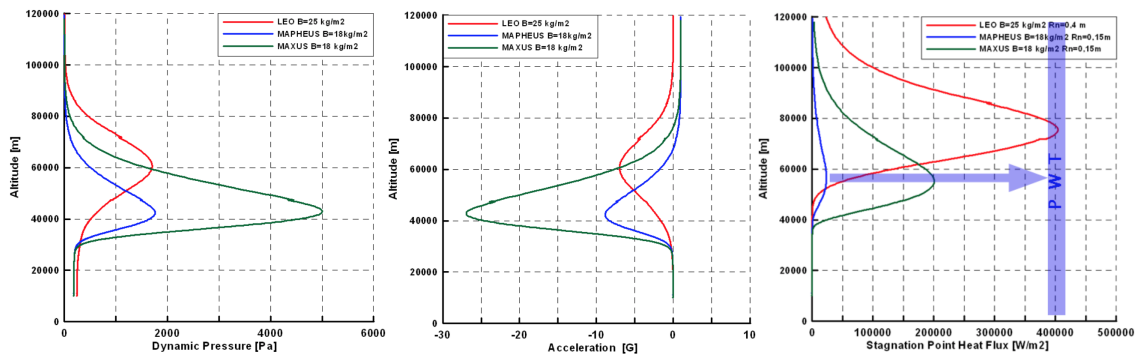
FIGURE 3.4: Dynamic pressure, acceleration and heat flux experienced by a same capsule in a LEO re-entry trajectory, on a MAXUS flight test and on a VSB-30 flight

structural worthiness of the whole system and the aerodynamic characteristics. It is here important to underline that the previously planned MAXUS flight was less representative of the LEO entry because even if it is more energetic the LEO fluxes are not matched, while the aerodynamic environment is excessively severe because of the steepness of the trajectory.

3.2   System Element Description

3.2.1   Deployable Mechanisms

One of the critical element of a deployable capsule is the deployable mechanism. The solution designed and implemented for the Mini-Irene project is based on a two phase deployment.

In a first phase the poles of the structure extends and are locked in the extended position. In this phase the flexible TPS is still lose. Then the ring where the poles are hinged slides along the avionic bay and preloads properly the TPS in its re-entry configuration.
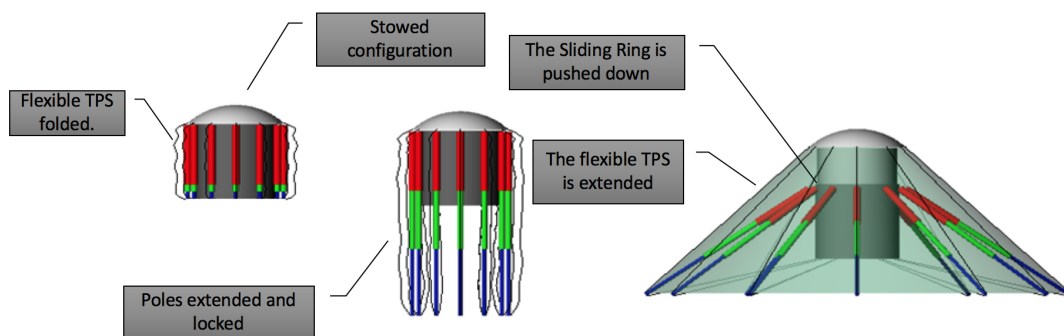
FIGURE 3.5: Deployment Concept

The systems utilizes gas springs for both the phases of the deployment. The gas springs are a well consolidated industrial technology and are produced in space qualified version too. The best benefit of the gas springs is that they are a compact system that provides at the same time the energy for the deployment and the damping capability.

The heat shield deployment is actuated by two different systems of gas springs, namely, 9 Umbrella Gas Springs (UGS) and 3 Nose Gas Springs (NGS). The two

systems of gas springs are activated simultaneously by the same Frangibolt device that is located in the middle of the Bottom Plate of the Main Body of the capsule. The separation of the two phases is achieved tuning differently the damping of the UGS and NGS. The NGS shall be more damped than the UGS and, because a slower deployment, will achieve the final TPS configuration when the UGS are already extended and locked.

The NGS's are not equipped with a similar locking mechanism, which, instead, is present on the external wall of the Payload Bay to lock the Sliding Ring, which is displaced by the NGS's.

The main parts of the deployment system are shown in the following simplified image.
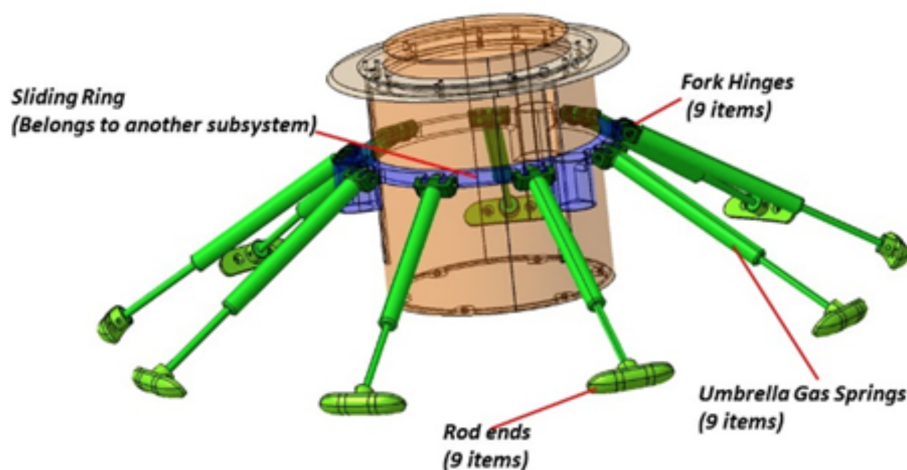
FIGURE 3.6: Main parts of the deployment system

In order to have a precise degree of stretching of the Skirt, a number of packed Belleville springs are placed inside the rod end of each Umbrella Gas Spring. Such Belleville springs, shall accommodate small deformations of the parts and can help distribute the tension in the fabric. The Second phase of the deployment is achieved displacing the sliding ring with respect to the avionic bay.

The Sliding Ring is pushed down by the three NGS's, partially visible in the image. The NGS's bodies are placed inside the reaction tubes.
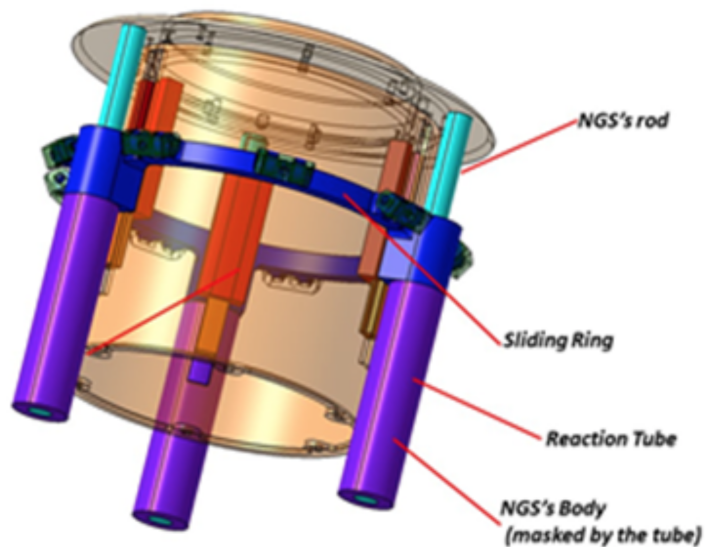
FIGURE 3.7: Umbrella Tensioning Mechanism

The Sliding Ring is connected to the NGS's Bodies through the Reaction Tubes. These three components have two main tasks:

- To transfer the force from the bottom of the NGS's Bodies to the Sliding Ring, avoiding any structural connection with the cylindrical wall of the NGS's Bodies, but only through the final plug of the Reaction Tube (in order to avoid any customization of commercial gas spring);

- To create a radiative shield and reduce the amount of radiative thermal power transmitted from the hot surface of the Nextel fabric to the NGS's bodies.

The Sliding Ring slides on three parallel rails, which bear all the components of the loads but the axial one. This way the NGS's will bear the axial component

of the load. This characteristic, joined with the high stiffness of the guides, is very useful in two cases:

- When the push of the NGS's is different from one to another.

- When asymmetric dynamic loads are applied to the fabric in the re-entry phase.

In order to accommodate minor misalignment between the three rails, that could prevent a smooth sliding, sets of Belleville springs are installed between the rails and the avionic bay.
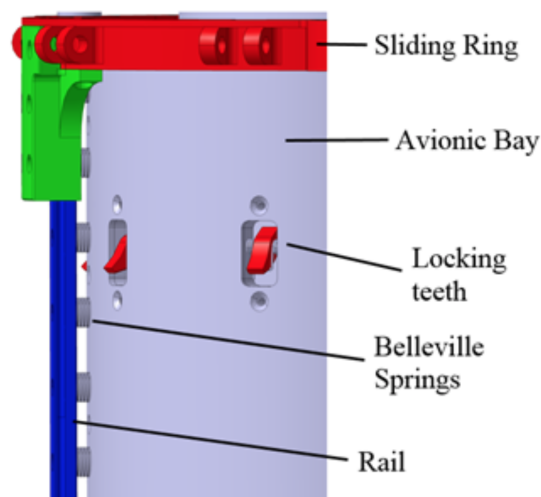
FIGURE 3.8: Detail of the Locking Teeth and rails springs

The UGS's are equipped with a locking device on their own that prevents the springs to retract, once they have reached their maximum elongation. Conversely, the NGS's are not equipped with a similar locking device. Instead, safety Locking Teeth are present on the external wall of the Payload Bay to lock the Sliding Ring, after it has been displaced by the NGS's (see next figure). Such Locking Teeth prevent the Skirt to completely collapse, in case of failure of one or more NGS's. In this case only a loss of preload of the TPS occurs.

3.2.2   Multi-Layer Thermal Protection

The thermal protection system (TPS) is a complex subsystem of both the Flight and the Ground demonstrators. In fact it will be substantially the same for the two models, with the sole difference that in the Ground demonstrator the maximum diameter of the skirt will not be larger than 600 mm, in order to avoid clogging problems in the Plasma Wind Tunnel test facility.

The TPS is composed by three main sections:

- Foldable Part

- Nose

- Internal Thermal Protections

The main component of the Foldable part is the Skirt which is composed by several layers of Nextel 312 AF10 whose characteristics are fully described in [100]. Also the sewing thread and the reinforcement bands will be made out of Nextel fibers as well.

The flexible TPS is the key element of the IRENE concept. The Nextel material has been identified as optimal material in past IRENE activities. Various test have been executed including a Plasma Wind Tunnel test in CIRA SCIROCCO facility and the material has always shown excellent performances, from both the thermal and structural point of view. The woven fabric identified is the AF-10. It is realized with the 312 fiber and has the most tight wowing and lowest permeability. Following images shoes some diagrams from the 3M official documentation.

Sewing of the Nextel and the interface between fabric and structure have been a critical aspect of the MINI IRENE design. In order to understand the Nextel behavior in these two conditions, a dedicated campaign have been carried out. Three different possible way to realize the umbrella have been conceived:

FIGURE 3.9: Examples of Nextel Fibers
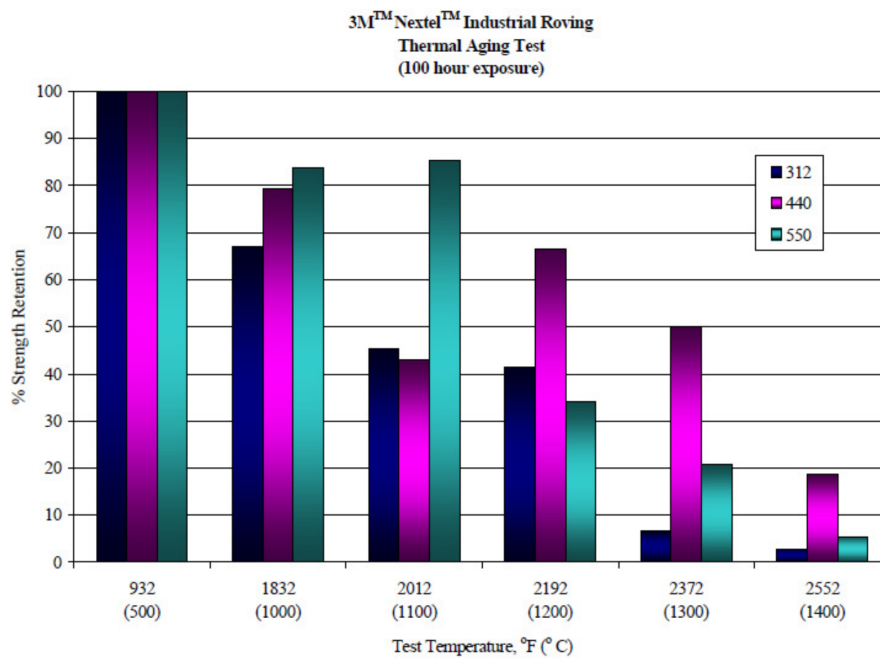
FIGURE 3.10: Nextel Thermal Aging Test
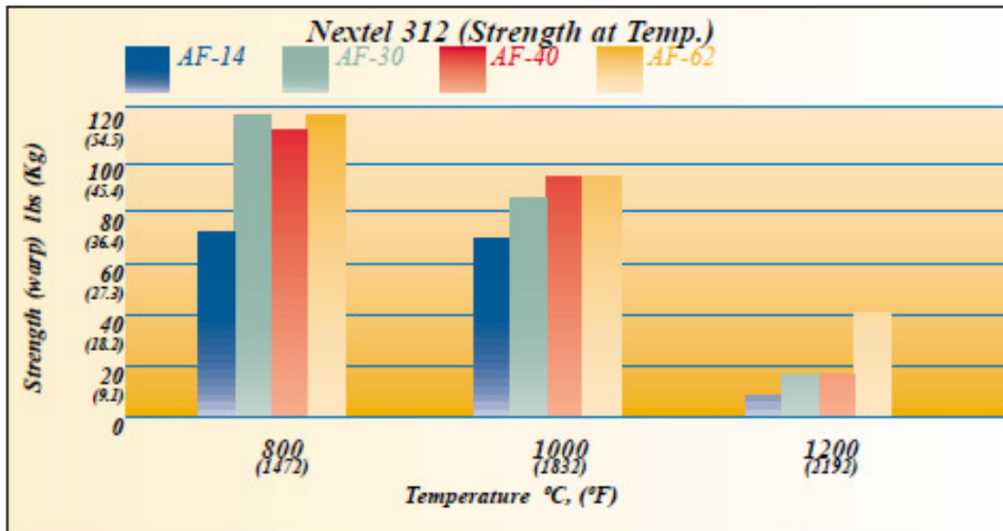
FIGURE 3.11: Nextel 312 Strength at Temperature

- One piece TPS

- Nine sectors joined on the rods

- Nine sectors joined in the middle of the flat faces

The following image shows three paper model that help understanding the warp and fill topology on the three-dimensional structure.
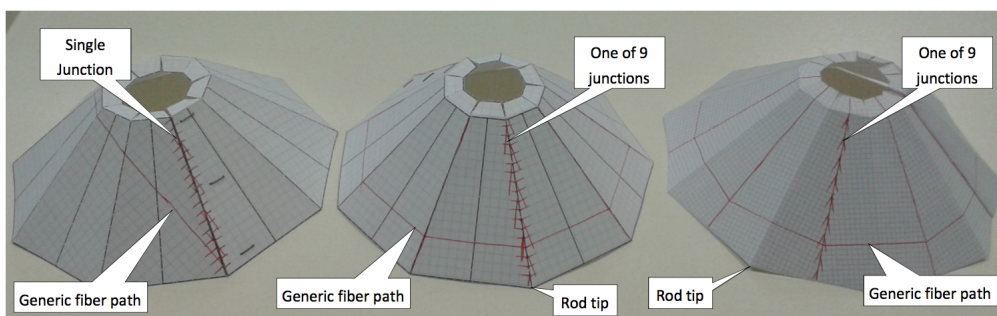
FIGURE 3.12: Possible warp and fill topology

The following table shows the pro and contra of the three proposed solutions:

After a test campaign the third solution, nine sectors joined in the middle of the flat faces, have been chosen and implemented.

Solution	Pro	Contra
One piece TPS	Minimum number of sewing. Less weak points. Easier folding.	The sectors have different fibre orientation. The cuts needed on the Nose encounter fibers at 45° also
Nine sectors joined on the rods	All sector will behave identically. On the nose all fibers are parallel.	More sewing. Sews in correspondence of the rods.
Nine sectors joined in the middle of the flat faces	All sector will behave identically No sewing on the rod tips	On the nose the longitudinal fibers have to be cut.

TABLE 3.1: Pro and contra of the three fill topology

Three number of layers have been selected after thermal analysis to compose the flexible skirt and additional Nextel tape have been used for reinforcing the critical areas around the rod tips.

The following image shows the effectiveness of Nextel fabric as thermal barrier.

The Nextel clothes are characterized by permeability. The Nextel handbook [100] provides a value of permeability that is measured in given pressure conditions.

The permeability is actually the felicity of the air flowing through an unitary surface of material, for a given pressure differential.

Darcy laws also model the phenomena with a linear behavior of the velocity with respect to the pressure differential. In order to evaluate the permeability in flight conditions the following simple equation can be written:

$$V_P = V_{P0} \left(P / P0 \right) \tag{3.1}$$
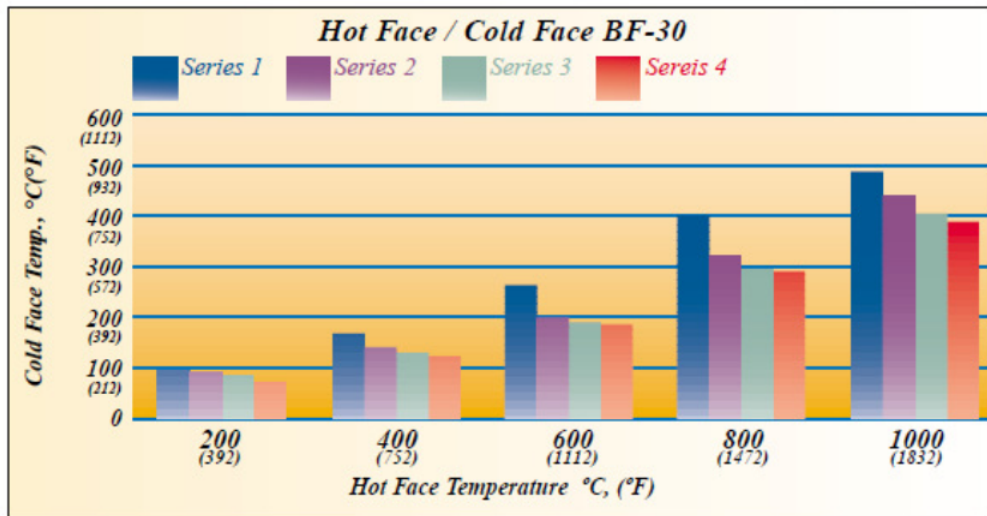
FIGURE 3.13: Nextel thermal resistence

Where $P0$ is the pressure jump in test conditions, V_{P0} is the permeability at the test pressure jump, P is the flight pressure jump and V_P is the permeability at the flight pressure jump.

The following diagram shows the results of permeability test carried on one layer of AF-10 Nextel. Diagram shows that at 2kPa pressure a permeability of 0.5-0.55 m/s is expected.

The following table resumes some of the data collected and calculates the permeability at 2KPa with Darcy law:

The energy flowing through the Nextel, under very conservative hypothesis can be evaluated as:

$$q = \rho V_P h \tag{3.2}$$

Where ρ is the air density and h is the total enthalpy of the free stream current; it can be assumed equal to $V_\infty^2/2$. In the peak heat flux conditions, for a LEO reentry trajectory from ISS, at 75km altitude:
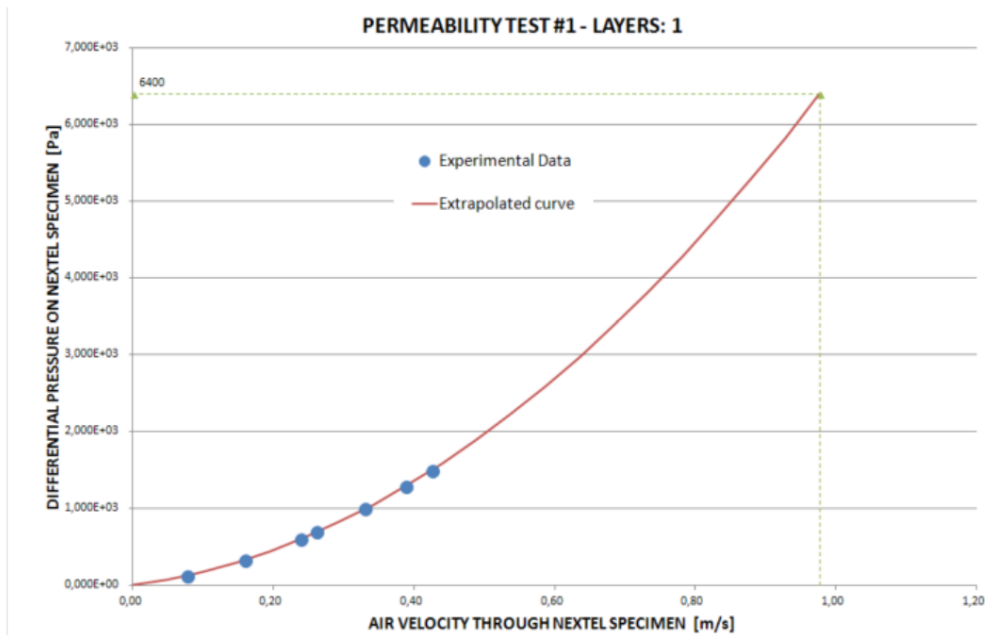
FIGURE 3.14: Permeability test results carried on one layer of AF-10
Nextel

V_{P0} [m/s]	P [Pa]	P0 [Pa]	V_P [m/s]	Source
0.0767	2000	125	1.23	Datasheet
0.0767	2000	200	0.77	Datasheet
0.08	2000	112	1.43	Past IRENE activities
0.43	2000	1488	0.58	Past IRENE activities

TABLE 3.2: Nextel Permeability

$$\rho = 2.27 \cdot 10^{-05} kg/m^3 \tag{3.3}$$

$$V_\infty = 6000 m/s \tag{3.4}$$

$$h = 18 MJ/kg \tag{3.5}$$

The heat flux passing through the TPS is here calculate:

$$q = 583 W/m^2 \tag{3.6}$$

That is a negligible heat flux if compared to the expected radiative heat flux. For comparison, a 65°C surface with 0.8 emissivity radiates more than 590 W/m^2.

The fabric of the skirt is shaped in the form of a truncated cone, with seams parallel to the cone slope (radial seams).

The radial seams of each layer will be located at different azimuth positions around the cone, not to weaken the skirt too much locally. Radial reinforcement bands are foreseen over the radial seams and were tensile stresses are stronger, i. e., at the UGS,'s end locations. The Skirt is fixed on the structure beneath the nose and at the UGS's ends. Beneath the nose, the skirt rim houses a drawstring, which has the twofold function to ease the skirt fixation and to prevent the slippage of the fabric under the Skirt Holding Ring. The Skirt Holding Ring fixes the upper part of the Skirt firmly distributing the force of nine Clamps uniformly on the fabric portion clamped between the Nose Plate and the Skirt Holding Ring itself. The Nose Plate rim is properly rounded, in order to avoid an excessive stress concentration on the fabric.

At the other end of the Skirt (the larger base of the cone) the fabric is wrapped around nine FD Fixation Inserts. Thanks to the rounded, elongated shape of these

parts the load on the fabric is best distributed. The longitudinal cross section of the FD Fixation Inserts is characterized by sections with different radiuses of curvature: the radius of the central section is equal to the radius of the base of the cone; the radiuses of the lateral sections becomes smaller and smaller as one moves aside. This is made to accommodate, without sharp angles, skirt deformations of variable size due to the external air pressure during the descent phase.

The nose is the rigid part of the heat shield. Several improvements have been made with respect to the design made in the first phases of the IRENE program.

Property	Rescor 310M (99% pure Silica) SiO_2
Max. operating Temp. (°C)	1650
Density (g/cm³)	0,80
Thermal expansion (10⁻⁶/°C)	0,54
Elastic Modulus (GPa)	73*
Compressive Strength (Kg/cm²)	84
Flexural Strength (Kg/cm²)	36,4
Resistivity (Ohm/cm)	10^9
Loss factor (@ 1 MHz)	0,0002
Dielectric constant (@ 1 MHz)	3,17
Thermal Conductivity (W/m·K)	0,187
Porosity (%)	63

* Data valid for the bulk material

FIGURE 3.15: Rescor 310M Properties

Past tests at the SPES facility of University of Naples and at the PWT facility of CIRA on material demonstrated the very good thermal performance of Rescor 310M for its intended application as the nose of our capsule. A drawback of these comparatively cheap nose designs, however, is that the silica foam has rather poor mechanical properties. As such it is prone to chipping, particularly where sharp edges are present. Therefore, only quite bulky parts can be machined out of

Cat. No.   Size
310M - 1 . . . . 4.5" x 6" x 9" .
310M - 2 . . . . 4.5" x 9" x 12"
310M - 3 . . . . 4.5" x 12" x 18"
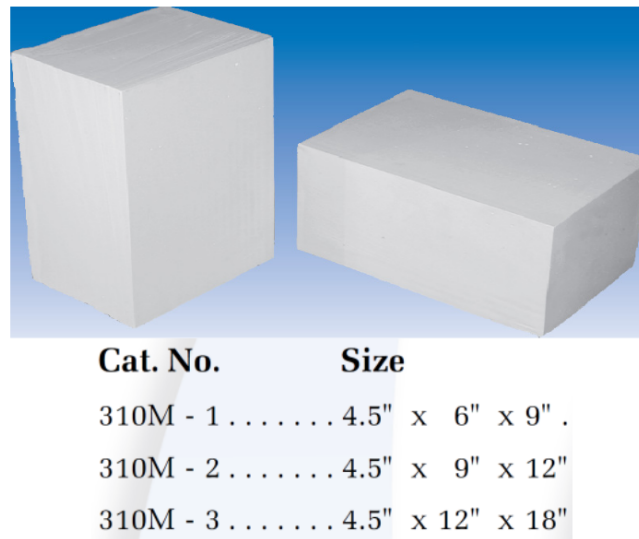
FIGURE 3.16: Commercially available blocs of Rescor 310M

this material. Here the nose is composed by two main parts, the Dome, which is made out of Rescor 310M, and the Frame, which is made out of an Oxide-Ceramic Matrix Composite (O-CMC), namely, Keramikblech FW 12, whose characteristics are reported in the following tables and graph.

This design, again, displays an ellipsoidal profile but exploits the best thermal properties of Rescor 310M in the area around the stagnation point and the best mechanical properties of O-CMC on the nose rim, making it possible to realize a much more slender shape, saving both mass and space. Moreover, this construction makes the mounting operations much easier because the nose can be fixed on its supporting structure (the Nose Plate) by means of three screws instead of ropes. In fact metallic, threaded inserts are embedded in the Connection Pillars of the O-CMC Frame. Now the space saved beneath the nose can be occupied by the heaviest portion of the payload compartment, contributing to displace the CoM forward.

For the best thermal insulation of the payload compartment, the Payload Bay is mechanically connected to the Nose Plate but is thermally isolated from it by

Mechanical properties of standard O-CMC materials developed by WPS and Fraunhofer ISC/HTL

	CerOx AZ-N6-F Keramikblech® FW12	CerOx AS-N7-F Keramikblech® SA12
Manufacturing technique	Lamination & mould technique	Lamination & mould technique
Fibre type	NextelTM 610 / corundum DF11 woven fabric	NextelTM 720 / corundum-mullite EF11 woven fabric
Matrix composition	Al_2O_3/ZrO_2	Al_2O_3/SiO_2
Density [g/cm³]	2,9	2,5
Fibre volume content [%]	35-45	35-40
Open porosity [%]	25-35	30-35
3-point bending strength at RT [MPa] (DIN EN 658-3)	300-500	150-200
Interlaminar sheer strength ILS at RT [MPa] (DIN EN 658-5)	20	12

FIGURE 3.17: Mechanical Properties of standard O-CMC material

means of nine spacers made of thermally insulating material, which dramatically reduce the heat flux transmitted by conduction from the nose to the Payload.

The Dome is fixed on the frame by means of a proper high-temperature bonding paste.

The main function of this part of the TPS is to protect the payload/avionics compartment from excessive heating during the descent phase. In fact, this compartment receives heat through all of the three heat transmission mechanisms:

- By conduction, from the nose plate

- By radiation, from the internal surface of the skirt

- By convection, from the aft flow and, in a smaller amount, from the flow passed through the fabrics of the Skirt

The first source of heat is limited by the thermally insulating spacers through which the Payload Bay is connected to the Nose Plate. In addition a thermally

"Keramikblech" Type	FW12
Fibre (Fabric)	Nextel 610/1500 denier (DF11)
Matrix	85% Al_2O_3 / 15% 3YSZ
Bending strength [MPa] at room temperature	310-320 [2], [1]
Young's modulus (bending) [GPa] at room temperature	92 [2], [1]
Tensile Strength [MPa] at room temperature	190 [3]
Young's modulus (tension) [GPa] at room temperature	122,8 [3]
Compression strength [MPa] at room temperature	207 [2]
Young's modulus (compression) [GPa] at room temperature	123 [2]
Shear strength (ILSS) [MPa] at room temperature	17 [2]
Thermal expansion [10^{-6} 1/K]	
25-300 °C	6,94 [1]
25-600 °C	7,69
25-900 °C	8,17
25-1100 °C	8,49
Thermal conductivity [W/mK]	
300 °C	3,80 [1]
600 °C	2,81
900 °C	2,30
1100 °C	2,02

FIGURE 3.18: O-CMC Material Characterization
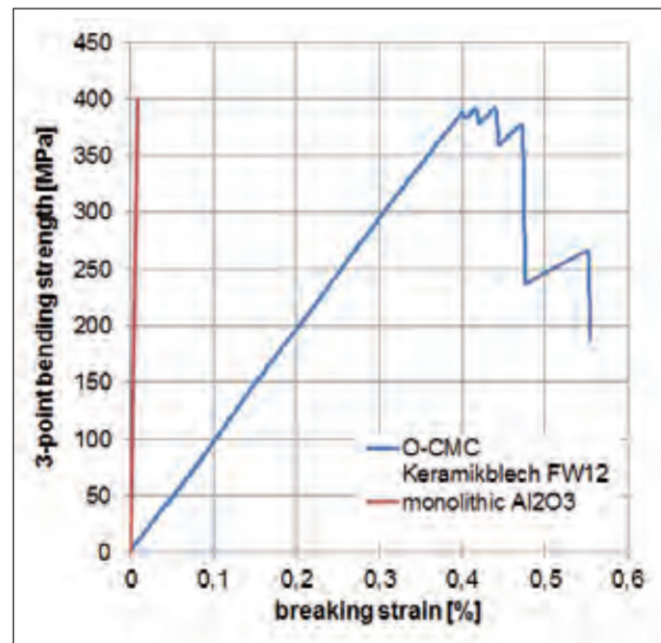
FIGURE 3.19: 3-point bending strength of Keramikblech FW12 compared with monolithic Al_2O_3
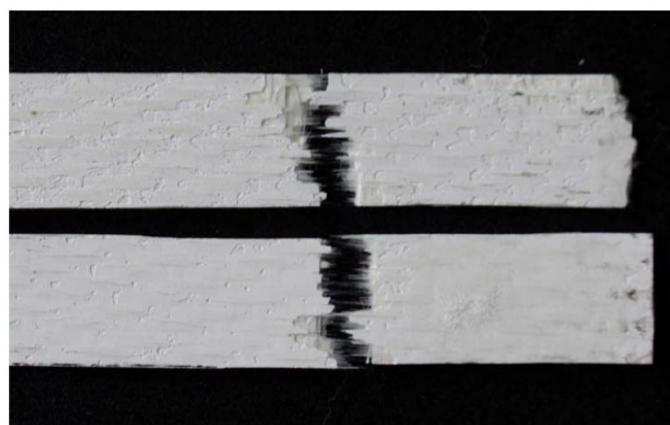
FIGURE 3.20: Samples of Keramikblech FW12 broken by bending

insulating blanket is foreseen between the upper surface of the Payload Bay and the Nose Plate/Frame subsystem.

The second and third heat transmission mechanism are inhibited by an high-emissivity barrier coating the entire lateral surface of the Payload Bay.

For the suborbital mission it is not needed an internal protection system. The PWT test will not accommodate avionics, but the structure still need protection. Since the radiation is the main source of heating for the structures below the umbrella, all the sensitive parts shell be coated with a reflective adhesive tape.

SHELDAHL
A Multek Brand

Aluminum
Polyimide
Acrylic (3M™ 966) PSA

PRODUCT BULLETIN

First Surface Aluminum Coated Polyimide Tape with Acrylic 3M™966 Adhesive

TAPES

Sheldahl® Brand Materials first surface aluminized polyimide tape with acrylic 3M™ 966 adhesive is used whenever a low emittance and low solar absorptance surface is needed. The acrylic 3M™ 966 adhesive is nominally 2.3 mils thick, provides a strong bond with low outgassing, and can be used over a moderate temperature range. These tapes may be bonded to structures to reduce radiative heat transfer. They can also be used on multilayer insulation blankets to close the edges or repair rips in the outer layers.

This product may be ordered with 0.5, 1, or 2 mil thick polyimide that conforms to the requirements of ASTM D-5213. The aluminum coating is nominally 1000 Å thick. Although the standard widths for this tape are 1, 2, 3, and 4 inches, it may be ordered in any width needed. Each roll is 108 feet (33 m) long.

PRODUCT CHARACTERISTICS

Parameter (independent of film thickness)	Specified Value
Solar absorptance (α)	≤ 0.14
Hemispherical emittance (ε_H)	≤ 0.035
Normal emittance (ε_N)	≤ 0.035
Typical α/ε	4 - 5
Adhesion to stainless steel	≥ 20 oz./inch of width
Intermittent temperature range	-185° C to 230° C (-300° F to 450° F)^A
Continuous temperature range	-60° C to 120° C (-75° F to 250° F)^A

^{A} Zero peel strength of acrylic pressure sensitive adhesive is at about –45°C (-50°F).

FIGURE 3.21: Reflective Tape Features

Part III

Methodology and Tool

Chapter 4

Flight Mechanics Tools

The high fidelity simulation environment utilized to perform mission analysis studies and to test the algorithms discussed in this thesis consists of two components. The orbital simulator is utilized to compute the spacecraft's trajectory during its orbital phase (above 100 km) and contains high fidelity gravitational and density models. The re-entry simulator models the trajectory below 100 km and more precisely characterizes the re-entry aero-thermodynamic environment experienced by the capsule. Two different simulator have been developed for the re-entry part. The first is a three degree of freedom simulator utilized to evaluate trajectories and perform Monte Carlo analysis. The second is a six degree of freedom simulator utilized to perform attitude and dynamic stability analysis.

4.1 Orbital Simulator

During the orbital phase of a satellite's trajectory, the dynamic pressure experienced by the satellite is low, and the aerodynamic environment is one of free molecular flow where the mean free path between particles is large and particles do not interact with each other. While the drag coefficient for a given satellite

geometry is not expected to change significantly during this regime, large atmospheric density variations can occur due to changes in solar and geomagnetic activity [101]. In addition, because a satellite may spend weeks or months on orbit during a period of interest, the perturbations due to the non-uniform gravitational field of the Earth can have a significant long-term effect and must be taken into account. To the scope of this work, solar pressure, solar gravity, lunar gravity, relativity, atmospheric winds, tidal effects, and Earth precession and nutation were not found not be significant and were not considered. Only aerodynamic drag and Earth's gravity were precisely modeled in this orbital simulator, but all algorithms in this work were designed to be usable in a higher fidelity simulation environment such as STK [102] if a higher accuracy is desired.

4.1.1   Gravitational Model

The simplest gravitational model assumes that the Earth is a point mass and that gravity always acts toward the center of earth. With this two-body model, the acceleration due to gravity is based on the ECI position of the satellite (**r**) and is given by Eq. 2.1 (pp. 15) in Ref. [103] as

$$\mathbf{a}_g = -\frac{\mu \mathbf{r}}{r^3} \tag{4.1}$$

where μ is Earth's gravitational parameter. A more realistic gravitational model provides $\mathbf{a}_g$ as the cumulative effect of gravitational perturbations. These perturbations are divided into zonal harmonics which capture variations in Earth's gravity at different latitudes, sectorial harmonics which capture longitude-dependent gravitational effects, and tesseral harmonics which capture gravitational effects that are dependent on both longitude and latitude [104]. Gravitational models such as EGM2008 [105] provide the normalized gravitational coefficients (C and

S) that are utilized to calculate the gravitational potential function at a given location. This can be done using Eq. 3.28 in Montenbruck's book (pp. 66-68) [103].

$$U = \frac{\mu_e}{R_\oplus} \sum_{n=o}^{\infty} \sum_{m=0}^{n} (C_{nm} V_{nm} + S_{nm} W_{nm}) \tag{4.2}$$

Where C_{nm} and S_{nm} are the coefficients of degree n and order m given by the EGM2008 model and V_{nm} and W_{nm} satisfy the recurrence relations

$$
\begin{aligned}
V_{mm} &= (2m-1) \left[\frac{xR_\oplus}{r^2} V_{m-1,m-1} - \frac{yR_\oplus}{r^2} W_{m-1,m-1} \right] \\
W_{mm} &= (2m-1) \left[\frac{xR_\oplus}{r^2} W_{m-1,m-1} + \frac{yR_\oplus}{r^2} V_{m-1,m-1} \right]
\end{aligned}
\tag{4.3}
$$

and

$$
\begin{aligned}
V_{nm} &= \left(\frac{2n-1}{n-m} \right) \frac{zR_\oplus}{r^2} V_{n-1,m} - \left(\frac{n+m-1}{n-m} \right) \frac{R_\oplus^2}{r^2} V_{n-2,m} \\
W_{nm} &= \left(\frac{2n-1}{n-m} \right) \frac{zR_\oplus}{r^2} W_{n-1,m} - \left(\frac{n+m-1}{n-m} \right) \frac{R_\oplus^2}{r^2} W_{n-2,m}
\end{aligned}
\tag{4.4}
$$

The acceleration of the spacecraft due to gravity is the gradient of the potential function in Eq 4.2 and can be written in Earth-Centered-Earth-Fixed (ECEF) Cartesian coordinates as [103]

$$\ddot{x} = \sum_{n,m} \ddot{x}_{nm}, \ddot{y} = \sum_{n,m} \ddot{y}_{nm}, \ddot{z} = \sum_{n,m} \ddot{z}_{nm} \tag{4.5}$$

where

$$
\begin{aligned}
\ddot{x}_{nm} &\overset{(m=0)}{=} \frac{\mu}{R_\oplus^2} \left[-C_{n0} V_{n+1,1} \right] \\
\ddot{x}_{nm} &\overset{(m>0)}{=} \frac{\mu}{2R_\oplus^2} \left[-C_{nm} V_{n+1,m+1} - S_{nm} W_{n+1,m+1} \right. \\
&\quad + \frac{(n-m+2)!}{(n-m)!} \left. (C_{nm} V_{n+1,m-1} + S_{nm} W_{n+1,m-1}) \right]
\end{aligned}
\tag{4.6}
$$

$$\ddot{y}_{nm} \stackrel{(m=0)}{=} \frac{\mu}{R_\oplus^2} \left[-C_{n0} W_{n+1,1} \right]$$

$$\ddot{y}_{nm} \stackrel{(m>0)}{=} \frac{\mu}{2R_\oplus^2} \left[-C_{nm} W_{n+1,m+1} + S_{nm} V_{n+1,m+1} \right. \tag{4.7}$$

$$\left. + \frac{(n-m+2)!}{(n-m)!} \left(-C_{nm} W_{n+1,m-1} + S_{nm} V_{n+1,m-1} \right) \right]$$

$$\dot{z}_{nm} = \frac{\mu}{R_\oplus^2} \left[(n-m+1) \left(-C_{nm} V_{n+1,m} - S_{nm} W_{n+1,m} \right) \right] \tag{4.8}$$

If considering a gravity model of degree 0, only the $C_{00} = 1$ term is considered and Eq. 4.1 is recovered for $\mathbf{a}_g$. The gravitational perturbation of degree two and order zero associated with the coefficient C_{20} is known as the J_2 perturbation and while three orders of magnitude smaller than the two body gravitational acceleration, is larger than the next biggest gravitational perturbation by approximately three orders of magnitude.

If J_2 or higher degree effects are included in the gravitational model and the calculation of orbital elements is required, it is best to use mean orbital elements instead of the traditional osculating elements. The mean elements serve to average out the short periodic oscillations in the osculating orbital elements caused by the J_2 perturbation. Each osculating orbital element can be written as the corresponding mean orbital element plus the short term periodic variation due to J_2. The short term periodic variations of each element are given in terms of the current mean elements on pages 653-654 of Vallado's book [106].

4.1.2   Aerodynamic Model

Aerodynamic drag force is discussed in Vallado's book (pp. 549-570) and is calculated by [106]

$$\mathbf{F}_d = -\frac{1}{2} C_d A \rho v_{rel} \mathbf{v}_{rel} \tag{4.9}$$

where C_d is the drag coefficient, A is a reference area, ρ is the ambient density, and $\mathbf{v}_{rel}$ is the velocity of the spacecraft relative to the atmosphere. Substituting the ballistic coefficient defined in Eq. 6.14 into Eq. 4.9, the acceleration due to drag can be written as

$$\mathbf{a}_d = -C_b \rho v_{rel} \mathbf{v}_{rel} \tag{4.10}$$

Drag is by far the most difficult force to accurately predict due to uncertainties in C_d and ρ. Note that because the atmosphere tends to rotate with Earth due to viscous forces, $\mathbf{v}_{rel}$ is not the satellite's inertial velocity ($\frac{d\mathbf{r}}{dt}$). The atmosphere has an average rotation rate between .7 and 1.4 times Earth's rotation rate ($\omega_\oplus$) based on altitude and latitude [107] with a rotation rate generally between 1 and 1.2 $\omega_\oplus$ [107] at altitudes between 200 and 320 km (the range in which targeting usually takes place) . As such, it is reasonable to assume that the atmospheric rotation rate is $\omega_\oplus$. Taking this into account, the velocity vector of the satellite relative to the rotating atmosphere is [106]

$$\mathbf{v}_{rel} = \frac{d\mathbf{r}}{dt} - \omega_\oplus \times \mathbf{r} \tag{4.11}$$

where $\mathbf{r}$ is the spacecraft position vector measured in the ECI frame.

Assuming a completely specular reflection of particles whereby each particle collides elastically with the satellite, the drag coefficient has a lower bound of 2 for a sphere and an upper bound of 4 for a flat plate [108]. The particles in low earth orbit, however, do not exhibit completely specular reflection and ionization of the particles due to Earth's magnetic field also has an effect on the drag coefficient. Sophisticated models based on theory and actual satellite observations have been developed to more accurately calculate the drag coefficient [101] and will be considered in greater detail in future work. Additionally, the drag coefficient can be estimated based on the observed orbital decay of the satellite.

Density is a highly uncertain parameter in the drag force equation. Because
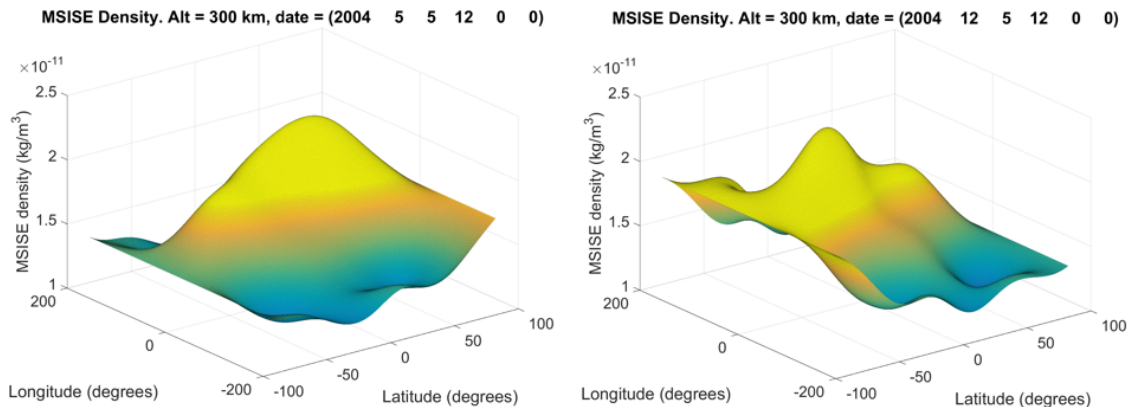
FIGURE 4.1: NRLMSISE-00 density around the Earth at a 300 km
altitude

density can vary by up to two orders of magnitude at a given altitude based on
time of day, latitude, longitude, and solar and geomagnetic activity as shown in
Figure 4.1, an atmospheric model such as the 1976 standard atmosphere that pro-
vides density as a function of altitude is not sufficient for the accurate simulation
of a drag-based maneuvering scheme. Instead, it is necessary to use models such
as DTM-2013, NRLMSISE-00, JB2008, or GOST17 that calculate the density at a
given location using a combination of solar and geomagnetic activity data, his-
toric satellite data, and atmospheric theories. The intricacies of these models are
discussed in greater detail in section 8.6.2 (pp. 549-570) of Vallado's book [106].

The NRLMSISE-00 model was utilized in this work because it is modern,
high performing [106], and an implementation is readily available in the MAT-
LAB aerospace toolbox. In addition to latitude, longitude, altitude, and time,
the NRLMSISE-00 model takes as inputs the F10.7 solar indices and the Ap ge-
omagnetic indices. Details about the inputs and implementation of MATLAB's
atmosnrlmsise00 function are provided on the MathWorks Website [109]. His-
toric F10.7 and Ap data can be found online at NASA's OmniWeb site [110]. For
the purposes of this work, a table of historic F10.7 and Ap values was created us-
ing the OmniWeb data and referenced every time the NRLMSISE-00 model was

called. 45 day forecasts of F10.7 and Ap are available online from the National
Oceanic and Atmospheric Administration (NOAA) [111]. Marcos et al. [112] dis-
cuss the accuracy of various density models by comparisons with satellite data.
Based on 69,932 density measurements on satellite between 200 and 620 km al-
titudes, the NRLMSISE-00 model exhibited a mean ratio of measured to actual
density of .9949 with a standard deviation of .1717.

4.1.3 Numerical Simulation Technique

To simulate the orbit of the spacecraft, the equations of motion are first written in
state space form and numerically integrated. The spacecraft state vector **x** consists
of the ECI (Earth-Centered Inertial) position and velocity.

$$
\mathbf{x} = \begin{bmatrix} \mathbf{r} \\ \\ \mathbf{v} \end{bmatrix}
\tag{4.12}
$$

where $\mathbf{r} = \begin{bmatrix} r_x & r_y & r_z \end{bmatrix}^T$, $\mathbf{v} = \begin{bmatrix} v_x & v_y & v_z \end{bmatrix}^T$. The ECI frame is defined as
aligned with the Earth-Centered-Earth-Fixed (ECEF) frame at the simulation epoch,
and the ECEF frame is assumed to rotate about the ECI z-axis (through the North
pole) at a constant rate of $\omega_\oplus = 7.292 \times 10^{-5}$ rad/s. The derivative of the state
vector in the ECI frame can be written as

$$
\dot{\mathbf{x}} = \begin{bmatrix} \mathbf{v} \\ \\ \mathbf{a} \end{bmatrix}
\tag{4.13}
$$

where **a** is the summation of the accelerations induced by all forces acting on the spacecraft. **a** can be computed by Newton's second law (assuming spacecraft mass is not changing) as

$$\mathbf{a} = \frac{\sum \mathbf{F}}{m} \tag{4.14}$$

Eq. 4.13 along with an initial state value are numerically integrated using MATLAB's ode113 [113] function which uses an Adams-Bashforth-Moulton multi-step predictor corrector method and was found to be faster than MATLAB's single-step ode45. The numerical integration process provides the evolution of the state vector over time in the ECI frame.

4.2   Re-Entry Simulator

A three and a six degree of freedom simulators were developed in SIMULINK to simulate the re-entry environment. The NRMLSISE-00 atmosphere model has been used to evaluate air density ρ and sound speed a values, depending on the current altitude, position and epoch. An aerodynamic database based on CIRA heritage projects is also used to help evaluate aerodynamic forces.

The core of the simulator is composed of the Equations of Motion block which takes aerodynamic forces as an input and integrates the differential equations of motion in order to compute the spacecraft's state over time.

4.2.1   Reference Frames

Since the objective of the simulation is to reproduce the motion of the re-entry capsule, the equations of motion must be integrated with respected to an inertial (non-moving) reference frame. The geocentric-equatorial Earth-centered inertial (ECI) reference frame (O, X, Y, Z) with its origin at the center of the planet, the

x-axis pointing in the direction of the vernal equinox, and the z-axis pointing through the North Pole is used for this. The y-axis completes the right-handed coordinate system and lies in the planet's equatorial plane.

Assuming the planet rotates with a constant velocity $\omega_\oplus$ around the z-axis, $\Omega = \omega_\oplus \Delta t$ represents the rotation rate between the inertial and the Earth-centered-Earth-fixed (ECEF) (X_R, Y_R, Z_R) reference frames. The two frames are aligned when $\Delta t = 0$.

In the ECEF reference frame, θ and ϕ represent the longitude and the geocentric latitude of the vehicle's position, respectively, while r represents the vehicle geocentric altitude (see Figure 4.2).

Note that the geocentric latitude ϕ is different from the geodetic latitude ϕ_G. while the first is defined as the angle between the radius r and the equatorial plane, the latter is defined as the angle between the local surface normal vector and the equatorial plane. This definition is related to distinction between "geocentric" and "geodetic" altitude (r and h respectively) as illustrated in Figure 4.3.
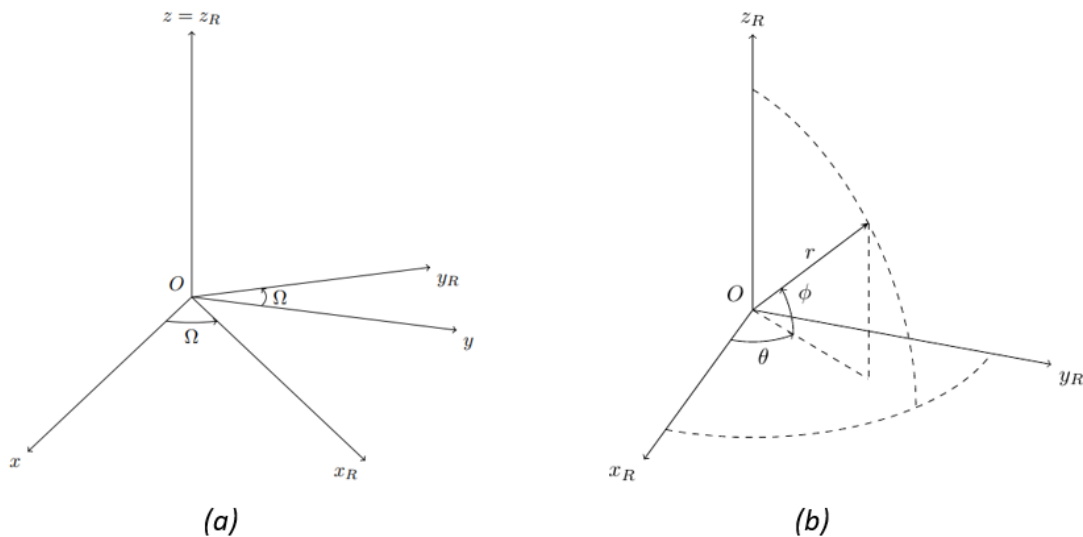
FIGURE 4.2: Inertial and Planet-Fixed reference frames (a), Vehicle pointing reference frame (b)
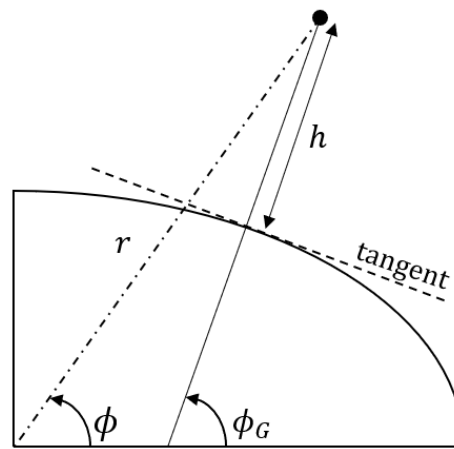
FIGURE 4.3: Geocentric and Geodetic reference frames

If a "local horizontal plane" is introduced as the plane perpendicular to the vector
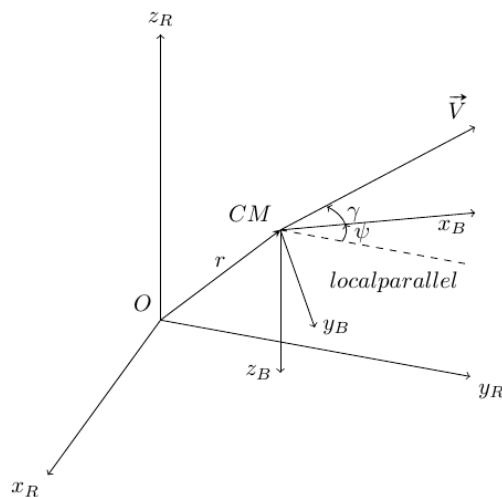
FIGURE 4.4: Body reference frame

from the surface of the Earth to the satellite at any given instant, the flight-path angle γ can be defined as the angle between the local horizontal plane and the capsule velocity vector $\vec{V}$. Similarly, the heading ψ is the angle between the local parallel of latitude and the projection of $\vec{V}$ on the horizontal plane.

By convention, γ is positive when $\vec{V}$ is above the local horizontal plane while ψ is increased when turns are made toward the left and is zero when facing east.
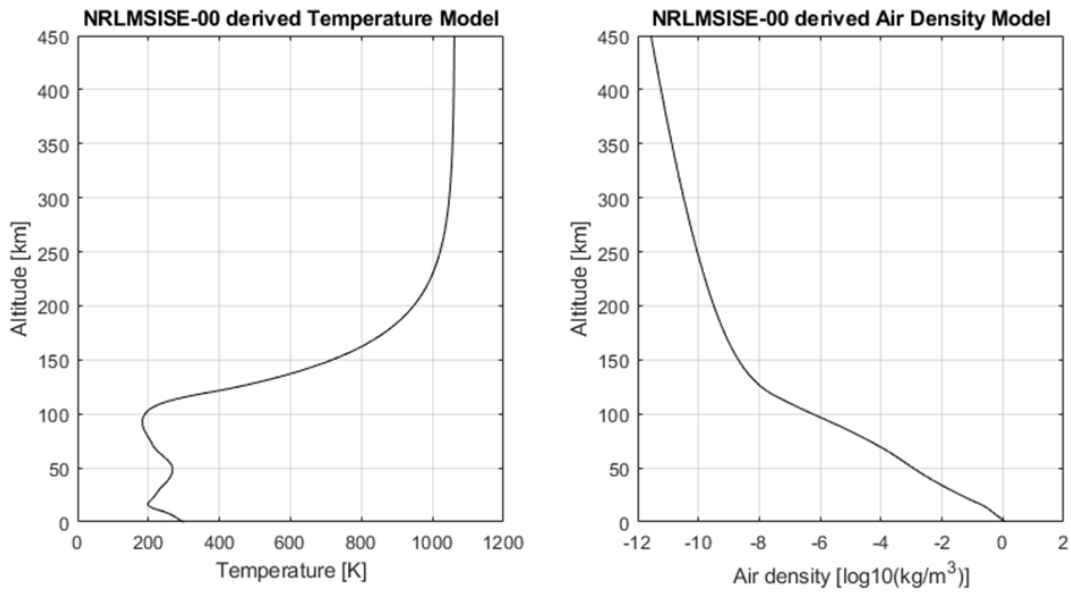
FIGURE 4.5: NRMLSISE-00 derived Temperature and Air Density
models

(CM, X_B, Y_B, Z_B) represents the body reference frame for the considered space-craft (see Figure 4.4).

4.2.2 Atmosphere and Gravitational Model

Different analytical and empirical atmospheric models exist for the computation of capsule re-entry trajectories. Their major objective is to provide air density ρ and temperature T values since these are essential for the computation of aerodynamic forces, Mach number, and other coefficients.

As in the orbital simulator, an empirical global reference atmospheric model called NRMLSISE-00 has been implemented in order to model density and airspeed values (see Figure 4.5).

As discussed in Sec. 4.1.1, the gravitational acceleration vector is given by the gradient of Eq. 4.2. Since the J_2 term is significantly larger than the higher order

$\omega_\oplus$	$7.292115 \cdot 10^{-5}$ *rad/s*
$R_\oplus$	6378137 *m*
μ	$3986004.418 \cdot 10^8$ m^3/s^2
J_2	$1.082629 \cdot 10^{-3}$

coefficients, a first or second order approximation is sufficient for re-entry modeling. When the J_2 effect is considered, the gravity vector remains in the plane containing the satellite position vector and the north pole but is given by two components. The first component is directed in opposite direction of the position vector $\vec{e}_r$, while the second is perpendicular to the position vector along the $-\vec{e}_\phi$ direction:

$$\vec{g} = -g_r \vec{e}_r - g_\phi \vec{e}_\phi \tag{4.15}$$

The two components are given by:

$$g_r = \frac{\mu}{r^2} \left[1 - \frac{3}{2} J_2 \left(\frac{R_\oplus}{r} \right)^2 (3 \sin^2 \phi - 1) \right] \tag{4.16}$$

$$g_\phi = \frac{3\mu J_2}{r^2} \left(\frac{R_\oplus}{r} \right)^2 \cos \phi \sin \phi \tag{4.17}$$

Comparing these two components, g_r (or z_g considering the vehicle-pointing frame) is considerably larger than g_ϕ (or x_g).

The Earth-related constants used inside the simulation are listed in Table 4.1.

4.2.3   Aerodynamic Forces

Aerodynamic forces can be decomposed in three main components: drag (D), lift (L) and side force (Y). Drag acts in opposite direction of the velocity vector.

Lift is perpendicular to the velocity vector, in the symmetry plane of the vehicle. Side force acts in the horizontal plane. While only drag is considered during the orbital simulation, all three aerodynamic force components are significant and must be considered during the re-entry.

The aerodynamic forces can be defined as:

$$D = \frac{1}{2}\rho(h)V^2 S C_D(\alpha, \beta, M) \tag{4.18a}$$

$$L = \frac{1}{2}\rho(h)V^2 S C_L(\alpha, \beta, M) \tag{4.18b}$$

$$Y = \frac{1}{2}\rho(h)V^2 S C_Y(\alpha, \beta, M) \tag{4.18c}$$

where C_D, C_L and C_Y are the non-dimensional drag, lift and side force coefficients while α and β are the spacecraft angle of attack and sideslip angles respectively. S represents the spacecraft reference surface area.

4.2.4 Heat Flux Model

In order to preliminary estimate hypersonic aerodynamic heating, the stagnation-point heat flux [kW/m^2] can be computed through the Tauber's engineering formula [114]:

$$\dot{q} = C \frac{1}{\sqrt{RN}} \sqrt{\rho} V^3 \tag{4.19}$$

where $C = 1.83e - 7$ is a constant and RN represent the nose radius of the spacecraft in meters.

4.2.5 Equations of Motion

A set of first order nonlinear ordinary differential equations is needed to simulate vehicle's 3DOF dynamics [115].

A set of 3 dynamic equations is needed to take into account forces acting on the spacecraft. Velocity, flight path angle and heading angle are the variables which describe vehicle's dynamic as:

$$
\frac{dV}{dt} = -\frac{D}{m} - z_g \sin\gamma + x_g \cos\gamma
$$
$$
+ r\omega_\oplus^2 \cos\phi(\cos\phi\sin\gamma - \sin\phi\sin\psi\cos\gamma) \tag{4.20a}
$$

$$
V\frac{d\gamma}{dt} = \frac{L}{m} - z_g\cos\gamma + x_g\sin\gamma\sin\psi + \frac{V^2}{r}\cos\gamma + 2V\omega_\oplus\cos\phi\cos\psi
$$
$$
+ rr\omega_\oplus^2\cos\phi(\cos\phi\cos\gamma - \sin\phi\sin\psi\sin\gamma) \tag{4.20b}
$$

$$
V\frac{d\psi}{dt} = \frac{Y}{m\cos\gamma} - \frac{V^2}{r}\cos\gamma\cos\psi\tan\phi + x_g\frac{\cos\psi}{\cos\gamma}
$$
$$
+ 2V\omega_\oplus(\sin\psi\cos\phi\tan\gamma - \sin\phi) - \frac{r\omega_\oplus^2}{\cos\gamma}\sin\phi\cos\phi\cos\psi \tag{4.20c}
$$

where m is the spacecraft's mass.

A set of 3 kinematic equations is needed to compute vehicle's position. Geocentric altitude, latitude, and longitude describe spacecraft's position over time as:

$$
\frac{dr}{dt} = V\sin\gamma \tag{4.21a}
$$

$$
\frac{d\phi}{dt} = \frac{V\cos\gamma\sin\psi}{r} \tag{4.21b}
$$

$$
\frac{d\theta}{dt} = \frac{V\cos\gamma\cos\psi}{r\cos\phi} \tag{4.21c}
$$

This system of equations is numerically integrated over time using a 4th order Runge-Kutta solver.

Chapter 5

Aero-thermodynamics Methodology and Tool

5.1 Surface Impact Method

Initial estimations for deployable heat shield capsule aerodynamic drag can be provided with analytical results available for blunt cone at hypersonic speed. Indeed, for a blunt cone with a semi vertex angle θ_c, nose radius R_N, and base radius R_B, the drag coefficient reads, for a very preliminary estimation, reads [116]:

$$C_D = 2sin^2\theta_c + \left(\frac{R_N}{R_B}\right)^2 cos^4\theta_c \qquad (5.1)$$

C_D is shown as a function of bluntness ratio R_N/R_B and cone-section semi-vertex angle θ_c in Figure 5.1. For example in the case of the reference capsule of this study the bluntness ratio (R_N/R_B) reads about 0.44; while the cone semi-vertex angle is 45 deg.

So the ballistic coefficient (Kg/m^2) reads:

$$\beta = \frac{m}{\pi \left(2R_B^2 sin^2\theta_c + R_N^2 cos^4\theta_c\right)} \qquad (5.2)$$
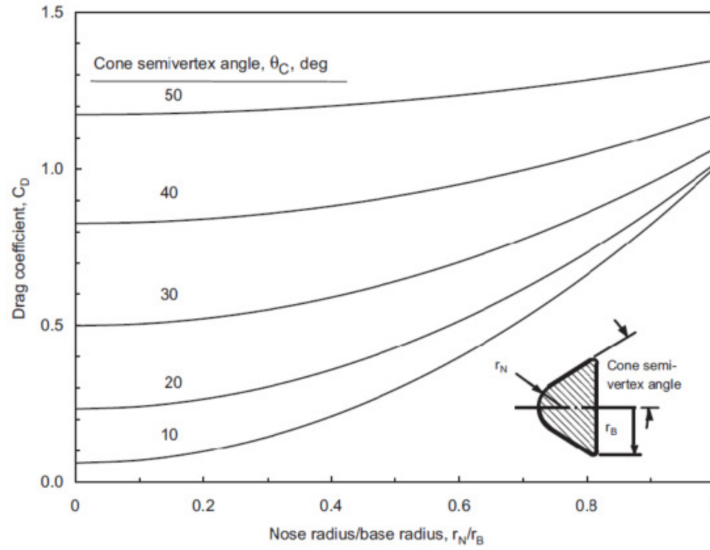
FIGURE 5.1: Hypersonic drag coefficient for sphere-cones

According to the Newtonian aerodynamics, the pressure distribution at capsule wall for hypersonic speed reads:

$$Cp = Cp_{t2}cos^2\theta \qquad (5.3)$$

where Cp_{t2} is the stagnation-point pressure coefficient that depends on the flow theory one considers while θ represents the angle between free-stream direction and radius vector from centre of curvature of nose.

If Newtonian flow theory holds Cp_{t2} is equal to 2 while in the case of modified Newtonian theory it follows that Cp_{t2} reads:

$$Cp_{t2} = \left(\frac{P_{t2}}{P_\infty} - 1\right)\frac{2}{\gamma M_\infty^2} \qquad (5.4)$$

Engineering based aerodynamic analyses were extensively performed by using a 3D Panel Method code available in CIRA [117]. This tool at high supersonic and hypersonic speeds is able to accomplish the aerodynamic and aerothermodynamic analyses of a complex re-entry vehicle configuration by using

simplified approaches as local surface inclination methods and approximate boundary-layer methods, thus avoiding the time consuming and complex grid generation and computation processes of CFD.

The capsule surface is approximated by a system of planar panels; the lowest level of geometry used in the analysis is a quadrilateral element, as shown in Figure 5.2.
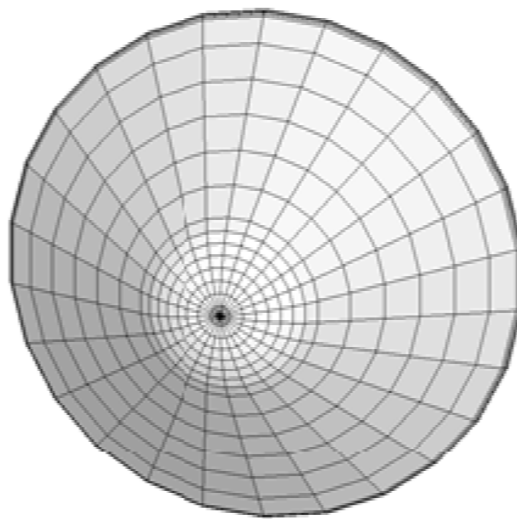
FIGURE 5.2: MINI-IRENE panel mesh

The pressure acting on each panel is evaluated by user-specified compression-expansion and approximate boundary-layer methods. The methods to be used in calculating the pressure in impact and shadow regions may be specified independently and can be selected by the user; several methods are available.

5.2 Aero-heating Engineering Method

The aero-heating at capsule stagnation point is calculated by using Anderson's relationship in the case of perfect gas, and Fay-Riddell formula for chemically reacting flow. The former yields:

$$\dot{q} = C\rho_\infty^a v_\infty^b \tag{5.5}$$

where *a*=0.5, *b*=3 and:

$$C = 1.83 \cdot 10^{-4} \frac{1}{\sqrt{R_N}} \left(1 - \frac{h_w}{h_o}\right) \tag{5.6}$$

$$h_w = c_p T_{rw} \tag{5.7}$$

$$h_o = c_p T_\infty + \frac{v_\infty^2}{2} \approx \frac{v_\infty^2}{2} \tag{5.8}$$

The Fay-Riddell relationship reads:

$$\dot{q}_{co} = 0.57 \left(\frac{4}{3}\right)^k Pr^{-0.6} (\rho_w \mu_w)^{0.1} (\rho_e \mu_e)^{0.4} \left[1 + (Le^\phi - 1) \left(\frac{h_d}{h_e}\right)\right] (h_e - h_w) \left(\frac{du_e}{dx}\right)_s^{0.5} \tag{5.9}$$

where the index k is equal to 0 for two-dimensional flow and k is equal to 1 for axisymmetric flow while the free-stream density ρ and velocity u are known from the re-entry trajectory solution. The wall enthalpy refers to radiative equilibrium conditions at a constant emissivity ε of 0.8. The exponent ϕ of Lewis number is 0.52 for the equilibrium boundary layer, 0.63 for the frozen case over a fully catalytic wall, and -∞ for frozen flow with non catalytic wall.

The term h_d is the chemical heat of formation of each of the species times the atomic mass fraction (Y_i) in the boundary layer edge flow:

$$h_d = \sum_i Y_i \left(\Delta h_f^o\right)_i \tag{5.10}$$

h_d represents the chemical energy stored by the molecular dissociation behind the shock.

The stagnation point velocity gradient $(du_e/dx)_s$ reads:

$$\left(\frac{du_e}{dx}\right)_s = \frac{1}{(R_N)_{eff}}\sqrt{\frac{2\,(\rho_e - \rho_\infty)}{\rho_e}} \tag{5.11}$$

It utilizes an effective nose radius $(R_N)_{eff}$ as a function of the fore-body bluntness parameter of the capsule. For what concerns surface aero-heating, Lee's approach shows that, for a blunt cone with nose radius R_N and semi aperture vertex angle of θ_c, at any point on the cone surface, the ratio of heat transfer $\dot{q}_w\,(s')$ to the stagnation value $\dot{q}_{co}$ reads for the nose:

$$\frac{\dot{q}_w\,(s')}{\dot{q}_{co}} = \frac{2\theta sin\theta cos^2\theta}{\sqrt{D\,(\theta)}} \tag{5.12}$$

and for the cone skirt:

$$\frac{\dot{q}_w\,(s')}{\dot{q}_{co}} = A(\theta)\frac{s'}{R_N}\left[B(\theta_c) + \left(\frac{s'}{R_N}\right)^3\right]^{-\frac{1}{2}} \tag{5.13}$$

This equation is valid for $s'/R_N \geq cot\theta_c$, where s' is the curve length measured along the cone surface of the effective sharp-nosed cone and, for high flight Mach number, it follows that:

$$A(\theta_c) \approx \frac{\sqrt{3}}{2}sin\theta_c\sqrt{\frac{\pi}{2} - \theta_c} \tag{5.14}$$

$$B(\theta_c) \approx \frac{3}{16}\frac{1}{sin^4\theta_c}\left[\frac{D(\theta)}{\theta}\right]_{\theta=\frac{\pi}{2}-\theta_c} - cot^3\theta_c \tag{5.15}$$

$$D(\theta_c) \approx \theta^2 - \frac{1}{2}\theta sin4\theta + \frac{1}{8}(1 - cos4\theta) \tag{5.16}$$

5.3   Forced Oscillation Technique

A method to study the dynamic response of a capsule inside a wind tunnel is to use the force oscillation technique.

Dynamic wind tunnel testing with a forced oscillation setup generally uses an axial sting that measures forces and moments, as well as the rates of change of these parameters with respect to changing pitch angle or angle of attack.

In order to capture the dynamic behavior, a motor attached to the sting imparts a one-degree-of-freedom oscillatory motion to the vehicle at a wide range of frequencies and mode shapes. Sinusoidal motion is usually applied. The vehicle is inclined at a wide range of angles of attack and at each condition undergoes a series of small amplitude pitch oscillations.

The damping response of the vehicle is measured as a function of pitch amplitude, angle of attack, Mach number and reduced frequency. Advantages of this technique are its direct measurement of the dynamic aerodynamic coefficients, controllability and repeatability, and its ability to match a wide range of reduced frequency parameters. Additionally, mass scaling is not generally required to obtain representative full-scale behavior in the sub scale environment [97].

Drawbacks of forced oscillation tests are the sting effects on the damping, which largely affects the values of the pitch damping coefficient. Also, due to the nature of the test setup itself, only the average damping over a pitch cycle can be obtained [99].

Employing state-of-the-art Computational Fluid Dynamics (CFD) tools to predict dynamic stability has been attempted in recent years in an effort to build on the semi-empirical methods.

One of the most recent works on this subject can be found in [118], where the dynamic stability of the Orion capsule was analyzed at two different subsonic Mach numbers (0.45 and 0.70) and a range of angles of attack (0° - 60°).

The "damping-in-pitch" coefficients were determined by applying the forced-oscillation method through CFD techniques.

The predicted damping coefficients match well with those from the experiments, both in terms of magnitudes of the damping coefficients and the range of angles of attack for which the capsule is dynamically unstable.

During this work, CFD Forced Oscillation Technique have been used to evaluate the characteristic of the deployable re-entry capsule under study, since it has shown good reliability in literature. Specifically, the equations used to evaluate the dynamic stability of the capsule are based on the energy method [119], which are now briefly discussed.

The principle of the energy resolution consists in integrating the work absorbed by the system (corresponding to amplification) or dissipated (corresponding to damping) during one oscillation cycle. Since the mechanical friction is not null in the driving system, some energy injection is always necessary to compensate the losses. The energy is injected by the power supply. Depending on the loop direction, one can deduce if the system oscillations would be amplified or damped while subjected to free oscillations. The first case is represented by a counter clockwise loop associated to a dissipation of energy, whereas the second situation is associated to a clockwise loop associated to an input of energy, as it is shown in Figure 5.3.

The general expression of the damping in pitch parameter is the following [120]:

$$C_{m_{\dot{\alpha}}} + C_{m_q} = \frac{\oint C_m d\theta}{\int_T \dot{\theta}^2 dt} \frac{2U}{D} \tag{5.17}$$

where U is the speed of the capsule at a certain altitude during the re-entry phase, D is the reference diameter, C_m is the pitching moment coefficient and θ is the pitch angle.
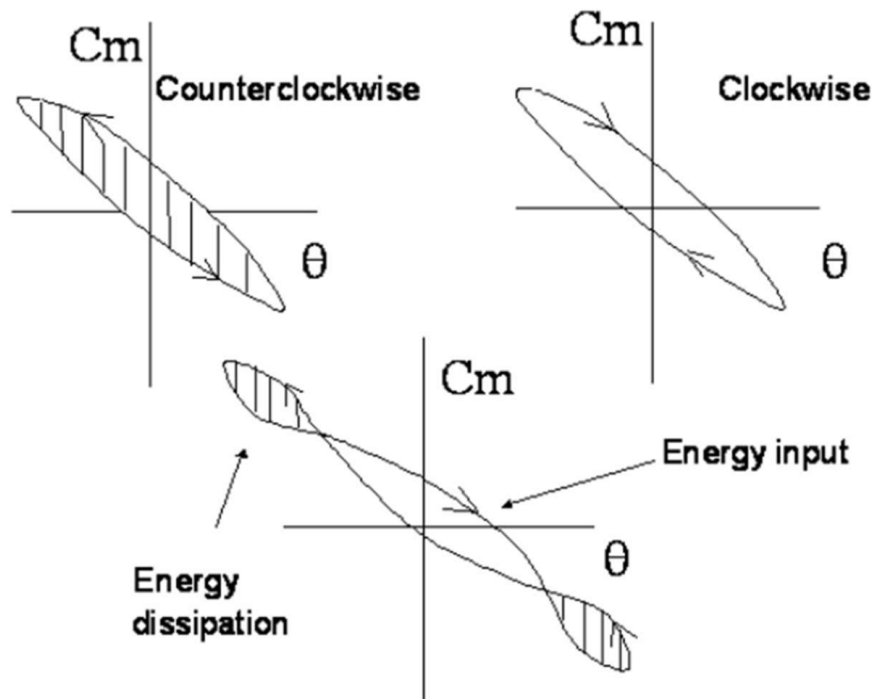
FIGURE 5.3: Energy method representation

It can be deduced that the damping-in-pitch parameter (averaged over one oscillation cycle) can be computed by evaluating the integral of the pitching moment coefficient and the pitch angular velocity squared in one oscillation cycle as it will be showed in Chapter 10.

5.4   Computational Fluid Dynamics Tool

Computational Fluid Dynamics (CFD) analyses rely on full 3-D Navier-Stokes simulations, carried out with FLUENT tool. This code solves the Reynolds Averaged Navier-Stokes (RANS) equations, including chemical and vibrational non-equilibrium, on hybrid grids by means of the Finite Volume approach.

FLUENT uses a Flux Difference Splitting (FDS) second order upwind scheme for the spatial reconstruction of convective terms, while for the diffusive fluxes a

cell centered scheme is applied.

An alternative way to compute the flux vector is also available by using a flux vector splitting scheme, namely Advection Upstream Splitting Method (AUSM). AUSM provides exact resolution of contact and shock discontinuities and it is less susceptible to Carbuncle phenomena. Implicit solver formulation is available and considered in the computations of this work.

Indeed, due to broader stability characteristics of the implicit formulation, a converged steady-state solution can be obtained much faster using the implicit formulation rather than the explicit formulation.

Global transport properties of the gas mixture rely on semi-empirical rules such as Wilke's mixing rule for viscosity and thermal conductivity. The viscosity and thermal conductivity of ith species is obtained by kinetic theory of gases. For the diffusion coefficient of the ith species in the mixture the multi-component diffusion coefficient is applied, where species Mass diffusivity is evaluated by kinetic theory.

Flow field chemical reactions proceed with forward rates that are expressed in the Arrhenius and reaction rate parameters are due to Park.

In particular, a number of in-house modifications, i.e. User Defined Functions (UDF), for the thermal non-equilibrium and radiative equilibrium temperature at wall have been developed since both vibrational non-equilibrium and wall radiative cooling boundary conditions are not basic code features.

In the UDF, vibrational relaxation is modeled using a Landau-Teller formulation, where relaxation times are obtained from Millikan and White, assuming simple harmonic oscillators; whereas to account for wall radiative cooling, during numerical simulations, the wall temperature is calculated by Stephan-Boltzman law and is implemented by means of a Newton-Raphson approach.

In doing CFD computations, the Earth atmosphere has been considered as a mixture of 79 % N_2 and 21 % Oxygen. The flow has been modeled as a reacting

gas mixture of 5 species (N_2, O_2, NO, N, and O).

The FLUENT code together with user defined functions, developed in order to simulate mixtures of gas in thermo-chemical non-equilibrium, has been used for these computations with a non-equilibrium chemical model suitable for Earth atmosphere.

Finally, in the FM flow conditions, Direct Simulation Monte Carlo (DSMC) simulations were carried out by collegues of the University of Naples (UNINA).

5.5 Plasma Wind Tunnel Facility

The SCIROCCO Facility used to obtain the results of this thesis is directly located at CIRA site in Capua, Italy, a little town positioned between Rome and Naples. It is operative from October 2001. It is a hypersonic wind tunnel, for long duration tests, realized to experimentally reproduce the atmospheric re-entry of space vehicles. The peculiarity of this facility is the test jet size: it reaches up to about 2 m diameter, allowing test on very large scale models, also in scale 1:1. A general description of the SCIROCCO Facility is depicted in the diagram in Figure 5.4, where the various components subsystem are reported.
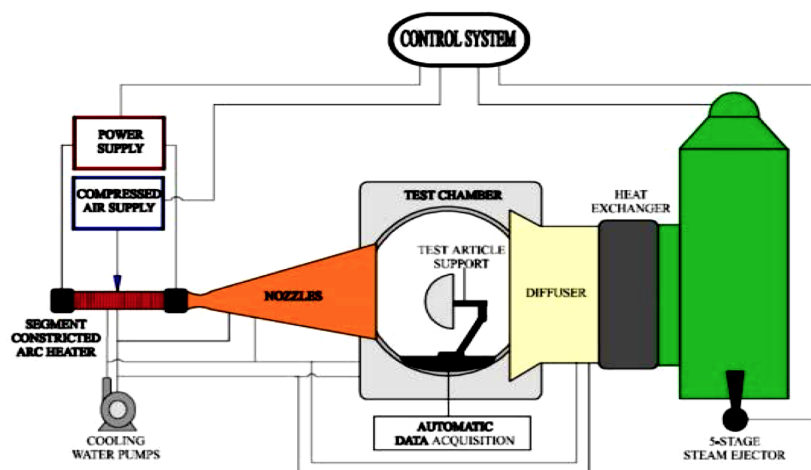
FIGURE 5.4: SCIROCCO Facility Diagram

The hypersonic flow exits from a conical nozzle (see Figure 9.9). The facility makes available four different interchangeable Nozzles (see Figure 5.4) with the following exit diameters:

Exit nozzles diameters in mm			
900	1150	1350	1950

TABLE 5.1: SCIROCCO facility exit nozzles

Each configuration realizes a convergent-divergent nozzle with a throat diameter of 75 mm. On the base of the test requirements the nozzle that have to be used is defined. The next table reports for each nozzle configuration the different flow performances. The gas used is air. It has to be taken into account that the nozzle exit composition is not the standard air one (0,77 Nitrogen and 0,23 Oxygen density ratios), because the generation of the hypersonic jet in SCIROCCO requires to increase the gas temperature into the reservoir and this determines chemical reactions. At the exit of the nozzle, depending from the test conditions, there are in general significant quantities of atomic oxygen, atomic nitrogen and other species as nitrogen oxide.

The model to be tested is installed on a Test Article Support (see Fig. 5.4, Fig. 9.8, Fig. 9.9). This system not only injects the model into the hypersonic flow, but also permits axial excursion of 1 m along the flow centerline and a pitch angle between -20 and +20 degree.

The max allowable overall size dimension of the model is 600 mm for each installed nozzle configuration except for the 900 mm diameter one; for this last nozzle the max size is 480 mm. In any case, it is possible, also test models with sizes larger than the previously mentioned ones. In this case a preliminary test, with a dummy model, very short duration (10-15 sec), is requested. This makes sure that flow blockage problems don't arise, due to the exceptional model size.

Figure 5.4 and Figure 9.8 put in evidence also the facility Test Chamber shape. It is a cylinder, vertically positioned, anchored to the ground, 5 m diameter, and 8 m height, equipped with windows to permits extensive use of non-intrusive diagnostics during the test.

Into the Test Chamber two calibration probes are installed. They are used before the model injection into the hypersonic flow. Two automated arms introduce the probes into the flow jet along an almost radial trajectory to reach the flow jet centerline to measure the stagnation conditions: pressure and heat flux. In the

Area ratio A/A*			
144	235	354	676
Mach number			
$6,2 \div 7,9$	$7,1 \div 9$	$7,8 \div 9,8$	$10 \div 11,8$
Flow speed in m/s			
$3000 \div 5300$	$3000 \div 5300$	$3000 \div 5300$	$3000 \div 5300$
Flow Static Pressure in mbar			
$0,25 \div 2,5$	$0,2 \div 2,0$	$0,1 \div 0,8$	$0,05 \div 0,5$
Flow density in Kg/m^3			
$.00013 \div .00128$	$.00009 \div .00079$	$.00008 \div .00058$	$.00003 \div .00027$
Flow Static Temperature in K			
$490 \div 750$	$380 \div 600$	$340 \div 530$	$210 \div 370$

TABLE 5.2: SCIROCCO facility flow jet performances

following table the allowable ranges of these two quantities are reported on the base of the nozzle configuration used.

Stagnation pressure in mbar			
$16 \div 120$	$10 \div 77$	$8 \div 60$	$5 \div 30$
Stagnation heat flux in kW/m^2			
$950 \div 3000$	$750 \div 2700$	$650 \div 2300$	$500 \div 1600$

TABLE 5.3: Stagnation flow performances

Each probe is realized in copper, which can be considered a fully catalytic material, it has a hemispherical shape with a radius of 100 mm and it works at a surface temperature of about 300 K because is cooled by a proper internal demineralized water re-circulation. The knowledge of these last data is important because, naturally, they are reference for stagnation heat flux as reported into the previous table. The maximum allowable test duration is 30 min, which is a very long-operation time for this kind of facilities.

The previous tables and descriptions have been relevant to the facility jet test performances. In the following some information about the facility subsystems are given. SCIROCCO is a very huge plant in terms of extension, complexity and involved energies. It is, currently, the most powerful hypersonic facility in the world (see Fig. 5.5 for an aerial view of the facility).

The facility hypersonic jet is realized thanks to the energized conditions of the air immediately before to the nozzle convergent section (inlet conditions), whose allowable ranges are reported in the following table. This reservoir is called Segmented Constricted Arc Heater. It is a column of 550 consecutive segments in cooled copper into which an electrical arc is realized to guarantee the requested gas temperature. The gas used for the test is air with a minimum argon addition.

FIGURE 5.5: Aerial view of part of SCIROCCO facility

Driving parameters	
Air Flow rate in Kg/s	0,3 ÷ 2,5
Argon Flow Rate in Kg/s	0,008 ÷ 0,04
Arc electrical current in A	1500 ÷ 6500
Reservoir conditions	
Max design Supplied Electrical Power in MW	70
Total enthalpy in MJ/kg	10 ÷ 30
Total pressure in bar	1,5 ÷ 11

TABLE 5.4: Arc heater conditions

The hypersonic flow conditions are also reached thanks to the suction of a 5-Stage Steam Ejector (See Fig. 5.4) Vacuum System plant. In SCIROCCO the flow jet, after entering the test chamber, is collected towards this system by a long Diffuser: a 50 m length and 3 m about diameter realized in steel with proper wall water cooling circuit.

The Vacuum System has capability to suck air from no-flow conditions to a maximum of 3,5 Kg/s with relevant pressure from 0,1 to 10 mbar about. The SCIROCCO Vacuum System is based on the steam ejectors technology. Twelve water steam ejectors are available and they can be used all or in part, realizing different possible configuration with different performances. The maximum powerful configuration of the Vacuum System requires to be supplied by 90 ton/hour of steam at a 250 C temperature and 30 bar pressure (80 MW power about).

In between the Diffuser and the Vacuum System is integrated a Heat Exchanger (see Fig 5.4). This component is necessary to completely eliminate the enthalpy supplied to the flow jet by the arc heater and to cool the gas under 200 C temperature. This temperature reduction is the maximum value allowable by the successive Vacuum System nominal working.

The guidance, conduction and maintenance of the SCIROCCO facility is very challenging because of the complex interaction between its powerful previously mentioned sub systems. A Control System based on different Local Control Unit's, between them interacting, is active during the test, devoted also to check all the involved safety aspects and to directly act if, necessary.

Chapter 6

Guidance and Control Methodology

6.1 Innovative Control System

In order to be able to control the entry trajectory, a vehicle must be able to produce lift. Typically, re-entry capsule generate lift by flying at a defined trim angle, as a consequence of a displacement of the centre of mass (CoM) from the model centerline [121]. In order to give the desired vertical and lateral components of lift, the capsule is also rolled during the re-entry according to the bank angle modulation logic using a reaction control system. The lift-to-drag ratio is different from zero and a lift force acts in a direction perpendicular to the velocity vector, changing with the variation in the vehicle orientation with respect to the airflow. By changing the bank angle, the vertical component of Lift in the vertical plane varies [86] [88] [122]. In contrast, in this section a control system for deployable re-entry capsule is proposed, which is able to generate forces on the spacecraft by deflecting aerodynamic surfaces.

The reference capsule is based on the design of the Mini Irene Flight demonstrator [60] [62] [68] [67] [66] presented in chapter 3. The capsule provides a ballistic re-entry, and is characterized by a low ballistic coefficient, which leads to a reduction of the peak heat flux and mechanical load, and an umbrella like mechanically deployable heat shield with a 45 deg half cone angle, that allows small

dimensions at launch and a larger exposed surface area during re-entry.

As illustrated in section 2.2, the only example of control system applied to a deployable heat shield capsule during re-entry was within the Inflatable Re-entry Vehicle Experiment (IRVE-3), which was successfully tested. The IRVE-3 re-entry vehicle was equipped with an inflatable heat shield and a CoM offset mechanism, which introduced a lateral CoM offset, generating a lift vector [34]. In this study, a different approach is used.

In order to provide the capsule with control capability an actuation system consisting of eight aerodynamic surfaces, referred to as flaps in this work, has been implemented. The flaps are placed at an angle of 45 deg from each other, as in Figure 6.1, and provide a moment coefficient contribution through their deflection, in terms of pitching and yawing moment (see Figure 6.4). It's assumed that the capsule doesn't roll, so that the flaps position is fixed with respect to the initial one.
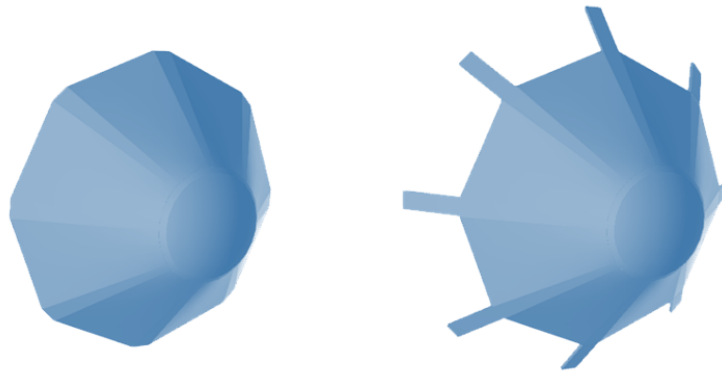
FIGURE 6.1: Re-entry Capsule clean configuration and flap configuration.

The proposed strategy is to change the natural trim of the capsule through the flaps independent deflection, in order to produce enough lift and side force to ensure the capsule maneuverability during the re-entry trajectory.

Therefore both the entity and the direction of the resulting force could be modulated by the control system, in contrast with what usually happens with re-entry capsule where a fixed CoM offset generate a fixed force that could only be orientated in different direction but never reduced to zero [82].
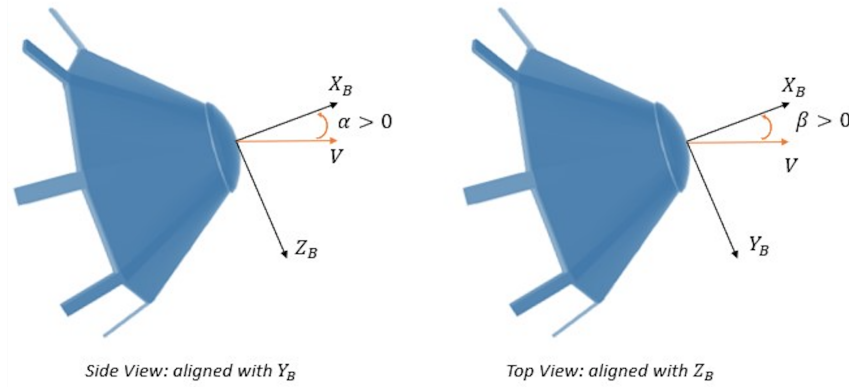
FIGURE 6.2: Capsule Control Parameters.

The assumed control parameters are α, the trimmed angle of attack in vertical direction, and β the trimmed sideslip angle in lateral direction, as shown in Figure 6.2. The deflection of the upper flaps leads to a positive α, while the deflection of the lower flaps leads to a negative α. Similarly, the deflection of the flaps placed along the negative Y_B axis leads to positive values for β, while the deflection of the flaps placed along the positive Y_B axis leads to a negative β.

A positive α value produces a negative lift, while a negative α value produces a positive lift. Analogously, a positive value for β generates a force pointing toward the right side of the capsule and a negative value for β generates a force pointing toward the left side of the capsule (see Figure 6.4).

Every α and β couple is associated to a couple of aerodynamic moment coefficients values C_m and C_n, the pitching moment coefficient and the yawing moment coefficient respectively, that the flaps deflection needs to generate to maintain the

desired trim angles. Since the capsule is axisymmetric, both the moment coefficients are equal for a same angle. The moment coefficients related to the angle variation and to the Mach number condition are shown in Figure 6.3.
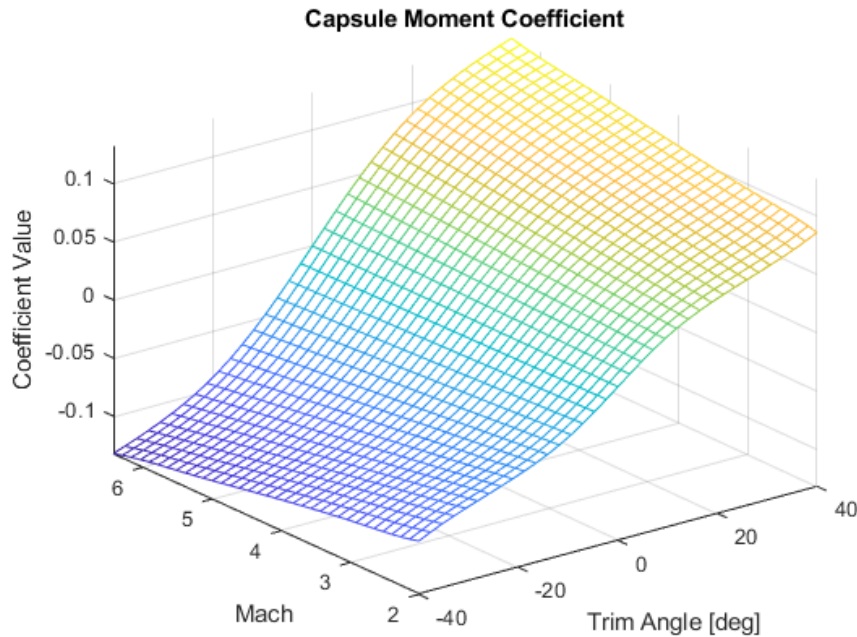
FIGURE 6.3: Moment Coefficients Database for different angles and for different Mach numbers

The first step in order to relate the flaps deflection to the commanded trim is to define the forces generated by the deflection itself. In fact, in order to trim the capsule, two conditions have to be fulfilled:

$$\begin{cases} C_m + \delta C_m = 0 \\ C_n + \delta C_n = 0 \end{cases} \tag{6.1}$$

where C_m and C_n are the moment coefficients of the capsule, for the set attitude, while δC_m and δC_n represent the aerodynamic moment coefficients contribution generated by the flaps. Some assumptions and some quantities must be defined in order to compute these contributions.
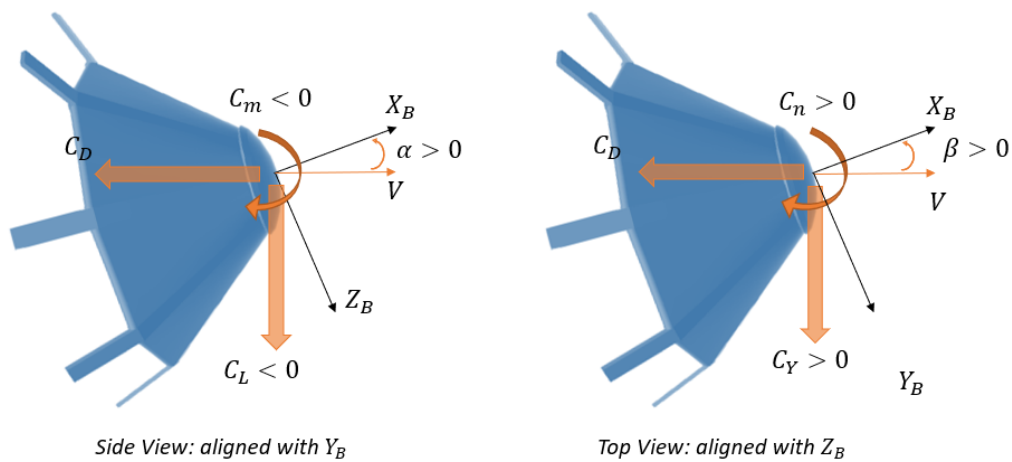
FIGURE 6.4: Forces, Moments and attitude sign convention, in the vertical and in the horizontal plane respectively
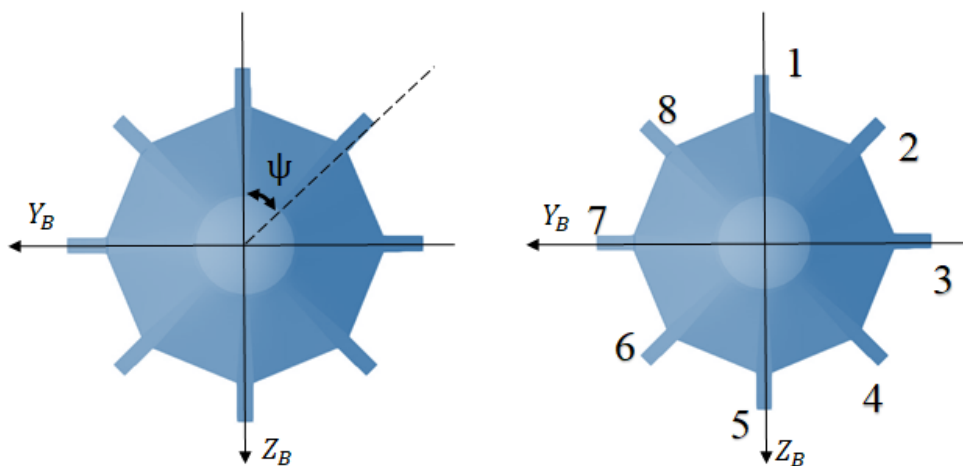
FIGURE 6.5: Definition of flaps through the angle Ψ

First of all, a sign convention is chosen. It is shown in Figure 6.4, in which the resulting forces of positive attitude in terms of α and β are represented too. Moments are calculated around the nose of the capsule, which is considered to be the CoM as first approximation.

Every flap is defined by the angle Ψ, clockwise starting from the upper flap on the Z_B axis (see Figure 6.5). The distances of the flaps CoM from the capsule body axes are defined as dx, dy and dz (see Figure 6.6). These values are not constant,
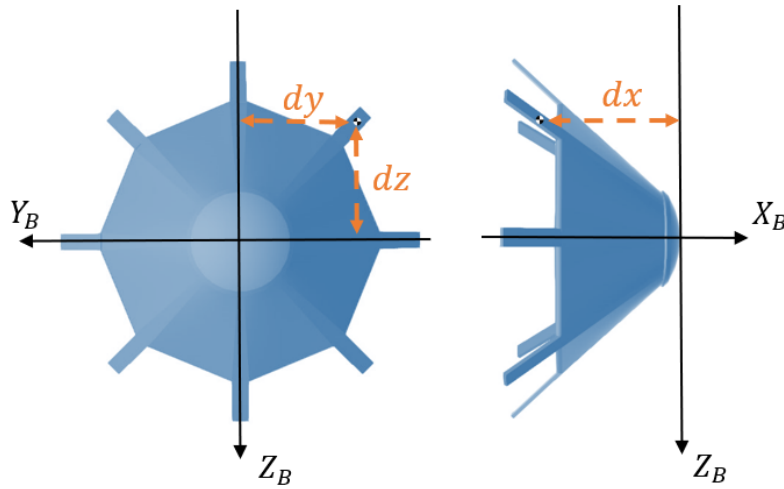
FIGURE 6.6: Definition of flaps CM distance fromt body axes
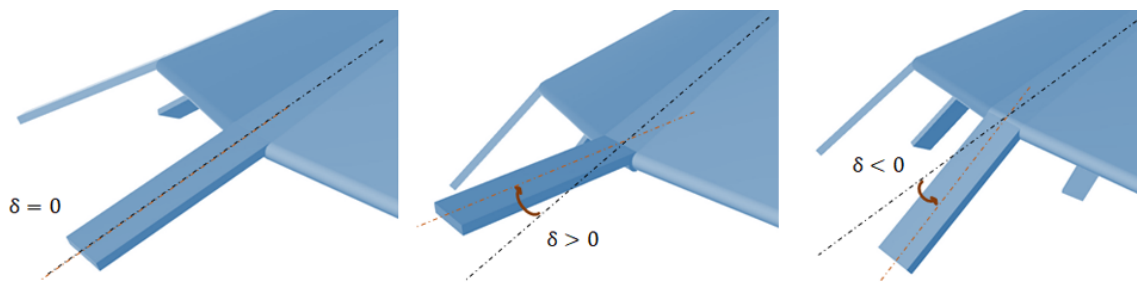
FIGURE 6.7: Flap deflection sign convention

since they change as the flap are deflected. The definition of these distances is essential in order to compute the contribution to moment coefficients δC_m and δC_n generated around the capsule's CoM deflecting the flaps. A sign convention for the flap deflection δ has been defined too and is pictured in Figure 6.7.

The deflection is defined to be null ($\delta = 0$) when is aligned with the heat shield, and is tilted of $45°$ with respect to the X_B body axis. The deflection is then considered to be positive when toward the external part of the capsule, and negative when toward the internal part of the capsule. This convention has been chosen because it is related to what physically happens on the flap due to the deflection.

In fact, at hypersonic speeds, when the deflection is null, the airflow passes undisturbed on the flap surface. On the contrary, when the deflection is positive, an oblique shock wave is caused by the flap, and when the deflection is negative, a Prandtl-Meyer expansion is caused.

Once all the sign conventions and all the involved terms have been introduced, their expressions can be derived, starting from the contribution to the moment coefficients:

$$\delta C_m = \sum_{i=1}^{8} (\delta C_{Di} dz_i + \delta C_{Li} dx_i) \tag{6.2a}$$

$$\delta C_n = \sum_{i=1}^{8} (\delta C_{Di} dy_i + \delta C_{Yi} dx_i) \tag{6.2b}$$

where i refers to the flaps as mentioned before and dx_i, dy_i and dz_i are the distances from the flap CM and depends on the flap's deflection. They can be derived as:

$$dx_i = L_{caps} + \frac{1}{2} L_{flap} \cos(45 + \delta_i) \tag{6.3a}$$

$$dy_i = \left(\frac{1}{2} D_{caps} + \frac{1}{2} L_{flap} \sin(45 + \delta_i) \right) |\sin \Psi_i| \tag{6.3b}$$

$$dz_i = \left(\frac{1}{2} D_{caps} + \frac{1}{2} L_{flap} \sin(45 + \delta_i) \right) |\cos \Psi_i| \tag{6.3c}$$

where L_{caps} is the capsule length, D_{caps} is the capsule diameter, L_{flap} is the flap length, and δC_{Di}, δC_{Li}, δC_{Yi} are the force coefficients generated by the flaps. Their total value can be expressed as:

$$\delta C_D = \sum_{i=1}^{8} \frac{F_N(\delta_i, M) \sin(\frac{\pi}{2} + \delta_i)}{q S_{ref}} \tag{6.4a}$$

$$\delta C_L = \sum_{i=1}^{8} \frac{F_N(\delta_i, M) \cos(\frac{\pi}{2} + \delta_i)}{q S_{ref}} \cos \Psi_i \tag{6.4b}$$
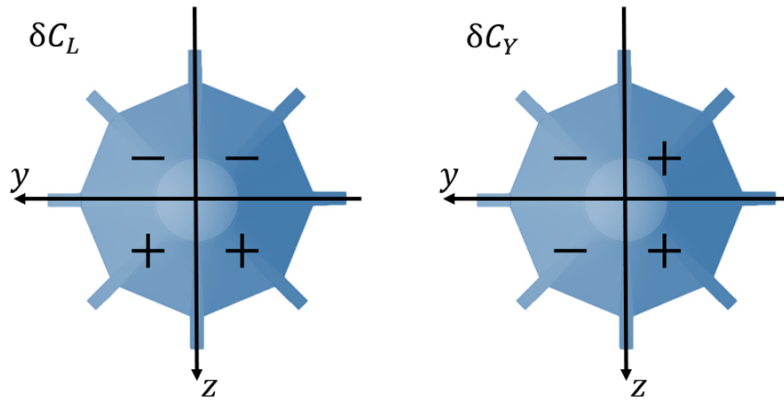
FIGURE 6.8: Force Coefficients contribution sign representation
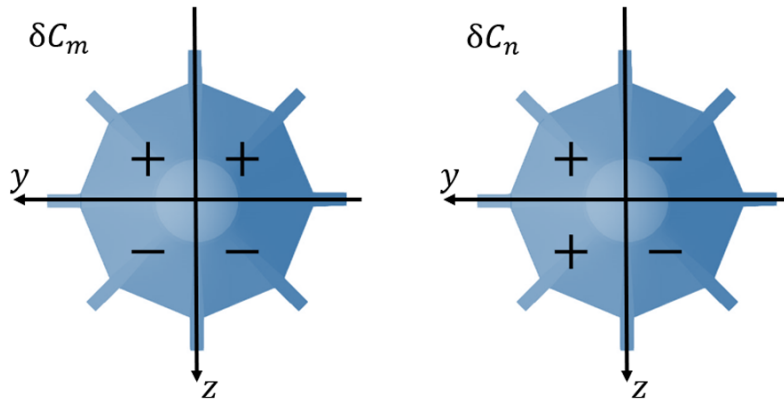
FIGURE 6.9: Moment Coefficients contribution sign representation

$$\delta C_D = \sum_{i=1}^{8} \frac{F_N(\delta_i, M) \cos\left(\frac{\pi}{2} + \delta_i\right)}{q S_{ref}} \sin \Psi_i \tag{6.4c}$$

where F_N is the normal force acting on the flap, in Newton. It can be expressed in its nondimensional form as:

$$F_n = \frac{F_N}{q S_{ref}} \tag{6.5}$$

It clearly appears how all the above statements depends on the definition of the normal force acting on the flaps, for different values of the Mach number, and

	Orbital Re-Entry	**Suborbital Re-Entry**
M	20.48	3.68
q [Pa]	701.1199	2721.616
M_1	2.5	1.5
P_1 [Pa]	675	2800
S_{flap} [m^2]	0.021	0.00525

TABLE 6.1: CFD simulations data

for the flap's deflection angle variation. Once the magnitude of the force, or its nondimensional value is known for the given conditions, the force coefficients can be computed, as well as the moment coefficients.

It should be noticed how the δC_{Di} value is always positive by definition, while δC_{Li} and δC_{Yi} can be positive or negative, depending on i. This leads to positive or negative values for the moment coefficients contribution δC_m and δC_n too. Looking at the equations 6.2 and 6.4, it's easy to compute their sign, which is shown in Figure 6.8 and Figure 6.9.

The next step was to define the values of F_n. First, two CFD (Computational Fluid Dynamics) simulation data for the clean configuration of the capsule (no flaps) have been used to exploit estimation of the local flow conditions (Mach number and surface pressure) at the flap hinge line. Then engineering surface inclination methods have been used to evaluate the force and moment contributions generated by the flaps deflection.

CFD main data are presented in Table 6.1. P_1 and M_1 refer to pressure and Mach number at the hinge line, while S_{flap} is the flap reference area. As mentioned before, for positive flap deflections, an oblique shock wave is caused. The

pressure value after the shock wave is computed with the well-known relation:

$$\frac{P_2}{P_1} = (\gamma_a + 1)^{-1}(2\gamma_a M_1^2 \sin^2 \delta - \gamma_a + 1) \tag{6.6}$$

where γ_a represents the air heat capacity ration.

For negative flap deflections, a Prandtl-Meyer expansion is caused. The pressure value after the expansion is computed through the relation:

$$\frac{P_2}{P_1} = \left[\frac{1 + \frac{\gamma_a - 1}{2}M_1^2}{1 + \frac{\gamma_a - 1}{2}M_2^2}\right]^{\frac{1}{\gamma_a - 1}} \tag{6.7}$$

where M_2 value is computed with the well-known methods in literature [123]. Thus:

$$F_N = \frac{P_2}{S_{flap}} \tag{6.8}$$

Two curves can then be computed for the two available Mach number conditions and are represented in Figure 6.10. It should be noticed that the possible deflection range varies for different Mach numbers, because the detached wave condition should be avoided.

Even though the deflection range varies with the Mach number, data extrapolation was used to compute the normal force behaviour before linearly interpolating the two available conditions, as shown in Figure 6.11. That was necessary in order to avoid false behaviours for the intermediate curves.

Nevertheless, the deflection range was considered to linearly vary with the Mach number, and it is represented in Figure 6.12. Non-dimensional force variation with flap deflection, within the relative range for different Mach number conditions, is shown in Figure 6.14.

It can be noticed how flaps deflection brings a contribute to the Drag force
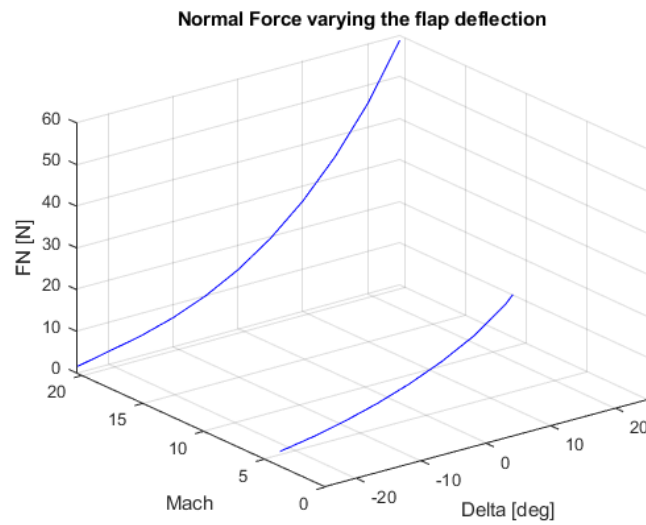
FIGURE 6.10: Normal Force acting on the flaps after their deflection
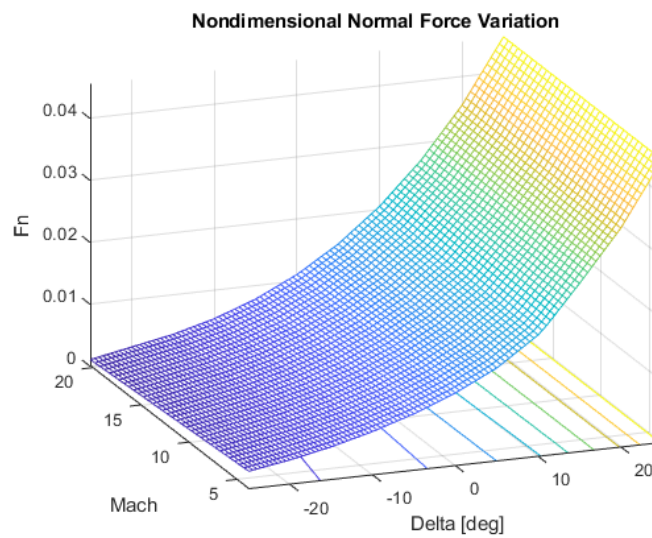
FIGURE 6.11: Nondimensional Force acting on the flaps after their deflection

δC_D. Increased Drag should usually be avoided since, as shown in the system of equations 4.20, it directly influences dynamic equations of motion, and could lead the trajectory to off-nominal conditions. That's why, in order to keep the Drag increment at minimum, the best idle condition for the capsule is with the
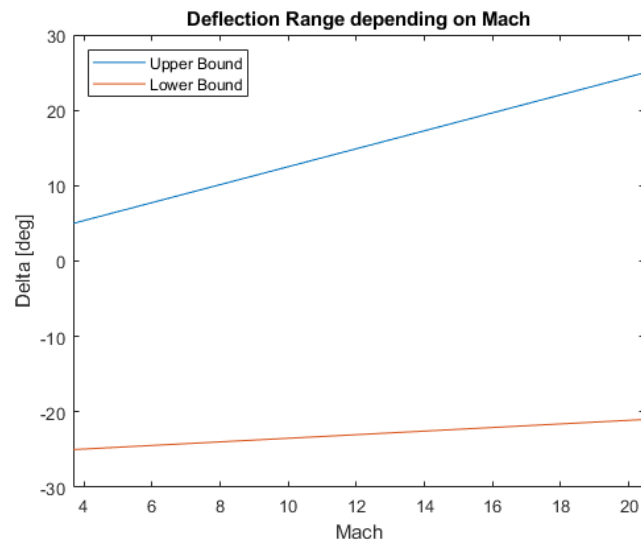
FIGURE 6.12: Deflection Range variation with Mach
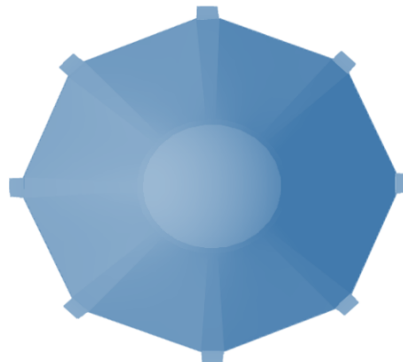
FIGURE 6.13: Capsule "closed" configuration

flaps folded inward, as the δC_D increases with flap positive deflections (see Figure 6.13).

Since to obtain a desired attitude (described by the angles α and β) it is possible to use eight different parameters (the flaps deflection angle δ), a criterion has to be chosen in order to relate any feasible trim condition to a single flaps deflection configuration. In dealing with this optimization problem, a Drag oriented approach was used.
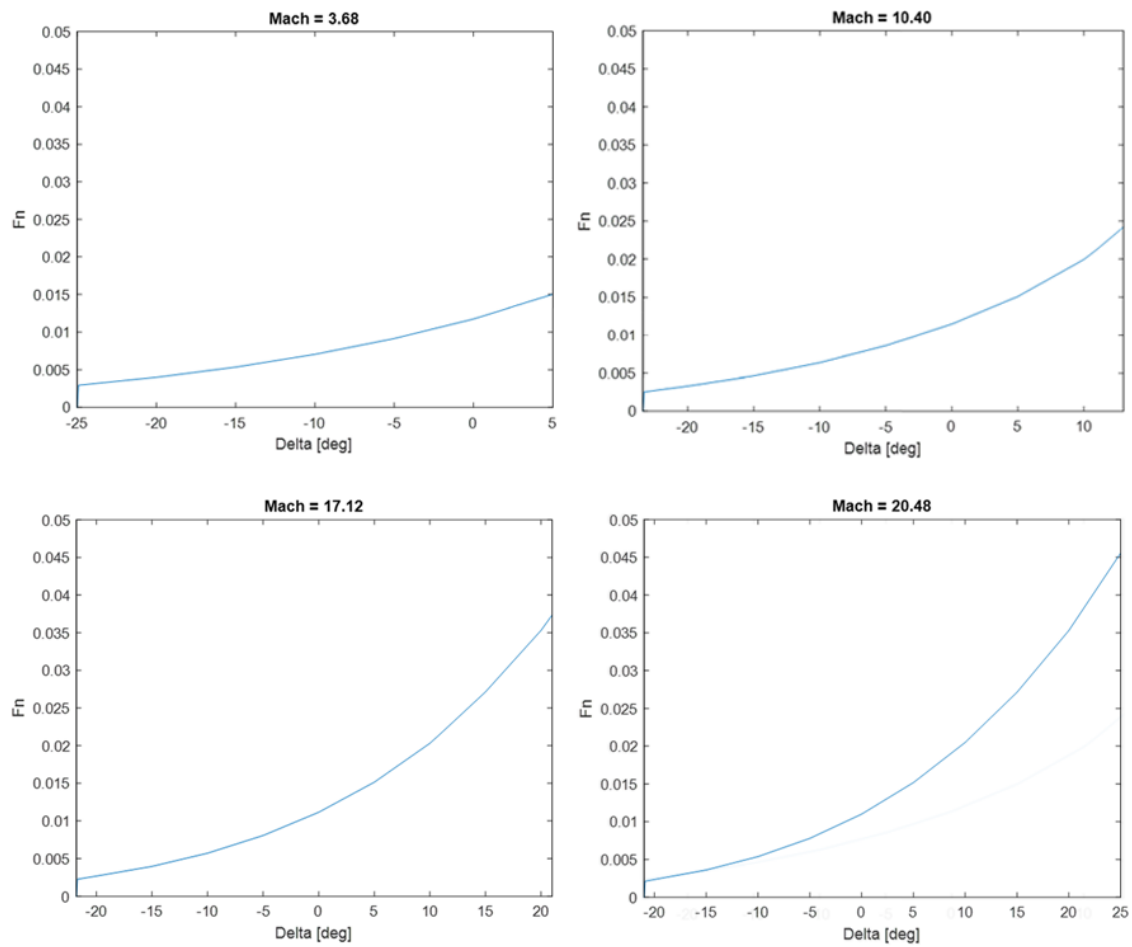
FIGURE 6.14: Nondimensional Force variation with flap deflection
for different Mach number values

In particular, for every commanded trim condition, the chosen flap deflection configuration will be the one which minimize Drag.

In order to solve the problem, a MATLAB optimization tool was used. It is the fmincon.m library function. It's suitable to find the local minimum for a constrained nonlinear multivariable function.

It solves the problem:

$$
\min_{x} f(x) \text{ such that} = \begin{cases} c(x) \leq 0 & \text{nonlinear inequality constraint} \\ ceq(x)) = 0 & \text{nonlinear iquality constraint} \\ A \cdot x \leq b & \text{linear inequality constraint} \\ Aeq \cdot x = beq & \text{linear equality constraint} \\ lb \leq x \leq ub & \text{bound constraint} \end{cases} \qquad (6.9)
$$

$f(x)$ is the equation to minimize. In this case it's the Drag equation, the first of the system of equations 6.4. The nonlinear equality constraint is defined by the two equations in the system 6.1, and that's where the trim condition is imposed. Moreover, there's a bound constraint, represented by the deflection range of the flaps for the given Mach number, in order to avoid the detached wave condition.

A feasible trim conditions database was then computed. For every Mach number, and commanded attitude, the deflection of every flap and the drag increment is associated. It has to be noticed that not every commanded attitude can be trimmed, since the system 6.1 depends on the equations 6.2 and 6.4, and the force generated by the flaps is limited and varies with the Mach number. That's why feasible and unfeasible trim conditions have been computed for a certain number of flight conditions. Some of these conditions are plotted in Figure 6.15.

It can be noticed how the maximum feasible trim condition changes with the Mach number, accordingly with the force value behavior for the flap deflection with Mach number previously showed in Figure 6.11 and to the limitation on flap deflection range.

Since the attitude commanded by the controller could be unfeasible, it is necessary to evaluate feasible condition before give a command to deflect the flaps.
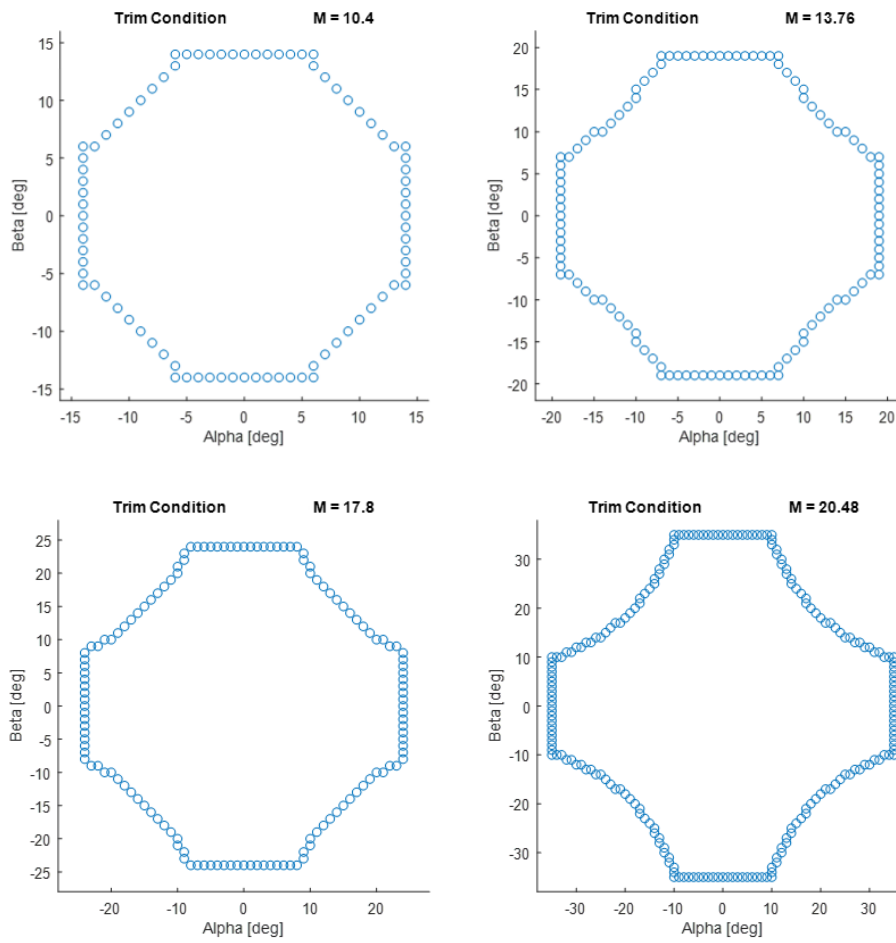
FIGURE 6.15: Trim conditions feasibility for different values of the Mach number

If the requested attitude from the control logic is feasible, then it becomes the output of the block and becomes the commanded attitude. If the requested attitude is unfeasible, then the closest feasible attitude is commanded, as shown in Figure 6.16.
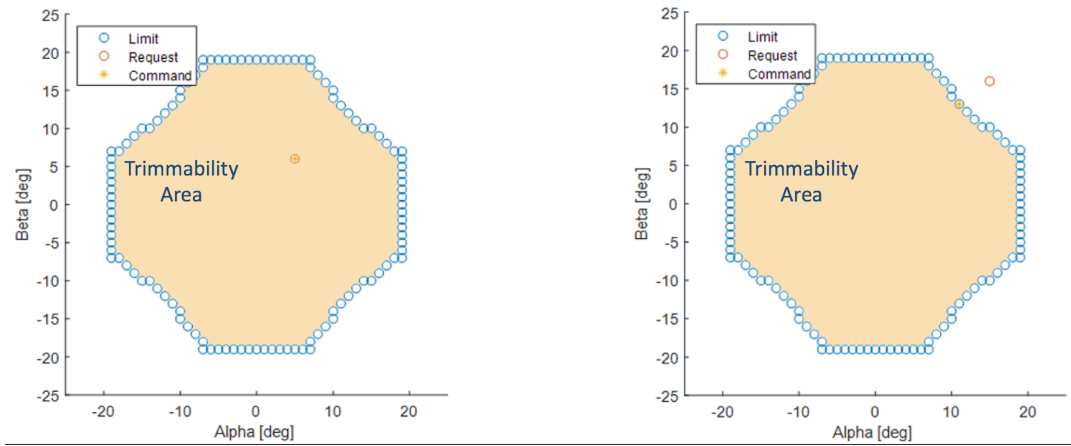
FIGURE 6.16: Trim Conditions Feasibility Logic

6.2 Guidance Methodology for Ground Targeting

Usually, before the re-entry phase, a spacecraft is directed toward the atmosphere from space with a propulsive de-orbiting maneuver to obtain a targeted re-entry trajectory with a precise flight path angle and a reduced dispersion on the ground. For this reason, vehicles that must be recovered from space by landing in a precise location have traditionally required propulsion systems.

However, it is not always possible to mount a propulsion system on board a satellite or a capsule. For example in the case of small satellites deployed from the International Space Station, on-board propulsion systems are forbidden for safety reasons.

In this section a new technological solution for re-entering and landing a spacecraft in a desired location from a low Earth orbit without the use of chemical propulsion is proposed.

6.2.1 Algorithm Overview

The goal of this algorithm is to compute a trajectory and corresponding ballistic coefficient profile, subject to constraints, that if followed leads a spacecraft to impact the ground in a desired location using only aerodynamic drag modulation (i.e. modulating the aperture ad closure of a deployable heat shield) [124]. This facilitates the propellant-free landing and recovery of a spacecraft in a precise location. The methods discussed in this section build on prior work by University of Florida on spacecraft de-orbit point targeting [125, 126, 127].

The first component of the guidance algorithm for ground targeting involves the selection of a de-orbit point. The desired de-orbit state is defined such that a numerical orbit propagation of the spacecraft from this state results in a ground impact in a desired location. The de-orbit point is the latitude, longitude, and altitude at the de-orbit state which in this work is at 100 km geocentric altitude.

The next phase of the algorithm involves computing a trajectory that guides the satellite to the de-orbit point from the initial conditions utilizing the range of ballistic coefficient modulation achievable by the satellite.

FIGURE 6.17: Ground Targeting Algorithm Steps

Finally, while a guidance trajectory to the de-orbit point may be achieved, the final velocity and atmospheric conditions may vary slightly from those in the originally desired de-orbit state. This may result in some along-track error in the landing location. A final correction is made to the last portion of the generated guidance trajectory before the de-orbit point to correct for this error and ensure that the desired landing point is achieved. After this correction, the complete guidance trajectory consists of a ballistic coefficient, position, and velocity time-series from the spacecraft initial conditions to the desired landing location.

6.2.2 De-Orbit Point Selection

The first component of the ground targeting algorithm involves computing the de-orbit location at 100 km altitude that the satellite must pass through to achieve a desired ground impact location. This is accomplished by initializing a simulation in a 140 km circular orbit defined by initial mean orbit elements $\mathbf{x}_{140} = (a, e, i, \Omega, \omega, \theta) = $ (6518 km, 0, i_{init}, 0, 0). These conditions are initially chosen to simulate only the last part of the satellite orbital decay and are not the actual initial condition that will be instead used next in the algorithm (see Sec. 6.2.3). The time is set equal to the approximate expected time of de-orbit. The satellite trajectory is simulated from this initial state using an orbit propagator until a geocentric altitude of 100 km and a re-entry simulator from 100 km until ground

impact. The increases in Ω and θ at $\mathbf{x}_{140}$ necessary to achieve a desired impact location are then computed. This is done as follows.

First, the argument of latitude at both the desired and actual (from numerical simulation) ground impact locations can be computed based on the orbital inclination and the latitude of each location. During the ascending (northbound) phase of the orbit, the argument of latitude u at a given latitude l is computed by

$$u_{asc} = sin^{-1} \left(\frac{sin(l)}{sin(i)} \right) \tag{6.10}$$

The argument of latitude during the descending portion of the orbit is given by

$$u_{desc} = \pi - u_{asc} \tag{6.11}$$

To compute the desired argument of latitude u_{des}, the user must specify whether they want the re-entry trajectory to occur during the ascending or descending portion of the orbit. To determine the actual argument of latitude u_{act} after a re-entry trajectory propagation, it is necessary to utilize the impact latitude in Eq. 6.10 and determine whether the trajectory is ascending or descending by examining trajectory points before the impact point to determine whether the latitude of each point is increasing or decreasing. The true anomaly increase necessary in $\mathbf{x}_{140}$ is to arrive at an impact point of the correct latitude is

$$\Delta u = u_{des} - u_{act} \tag{6.12}$$

The $\Delta\Omega$ necessary to correct for the longitude error can be computed by first calculating the longitude increase $\Delta\lambda_u$ that occurs when a satellite travels from an argument of latitude u_{act} to u_{des}. This is most easily done by setting $\theta = u_{des}$ in $\mathbf{x}_{140}$ and computing the longitude associated with the orbital element set. $\theta = u_{act}$ can then be set in $\mathbf{x}_{140}$ and the longitude can be once again computed. The

longitude at u_{act} can be subtracted from the longitude at u_{des} to get the longitude increase that occurs as the satellite traverses a true anomaly increase of Δu. The right ascension change in $\mathbf{x}_{140}$ necessary to correct the longitude error is then

$$\Delta\Omega = \lambda_{des} - \lambda_{act} - \Delta\lambda_u \qquad (6.13)$$

where λ_{des} is the longitude of the desired ground impact location and λ_{act} is the impact-point longitude after the trajectory simulation.

The desired orbital element increases $\Delta\Omega$ and $\Delta\theta = \Delta u$ can be applied to the initial state at $\mathbf{x}_{140}$ and the trajectory re-propagated. The process of computing the change in $\mathbf{x}_{140}$ necessary for a desired landing location and re-propagating the trajectory can be continued until a $\mathbf{x}_{140}$ is found that results in a trajectory that impacts that ground in the desired location. When the proper $\mathbf{x}_{140}$ is found, the latitude, longitude, and altitude where the trajectory crosses 100 km geocentric altitude is returned as the target de-orbit point.
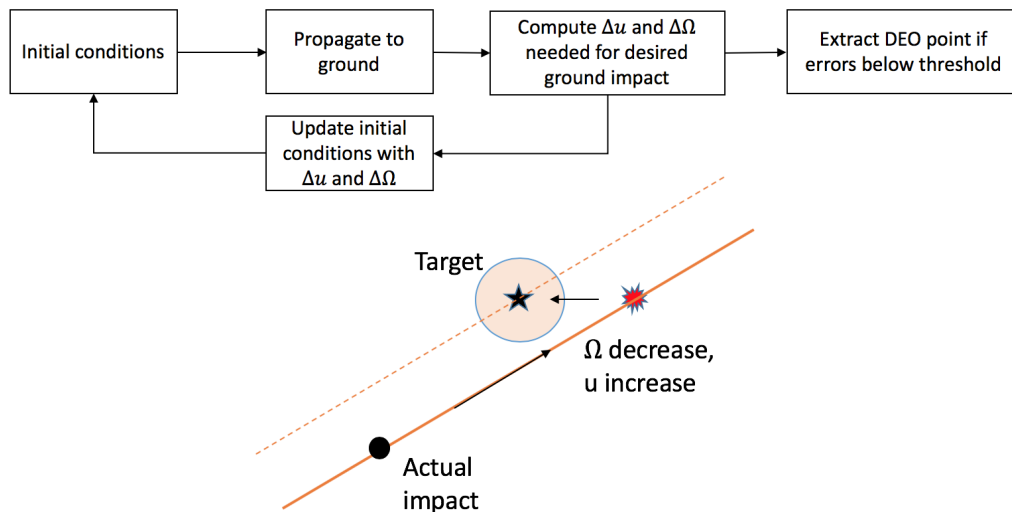
FIGURE 6.18: De-Orbit Point Selection Flowchart

Note that in some cases, directly applying the desired Δu to $\mathbf{x}_{140}$ and propagating the trajectory results in a convergence failure. On one trajectory simulation, an overshoot of the desired landing location may occur, but on the next an undershoot occurs. This overshoot-undershoot cycle continues indefinitely in some cases. To remedy this, a change in argument of latitude of $k\Delta u$ instead of Δu can applied to $\mathbf{x}_{140}$ where k is a scaling factor initially set to 1. Each time the sign of the desired Δu changes between iterations of trajectory propagation, k is reduce by a factor of two. This reduction in k breaks the undershoot-overshoot cycle and helps ensure convergence.

6.2.3   De-Orbit Point Targeting

Once the desired de-orbit point at 100 km geocentric altitude is selected, a trajectory and corresponding drag profile can be computed to guide the satellite to this de-orbit point from the actual orbital initial condition (i.e. at 400 km), using the techniques discussed in Ref. [125]. A flow chart of this de-orbit point targeting algorithm is shown in Figure 6.19. Note that a geocentric instead of geodetic altitude is used to define the de-orbit point since the targeting algorithm is designed to work with geocentric altitude.

The details of the de-orbit point targeting algorithm can be summarized as follows.

Define the spacecraft ballistic coefficient as

$$C_b = \frac{C_d A}{2m} \tag{6.14}$$

Where C_d is the drag coefficient, A is a reference area, and m is the spacecraft mass. The acceleration due to aerodynamic drag (a_d) acting on the spacecraft is

$$\mathbf{a}_d = -C_b \rho v_\infty \mathbf{v}_\infty \tag{6.15}$$
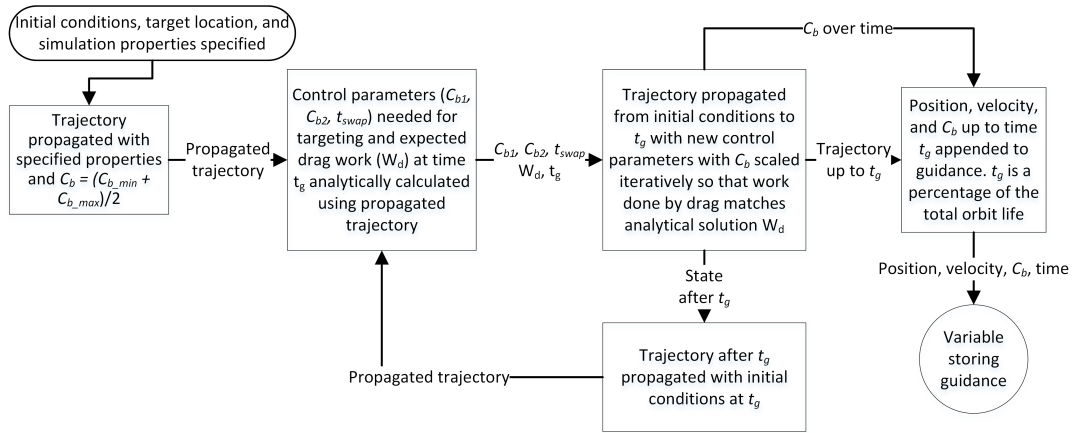
FIGURE 6.19: De-Orbit Point Targeting Algorithm Flowchart

Where ρ is the ambient atmospheric density and $\mathbf{v}_\infty$ is the spacecraft velocity vector relative to the free stream. It is shown that given the ability to vary an initial C_{b1}, a second ballistic coefficient C_{b2}, and the time t_{swap} at which the ballistic coefficient is changed from C_{b1} to C_{b2}, it is possible to target any point on the Earth with latitude below the orbit inclination if maneuvering is initiated early enough. We will define $(C_{b1}, C_{b2}, t_{swap})$ as the control parameters. Note that C_{b2} is maintained until some terminal semi-major axis at which point some pre-set $(C_{b_{term}})$ is maintained until de-orbit.

The basis of the analytical solution for determining the control parameters needed for proper targeting is the ability to calculate the effect that a perturbation in the control parameters will have on a given trajectory. While a satellite in an unperturbed two-body orbit (spherical Earth) will experience a constant semi-major axis, a satellite in a two-body orbit with drag will experience a monotonically decreasing semi major axis over time. It can be shown that in a circular orbit around a spherical Earth, if a constant, invariant density is assumed at each altitude, then the time and argument of latitude (true anomaly plus argument of perigee) required for a spacecraft to decay from an initial to final semi major axis due to aerodynamic drag increase linearly with decreasing ballistic coefficient.

Assume a satellite with ballistic coefficient C_{b1} takes time Δt_1 to achieve some drag-induced change in semi major axis Δa and undergoes argument of latitude change Δu_1 while achieving this Δa. The time and argument of latitude change a satellite with the same initial conditions and some different C_{b2} will undergo to achieve the same Δa (same orbital decay) are given by

$$\Delta t_2 = \frac{C_{b1} \Delta t_1}{C_{b2}} \tag{6.16}$$

$$\Delta u_2 = \frac{C_{b1} \Delta u_1}{C_{b2}} \tag{6.17}$$

Since the average rate of change of right ascension ($\dot{\Omega}_{avg}$) is independent of C_b, the change in Ω experienced during the orbital decay can be calculated by

$$\Delta \Omega = \dot{\Omega}_{avg} \Delta t \tag{6.18}$$

As shown in Figure 6.20, if the trajectory of a satellite with some initial set of control parameters has been numerically propagated (initial trajectory), the de-orbit location of a new trajectory corresponding to the same initial conditions but a different set of control parameters can be analytically estimated by dividing the trajectories into phases where the C_b is not changing in either trajectory. In each trajectory, the phases are demarcated by the ballistic coefficient swap point (t_{swap}), the point at which the semi major axis (orbit energy level) is the same as at the swap point of the other trajectory (t_{eq}), and the terminal point (t_{term}). Note that in Figure 6.20, the subscript "old" refers to a parameter in the initial numerically propagated trajectory, and the subscript "new" refers to a parameter in the new trajectory that one wishes to analyze without numerically propagating. In phase 4 (below the terminal point) both trajectories have the same C_b so they can
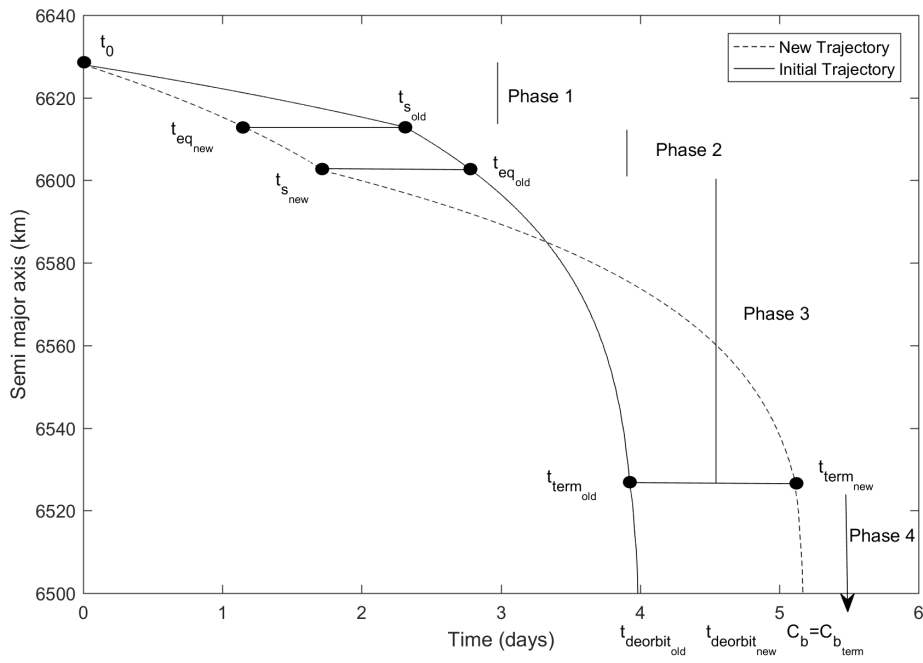
FIGURE 6.20: Characterizing Behavior of New Trajectory Based on Old Trajectory

be assumed to experience the same change in orbital elements between the terminal point and the de-orbit point. For the three phases before the terminal point, Eqs. 6.16-6.18 can be utilized to calculate the changes in time and orbital elements experienced in each phase of the new trajectory. All changes in time and orbital elements can be added to calculate the final time and orbital elements, and hence the latitude and longitude, at the de-orbit point.

Additionally, a closed form analytical solution is derived in [125] to compute the control parameters (C_{b1}, C_{b2}, and t_{swap}) needed to achieve a desired total time (Δt_t) and total change in argument of latitude (Δu_t) to the terminal point based on C_{b10}, C_{b20}, Δt_{10}, Δt_{20}, Δu_{10}, and Δu_{20} from an original numerically propagated trajectory. These relations are

$$C_{b2} = \frac{C_{b20}(\Delta t_{20}\Delta u_{10} - \Delta t_{10}\Delta u_{20})}{\Delta t_t \Delta u_{10} - \Delta t_{10}\Delta u_t} \tag{6.19}$$

$$C_{b1} = \frac{\Delta u_{10} C_{b10} C_{b2}}{\Delta u_t C_{b2} - \Delta u_{20} C_{b20}} \tag{6.20}$$

$$t_{s_{new}} = \frac{t_{s_{old}} C_{b10}}{C_{b1}} \tag{6.21}$$

Note that C_{b10}, Δt_{10}, and Δu_{10} are the ballistic coefficient, time change, and argument of latitude change between the initial time and the swap point in the initial numerically propagated trajectory and C_{b20}, Δt_{20}, and Δu_{20} apply between the swap point and the terminal point. Note that the subscript "0" indicates a parameter applicable to the numerically propagated trajectory while parameters without the subscript "0" apply to the new trajectory that has not been propagated. Given a numerically propagated trajectory with some final impact longitude and latitude, the total argument of latitude (Δu_t) and longitude increase

($\Delta\lambda$) required to de-orbit in the desired location can be calculated using the procedures in Sec. 6.2.2 and Sec. 6.2.2 and Eqs. 6.10 and 6.13. The total orbit lifetime required to achieve the de-orbit longitude change $\Delta\lambda$ is computed by

$$\Delta t_t = \Delta t_{t0} - \frac{\Delta\lambda}{\omega_\oplus} \tag{6.22}$$

Where $\omega_\oplus$ is the rotation rate of the Earth. The Δt_t value can be adjusted using the method in [125] to ensure that the minimum targeting error is achieved within the range of feasible satellite ballistic coefficients. Note that with this method, the desired Δu_t will always be achieved, and a Δt_t as close as possible to the desired one will be achieved.

A key aspect of the guidance generation algorithm is the drag-work-enforcement method that is merged into the shrinking horizon guidance generation approach. Due to the assumptions of a spherical Earth and constant density vs. altitude profile used in the analytical solution, there are often discrepancies between the numerical and analytical trajectory solutions, especially if the trajectories extend far into the future. To ensure sufficient controllability to target any point with latitude below the orbit inclination, maneuvering must begin almost two weeks in advance of the expected de-orbit. When this trajectory is simulated, the long propagation time causes the analytical and numerical solutions to diverge because small errors due to the analytical solution assumptions grow over time. Conversely, if maneuvering is initiated very close to the de-orbit time (2-3 days), the analytical and numerical solutions will agree very well, but there may not be sufficient controllability to target any point on the Earth's surface.

In the shrinking horizon approach, when the trajectory is propagated to the de-orbit point with the ballistic coefficient profile dictated by the analytical solution, the first t_g seconds of this trajectory are stored as a part of the guidance

and the trajectory after t_g is utilized to compute another analytical ballistic coefficient profile that will be numerically propagated and will be approximately t_g seconds shorter than the previously propagated trajectory. This process continues until a certain error threshold is reached or a trajectory is propagated that has less than a certain amount of orbit lifetime remaining. In the drag-work enforcement method, the work done by aerodynamic drag is recorded during the trajectory propagation, and the ballistic coefficient of the satellite during the first t_g seconds of propagation is varied so that the total work done by drag at t_g is equal to the work that should have been done by this time according to the analytical solution. In the trajectory propagation, the power or rate of change of work done by drag per unit mass can be calculated as

$$P = \dot{W}_d = -C_b \rho v_\infty (\mathbf{v}_\infty \cdot \mathbf{v}) \tag{6.23}$$

This expression is equivalent to the drag force (per unit mass) multiplied by the distance over which the drag is acting, divided by the time over which that distance is acted through which is the definition of power. Work done by drag is considered as a seventh state variable (in addition to the ECI position and velocity vectors) and is numerically integrated along with the position and velocity by computing $\dot{W}_d$ using Eq. 6.23 at each time step. Given a numerically propagated trajectory with some C_b and W_d available at each time step, the work that should be done by drag for a trajectory with the same initial conditions but a different C_b can be calculated at some time t as follows.

1. Eq. 6.16 is used to calculate the time (t_{eq}) at which the old trajectory has the same orbital energy (same semi-major axis) as the new trajectory at time t. If the ballistic coefficient is unchanging in both trajectories, this is computed by

$$t_{eq} = \frac{C_{b_{new}} t}{C_{b0}} \tag{6.24}$$

2. The new trajectory should have the same W_d at t as the old, numerically
propagated trajectory did at t_{eq}.

By scaling the C_b during each propagation phase to force the actual W_d to
equal the analytically expected W_d, the numerically propagated trajectory is made
to behave more like the analytically predicted trajectory, and thus the errors be-
tween the analytical and numerical trajectories are reduced.

6.2.4   Terminal Orbit Adjustment

Once a guidance trajectory that leads from the spacecraft initial conditions to the
desired de-orbit point is computed, propagation of this trajectory from the de-
orbit point to the ground impact point may not necessarily result in a ground
impact at the desired location. This is because the final velocity and flight path
angle at the de-orbit point as well as the density profile may not be identical to
those at the initially calculated de-orbit state, even if the latitude, longitude, and
altitude are the same. Fortunately, the impact-point errors that result from this are
almost entirely in the along track direction and can be corrected by modifying the
ballistic coefficient during the final portion of the guidance trajectory before the
de-orbit point.

To do this, the argument of latitude increase Δu_{des} needed to achieve the de-
sired ground impact location can be computed using the procedure in Sec. 6.2.2.
To achieve this desired Δu_{des}, all ballistic coefficient values between time t_{adj} and
the de-orbit point (t_{deo}) can be modified according to

$$C_b = C_{b0} \frac{\Delta u_0}{\Delta u_0 + \Delta u_{des}} \qquad (6.25)$$

where C_{b0} is the original ballistic coefficient and Δu_0 is the argument of latitude
change between t_{adj} and the de-orbit point in the initially propagated trajectory.
To compute the t_{adj} that should be used to ensure that the ballistic coefficient

change is not excessive, the user can first define the maximum allowable percentage of ballistic coefficient change q. In this work $q = .04$ was used. If T is the approximate orbital period at the semi-major axis of the de-orbit point, t_{adj} can be computed by

$$t_{adj} = \frac{\Delta u_{des}}{2\pi q} T \tag{6.26}$$

where the orbital period T is given by [128]

$$T = 2\pi \sqrt{\frac{a^3}{\mu}} \tag{6.27}$$

This ensures that the percentage change in ballistic coefficient associated with Eq. 6.25 will be less than q.

A new trajectory from t_{adj} to the ground is simulated with the modified C_b profile prescribed by Eq. 6.25. The process of updating the C_b profile and numerically propagating to the ground continues until a trajectory is found that with an impact latitude error below a specified tolerance. Note that the process explained in the second paragraph of Sec. 6.2.2 can be utilized to reduce Δu_{des} by a shrinking scaling factor k to aid in the convergence to a trajectory with the desired impact latitude. The trajectory and C_b profile after t_{adj} are appended to the trajectory and C_b profile before t_{adj} to obtain a complete guidance trajectory and C_b profile from the spacecraft initial conditions to the desired ground impact point.

6.3   Control Methodology for Trajectory Tracking

6.3.1   Orbital Trajectory Tracker

Due to uncertainties in the drag force, the spacecraft will eventually drift from the guidance trajectory if the desired ballistic coefficient profile is applied open loop. While it is possible to re-generate the guidance trajectory once the drift exceeds a given threshold, guidance trajectory generation is computationally expensive and there is no guarantee that a new guidance trajectory with equally low error will exist from the new spacecraft initial conditions. For this reason, feedback control techniques must be utilized to vary the commanded spacecraft C_b based on the difference between the actual and desired state to ensure that the computed guidance trajectory is followed. While the spacecraft is tracking an initial guidance trajectory, new guidance trajectories can be periodically generated and tracked to take into account updated density forecasts.

The Schweighart Sedwick (SS) equations of relative motion [129] can be utilized to specify the evolution of the position and velocity of the spacecraft relative to the guidance trajectory at any given time when the separation between the spacecraft and the guidance trajectory is small compared to the radius of Earth. The in-plane SS linearization considering the effects of differential aerodynamic
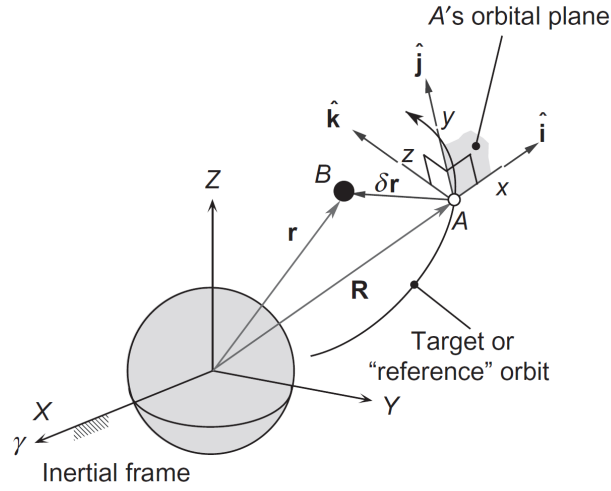
FIGURE 6.21: Local Vertical Local Horizontal (LVLH) Frame [128]

drag can be written as [129]

$$
\begin{bmatrix} \delta\dot{x} \\ \delta\dot{y} \\ \delta\ddot{x} \\ \delta\ddot{y} \end{bmatrix} = \begin{bmatrix} 0 & 0 & 1 & 0 \\ 0 & 0 & 0 & 1 \\ b & 0 & 0 & d \\ 0 & 0 & -d & 0 \end{bmatrix} \begin{bmatrix} \delta x \\ \delta y \\ \delta\dot{x} \\ \delta\dot{y} \end{bmatrix} + \begin{bmatrix} 0 \\ 0 \\ 0 \\ -\rho v_g{}^2 \end{bmatrix} \Delta C_b \tag{6.28}
$$

where

$$
\Delta C_b = \left(C_{b_{sc}} - C_{b_g} \right) \tag{6.29}
$$

$$
n = \sqrt{\frac{\mu}{a^3}}, c = \sqrt{1 + \frac{3 J_2 R_e{}^2}{8 a^2} [1 + 3\cos(2i)]}, d = 2nc, b = \left(5c^2 - 2 \right) n^2 \tag{6.30}
$$

Note that $C_{b_{sc}}$ is the current spacecraft ballistic coefficient and C_{b_g} is the guidance ballistic coefficient.

With the dynamics of the relative motion between the spacecraft and the guidance trajectory given by Eq. 6.28 in the classic state-space form

$$\dot{\mathbf{x}} = \mathbf{A}\mathbf{x} + \mathbf{B}\mathbf{u} \tag{6.31}$$

it is possible to use a linear quadratic regulator (LQR) [130] control approach to drive the relative position and velocity to zero. An LQR controller derives the gain $\mathbf{K}$ to yield the feedback control law

$$\mathbf{u} = -\mathbf{K}\mathbf{x} \tag{6.32}$$

that drives the state to zero and minimizes the cost functional

$$J = \int_0^\infty \left(\mathbf{x}^T \mathbf{Q} \mathbf{x} + \mathbf{u}^T \mathbf{R} \mathbf{u} \right) dt \tag{6.33}$$

where $\mathbf{Q}$ and $\mathbf{R}$ are square weighting matrices of appropriate dimension. Because the state is four-dimensional and the control is one-dimensional, $\mathbf{Q}$ and $\mathbf{R}$ will be 4 by 4 and 1 by 1 matrices respectively and $\mathbf{K}$ will be a 1 by 4 gain matrix with the control given by

$$\Delta C_b = - \begin{bmatrix} K_1 & K_2 & K_3 & K_4 \end{bmatrix} \begin{bmatrix} \delta x \\ \delta y \\ \delta \dot{x} \\ \delta \dot{y} \end{bmatrix} \tag{6.34}$$

The LQR gain is optimal in the sense that no linear feedback control law can be derived that yields a lower value of J as $t \rightarrow \infty$. However, the practical performance of the controller is heavily dependent on $\mathbf{Q}$ and $\mathbf{R}$ which weight the relative importance of driving the state to zero as fast as possible and executing minimal control effort respectively. Ref. [125] discusses a method of selecting $\mathbf{Q}$ and $\mathbf{R}$ whereby $\mathbf{Q}$ is set to

$$\mathbf{Q} = \begin{bmatrix} 0 & 0 & 0 & 0 \\ 0 & 1 & 0 & 0 \\ 0 & 0 & 0 & 0 \\ 0 & 0 & 0 & 0 \end{bmatrix} \tag{6.35}$$

to prioritize the minimization of along-track error and $\mathbf{R}$ is adjusted to determine how responsive the controller should be to observed tracking errors. An Extended Kalman filter can be applied to the GPS measurements to reduce the noise in the relative position and velocity estimates used for the control. The LQR gain can also be periodically updated as the $\mathbf{A}$ and $\mathbf{B}$ matrices in the SS dynamics change due to the different densities and semi-major axes experienced during the orbital decay.

Note that in the last few orbits, $\mathbf{R}$ can be decreased and a $\mathbf{Q}$ matrix can be utilized with finite values along the diagonal. This creates a more "aggressive" controller that will respond with a greater actuator effort (larger ΔC_b) to any observed position or velocity errors and will help ensure that the spacecraft is as close to the guidance trajectory as possible at the de-orbit point after which control may be limited due to thermal and dynamic pressure constraints.

6.3.2   Re-Entry Trajectory Tracker

An LQR control approach is utilized also for the re-entry tracker. LQR controllers, in general, are robust, simple, and widely used in re-entry applications [131]. In order to design a linear controller, it is necessary to define a linear system model, derived from the ordinary differential equations system describing the system dynamics.

Considering the equations of motion (4.20 - 4.21) for a point mass moving over the rotating Earth, the state vector of the model is:

$$x = [V \ \gamma \ \psi \ r \ \theta \ \phi] \tag{6.36}$$

In order to design a linear controller, it is necessary to define a linear system model, derived from the ordinary differential equations system previously introduced.

One of the most common procedures in literature ([132] [133]) is to reduce the system order by considering the simplified-state equations for a stationary Earth, which neglect Coriolis and centrifugal forces, and exploit the Newtonian gravity law expression.As shown in Table 6.2, the assumption of a stationary Earth decouples the vertical dynamic [V - γ - r plane] from the one in the perpendicular direction. Thus $\dot{V}$, $\dot{\gamma}$ and $\dot{r}$ equations become functions only of the associated states V, γ and r. The assumption reduces the system state vector from six to three variables:

$$x(t) = [V \ \gamma \ r] \tag{6.37}$$

The assumption is valid because for re-entry problems the vertical dynamic is much faster than the one in the perpendicular plane. Furthermore, this approach is very convenient in classic applications because by decoupling the vertical and

Equation	States					
	V	γ	r	θ	ϕ	ψ
$\dot{V}$	+	+	+		$\oplus$	$\oplus$
$\dot{\gamma}$	+	+	+		$\oplus$	$\oplus$
$\dot{r}$	+	+				
$\dot{\theta}$	+		+			
$\dot{\phi}$	+	+	+			+
$\dot{\psi}$	+	+	+		+	$\oplus$

TABLE 6.2: Equations of motion interdependency. (+) marks the dependency in the stationary Earth form, ($\oplus$) in the rotating Earth form

lateral dynamics, the state can be controlled by the LQR while the lateral dynamic is controlled by using the bank reversal logic, exploiting the only degree of freedom available as in the Soyuz and Apollo case scenarios.

Therefore, the system state equation is usually composed by the state vector defined in Equation 6.37 and by the input vector

$$u(t) = [\sigma] \tag{6.38}$$

where σ represents the bank angle.

The vehicle is kept around a nominal trajectory in the vertical plane by using the full state feedback LQR controller, while is pointed toward the target through bank reversal manoeuvres.

Starting from the literature references, some changes were made in order to adapt the LQR approach to the considered problem. Vertical and lateral dynamic

have not been decoupled, and further state equations were considered in order
to improve the controller performances.

Considering the system as an equilibrium trajectory, and assuming to add
small deviations to the equilibrium path, the perturbed system can be written as
the sum of an equilibrium condition and a perturbation. E.g., for the Velocity:

$$V = V_0 + \Delta V \tag{6.39}$$

where $()_0$ refers to the equilibrium conditions, and Δ indicates the perturbation.
The perturbation value is computed by solving the equation for the variable in Δ.
All the state variables are described as sum of a nominal state and a deviation as:

$$V = V_0 + \Delta V \qquad\qquad \gamma = \gamma_0 + \Delta\gamma \qquad\qquad r = r_0 + \Delta$$

$$\psi = \psi_0 + \Delta\psi \qquad\qquad \theta = \theta_0 + \Delta\theta \qquad\qquad \phi = \phi_0 + \Delta\phi \tag{6.40}$$

Similarly,

$$D = D_0 + \Delta D \qquad\qquad L = L_0 + \Delta L \qquad\qquad Y = Y_0 + \Delta Y \tag{6.41}$$

and

$$\alpha = \alpha_0 + \Delta\alpha \qquad\qquad \beta = \beta_0 + \Delta\beta$$

$$M = M_0 + \Delta M \qquad\qquad g = g_0 + \Delta g \tag{6.42}$$

Concerning the the gravitational acceleration expression, since it changes with altitude, Δg can be expressed as:

$$g = g_0 + \Delta g = \frac{\mu}{(R_\oplus + \Delta r)^2} = \frac{\mu}{R_\oplus^2}\left(1 - \frac{2\Delta r}{R_\oplus}\right) \tag{6.43}$$

thus,

$$\Delta g = -2\frac{\mu}{R_\oplus^2}\frac{\Delta r}{R_\oplus} = -2g_0\frac{\Delta r}{R_\oplus} \tag{6.44}$$

Considering the equations for the vertical dynamics, exploiting the results above and approximating the cosine of a perturbation with 1 and the sine of a perturbation with 0, the following expressions can be derived by writing the perturbed state equations and subtracting the nominal states, neglecting higher-order terms as the product of two perturbations and their powers.

Starting from the simplified equations for the non-rotating Earth:

$$\dot{V} = -\frac{D}{m} - g\sin\gamma \tag{6.45a}$$

$$\dot{\gamma} = \frac{L}{mV} - \frac{g\cos\gamma}{V} + \frac{V}{r}\cos\gamma \tag{6.45b}$$

$$\dot{r} = V\sin\gamma \tag{6.45c}$$

The small perturbation theory linearization leads to the expressions:

$$\Delta\dot{V} = -\frac{1}{m}\Delta D - g_0\cos\gamma_0\Delta\gamma + 2\left(\frac{g_0\sin\gamma_0}{r_0}\right)\Delta r \tag{6.46a}$$

$$\Delta\dot{\gamma} = \left(\frac{2\cos\gamma_0}{r_0}\right)\Delta V - \left(\frac{V_0^2}{r_0} - g_0\right)\frac{\sin\gamma_0}{V_0}\Delta\gamma$$
$$+ \left(\frac{2g_0}{r_0} - \frac{V_0^2}{r_0^2}\right)\frac{\cos\gamma_0}{V_0}\Delta r + \frac{1}{mV_0}\Delta L \tag{6.46b}$$

$$\Delta \dot{r} = \sin \gamma_0 \Delta V + V_0 \cos \gamma_0 \Delta \gamma \tag{6.46c}$$

Regarding the aerodynamic forces, indicating with X the generic force, it can be expressed as function of state and control variables:

$$\begin{aligned}
\Delta X &= \frac{\partial X}{\partial M} \Delta M + \frac{\partial X}{\partial \alpha} \Delta \alpha + \frac{\partial X}{\partial \beta} \Delta \beta \\
&= \frac{\partial X}{\partial M} \frac{M_0}{V_0} \Delta V + \frac{\partial X}{\partial \alpha} \Delta \alpha + \frac{\partial X}{\partial \beta} \Delta \beta
\end{aligned} \tag{6.47}$$

Passing from forces to nondimensional forces, it leads to:

$$\Delta D = q_0 S_{ref} \frac{M_0}{V_0} C_{DM} \Delta V + q_0 S_{ref} C_{D\alpha} \Delta \alpha + q_0 S_{ref} C_{D\beta} \Delta \beta \tag{6.48a}$$

$$\Delta L = q_0 S_{ref} \frac{M_0}{V_0} C_{LM} \Delta V + q_0 S_{ref} C_{L\alpha} \Delta \alpha \tag{6.48b}$$

$$\Delta Y = q_0 S_{ref} \frac{M_0}{V_0} C_{YM} \Delta V + q_0 S_{ref} C_{Y\beta} \Delta \beta \tag{6.48c}$$

Substituting the Equations 6.48 in the system 6.46 it becomes:

$$\Delta \dot{V} = -\frac{1}{m} \left(q_0 S_{ref} C_{DM} \frac{M_0}{V_0} \right) \Delta V - g_0 \cos \gamma_0 \Delta \gamma + 2 \left(\frac{g_0 \sin \gamma_0}{r_0} \right) \Delta r$$
$$- \frac{1}{m} \left(q_0 S_{ref} C_{D\alpha} \right) \Delta \alpha - \frac{1}{m} \left(q_0 S_{ref} C_{D\beta} \right) \Delta \beta \tag{6.49a}$$

$$\Delta \dot{\gamma} = \left(\frac{2 \cos \gamma_0}{r_0} + \frac{1}{mV_0} q_0 S_{ref} C_{LM} \frac{M_0}{V_0} \right) \Delta V - \left(\frac{V_0^2}{r_0} - g_0 \right) \frac{\sin \gamma_0}{V_0} \Delta \gamma$$
$$+ \left(\frac{2g_0}{r_0} - \frac{V_0^2}{r_0^2} \right) \frac{\cos \gamma_0}{V_0} \Delta r + \frac{1}{mV_0} q_0 S_{ref} C_{L\alpha} \Delta \alpha \tag{6.49b}$$

$$\Delta \dot{r} = \sin \gamma_0 \Delta V + V_0 \cos \gamma_0 \Delta \gamma \tag{6.49c}$$

It is suggested to add a further kinematic equation to the system, since even a perfect tracking of the considered variables could lead to large landing dispersions [133].

The range-to-go variable is then considered. It represents the distance between the vehicle and the landing site, measured along a great circle through the same points.

The range-to-go can be expressed as:

$$R_{TG} = R_\oplus \cos^{-1}[\sin\phi_T \sin\phi + \cos\phi_T \cos\phi \cos(\theta_T - \theta)] \tag{6.50}$$

while its variation in time can be expressed as:

$$\dot{R}_{TG} = -\left(\frac{R_\oplus}{r}\right) V \cos\gamma \cos(\tilde{\psi} - \psi) \tag{6.51}$$

where $\tilde{\psi}$ represents the angle between the local parallel and the great circle connecting the target with the current vehicle location. It can be expressed as:

$$\tilde{\psi} = \frac{\pi}{2} - \tan^{-1}\frac{\sin(\theta_T - \theta)\cos\phi_T \cos\phi}{\sin\phi_T - \sin\phi \cos\frac{R_{TG}}{R_\oplus}} \tag{6.52}$$

After applying the same linearization procedure used for the other state variables, the range-to-go perturbation can be written as:

$$\Delta\dot{R}_{TG} = -\left(\frac{R_E}{r_0}\right)\cos\gamma_0 \cos(\tilde{\psi} - \psi_0)\Delta V + \left(\frac{R_E}{r_0}\right) V_0 \sin\gamma_0 \cos(\tilde{\psi} - \psi_0)\Delta\gamma$$
$$+ \left(\frac{R_E}{r_0^2}\right) V_0 \cos\gamma_0 \cos(\tilde{\psi} - \psi_0)\Delta r \tag{6.53}$$

The classical approach discussed in Sec. 2.2 is utilized to control the vertical dynamics by modulating the L/D ratio through changes in the bank angle and the use of bank reversal logic. In this case, the same approach is used to control

the lateral dynamic with the LQR [134].

Starting from a simplified expression for the heading

$$\dot{\psi} = \frac{Y}{mV \cos \gamma} \tag{6.54}$$

it has been linearized as follows and implemented in the equations system, as:

$$\Delta\dot{\psi} = -\frac{1}{V_0} \left(\frac{Y}{mV_0 \cos \gamma_0} \right) \Delta V + \left(\frac{Y_0}{mV_0 \cos \gamma_0} \tan \gamma_0 \right) \Delta\gamma$$
$$+ \frac{1}{mV_0 \cos \gamma_0} \Delta Y \tag{6.55}$$

Substituting the Equations of the system 6.48 into the expression above, it becomes:

$$\Delta\dot{\psi} = \left(\frac{1}{mV_0 \cos \gamma_0} q_0 S_{ref} C_{YM} \frac{M_0}{V_0} - \frac{Y_0}{mV_0^2 \cos \gamma_0} \right) \Delta V$$
$$+ \left(\frac{Y_0}{mV_0 \cos \gamma_0} \tan \gamma_0 \right) \Delta\gamma + \frac{1}{mV_0 \cos \gamma_0} q_0 S_{ref} C_{Y\beta} \Delta\beta \tag{6.56}$$

Once the linearized model is defined, by the equations 6.49, 6.51 and 6.56, the LQR logic can be applied to the system.

The linearized model is described by the perturbed state and the control variables, defined as:

$$\delta x = [\Delta V \ \Delta\gamma \ \Delta r \ \Delta R_{TG} \ \Delta\psi]^T$$
$$\delta u = [\Delta\alpha \ \Delta\beta]^T \tag{6.57}$$

Thus, the system can be written as:

$$\delta\dot{x} = A(t)\delta x + B(t)\delta u \tag{6.58}$$

and the control law as:

$$\delta u = -K(t)\delta x(t) \tag{6.59}$$

As anticipated, the control law is derived only for a certain number of points along the trajectory, where the system is linearized. Since $A(t)$ and $B(t)$ are functions of time, but are slowly varying, constant matrices $A(t_k)$ and $B(t_k)$ are derived for 20 discrete times t_k, as in the equation 6.63. The control law is then linearly interpolated through these points.

It has to be noticed that a full state feedback is considered, but while the variables of the vertical dynamic $[V \, \gamma \, r \, R_{TG}]$ are controlled with feedback gains on the error with respect to the reference state, the heading is controlled with a feedback gain on the difference between the current Heading angle, and the Heading angle to the target point.

$$\delta V = V - V_{ref} \qquad \delta\gamma = \gamma - \gamma_{ref} \qquad \delta r = r - r_{ref}$$

$$\delta R_{TG} = R_{TG} - R_{TGref} \qquad \delta\psi = \psi - \psi_r ef \tag{6.60}$$

The cost function to be minimized is characterized by the three matrices Q, R and N. N is chosen to be null, so that:

$$J(u) = \int_0^\infty (x^T Q x + u^T R u) dt \tag{6.61}$$

Q and R are diagonal weighting matrices, computed through a trial and error process, and can be defined as:

$$Q = \text{diag} \left(q_V \, q_\gamma \, q_r \, q_{RTG} \, q_\psi \right) \qquad\qquad R = \text{diag} \left(r_\alpha r_\beta \right) \tag{6.62}$$

$$A =
\begin{bmatrix}
-\frac{1}{m}\left(q_0 S_{ref} C_{DM}\frac{M_0}{V_0}\right) & -g_0\cos\gamma_0 & \frac{2g_0\sin\gamma_0}{r_0} & 0 & 0 \\[2ex]
\frac{2\cos\gamma_0}{r_0}+\frac{1}{mV_0}q_0 S_{ref} C_{LM}\frac{M_0}{V_0} & -\left(\frac{V_0^2}{r_0}-g_0\right)\frac{\sin\gamma_0}{V_0} & \left(\frac{2g_0}{r_0}-\frac{V_0^2}{r_0^2}\right)\frac{\cos\gamma_0}{V_0} & 0 & 0 \\[2ex]
\sin\gamma_0 & V_0\cos\gamma_0 & 0 & 0 & 0 \\[2ex]
-\left(\frac{R_E}{r_0}\right)\cos_0\cos(\tilde\psi-\psi_0)) & \left(\frac{R_E}{r_0}\right)V_0\sin\gamma_0\cos(\tilde\psi-\psi_0) & \left(\frac{R_E}{r_0^2}\right)V_0\cos\gamma_0\cos(\tilde\psi-\psi_0) & 0 & 0 \\[2ex]
\frac{1}{mV_0\cos\gamma_0}q_0 S_{ref} C_{YM}\frac{M_0}{V_0}-\frac{Y_0}{mV_0^2\cos\gamma_0} & \frac{Y_0}{mV_0\cos\gamma_0}\tan\gamma_0 & 0 & 0 & 0
\end{bmatrix}$$

$$B =
\begin{bmatrix}
-\frac{1}{m}q_0 S_{ref}\frac{dC_D}{d\alpha} & -\frac{1}{m}q_0 S_{ref}\frac{dC_D}{d\beta} \\[2ex]
\frac{1}{mV_0}q_0 S_{ref}\frac{dC_L}{d\alpha} & 0 \\[2ex]
0 & 0 \\[2ex]
0 & 0 \\[2ex]
0 & \frac{1}{mV_0\cos\gamma_0}q_0 S_{ref}\frac{dC_Y}{d\beta}
\end{bmatrix}$$

(6.63)

Part IV

Analysis and Results

Chapter 7

Trajectory Analysis

In this chapter the flight mechanics activities performed to design an ESA demonstration mission for a capsule with a deployable heat shield are presented. First the trajectory of the selected sub-orbital rocket have been computed. Starting from this data the nominal trajectory of the capsule after release of the rocket have been evaluated and studied, in particular evaluating the influence of some critics parameter on the trajectory. At the end an orbital re-entry trajectory is presented that have been used for the aero-thermodynamics analysis to design a plasma wind tunnel test which will demonstrate the capability of the proposed design to survive the re-entry environment.

7.1   VSB-30 Nominal Trajectory

The proposed sounding rocket for the ESA Mini Irene mission is a VSB-30 rocket. The typical vehicle trajectory and performance is approx. 260 km altitude and 285 kg scientific payload mass (> 6 minutes micro gravity). Mini Irene will flight as a secondary payload and it is foreseen that it will separate from the main payload 5 seconds after the motor separation, which normally occurs 59 seconds after lift-off (Hence, Mini-Irene separation from the payload will occur 64 seconds after lift-off).

For calculation of the main payload suborbital trajectory with VSB-30 motor, the following input data were used:

- Rocket motor: VSB-30

- Payload mass: 390.00 kg

- Launch Elevation: 87.90 deg

- Launch Azimuth: 352.00 deg

- Launch Latitude: 67.89 deg

- Launch Longitude: 21.11 deg

- Launch Altitude: 0.335 km

FIGURE 7.1: Typical ground track and impact point prediction for VSB-30

Note that these data are typical data. The payload mass will be known after at the Flight Acceptance Review a couple of months before launch. The final launcher settings will depend on actual wind data, payload mass and safety considerations for the impact area, and are generally set only some minutes before launch. The resulting trajectory data for the mission is summarized below:

- Apogee time: 262.12 s

- Apogee height: 261.435 km

- East position at apogee: -7.584 km

- North position at apogee: 37.130 km

- Range at apogee: 37.897 km

- Time at ground impact: 500.75 s

- East position at ground impact: -13.442 km

- North position at ground impact: 71.654 km

- Range at ground impact: 72.904 km

- Azimuth at ground impact: 349.375 deg

Below are provided trajectory plots for the full flight, with indication of Mini-Irene separation from the payload, 64 seconds after lift-off: a) ground track north/east b) ground track lat/long c) dynamic pressure and Mach vs. time d) altitude vs. time e) vertical, north and east velocities vs. time and finally f) velocity vector angles vs. time for the calculated trajectory.
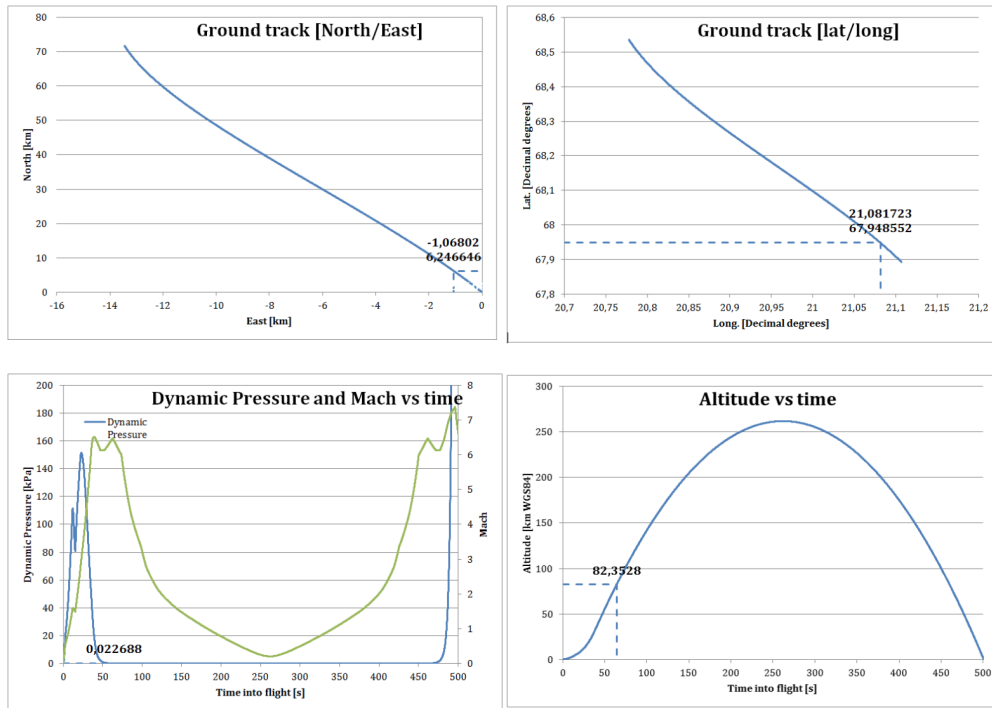
FIGURE 7.2: Trajectory plots for the full flight
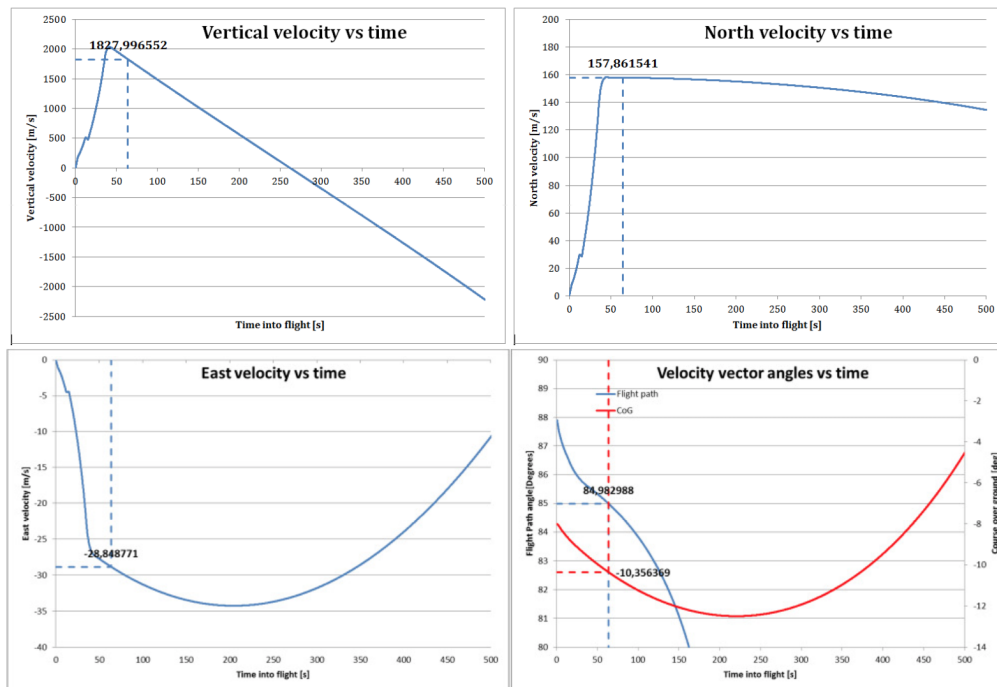
FIGURE 7.3: Velocity plots for the full flight

The calculated flight data at the time of Mini-Irene separation based on the nominal VSB-30 calculated trajectories is as follows.

Position data:

- Latitude: 67.948552

- Longitude: 21.081723

- Altitude (WGS-84 ref ellipsoid): 82.352 km

Velocity data:

- Total speed: 1835 m/s

- Flight path angle: 84.9 deg

- Heading angle: -10.36 deg

Flight path angle and Heading are in the topocentric-horizon system. The origin of the topocentric-horizon system is located at the launch pad. The system is defined by the x- axis pointing upwards, the y-axis pointing to east and the z-axis pointing to true north. The up direction is defined as the normal to the earth's reference ellipsoid

Below are provided trajectory plots up to 100 seconds after Lift-off, indicating Mini-Irene separation from the payload, 64 seconds after lift-off: a) ground track north/east b) dynamic pressure and Mach vs. time c) vertical, north and east velocities vs. time with separation and finally d) velocity vector angles vs. time for the calculated trajectory.
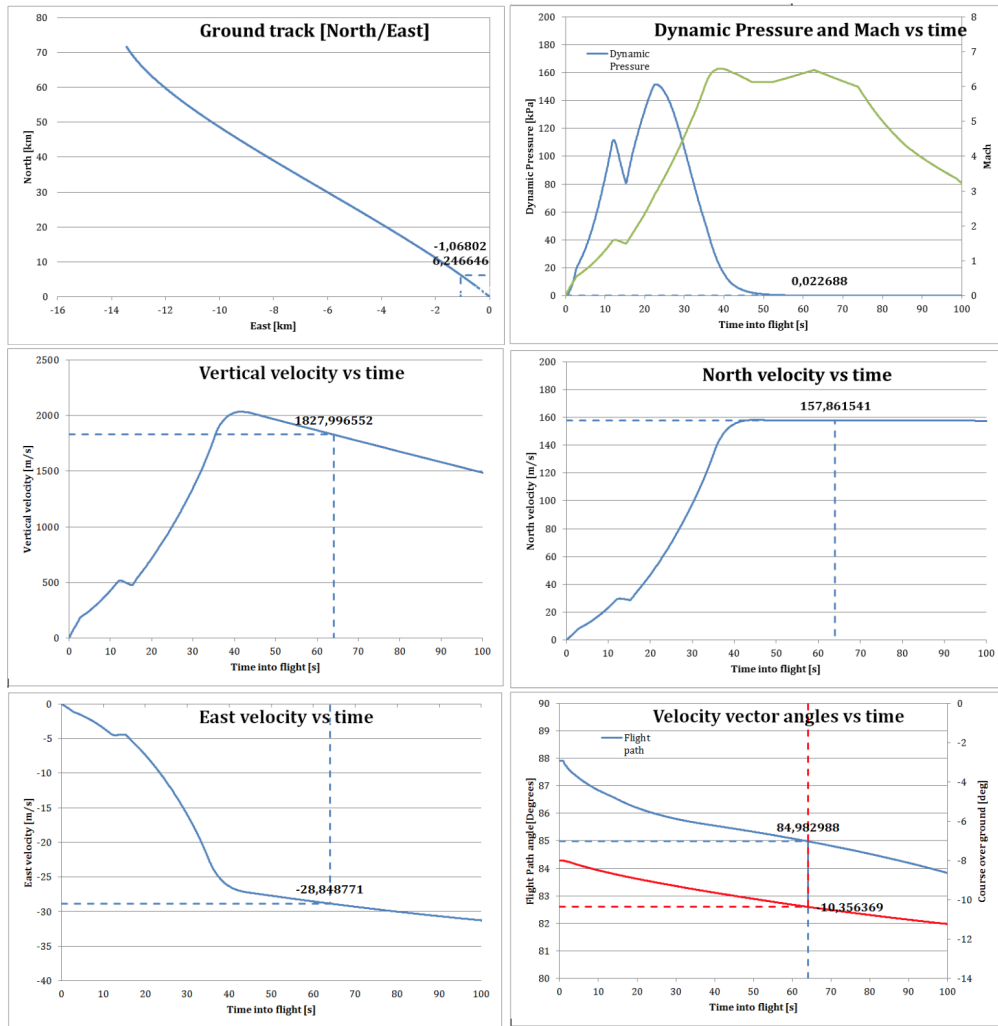
FIGURE 7.4: Trajectory plots up to 100 seconds after Lift-off

7.2 Capsule Reference Trajectory

On the basis of the previous data, some calculations have been performed to obtain the capsule re-entry trajectory, assuming that the capsule-payload separation instant corresponds 5 seconds after motors separation (nominally Lift off + 64 seconds). Initial conditions and capsule ballistic data are reported below, where the heading angle has been computed clockwise from the north direction:

- Separation time: 64 s

- Altitude: 82.352 km

- Velocity: 1834 m/s

- Flight Path Angle: 84.9 deg

- Heading Angle: -10.36 deg

- Mass: 12 kg

- Reference Surface: 0.4596 m^2

- Drag Coefficient: Function of Altitude

- Nose Radius of Curvature: 0.327 m

The initial velocity has been computed considering a 1 m/s ΔV between the capsule and the main payload, due to the separation. For the analyses an altitude dependent coefficient has been used as illustrated in the Aerodynamic Database Assessment paragraph of this thesis.

In Figure below a representation of the reference trajectory is presented:
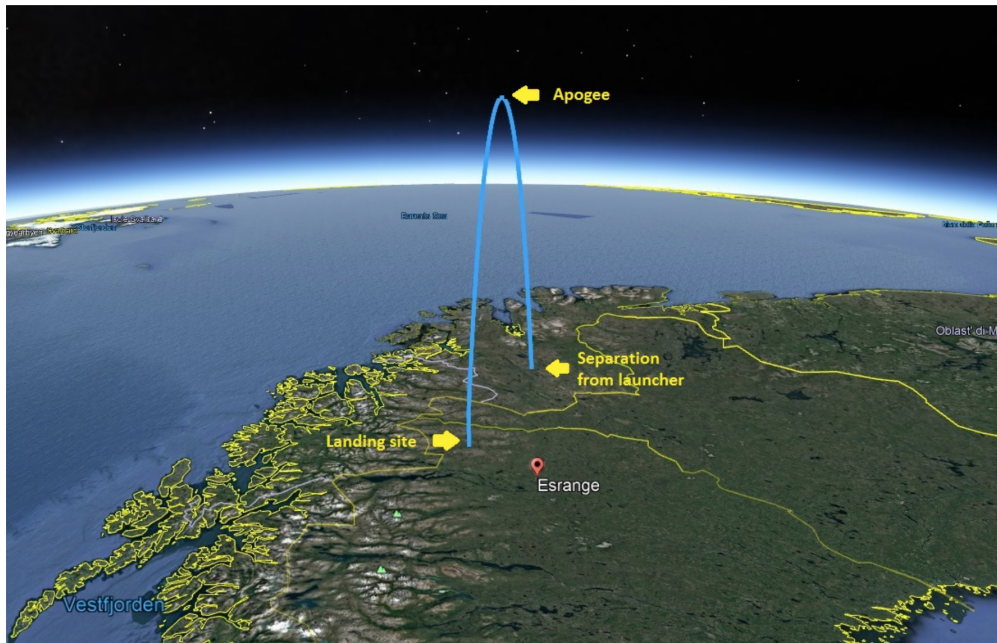
FIGURE 7.5: 3D Reference Trajectory

In the next Figures the main element (Altitude, Down Range, Velocity, Load factor, Dynamic Pressure and Heat Flux) of the reference trajectory are illustrated.

For what concerns aero-thermodynamic loads, it is possible to see that the highest values of pressure and deceleration are experienced by the capsule at an altitude of 40-45 km, whereas the peak of heat flux occurs at around 50 km. The maximum deceleration is in the order of 10 g_0 while the dynamic pressure is around 2 kPa. The maximum heat flux is in the order of 45 kW/m^2.
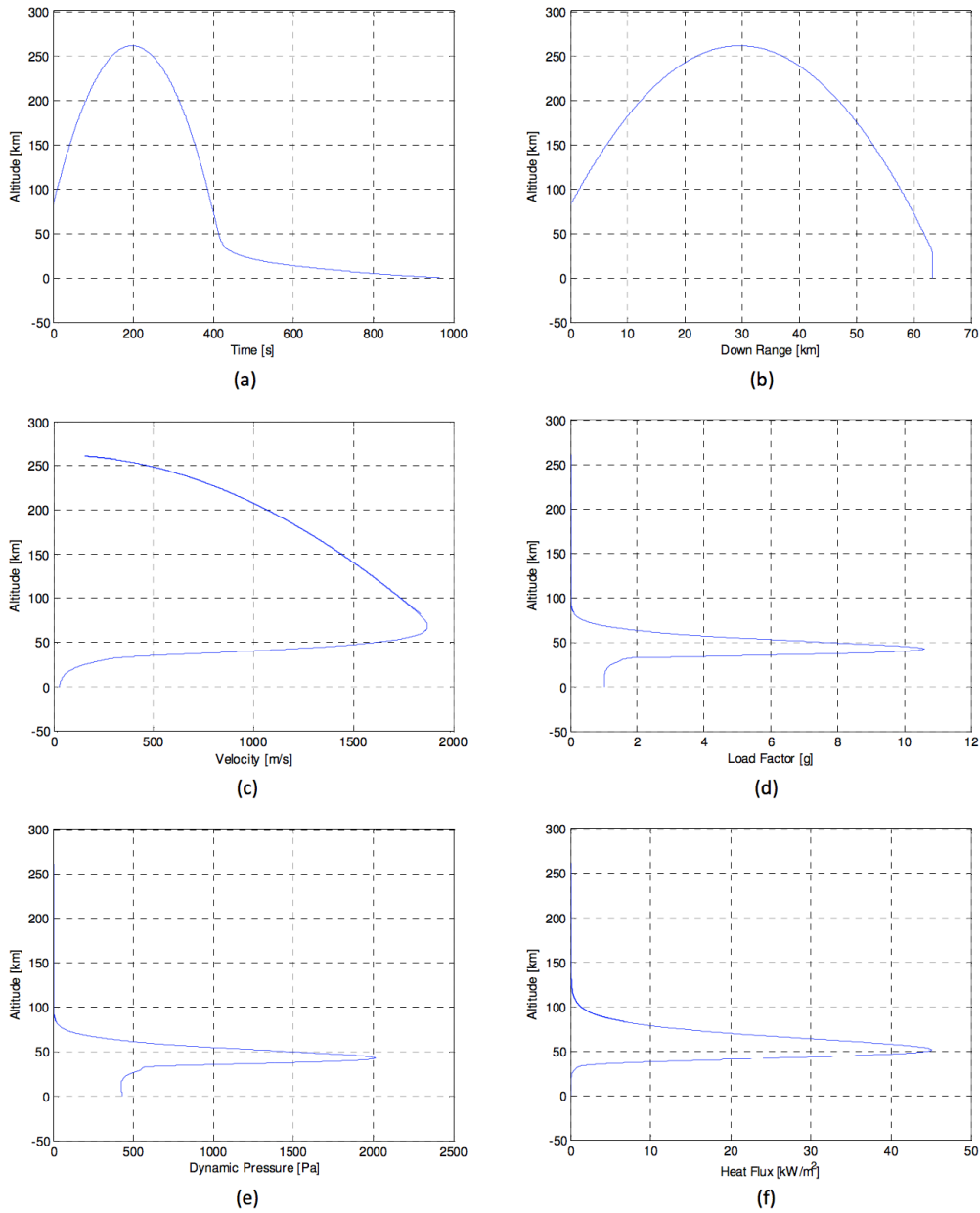
FIGURE 7.6: (a) Altitude versus time, (b) Downrange, (c) Velocity, (d) Load factor, (e) Dynamic Pressure and (f) Heat Flux versus altitude for the reference trajectory.

7.3　Drag Coefficient Variation Effect

The present section resumes the effect of a variation +/- 10% variation of the drag coefficient on the reference trajectory. For the analyses an altitude dependent coefficient has been used. In the following images, after the tridimensional trajectory representation, the altitude is plotted with respect to: Time, Down Range, Velocity, Load Factor, Dynamic pressure and Heat Flux.
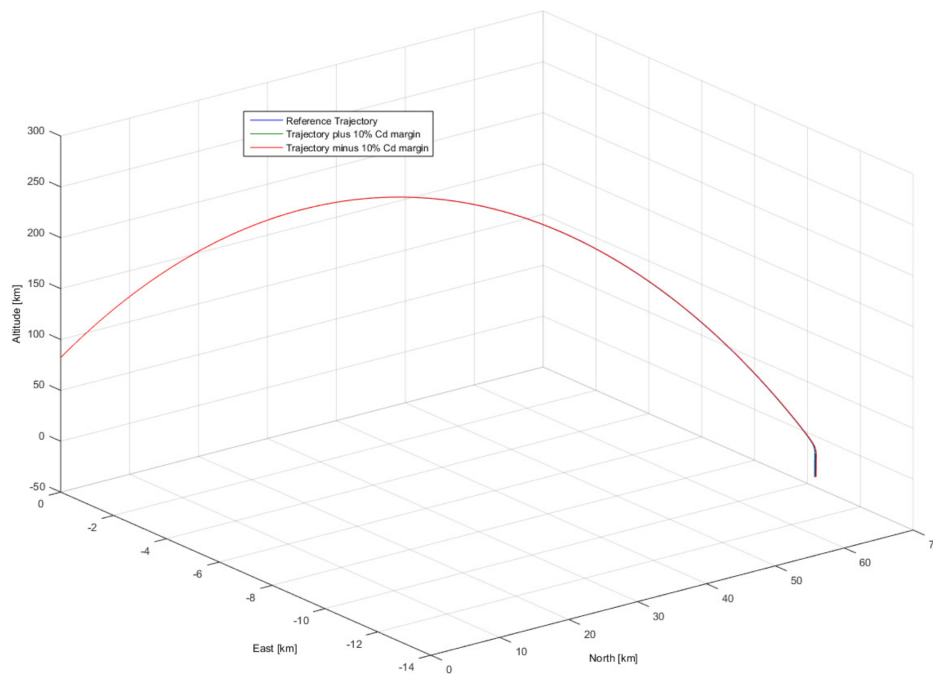
FIGURE 7.7: 3D Trajectories for nominal drag coefficient and +/-10% (axes have different scale)

The Cd variation affects the whole trajectory by a minimal amount, and in the final part of the flight, when the drag forces are significant.
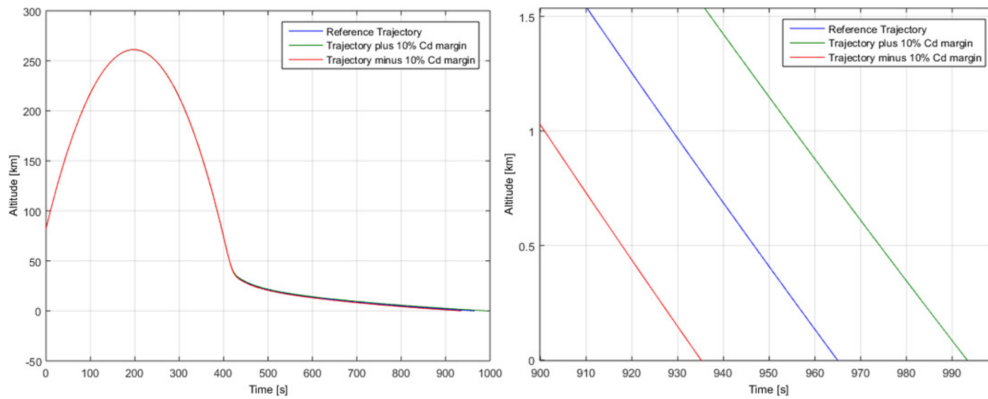
FIGURE 7.8: Time of flight for nominal drag coefficient and +/- 10% variation (zoom on the last part of the trajectory on the right)

Drag coefficient variation affects the flight time by +/- 30 seconds. The capsule characterized by a lower drag experience a shorter flight time.
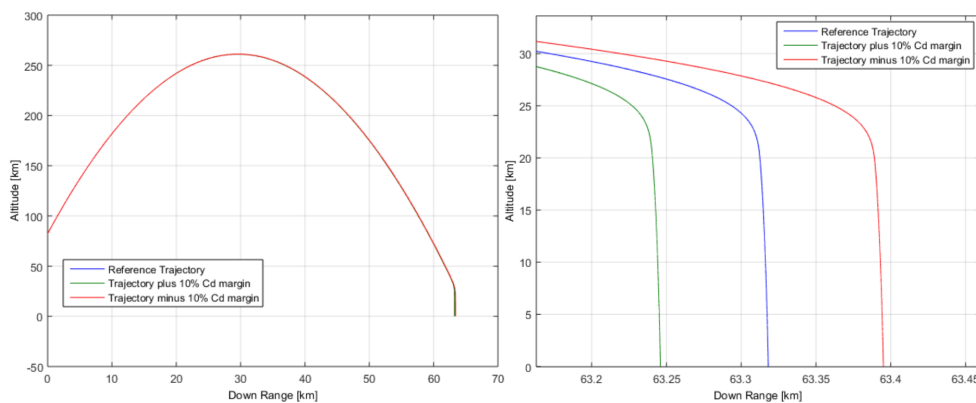
FIGURE 7.9: Down Range for nominal drag coefficient and +/- 10% variation

Drag coefficient variation affects the Down Range time by +/- 700m. The capsule characterized by a lower drag has a longer downrange.
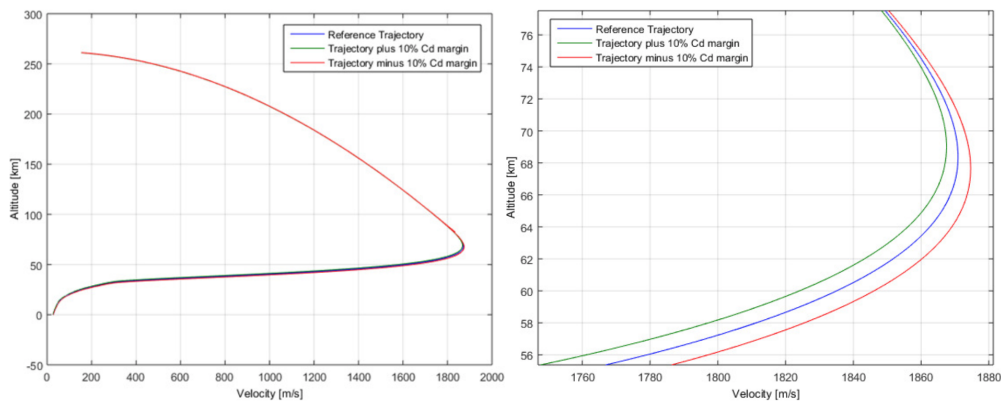
FIGURE 7.10: Velocity for nominal drag coefficient and +/- 10%
variation

Drag coefficient variation affects the peak velocity by +/- 5m/s. The capsule
characterized by a lower experiences higher peak velocity.
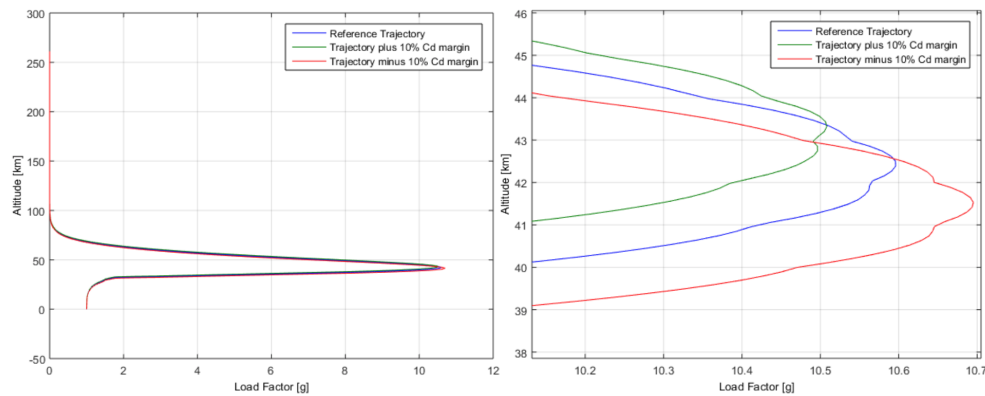
FIGURE 7.11: Load factor for nominal drag coefficient and +/- 10%
variation

Drag coefficient variation affects the peak load factor by +/- 0.1g. The capsule
characterized by a lower drag experiences higher load factor.
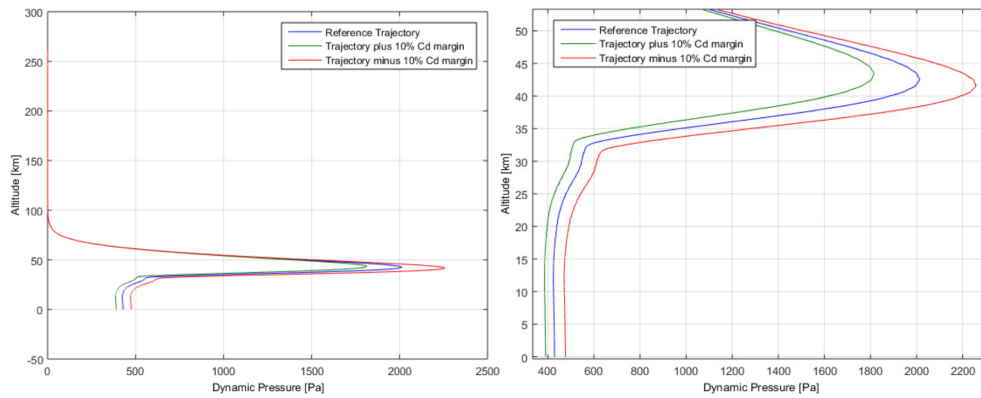
FIGURE 7.12: Dynamic Pressure for nominal drag coefficient and
+/- 10% variation

Drag coefficient variation affects the peak dynamic pressure by +/- 200Pa.
The capsule characterized by a lower drag experiences higher dynamic pressure,
this variation causes also the load factor difference.
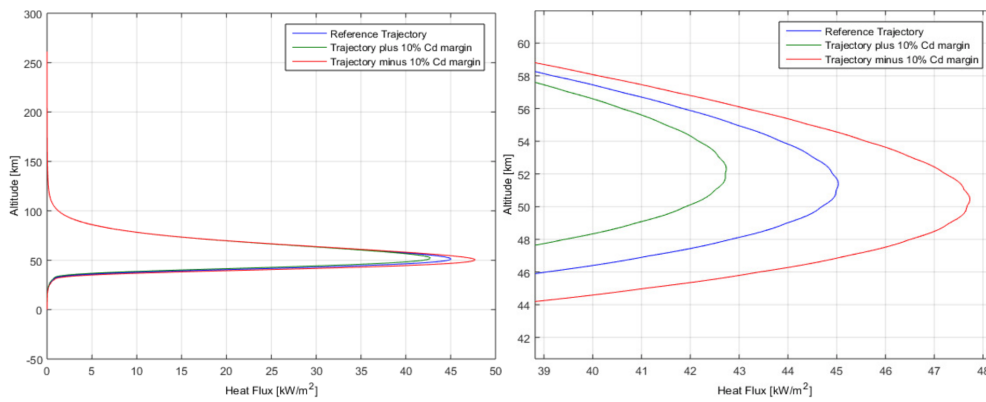
FIGURE 7.13: Stagnation point Heat Flux for nominal drag coeffi-
cient and +/- 10% variation

Drag coefficient variation affects the peak stagnation point heat flux by +/-
$3kW/m^2$. The capsule characterized by a lower drag experiences higher heat
flux.

The overall variations are marginal, the limited variation in the down range are a consequence of the almost vertical flight path angle. All other variations are a direct consequence of the variation of the ballistic coefficient.

7.4 Simulation of a Re-entry from LEO

In order to provide data for the design of the ground demonstrator to be tested in the Plasma Wind Tunnel to prove the thermal protection system, also a re-entry trajectory from LEO (Low-Earth-Orbit) conditions has been investigated. A capsule with the same ballistic coefficient, but twice the size as the flight demonstrator, has been considered. The initial conditions assumed for the simulation, corresponding to a re-entry from the orbit of the International Space Station, are summarize below.

- Altitude: 306 km

- Velocity: 7164 m/s

- Flight Path Angle: 0 deg

- Heading Angle: -3.11 deg

- Mass: 48 kg

- Reference Surface: 1.8384 m^2

- Drag Coefficient: Function of Altitude

- Nose Radius of Curvature: 0.654 m

The following Figures show the main aero-thermodynamic loads expectable on the capsule during the trajectory. In particular, it is interesting to see that the thermal loads are almost one order of magnitude higher than in the case of the

sub-orbital flight. These data will be useful to design the Plasma Wind Tunnel test conditions.
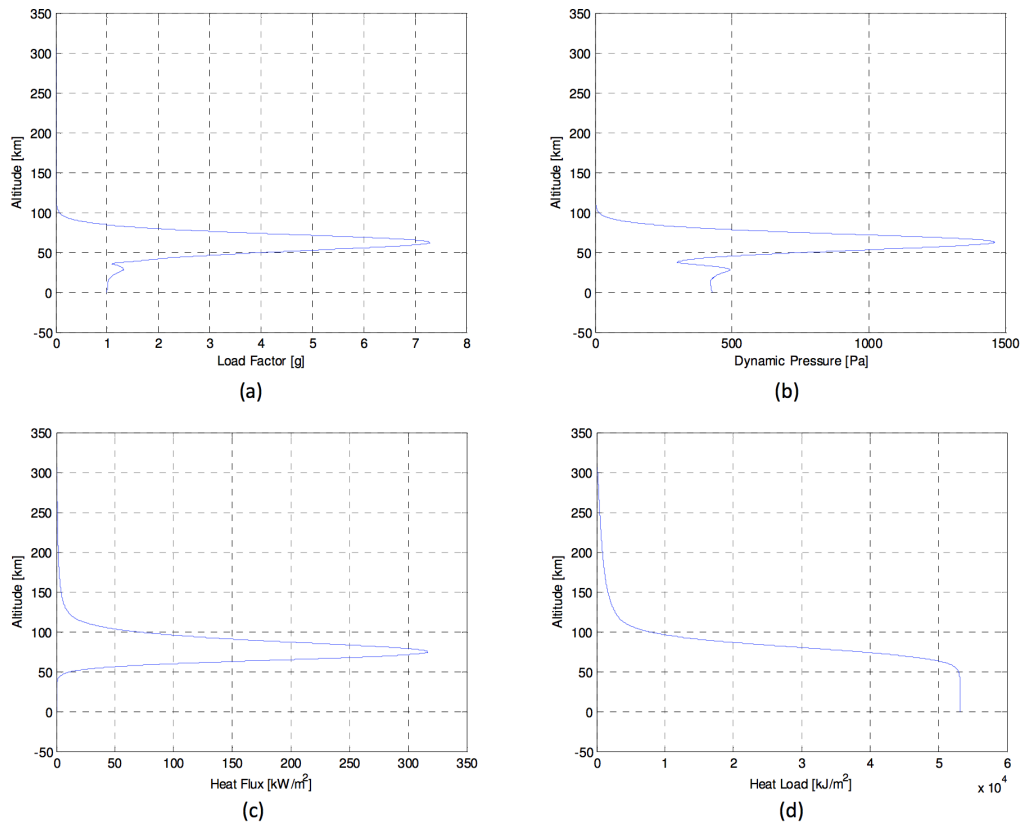
FIGURE 7.14: (a) Load Factor, (b) Stagnation point pressure, (c) Stagnation point heat flux and (d) Heat load versus altitude in case of a re-entry from LEO

Chapter 8

Aero-thermodynamics Results

The reference capsule concept has a number of extreme loading flight conditions for which analyses are required. It is a rather small capsule (i.e. strong Reynolds number effects) that must return to Earth by flying trimmed throughout hypersonic up to subsonic regimes. Thus, the whole Mach number range foreseen for the reference flight scenario was analyzed in this research work.

The aerodynamic coefficients have been provided for different flight conditions of the reference flight scenario, according to the space-based design approach
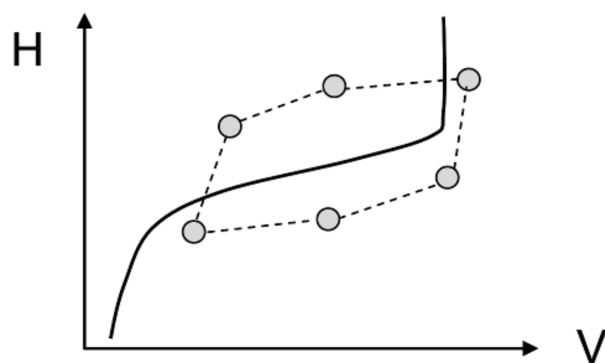
FIGURE 8.1: Space-based design approach in the Altitude-Velocity map

This design approach dictates the generation of a complete dataset as function of a number of independent parameters (i.e., M_∞, Re_∞, and α) as schematized in

Figure 8.1.

On the other hand, surface convective heat flux and pressure distributions at capsule wall have been provided for different flight conditions along with the reference flight trajectory, according to the trajectory-based design approach

This design approach consists in performing the aero-thermal computations at a finite number of "critical" points on the given nominal design trajectory, as schematized in Figure 8.2.
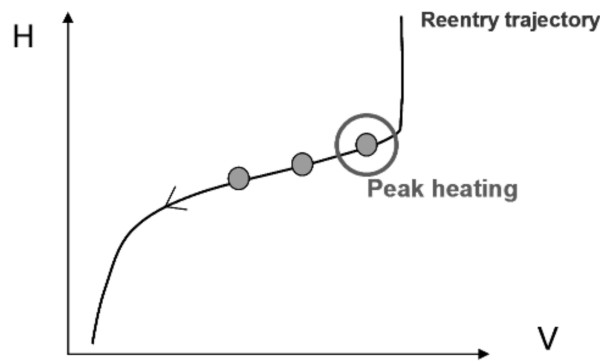
FIGURE 8.2:   Trajectory-based design approach in the Altitude-
Velocity map

For the transitional flow regime (the one bridging the continuum and the free molecular regimes), the bridging relationship approach was applied.

Finally, it is worth noting that in the present design, MINI-IRENE aerodynamics and aero-thermodynamics have been provided with both engineering-based/panel methods approach and more reliable Computational Fluid Dynamics (CFD) analyses.

8.1   Aerodynamic Database Assessment

MINI-IRENE aerodynamics has been provided with both engineering-based and thermo-chemical non-equilibrium CFD simulations; while capsule aero-heating

was accomplished by means of only CFD simulations.

For instance, capsule engineering-based aerodynamics were performed by means of 3D Panel Method tool. This tool at high supersonic and hypersonic speeds is able to accomplish the aerodynamic and aero-thermodynamic analyses of a complex re-entry vehicle configuration by using simplified approaches as local surface inclination methods (i.e., Newtonian aerodynamics) and approximate boundary-layer methods.

The aerodynamic analysis is shown in term of lift force (C_L), drag force (C_D), and pitching moment (C_M) coefficients:

$$C_L = \frac{L}{\frac{1}{2}\rho_\infty V_\infty^2 S_{ref}} \tag{8.1a}$$

$$C_D = \frac{D}{\frac{1}{2}\rho_\infty V_\infty^2 S_{ref}} \tag{8.1b}$$

$$C_M = \frac{M}{\frac{1}{2}\rho_\infty V_\infty^2 S_{ref}} \tag{8.1c}$$

where the geometric reference parameters that have been chosen in order to make aerodynamic forces non-dimensional coefficients are $S_{ref} = 0.342m^2$ (i.e., L_{ref} = 0.66 m (i.e., maximum capsule diameter). The pole for moment reduction is at 35% of L_{ref} from capsule nose.

The aerodynamic sign convention for forces and moments coefficients is provided in Figure 8.3 (directions are positive as shown).

Therefore,

- Angle of Attack (α) is positive when free stream arrives from down of the MINI IRENE;

- Sideslip angle (β) is positive when free stream arrives from right of the MINI IRENE;
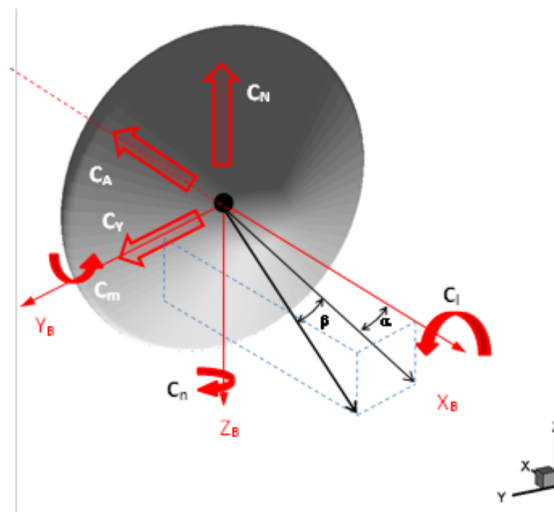
FIGURE 8.3: Aerodynamic sign convention

- Axial force coefficient (C_A) is positive when force is pushing in front of capsule toward the base;

- Normal force coefficient (C_N) is positive when force is pushing on belly side of capsule toward up;

- Side force coefficient (C_Y) is positive when force is pushing on left side of capsule toward the right;

- Pitching moment coefficient (C_m) is positive when the capsule puts the nose up;

that is the convention usually adopted in Flight Mechanics.

The stability conditions for the vehicle are the following:

- Longitudinal stability: $C_{m_\alpha} < 0$

- Lateral-directional stability: $C_{n_\beta} > 0$; $C_{l_\beta} < 0$

- Pitch damping: $C_{m_q} + C_{m_{\dot\alpha}} < 0$

Aerodynamic data, discussed in thist section, are obtained starting from those provided by previous work of University of Naples (UNINA). Starting from this data, and in the light of the flow regime classification, a more populated capsule AEDB have been developed

The available capsule's AEDB data, are summarized in Figure 8.4 for each flow regime and for angle of attack (AoA) ranging from 0 to 180 deg with step 10 deg. This figure provides the MINI-IRENE trajectory in the Altitude-Mach map, flow regime domains, as well as the points where capsule aerodynamics was investigated and available.
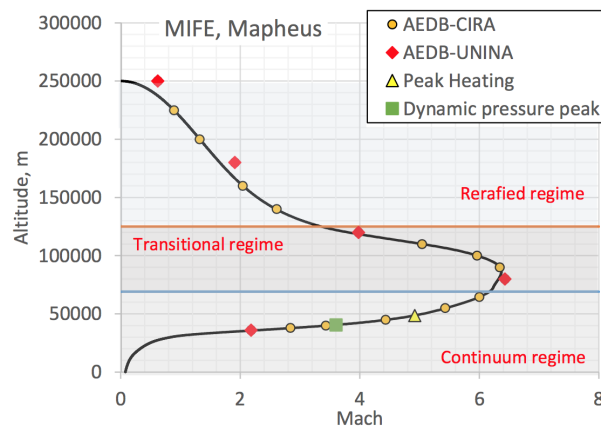
FIGURE 8.4: Flow regime scenario with available AEDB

In the FM flow conditions, Direct Simulation Monte Carlo (DSMC) simulations were carried out by colleagues of the University of Naples "Federico II" (UNINA). It is possible to note that the Navier-Stokes (continuum) predictions compare favorably with the DMCS predictions, starting to show more difference at high altitudes, as expected. For instance, profiles of drag coefficient versus Kn number, at 0, 20 and 30 deg AoA are provided in Figure 8.5.

As one can see, capsule C_D features a linear behavior versus the Knudsen number. Note that, this linear trend was assessed by interpolating available DSMC drag coefficients data along with the Knudsen number.
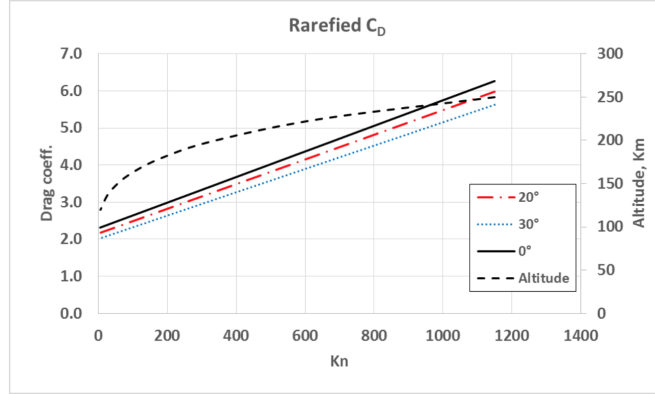
FIGURE 8.5: Drag coefficient versus Kn in FM flow

In the transitional flow regime, a very simple relationship [135] to bridge the FM to continuum flow aerodynamic coefficients have been exploited:

$$C_{i,trans} = C_{i,cont} + (C_{i,FM} - C_{i,cont})\,\overline{C}_i \tag{8.2}$$

where the normalized coefficient $\overline{C}_i$ uses Knudsen number as the independent parameter:

$$\overline{C}_i = \frac{C_i - C_{i,cont}}{C_{i,FM} - C_{i,cont}} = F(Kn_\infty) = sin^2\left[\frac{\pi}{8}\left(3 + Log_{10}Kn_\infty\right)\right] \tag{8.3}$$

with $10^{-3} < Kn_\infty < 10$ and, $C_{i,cont}$ and $C_{i,FM}$ are the aerodynamic coefficients in continuum and FM flow regimes, respectively. Results for C_D at 0, 20 and 30 deg AoA in transitional flow regime are provided in Figure 8.6.

As shown, the drag profile versus Knudsen features the classical s-shape ranging from rarefied to continuum flow conditions, as expected.

As far as continuum flow aerodynamic is concerned, Navier-Stokes simulations were accomplished. Engineering-based estimates were also performed, as closed-form solutions, available in literature, and panel methods, typical of Hypersonic's.
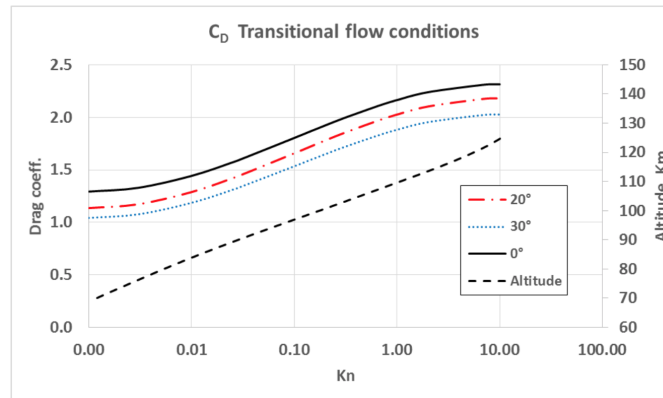
FIGURE 8.6: Drag coefficient versus Kn in transitional flow

The drag coefficients versus Mach in hypersonic continuum flow conditions and at 0, 20 and 30 deg AoA, are shown in Figure 8.7.
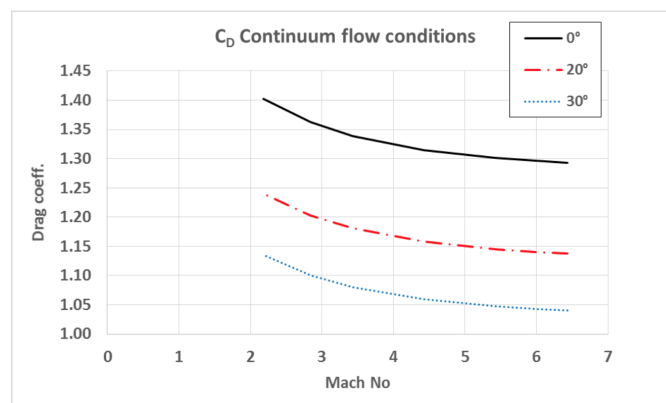
FIGURE 8.7: Drag coefficient versus Mach number in continuum flow

Looking at Figure 8.7, one can appreciate an overview of capsule C_D for the whole Mach number regimes and for 0, 20, 30 deg AoA. As clearly shown, the Oswatich principle, i.e. independence of aerodynamic coefficients to high Mach number, is envisaged starting from about $(M_\infty) = 5$.

Mini-Irene aerodynamics for transonic and subsonic flow conditions has been addressed by exploiting Marco Polo AEDB, provided by ESA. Indeed, curves of

Marco-Polo aerodynamics versus Mach have been anchored on Mini-Irene available data, thus populating the AEDB of capsule where nor engineering neither numerical data exist. In doing this, the sub-transonic AEDB of Mini-Ireneis obtained.

By conclusion, Figure 8.8 provides the pitching moment coefficients versus AoA and for all flow regimes, namely FM flow, TF, and CF conditions. As one sees, MINI-IRENE is expected statically stable at AoA lower than about 50°, for centre of gravity located at 0.25 L_{ref} from nose, since $C_{M\alpha} < 0$. The Stability Physical meaning of $C_{M\alpha} < 0$ is that, as a consequence of a positive increase in AoA disturbance, a moment is generated which tends to oppose the disturbance and to reduce the angle of attack.
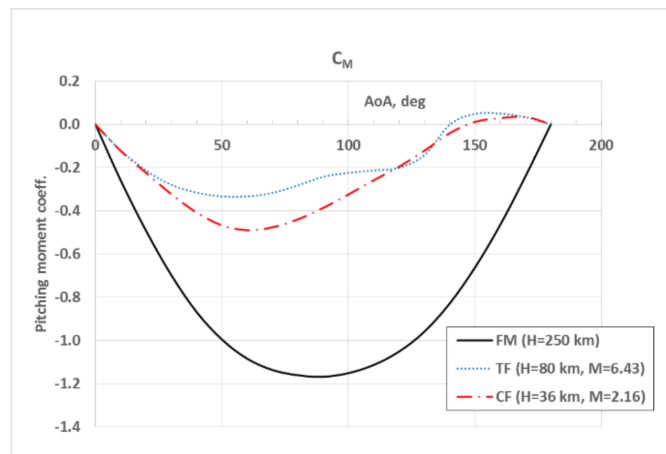
FIGURE 8.8: C_M versus AoA for all flow regime

Trim analysis of MINI-IRENE in free molecular flow, highlights that the capsule features just two trim angles of attack (i.e., where the pitching moment at the centre of gravity is equal to zero), namely $\alpha = 0$ and 180 deg. However, the sign of $C_{M\alpha}$ points out that only $\alpha = 0$ deg is a statically stable pitch trim AoA. In continuum hypersonic flow, there are three trim angles of attack (i.e., AoA = 0 deg, 140/150 deg and 180 deg. The angle of attack is 150 deg and 140 deg for the lower and higher hypersonic speeds, respectively). Nevertheless, for the 140/150

deg AoA, the slope of the pitching coefficient ($C_{M\alpha}$) is positive and consequently for the aero-shape this angle of attack is statically unstable.

8.2 Aero-Thermal Loads Assessment

This section provides an overview of the research activities performed for the aero-thermodynamic design of the MINI-IRENE Capsule.

The assessment of capsule aero-thermal loads for designing MINI-IRENE flexible heat shield relies on CFD analyses of the flow field past the capsule, expected at the peaks loads of dynamic pressure and heat flux.

Indeed, the dynamic pressure peak of the VSB-30 trajectory was investigated to address more conservative mechanical loads estimations; while the ISS trajectory aero-heating peak was analyzed for the assessment of thermal loads by considering a two times up-scaled version of MINI-IRENE aero shape.

Several views of capsule configuration, investigated in the present CFD analyses, are shown in Figure 8.9.
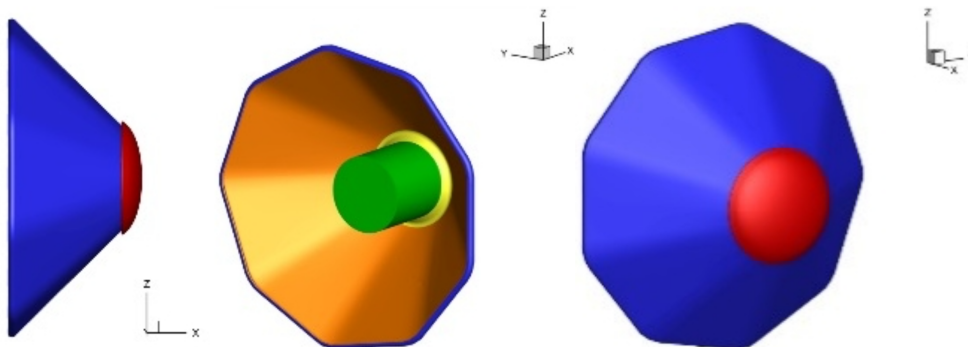
FIGURE 8.9: Capsule CAD Configuration

The aero shape features a sphere-conical fore-body umbrella, with cone semi-aperture angle of 45 deg, and a cylindrical central body. In the case of re-entry from a sounding rocket mission (VSB- 30), capsule diameter is about 0.758 m. On the other hand, re-entry from ISS refers to a capsule two times up-scaled (i.e., body diameter of about 1.516 m).

The flight design scenario for the assessment of capsule aerodynamics and aero-thermal loads is summarized in Figure 8.10. In this figure, the comparison between ISS and VSB-30 preliminary re-entry trajectories are provided in the altitude-velocity map.
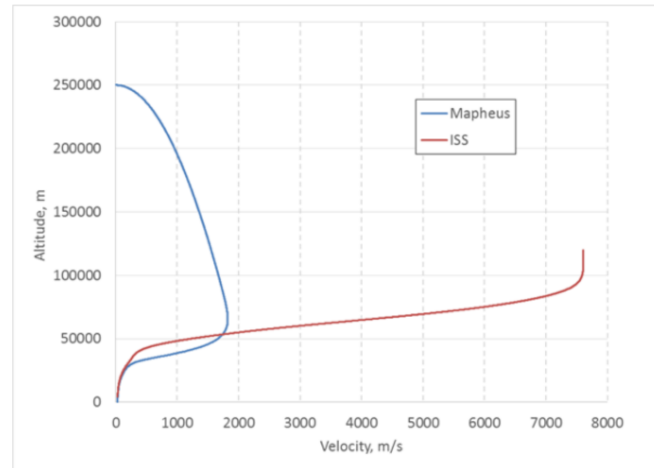
FIGURE 8.10: Altitude versus velocity

A capsule mass of 12 kg and 48 kg are considered for VSB-30 and ISS re-entry, respectively.

The flight-scenario of Figure 8.10 results in the aero-thermal loading environment of Figure 8.11.
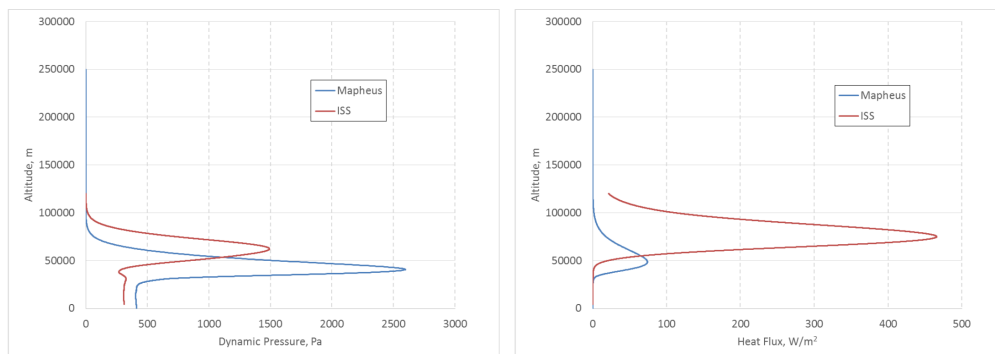
FIGURE 8.11: Altitude versus dynamic pressure and heat Flux

Figure 8.11 shows profiles of altitude versus dynamic pressure and convective heat flux for both trajectories, as expected at capsule stagnation point. As one can see, VSB-30 flight features higher mechanical and lesser heating loads than the ISS re-entry, as expected. Therefore, above results suggest that the assessment of capsule aero-thermal loads must rely on CFD analyses of the flow field past the capsule, expected at the dynamic pressure peak of the VSB-30 trajectory (i.e., mechanical loads) and at the peak heating of the ISS trajectory (i.e. heating loads), according to the trajectory-based design approach. Free-stream conditions of dynamic pressure and aero-heating peaks are summarized in Table 8.1.

	Dynamic Pressure Peak (VSB-30 Trajectory)	**Convective Heat Flux Peak (ISS Trajectory)**
H_∞, [km]	40.50	74.70
M_∞, [-]	3.68	20.48
T_∞, [k]	250.35	208.40
P_∞, [Pa]	287.10	2.39

TABLE 8.1: Free-stream conditions of aero-thermal load

Indeed, these free-stream conditions are considered, in the present research effort, in designing the capsule flexible heat shield. In fact, the aero-heating environment dictates the type and size of the TPS to be used. Peak heat rate generally determines the range of possible thermal protection material, while the integrated heat load determines the thickness and hence the mass of the heat shield.

Finally, pressure and shear stress at capsule surface determine the mechanical loads the heat shield has to withstand during descent.

The appraisal of Mini-Irene aero-thermal loads relies on several 3-D fully laminar CFD simulations, according to the test matrix in Table 8.2.

No.	Trajectory Point	Attitude [deg]	Wall Boundary Conditions
1	Dynamic pressure peak, VSB-30 Trajectory	0	Adiabatic wall
2	Dynamic pressure peak, VSB-30 Trajectory	10	Adiabatic wall
3	Peak heating, ISS Trajectory	0	NCW
4	Peak heating, ISS Trajectory	0	FCW
5	Peak heating, ISS Trajectory	10	FCW

TABLE 8.2: CFD Test matrix

The atmosphere composition is considered made of Y_{N_2} = 0.79 and Y_{O_2} = 0.21; while the model proposed for the air mixture is constituted by seven species: N_2, O_2, N_O, N, and O. The chemical model, based on Park [136], is constituted of 7 species and 22 chemical reactions that also account for third body efficiency.

CFD computations have been carried out on multi-block structured grids similar to those shown in Figure 8.12. A 3-D symmetric computational domain (half body) for the whole flow field past the capsule has been considered. The effective dimensions of the outflow and outer boundaries are modified in each simulation in order to obtain a grid compliant to the flow-field conditions of Table 8.1 and Table 8.2. The strategy adopted in the grid generation activities was to build the volume mesh be large enough to accommodate the free-stream Mach number; while the distribution of grid points in the wall-normal direction is driven by free-stream Reynolds number.
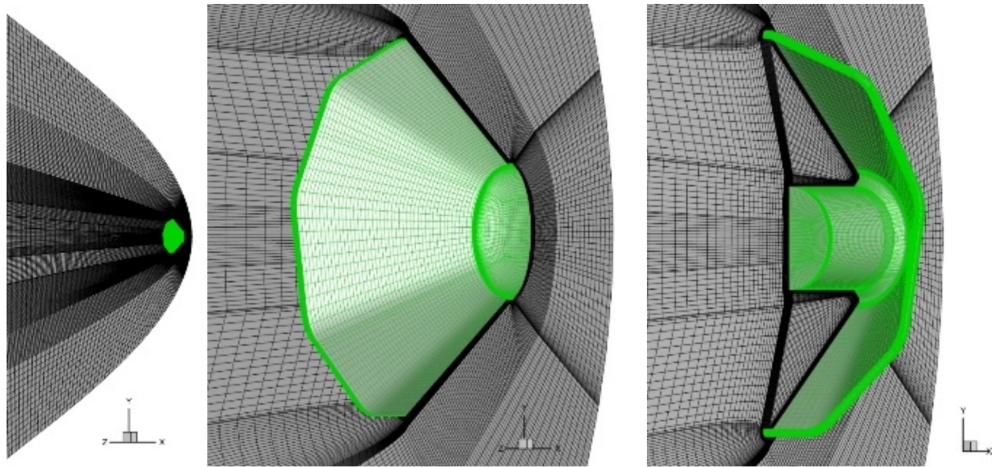
FIGURE 8.12: CFD multi block computational domains

Hence, the distribution of surface grid points was dictated by the level of resolution desired in various areas of capsule, such as stagnation region and base fillet, according to the computational scopes. For instance, the grid has sufficient points in the shoulder region to capture the rapid expansion and accurately predict the flow separation point and the angle of the resulting shear layer in the wake region. Further, there are also enough points in the separated flow region to resolve the vortical structure at the beginning of the wake flow field.

A local grid refinement has been also done in the shock region, in front of the capsule, to better resolve the steep gradients due to the bow shock, by aligning the grid with the shock and clustering points into the shock and boundary layers. This reduced the spurious oscillations in the stagnation area that are often observed in hypersonic flows, especially for large bluff-body flow field computations.

The computational domain is made of 80 blocks for an overall number of about 2M cells. The grid (front shield region) is constituted by 100x86 cells (longitudinal x normal to the wall direction) and assures fully spatially converged results. The minimum spacing at the wall is equal to 10^{-6} m to accurately predict

velocity and temperature gradients normal to wall (e.g., convective heat transfer at the vehicle surface for the simulations at ISS trajectory peak heating).

As far as wall boundary conditions are concerned, all simulations carried out at peak dynamic pressure of VSB-30 flight are performed with adiabatic wall; while simulations related to ISS trajectory peak heating are performed assuming radiative cooling (wall emissivity equal to 0.8) and both Non-Catalytic Wall (NCW) and Fully-Catalytic Wall (FCW) assumptions.

All CFD results refer to both converged and grid independent computations. In order to assess numerical solution convergence, equation residuals and aerodynamic drag coefficient, as well as the stagnation point heat flux, have been monitored during iterations.

Solution convergence has been assumed when residuals dropped more than three orders of magnitude and the drag coefficient and the stagnation point heat flux plots reached a constant value. So, convergence is assessed by matching both criteria.

8.2.1 Results at Dynamic Pressure Peak

Some results of 3-D numerical analysis at dynamic pressure peak can be found from Figure 8.13 to Figure 8.14. These figures provide very interesting flow field features, as the flow expansion at capsule shoulder and the complexity of the base flow. Indeed, in Figure 8.13 there are contours of the pressure field past the MINI-IRENE and on the capsule front shield at M=3.68 and α=0 deg (i.e., dynamic pressure peak of VSB-30 descent trajectory).

The effect of 10 deg Angle of Attack (AoA) on the flow field and pressure distribution on capsule fore-body, at this flight condition, can be appreciated by comparing Figure 8.13 and Figure 8.14.
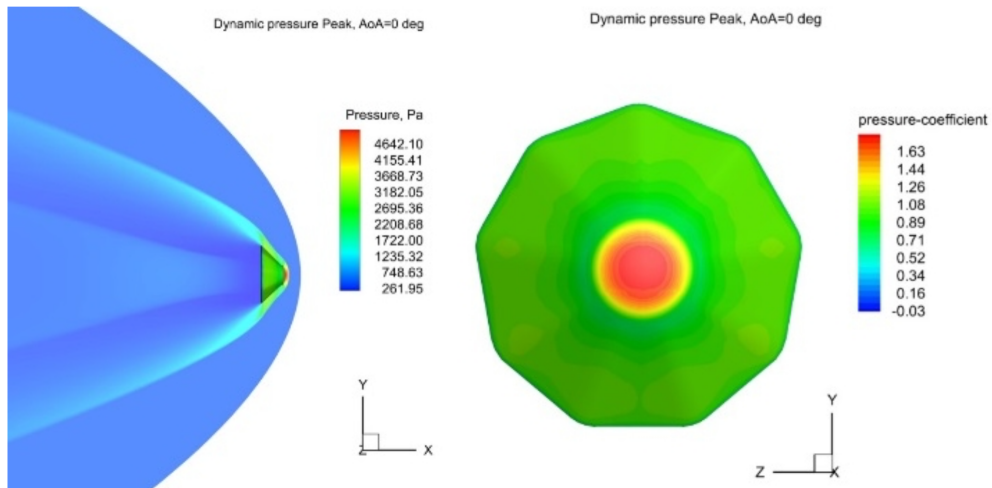
FIGURE 8.13: Contours of static pressure on capsule fore-body and symmetry plane at dynamic pressure peak and AoA=0 deg
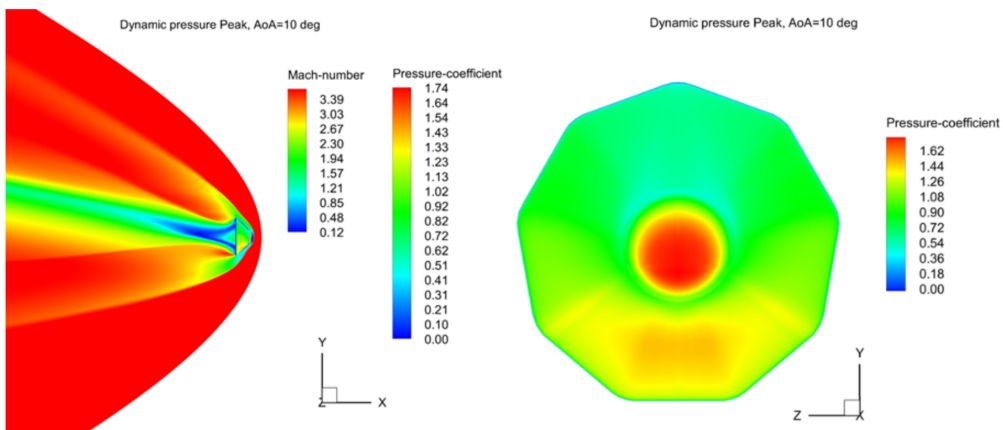
FIGURE 8.14: Contours of static pressure on capsule fore-body and of Mach on symmetry plane at dynamic pressure peak and AoA=10 deg

In fact, Figure 8.14 shows the Mach number contours field past the capsule and the pressure distribution on the umbrella front shield at α=10 deg.

As one sees, when the angle of attack α increases the surface pressure distribution changes, thus increasing on the capsule wind-side, as expected. At the same time, flow expansion on the capsule lee-side determines locally lower pressure contours.

Profiles of pressure (C_p) and local skin friction (c_f) distributions on the capsule centerline for α=0 and 10 deg are provided in Figure 8.15.

FIGURE 8.15: Pressure and skin friction distribution on capsule centerline at dynamic pressure peak and for α =0 deg and 10 deg. Effect of angle of attack on C_p

As expected, large shear stresses at nose cap and front shield shoulders are found. The effect of AoA on pressure and skin friction distributions on the capsule centerline can be appreciated as well.

8.2.2 Results at Convective Heat Flux Peak

Loads distribution on the capsule aft-body are, instead, negligible. As far as peak heating results are concerned, following Figure 8.16 and Figure 8.17 report on the flow field predicted past the capsule at M=20.48 and for α=0 deg. For instance,

Figure 8.16 shows the pressure contour distributions provided on the capsule pitch plane and fore-body; while in Figure 8.17 contours field refer to static temperature for NCW.
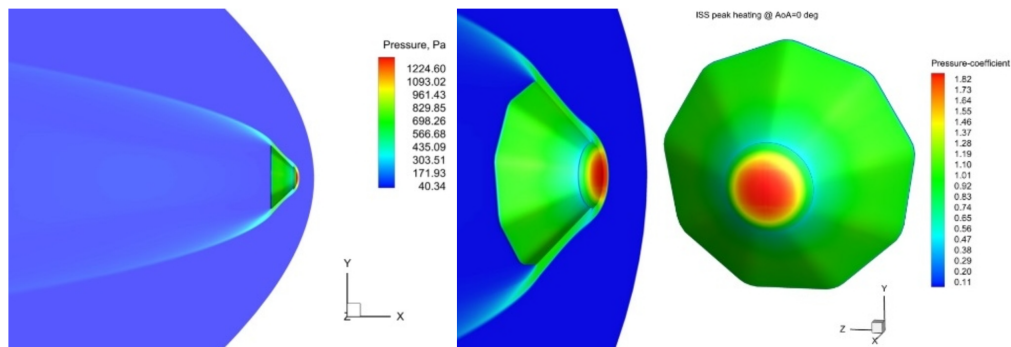
FIGURE 8.16: Contours of static pressure on capsule front shield and symmetry plane at ISS peak heating and AoA=0 deg
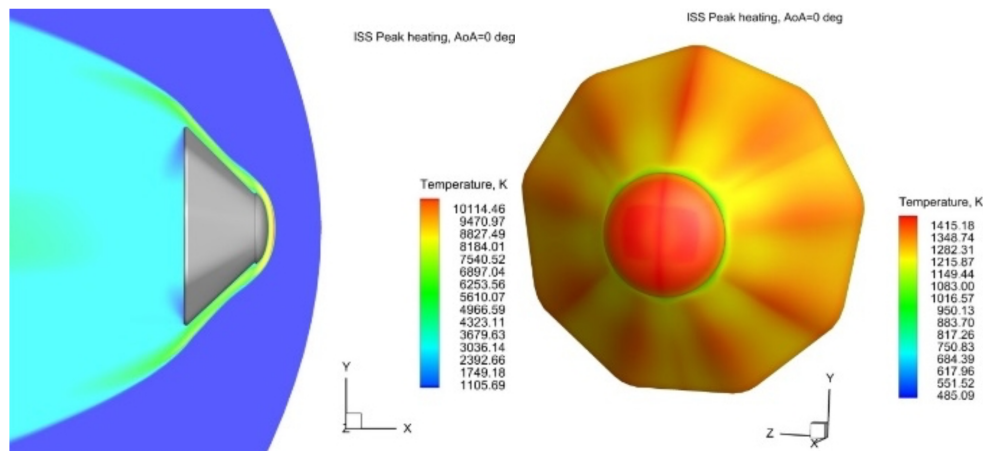
FIGURE 8.17: Contours of static temperature on capsule forebody and symmetry plane at dynamic pressure peak and AoA=0 deg. NCW wall.

As shown in these figures, at hypersonic speed the flow field is dominated by a strong bow shock and is characterized by all the typical hypersonic flow features as shock waves very close to the body surface (i.e., thin shock layer), thick boundary layers, and high temperatures.

Further, the strong shock wave causes a large sonic region, a smooth conical flow along the capsule conical part, and a strong flow expansion at the shoulder.

As one sees, the flow crossing the bow shock suddenly decelerates, thus increasing the pressure and temperature in the shock layer close to the stagnation region.

Details about pressure and skin friction distributions on the capsule fore-body and centerline for α =0 and 10 deg are provided in Figure 8.18.
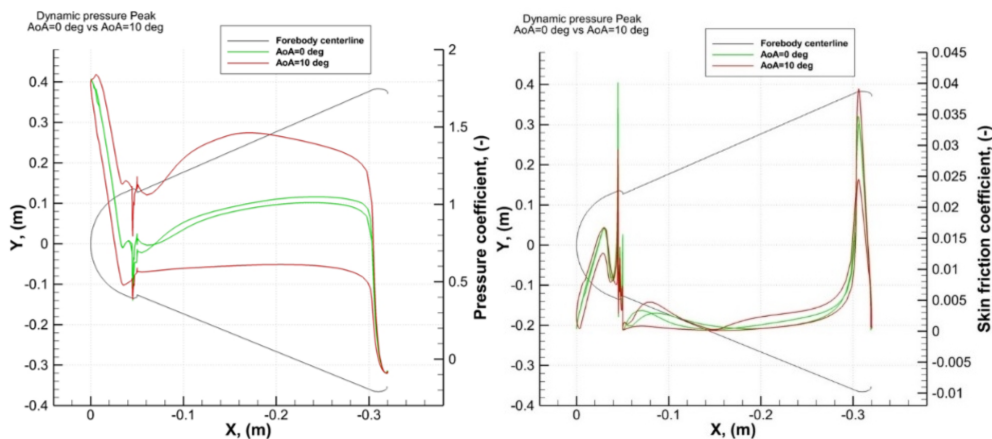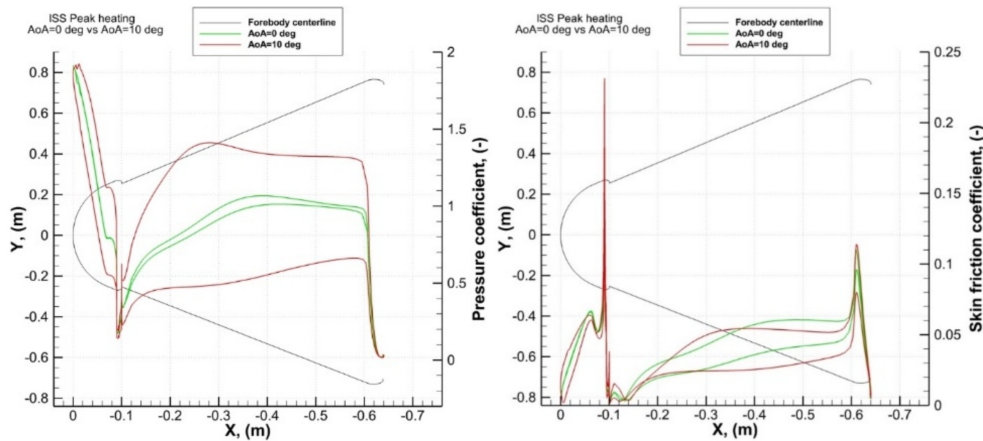

FIGURE 8.18: Pressure and skin friction distribution on capsule centerline at ISS peak heating and for α =0 deg and 10 deg. Effect of angle of attack on C_p

As expected, large shear stresses at nose cap and front shield shoulders are found. The effect of AoA can be also inferred.

As far as flow species recombination at wall is concerned, effects of wall catalyticity on the convective heat flux $\dot{q}$ distribution on the capsule centerline are shown in Figure 8.19.

In Figure 8.19 is possible to notice that the re-entry trajectory peak heat flux is 219 kW/m^2 in a non-catalytic hot wall condition (NVW).

As expected, in the case of FCW, a larger heat flux is found at wall. Anyway, above figures point out that the convective heat flux at capsule stagnation

FIGURE 8.19: Convective heat flux distribution on capsule centre-
line at ISS peak heating and for NCW and FCW at α =0 deg. Effect
of wall catalyticity behavior on $\dot{q}$

point is close to 400 KW/m^2. Note that, this value agrees with that expected by
engineering-based relationships, as shown in Table 8.3, see Reference [137].

Relationship	Heat Flux value [W/m^2]
Zoby	4.17E+05
Fay-Riddell	4.20E+05
DKR	4.14E+05

TABLE 8.3: Engineering-based estimations of stagnation point heat
flux

Further, the effect of AoA on $\dot{q}$ and radiative cooling temperature (T_{radeq}) pro-
files at capsule centerline (for FCW) are shown in Figure 8.20.

By concluding, it is worth noting that above centerline profiles highlight that
the high semi aperture cone angle (i.e., 45 deg) causes the curvature of the shock
wave and, therefore, the presence of an entropy layer that affects the results at
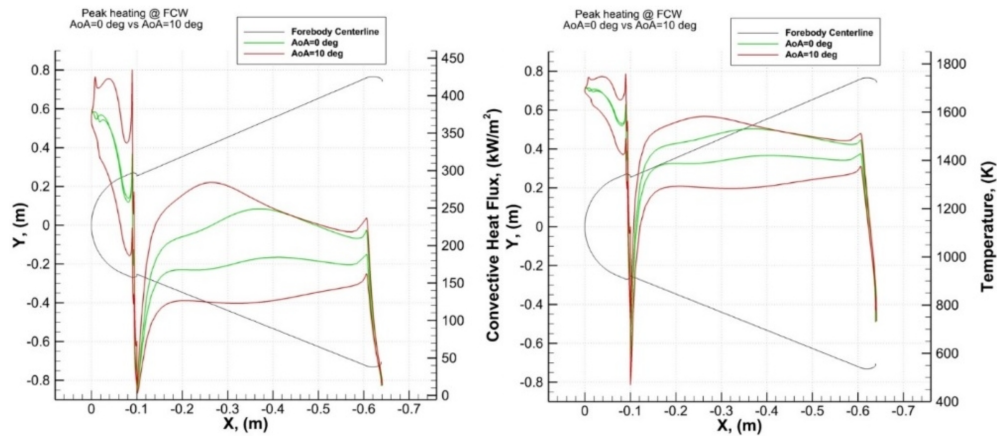
FIGURE 8.20: Convective heat flux and radiative equilibrium temperature distribution on capsule centerline at ISS peak heating and for FCW, α=0 deg and 10 deg. Effect of angle of attack on $\dot{q}$

the wall. Further, a non-negligible effect of 10 deg AoA is remarkable on both mechanical and thermal loads. Loads distribution on the capsule aft-body are, instead, negligible.

Chapter 9

Plasma Wind Tunnel Testing

In this chapter the activities performed to design and conduct a Plasma Wind Tunnel test for an ESA capsule are presented, together with the analysis of the results obtained.

9.1 Test Specification

The Test Specifications have been designed based on the trajectory and aero-thermal analysis presented in the previous chapter. Test heat flux has been derived from the nominal orbital re-entry trajectory, used for the design, by means of CFD computation in PWT environment. The reference orbital re-entry trajectory peak heat flux is 219 kW/m^2 in a non-catalytic hot wall condition. It was obtained in the aero-thermodynamics results chapter and it is here reported for simplicity (Figure 9.1).

The closest PWT condition found, able to reproduce a close heat flux is characterized by the following values of total pressure and total enthalpy:

An additional CFD run representative of the flow-field conditions and aero-heating loads expected during the PWT test of Mini Irene Ground Demonstrator (GD) have been simulated. Figure 9.2 shows the meshes for the probe and the GD simulations inside the PWT chamber.
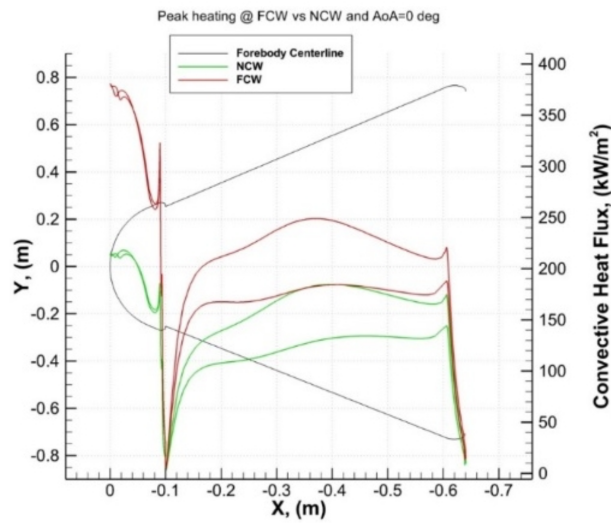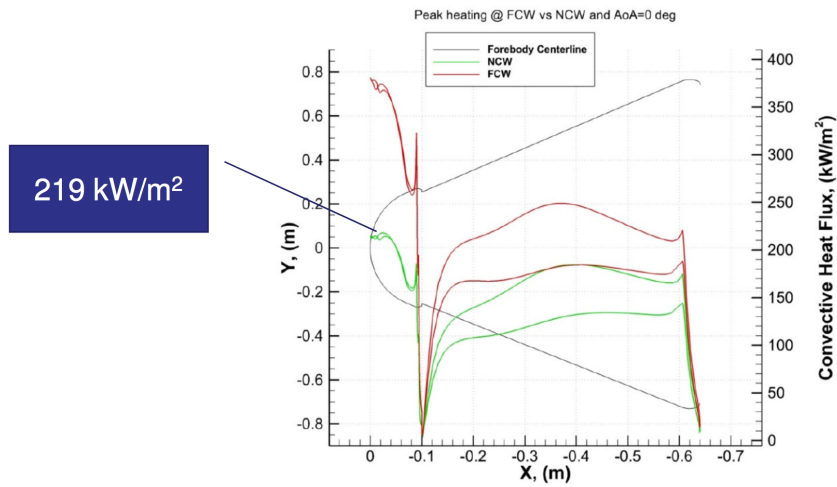
FIGURE 9.1: Convective heat flux distribution on capsule centerline
at ISS peak heating and for NCW and FCW at α =0 deg

Parameter	Symbol	Value	Units
Total Enthalpy	H_0	10.8	Mj/kg
Total Pressure	P_0	2.5	bar_a

TABLE 9.1: Total Enthalpy and Total pressure chosen for the test
conditions
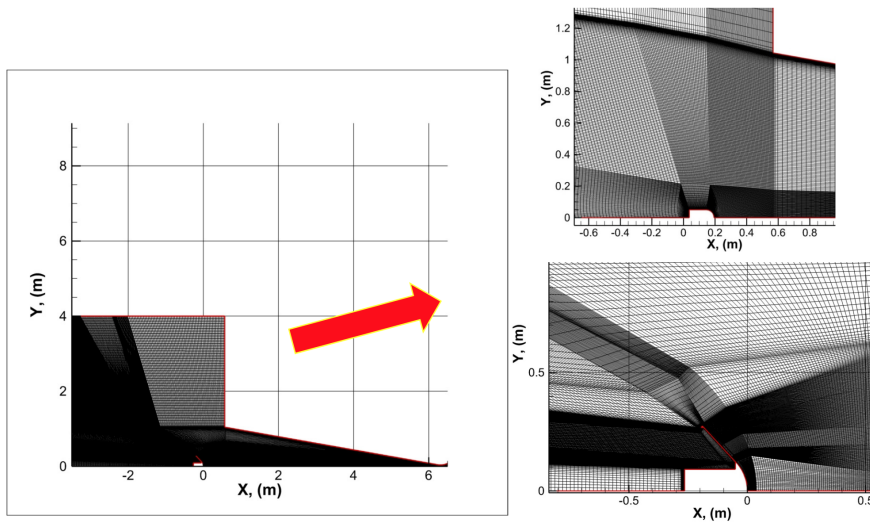
FIGURE 9.2: Computational Mesh Domain for the Probe and the GD
simulations inside the PWT chamber

This additional CFD analysis, see Figures 9.3 and 9.4, confirm a heat flux on the stagnation point of the test article, equal to 215 kW/m^2 that is very close to the peak heating of the nominal orbital re-entry trajectory, compare with Figure 9.1.
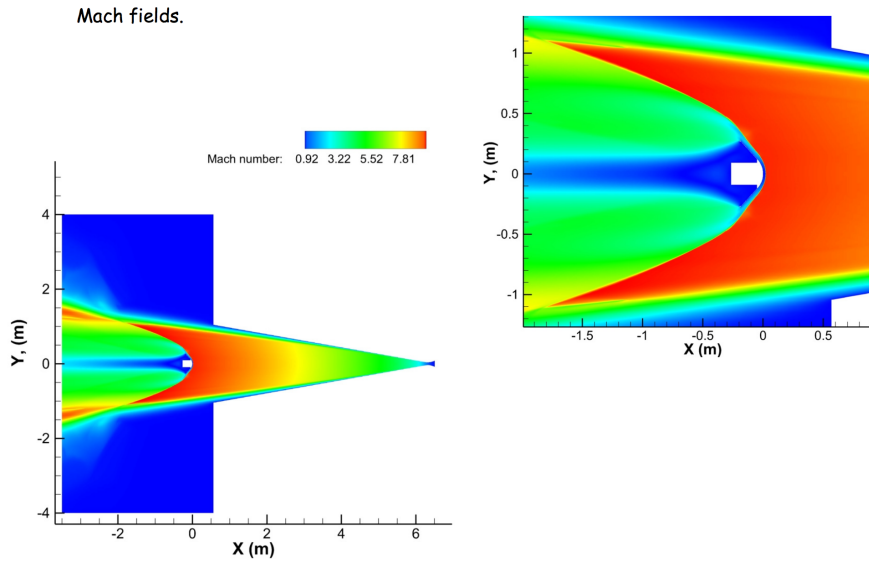
FIGURE 9.3: Contours of Mach on capsule front shield and symmetry plane inside PWT chamber at α =0 deg

The determination of the test duration depends on the heat load of the re-entry trajectory presented in the previous chapters. In fact it is chosen in order to reproduce the same heat load as the flight.

Trajectory	Initial Altitude [Km]	Initial flight path angle [Km]	Peak Heat Flux [kW/m^2]	Heat Load [MJ/m^2]
Nominal	300	0	219	36.8
Steeper Trajectory	300	-1.5	258	29.9

TABLE 9.2: Initial conditions of the two selected trajectories
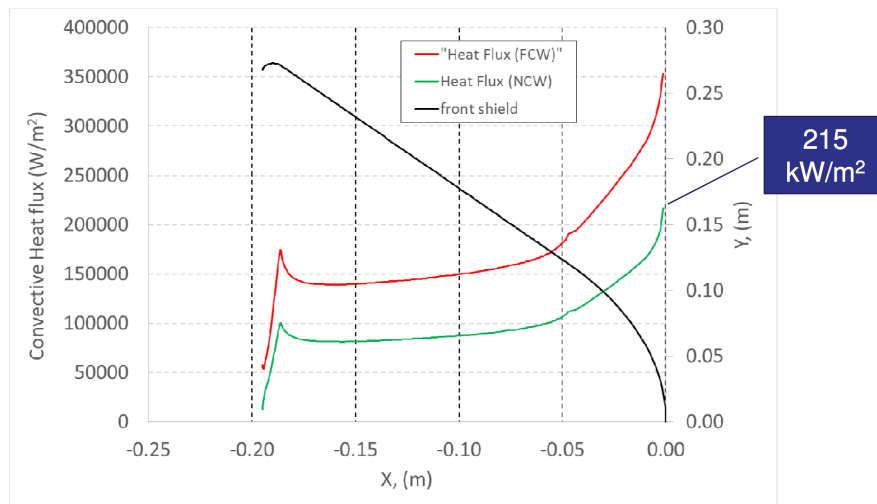
FIGURE 9.4: Convective heat flux distribution on capsule centerline
inside PWT chamber and for NCW and FCW at α =0 deg

Besides of the nominal trajectory, a second steeper trajectory has been selected for the definition of the heat load and the consequent test time. The steeper trajectory experiences a higher peak heat flux, but a lower overall heat load. The following table resumes the initial conditions of the two trajectories considered.

Assuming the calculated value of 215 kW/m^2 on the stagnation point of the test article, two test durations are computed. The following graphs show the two heat flux time histories, compared to the test time histories.

The steeper trajectory heat flux is higher than the heat flux reproduced in the PWT but it is still representative. For the nominal trajectory PWT reproduces a heat flux very close to the flight peak for a time long enough to reproduce the flight heat load. Because of this, and the steep heat flux variation, the PWT condition is more demanding than the shallow flight. The following table resumes the two test conditions.

The shorter duration shall be considered as the minimum requirement for a successful test.

If, approaching the shorter test duration, the following conditions are met the
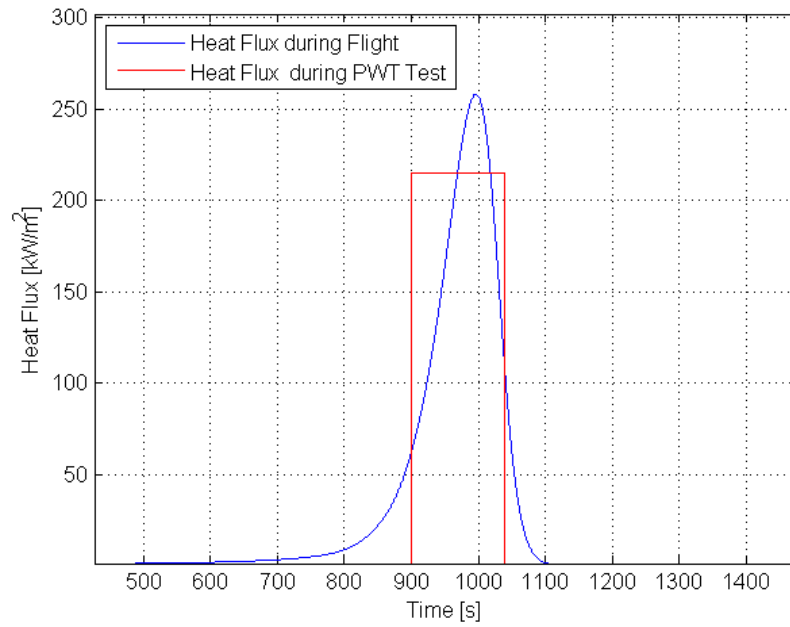
FIGURE 9.5: Steep trajectory: PWT and Flight heat flux time history
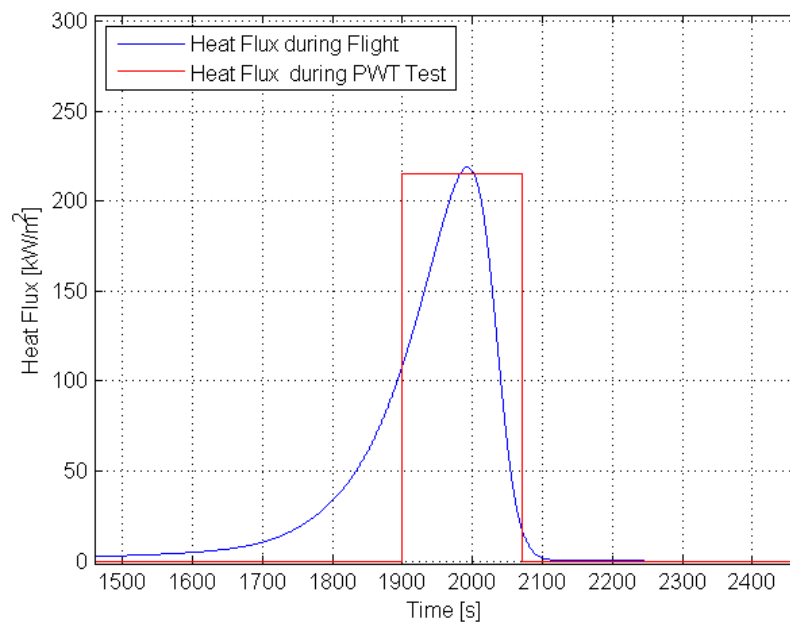
FIGURE 9.6: Shallow trajectory: PWT and Flight heat flux time history

Test	Heat Flux [kW/m^2]	Test Time [s]
Minimum duration	215	139
Extended duration	215	171

TABLE 9.3: Heat flux and duration requirements

test shall be considered successful, and the duration can be extended, in order to verify the ability of the system to sustain the higher thermal load of the shallow trajectory:

- Temperatures measured by the thermocouples within the Nextel layers are below 900 °C;

- Pyrometer on the external surface of the Nextel is below 1100 °C;

- Cold structure temperature still within the limits.

9.2 Test Setup

Different pyrometers (see Table 9.4) have been used to measure the surface temperature of the GD in two different locations (see Figure 9.7). All the pyrometers were of the dual-color type. The two-color mode allows to measure the surface temperature independently from the material surface emissivity, instead the single-color mode requires an emissivity value as input. In this test when the pyrometers were operated in single-color mode, it was set an emissivity value of 0.80.

The pyrometers are equipped with a red laser to perform the pointing on the surface where the temperature has to be measured. The lasers of the D800 and P300 pyrometers indicate also the area where the measurement is performed. The

Tag	Manufacturer	Model	Operative Mode	Range [°C]	Wavelength [μm]
D800	DIAS	DSRF 11N	Two/Single-Color	800 ÷ 2500	0.7 ÷ 1.1
P300	IMPAC	IGAR 12LO	Two/Single-Color	300 ÷ 1000	1.52 ÷ 1.64
P800	IMPAC	ISQ5	Two/Single-Color	800 ÷ 2500	0.9 ÷ 1.05

TABLE 9.4: Pyrometers used during the Test
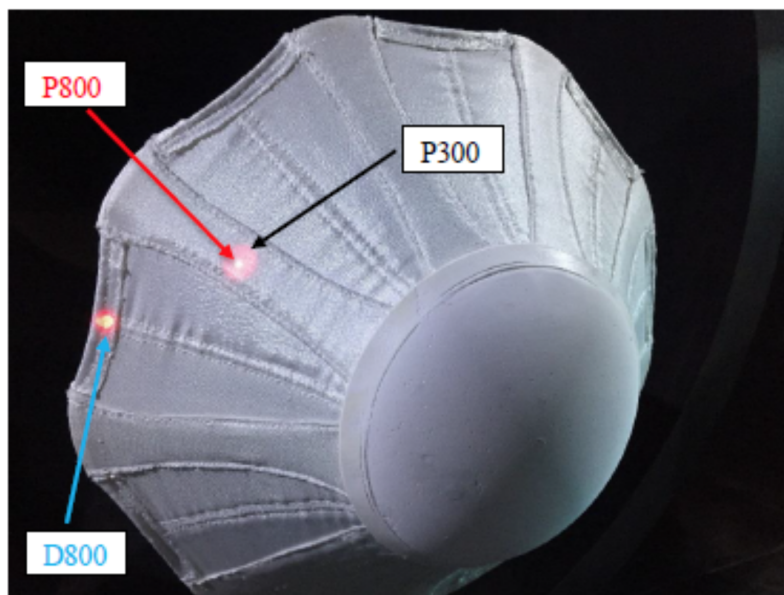
FIGURE 9.7: GD image with pyrometers spots

laser of the P800 pyrometer is indicated by a red dot only that visualizes only the pointing position and not the area of the temperature measurement.

Two IR cameras of the type reported in the next Table have been used to obtain temperature maps of the top and side view of the GD.

IR Camera	Range [°C]	Wavelength [μm]
Flir A655s	300 ÷ 2000	7.5 ÷ 14

TABLE 9.5: IR cameras used during the test

The GD was instrumented with 23 K-Type thermocouples. 24 thermocouple channels acquired via K-Type extension cables were setup as K-Type on facility DAS and characterized end-to-end by Beamex MC6 multifunction calibrator, finding practically no offset in the temperature range -100 ÷ 1200°C. Finally, all the test article thermocouples were positively checked in stand-alone and connected to the facility DAS interfaces.

The GD was instrumented with two pressure ports, one at the stagnation point and the other in the base region. Two pressure sensors with a range of 0-10 mbar were setup inside the MSS and connected to proper interfaces on facility DAS. Finally, all the pressure ports passed a pneumatic check and were connected to the pressure sensors inside the MSS.

Figures 9.8 and 9.9 show the GD in the SCIROCCO chamber after the installation using the SCIROCCO MSS holder. The Test article interface flange was secured to the facility holder flange by means of M10 bolts.

Prior to the installation of the Test Article all the 24 thermocouples were checked with the calibrator; all the sensors showed approx. the same measurement, no issue was noticed.

After the installation of the test article onto the MSS holder the sensors were connected to the PWT DAS connectors in order to check their proper functioning
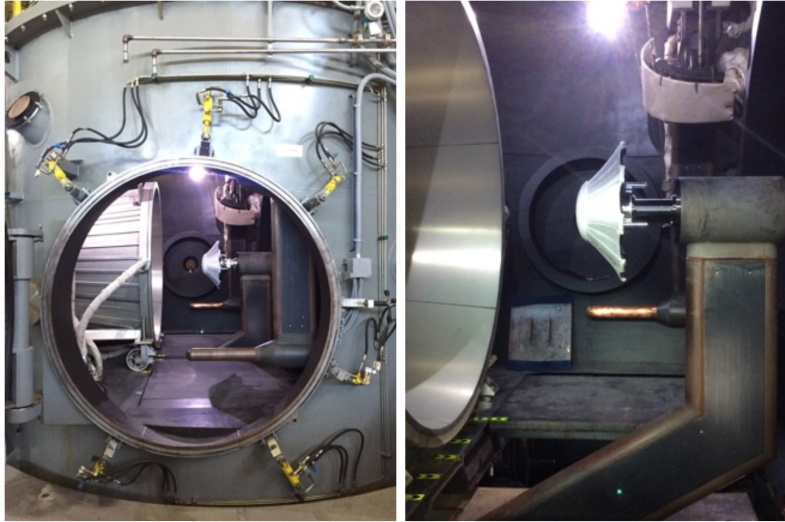
FIGURE 9.8: MIFE Ground Demonstrator installed into the SCIROCCO chamber - side view

FIGURE 9.9: MIFE Ground Demonstrator installed into the SCIROCCO chambers - back view

and eventually that of the entire measurement chain from the DAS located into the PWT control room; all the thermocouples showed the same values and additionally the same as measured by the calibrator. Some of the sensors were also excited by slightly warming them up and measurement showed an increment of the temperature compliant with the entity of the excitation.

Figure 9.10 summarizes the sensor locations within the test article.
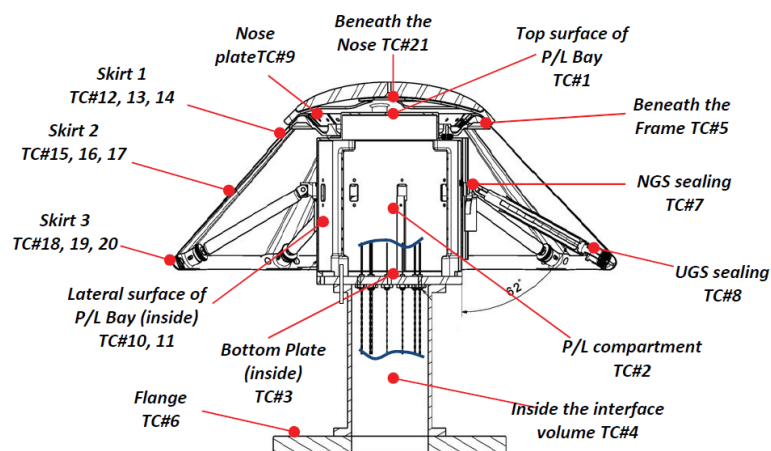
FIGURE 9.10: MIFE Ground Demonstrator Thermocouples installation scheme

Pyrometers and Infrared camera were pointed to the test article measuring points, according to the scheme provided in figure 9.11.

Figure 9.12 shows the Pyrometers pointing the Test Article measuring points.

Two pressure sensors were also installed, to measure the pressure at the stagnation point and inside the test article. They were connected to the relevant PWT DAS tubes and successfully functionally verified.

9.3 Test Results

The following figures show the Test Article recorded by the top camera of SCIROCCO under the plasma flow during the 180 seconds of the test campaign. The starting
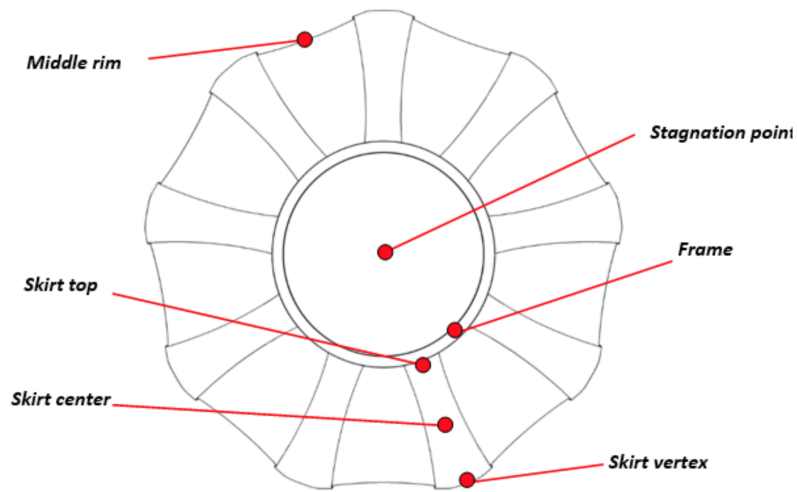
FIGURE 9.11: Top view of GD with the key positions for thermography measurements on the external surface of the heat shield
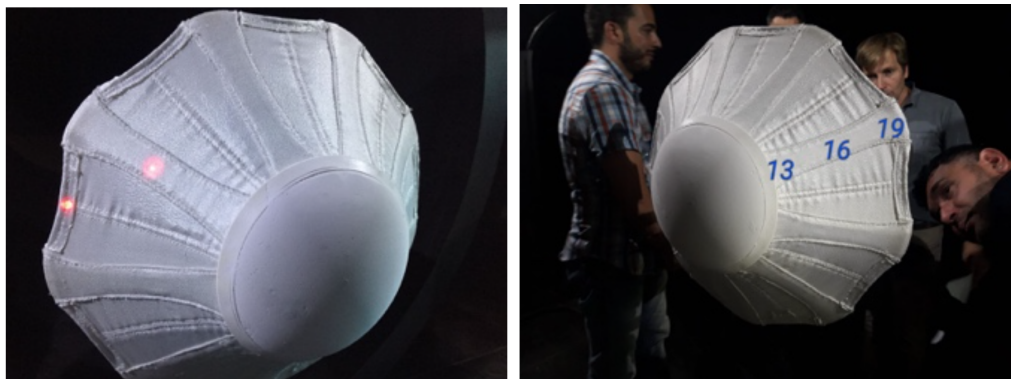
FIGURE 9.12: Key positions for thermography measurements before the test

time is 16:55:15.

FIGURE 9.13: The GD underneath the PWT Chamber and after insertion in the flow

FIGURE 9.14: The GD at second 60 and 180 during the PWT test

Figure 9.16 shows the Ground Demonstrator after the end of the test campaign. The test article was able to sustain even the extended duration test which is representative of the heat flux and heat load of the shallow trajectory used for the design of the TPS (see Table 9.3).

FIGURE 9.15: The GD cooling down after the PWT test

FIGURE 9.16: The GD approx. three minutes after the PWT test con-
clusion

For the test campaign, the following values of heat flux and stagnation pressure have been considered:

Test ID	$\mathbf{q}_S$ $[kW/m^2]$	$\mathbf{p}_S$ $[mbar]$
SCI-MIFE-509	657	7.5

TABLE 9.6: Heat flux and Stagnation Pressure Settings

The Heat Flux and Stagnation Pressure measured by the Facility Data Acquisition System at the Probe and represented in Figure 9.17 show the fully compliance with the Test Specification and Conditions.
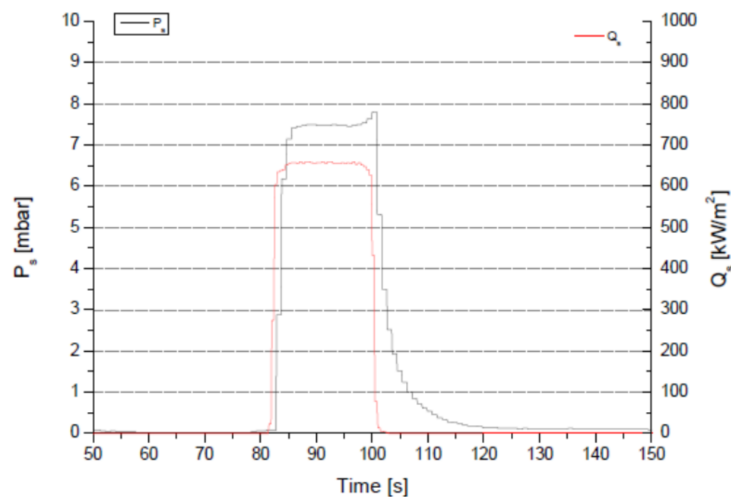
FIGURE 9.17: Heat Flux and Stagnation Pressure measured by the
Facility Data Acquisition System at the Probe

In the next paragraph are reported the analysis performed by means of the sensors installed in the test article, sorted by subsystem. The reported graphs have been obtained from the raw data provided by the Facility Data Acquisition System.

9.3.1 Nose

The trends of the Temperature show that the Rescor dome of the GD reduces the expected 1400°C at the stagnation to max 600°C underneath the Rescor and that the insulation provided by the combination of Rescor and O-CMC brakes down the Temperature to approx. 100°C at the Nose Plate level.
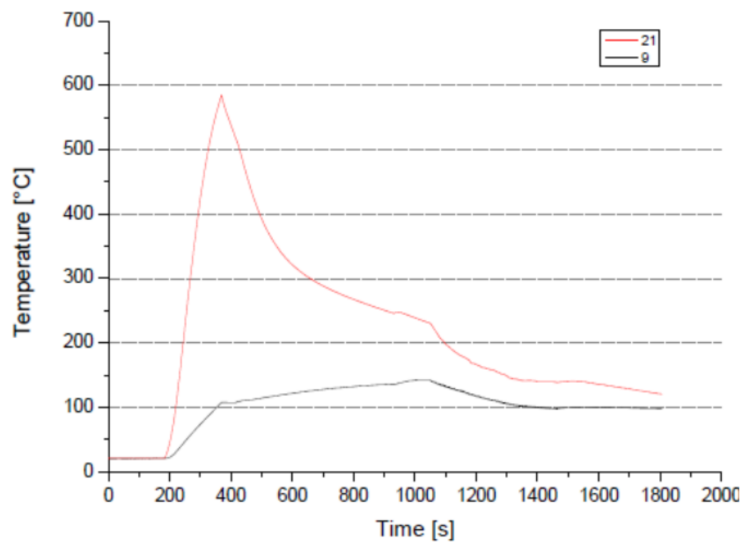
FIGURE 9.18: Nose K-Type thermocouples measurements (hot + cooling phase)

This definitely remarks the excellent performances of the Nose Design of Mini-Irene as Thermal Protection System.

9.3.2 Thermal Protection System

The plots of the upper circle temperatures show the upper-inner part of the Nextel skirt ranging between 750°C and 650°C, while those of the bottom circle show higher values, slightly below 1000°C. The middle circle average is just in between with a range 750°C – 950°C.

It is important to remark that the inspection of the Test Article has explained the trend of the Thermocouple #17 of the bottom circle significantly beyond the average, approx. 1100°C. This is due to the protrusion of its sensor element all the way through the three Nextel layers, most likely caused during the AIT of the Test Article.

The measured internal temperatures after the three Nextel layers are in line with the Thermal Analysis results.

Additionally, being all the temperature trends of the inner layer (that is designed to sustain by alone with a 200% SF all the tension after an orbital re-entry) below 1000°C, corresponding to the 50% of the Nextel Strength Retention (see Figure 9.19), the test results fully confirm the suitability of the Mini-Irene flexible TPS to fully cope the thermal-structural environment and eventually the reference orbital re-entry mission.
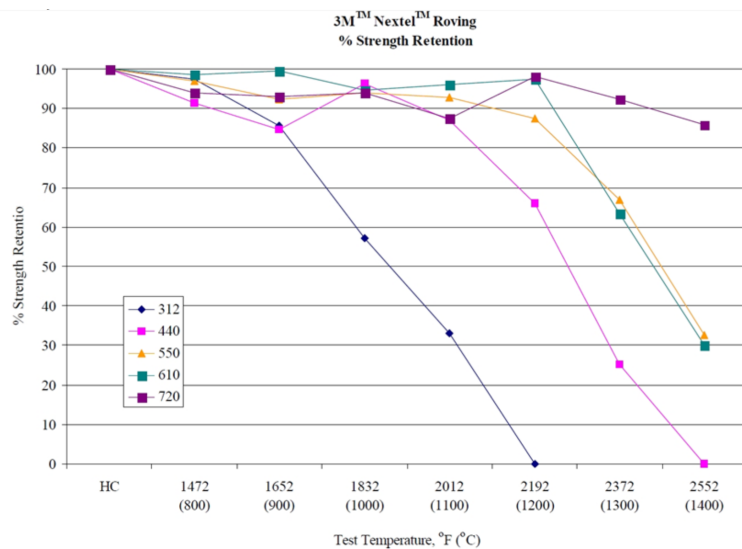
FIGURE 9.19: 3M Nextel Strength Retention versus Temperatures
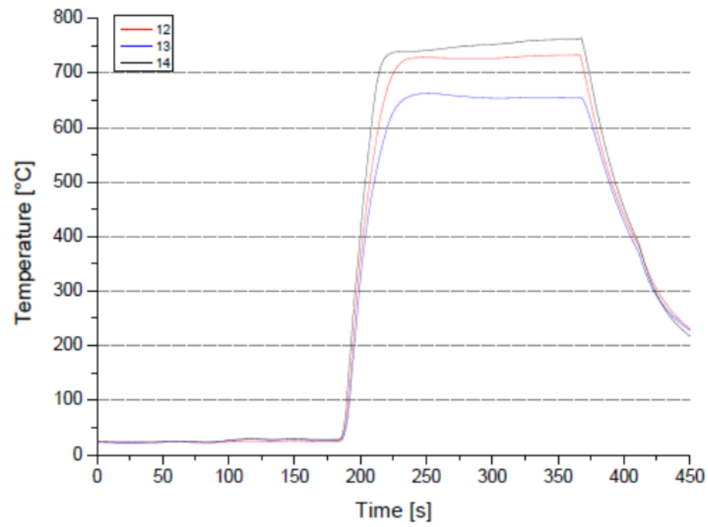
FIGURE 9.20: Nextel upper circle K-Type thermocouples measurements (hot phase)
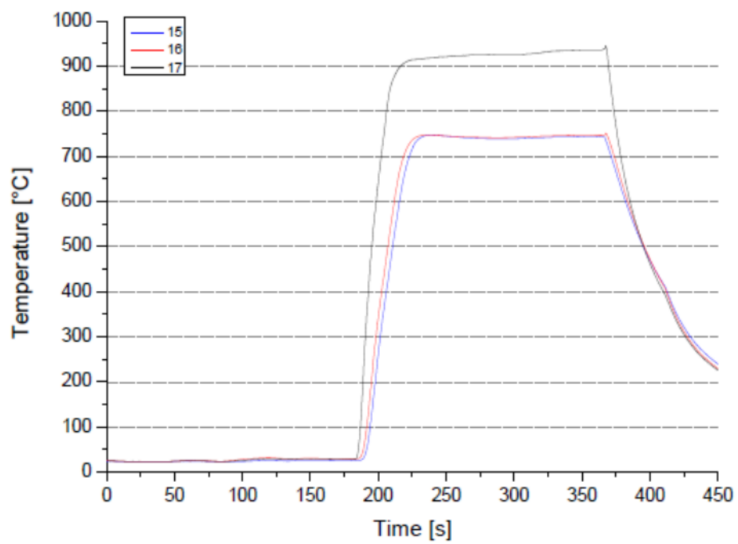
FIGURE 9.21: Nextel medium circle K-Type thermocouples measurements (hot phase)
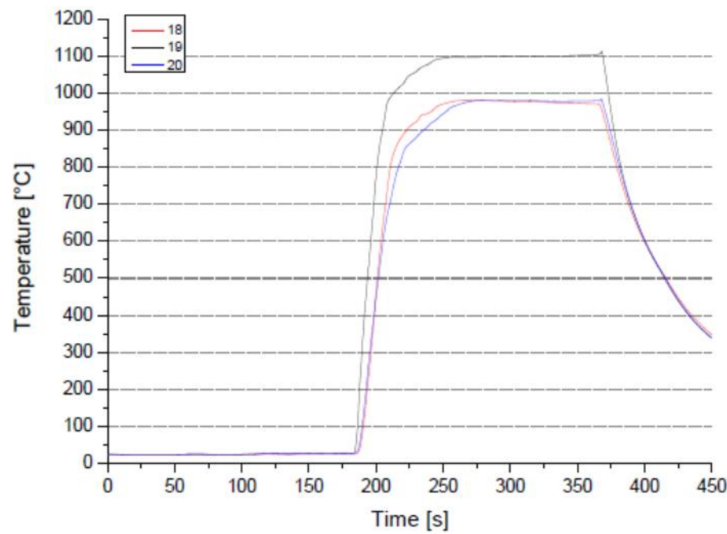
FIGURE 9.22: Nextel bottom circle K-Type thermocouples measurements (hot phase)

9.3.3 Cold Structure and Avionic Bay

Thermocouple #2, and #10 measure the outer and inner Aluminium surface temperature of the Payload Bay, both beyond the Sheldahl Radiation Insulator tape show maximum values around 70°C. This temperature level is fully compatible with the installation of any electronic device inside the bay (i.e. maximum temperature 55°C in case of extended range component) in presence of an additional, thin layer of internal insulator, i.e. ceramic paper.

Thermocouple #2.1, and #11 measure the outer and inner Aluminum surface temperature of the payload bay, beneath a Nextel insulator fabric coated by an aluminum foil, locally used instead of the Sheldahl tape only in a limited portion of the payload bay, show relative maximum values around 55°C. This level is already compliant with the installation of the Avionic inside the Bay, without additional internal thermal protections.

Thermocouple #3 shows the temperature at the bottom of the payload Bay, where in case of the Flight Demonstrator and even an IRENE concept design the
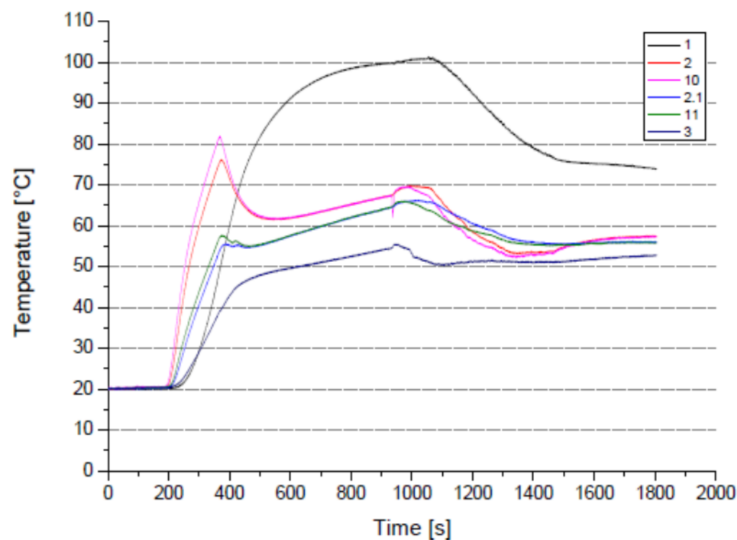
FIGURE 9.23: Cold Structure K-Type thermocouples measurements
(hot + cooling phase)

Avionic is installed, and its value is 55°C.

Thermocouple #1 shows the temperature at the top of the payload Bay, around 100°C, where no electronic is supposed to be installed in all configurations.

9.3.4 Pyrometers Measurement

The P800 and P300 pyrometer trends are shown in Figure 9.24. It is possible to observe that the P300 measured the temperature up to 1000°C in two-color mode, which is its higher range limit. After two switches from two-color to single-color have been performed measuring a decreasing temperature at surface from 700°C to about 640°C.

The P800 pyrometer measured the temperature up to about 1350°C in two-color mode, after it was not able to measure the temperature in that operating mode. In fact, during the test three switches have been performed from two-color to single-color and the temperature was measured. The reason why the temperature was not measured in two-color mode over 1350°C, is probably due

to a change of the material surface properties that affected the pyrometer operation in two-color mode only. A similar problem already occurred with the P800 pyrometer in a previous test campaign done in the SCIROCCO facility with the same Nextel in the year 2010. There is the possibility that due to the aerothermodynamic conditions of the flow in the zone of the pyrometer measuring spot, occurred the generation of a melting phase that covered the surface of the material affecting the operation of the pyrometer in two-color mode.
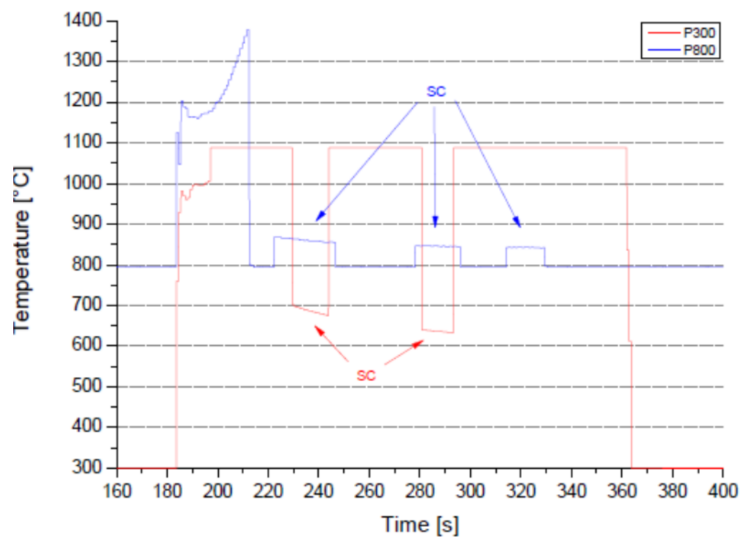
FIGURE 9.24: P800 and P300 pyrometers measurements

The pyrometer D800, whose data are shown in Figure 9.25, has given useful information in two-colour mode throughout the test, showing a sort of noisy behaviour during the heating phase and near the end of the test.

Such a strange behaviour at the beginning of the test may be due to a change in the physical properties of the material surface that affected the two-color operation mode of the pyrometer.

Several switches from two-colour to single colour mode SC and back were performed on the D800 pyrometers for spectral emissivity evaluation.

The low temperatures measured by all the pyrometers in single-color mode are considered indicative of an extremely low spectral emissivity value of the Nextel fabric at the pyrometer single-color mode wavelength and angle of view.
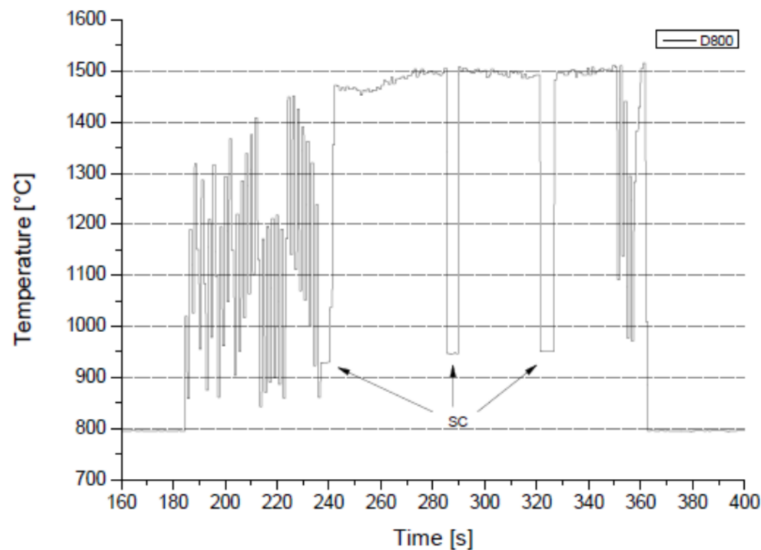
FIGURE 9.25: Nextel trailing edge D800 pyrometer measurements

9.3.5 Infrared Cameras Measurements

In Figure 9.26, the temperature measured by the D800 pyrometer has been compared with the IR temperature at the same spot location and at different emissivity values.

Assuming the temperature measured by the pyrometer in two-color mode as the true temperature, we can obtain the experimental emissivity of the Nextel surface ϵ_{IR} at the IR camera wavelength range of $7.5 \div 14 \, \mu$ m and angle of view.

Starting from the achievement of a quasi-steady state temperature of 1500°C, the IR temperature matches the two-color temperature for an ϵ_{IR} value close to 0.80. So this is the estimated value of the Nextel surface emissivity at a temperature around 1500°C.
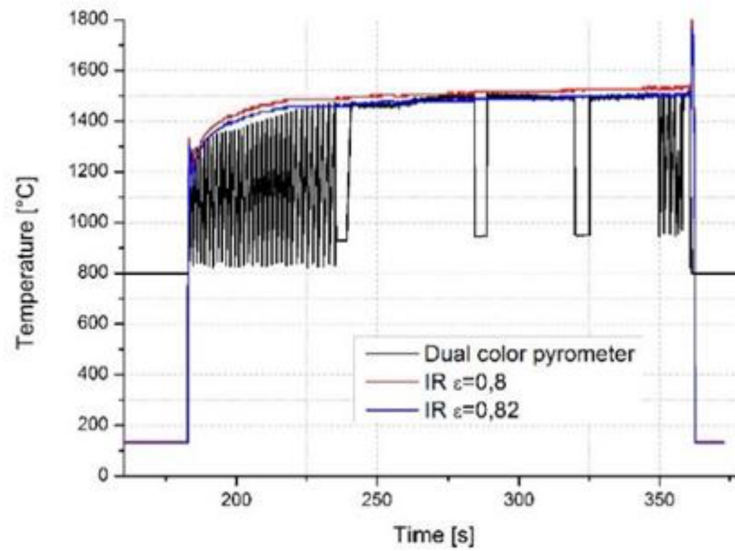
FIGURE 9.26: D800 vs. IR Temperature (at different ϵ_{IR}) on pyrometer spot
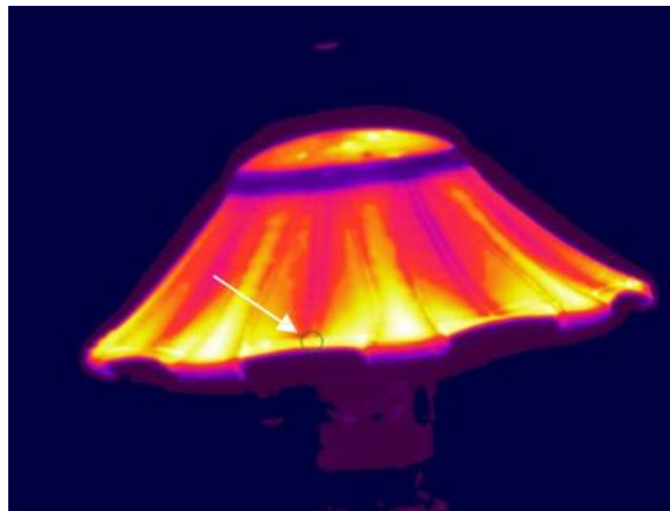
FIGURE 9.27: Infrared Cameras Picture of GD during PWT Test

9.3.6 Summary Results

The Ground Demonstrator of Mini-Irene was successfully qualified in the CIRA SCIROCCO Plasma Wind Tunnel.

The test article was able to sustain the extended duration test which is representative of the heat flux and heat load of the shallow trajectory used for the design of the TPS (see Table 9.3).

The external layer of Nextel, exceeding 1200°C in some areas, and the internal layers, experiencing temperatures up to 900°C, appear to preserve the original properties.

The TPS has proven the ability to protect the cold structure, which temperatures have remained below 80°C all the time.

Chapter 10

Dynamic Stability Analysis

In this chapter a particular focus has been reserved to the study of the problem of dynamic stability. In particular aero-thermodynamic analysis have been conducted to characterize the dynamic response in the supersonic, transonic and subsonic regime of a capsule with a 45° sphere-cone geometry by applying the forced-oscillation method through Computational Fluid Dynamics. The output of these analysis have been used in a six degree of freedom simulator to study the oscillating behavior during a sub-orbital re-entry trajectory.

10.1 CFD Results

10.1.1 Test Cases

The model used in this investigations is a capsule with a sphere-conical fore-body heat shield. The cone semi-aperture angle ε is 45 deg. The body diameter D is 0.765 m, the position of centre of mass (CoM) X_{CoG}, evaluated from the nose of the capsule, is 0.161 m, the distance of the shoulder from the nose L is 0.320 m, evaluated in the axial direction, and the nose radius is 0.328 m. The mass M is 12 kg and the reference surface S, estimated taking as reference length the body diameter D, is about 0.46 m^2.

The geometric characteristics are illustrated in Figure 10.1 and are summarized in Table 10.1. Figure 10.2 shows the CAD model. Clearly, only half capsule will be used for CFD simulation because of the body axial symmetry. Since our purpose is to determine dynamic stability by using the forced oscillation technique, a 3D domain is required for our case.
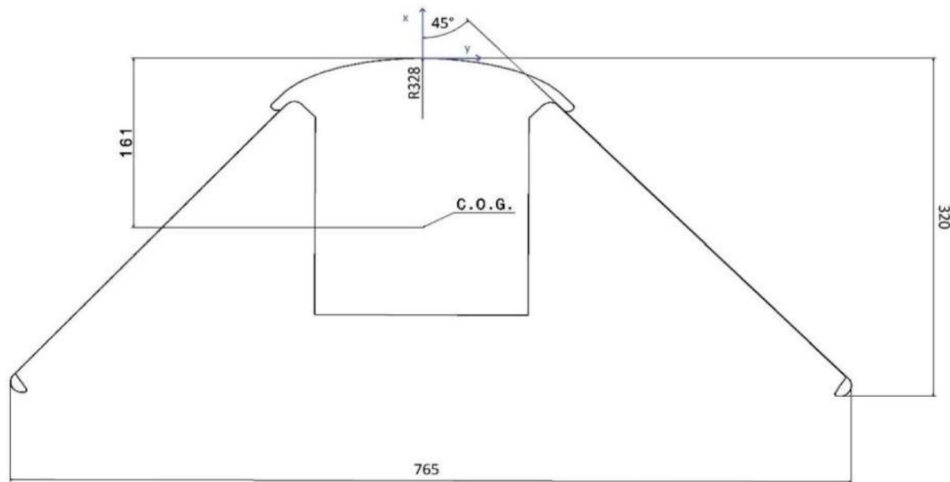
FIGURE 10.1: Capsule geometry. Dimensions are given in mm.

The domain, also shown in Figure 10.2, is a 3D C-type domain, where a half sphere centered in the CoM of the capsule model is placed. The capsule, placed inside the sphere, has been subtracted through a Boolean Operation. The sphere has a diameter equal to about five times the diameter of the capsule D. The C-domain, instead, has dimensions equal to about fifteen times the reference diameter D all around the capsule. This configuration of the domain allows the capsule, fixed to the sphere, to perform a rigid oscillatory rotation around its centre of mass, in order to numerically reproduce the forced oscillation setup.

The domain CAD model have been imported in STAR-CCM+ to generate the mesh needed for the simulations. To provide a fast evaluation of the dynamic

Body diameter, D	0.765 m
Position of centre of mass, X_{CoG}	0.161 m
Maximum length, L	0.320 m
Nose Radius, Rc	0.328 m
Capsule semi-aperture angle, ε	45 deg
Reference surface, S	0.46 m^2
Mass, M	12 kg
Ballistic coefficient, β	23 kg/m^2

TABLE 10.1: Geometric characteristics, mass and ballistic coefficient.
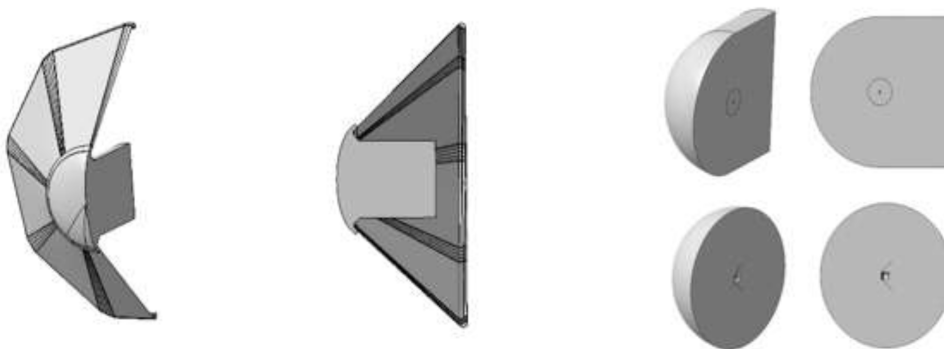
FIGURE 10.2: CAD model front and symmetry plane view (left). C-Domain cad model (right).

stability of a re-entry capsule, at the present stage a simple unstructured mesh has been developed and employed for both Eulerian and Turbulent simulations.
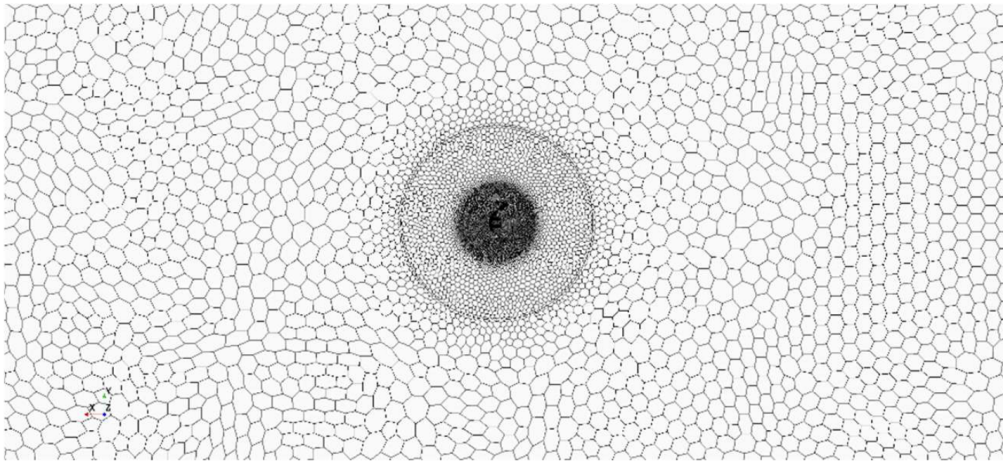
FIGURE 10.3: Polyhedral unstructured mesh

The mesh generated is shown in Figure 10.3. The base size is 0.2m, and the core volume has a growth rate of 1.3. Therefore, the cells far from the capsule, has greater dimensions, which is a benefit in terms of computational load.

It must be pointed out that two different mesh operation have been necessary, because the domain consists in two different zone: C-domain and Sphere. The surfaces in contact between these parts are treated as interface so that the solver would treat both Sphere and C-domain as a continuous fluid domain. The Sphere part was needed to simulate the oscillations of the capsule and so to apply the forced oscillation technique. In fact, it will rotate around its centre (that coincides with the CoM of the capsule) with a sinusoidal motion law.

Moreover, around the capsule a volume control has been applied in order to better represent the fluid flow around the capsule and to better capture the shock-wave ahead of the capsule. All these operations led to a volume cell number of 502203.

The first simulation attempt has been a compressible inviscid one. Analyzing the results, which are shown in the next section, it has been clear that Euler
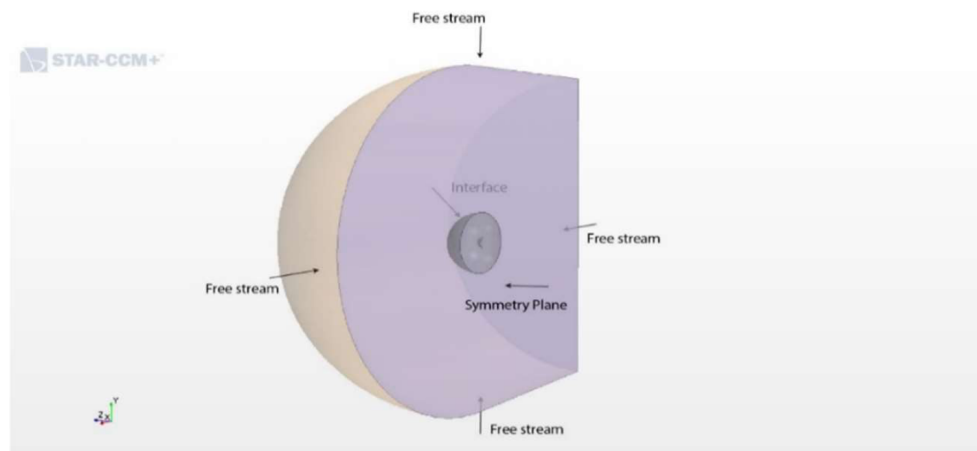
FIGURE 10.4: Simulation boundary conditions

simulations were not able to capture properly the wake and the results were not reliable. Thus, a turbulence model has been introduced. Specifically, a k-ω turbulence model has been used.

For both the models the boundary conditions, shown in Figure 10.4, are free stream, symmetry-plane, interface and wall. Free stream has been applied to all the faces of the fluid domain except for the plane of symmetry for both the C-domain and Sphere. Besides, there is the interface condition for the surfaces of Sphere and C-domain that are in contact and, obviously, the wall of the capsule. It must be pointed out that:

- The Spatial discretization scheme is a 2nd order implicit integration of the equations.

- Time discretization scheme is a 1st order implicit. The number of inner iterations is 200 and has been set in order to reach a good convergence of residuals and coefficients.

- Time step that has been chosen is 0.001 s, which ensures to be able to properly capture all the unsteady phenomena, considering the frequency chosen for the oscillations (1 Hz), and the frequency of the phenomena that has

been found to be about 14 Hz [138].

In order to predict the dynamic behavior of the capsule, the Sphere, which is a region within the fluid domain, must oscillate sinusoidally in time with a certain amplitude A and frequency f according to the following equation:

$$\theta = A \cdot sin\left(2\pi f t\right) \tag{10.1}$$

Values of A and f of interest for the present analyses were selected based on the results of 6-DOF trajectory simulations carried out without taking into account damping dynamic derivatives. These analyses pointed out that the capsule is subjected to oscillations with a maximum amplitude of $10°$ and a frequency from 1 Hz to 10 Hz.

Considering such results, it has been chosen to perform oscillations with a frequency of 1 Hz and with an amplitude equal to 2 deg, 5 deg and 10 deg. Furthermore, it has been estimated the natural pitching frequency of the capsule is 1 Hz one order of magnitude lower than the aerodynamic buffeting frequency.

It has been mentioned that the most critical part of the re-entry trajectory in the frame of dynamic stability is the transonic regime. Therefore, in order to predict the dynamic behavior of the capsule, the conditions chosen for the simulations are the supersonic, transonic and subsonic one reached during re-entry. Two supersonic (M=3, M=2), two near transonic (M=1.2, M=0.8) and one subsonic (M=0.3) conditions have been selected. Density ρ, pressure p, temperature T and dynamic viscosity μ have been evaluated according to the standard atmosphere model US1976. Table 10.2 shows all the conditions selected.

For each of the conditions gathered in Table 10.2, at least three simulations have been performed in the turbulent case varying the amplitude of the oscillation as mentioned in the previous subsection. In the inviscid case, instead, only

H (km)	M	$p \cdot 10^{-2}$(kg/m^3)	p (Pa)	T (K)	$\mu \cdot 10^{-5}$ (Pa · s)
32.8	1.2	1.16	771	231	1.512
22.9	0.3	5.57	3520	219	1.449
30.9	0.8	1.61	1050	227	1.493
35.6	2	0.78	531	238	1.555

TABLE 10.2: Selected conditions along the re-entry trajectory

the transonic condition (M = 1.2) with an amplitude *A* of 10 deg have been simulated. Only for the 1.2 Mach case the inviscid model has been used because it did not give reliable results, as it is shown in the next chapter. Moreover, for both the models, a frequency of 1 Hz has been set. In Table 10.3 all the simulation cases are shown and their results are discussed in the next section.

Model	Mach	A (deg)
Inviscid	1.2	10
Turbulent k-ω	0.3, 0.8, 1.2, 2	2, 5, 10

TABLE 10.3: Simulation cases

10.1.2   Simulation Results

The first analysis being run is an unsteady compressible inviscid simulation with an oscillation amplitude of 10 deg and a frequency of 1 Hz. The flight condition is referred to a Mach number of 1.2 and the corresponding atmospheric quantities values are summarized in Table 10.2.

Four oscillation periods, hence four seconds, have been simulated. The moment coefficient evaluated with the respect to the CoM of the capsule as a function of the time and of the pitch angle is shown Figure 10.5.
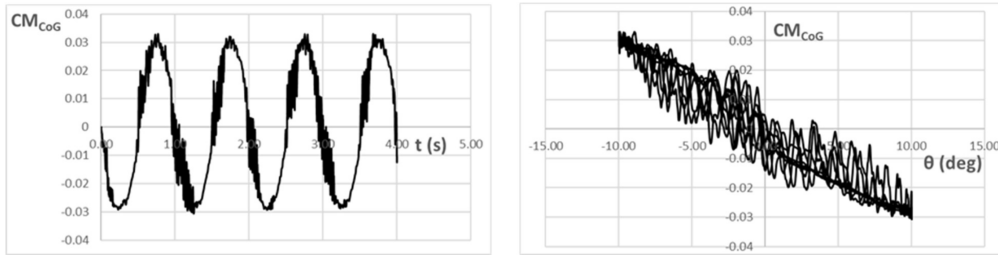
FIGURE 10.5: Four periods of the $C_{M_{CoG}}$ as a function of time (left). Four cycles of $C_{M_{CoG}}$ as a function of the pitch angle (right). Inviscid case.

It is clear, by looking at the figures, that no information can be carried out from these data. Thus, a smoothing operation is needed. Specifically, the C_M values are smoothed by using the "smooth" function in MATLAB. This function works by smoothing data using a specified filter method and span (a percentage of the total number of data points, less than or equal to 1).

Good results are achieved using a span of 0.1 and a filter method called "rloess", a robust version of "loess" (local regression) that assigns lower weight to outliers in the regression and assigns zero weight to data outside six mean absolute deviations [139].

The result of these operations is shown in Figure 10.6, where the smoothed C_M is called "C_M clean".

The first thing that can be seen is the direction of the cycle, which is clockwise. Hence, the value of the damping sum is expected to be positive, which means that the capsule is dynamically unstable. Applying equation 5.17 the value of the pitch damping sum is:

$$C_{m_{\dot{\alpha}}} + C_{m_q} = 0.934 (rad^{-1}) \qquad (10.2)$$
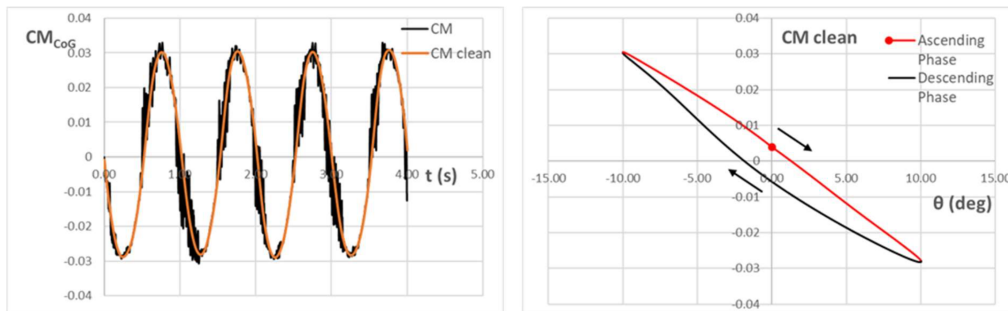
FIGURE 10.6: Four periods of the $C_{M_{CoG}}$ (black line) and of the smoothed $C_{M_{CoG}}$ (orange line) as a function of time (left). Cycle of CM clean in the ascending (red) and descending (black) phase of the oscillation. Direction of the cycle is also shown(right).

Therefore, in inviscid case, the capsule is dynamically unstable. Nevertheless, the highly oscillating CM profiles, shown in the previous figures, reveal the inviscid model poor capability to describe the phenomenon properly. This is also confirmed by the contours of velocity, shown in Figure 10.7, where it can be seen that the wake has not been captured correctly, suggesting that the result is not reliable.
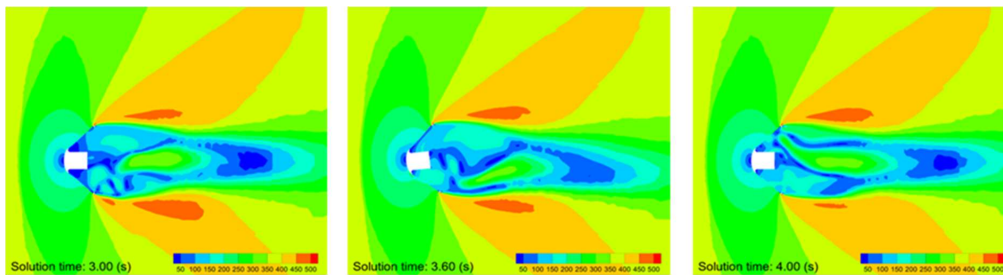
FIGURE 10.7: Velocity Magnitude (m/s) Contour at different time instants. Mach 1.2 inviscid case, A = 10 deg

In order to make a comparison with the inviscid case, the results of the Mach 1.2 turbulent simulation are presented. Figure 10.8 shows the $C_{M_{CoG}}$ as a function of the time (left) and pitch angle (right), respectively. The hysteresis cycles over the four period are narrow in this case as well. For a better visualization of the cycle, the C_M values have been altered with a ΔC_M, which is equal to:
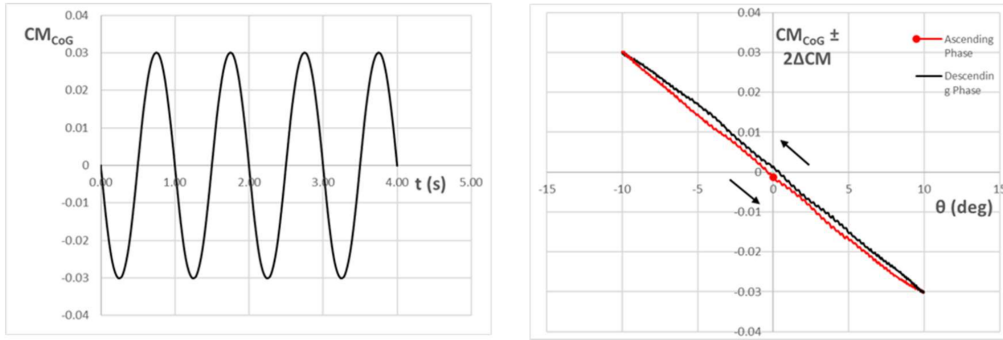
FIGURE 10.8: Four periods of the $C_{M_{CoG}}$ as a function of time (left). Cycle of CM clean in the ascending (red) and descending (black) phase of the oscillation. Mach 1.2 turbulent case, A=10 deg.

$$\Delta C_M = \left(C_{M_{up}} - C_{M_{down}} \right) \tag{10.3}$$

where $C_{M_{up}}$ and $C_{M_{down}}$ are maximum and minimum value of $C_{M_{CoG}}$ at the same angle θ. Therefore, to enlarge the results a quantity equal to $2\Delta C_M$ is added to $C_{M_{up}}$ and the same quantity is subtracted from $C_{M_{down}}$.

The loop direction is counter-clockwise. Thus, the capsule is dynamically stable in this case, as can be confirmed by the sign of the average damping-in-pitch parameter:

$$C_{m_{\dot{\alpha}}} + C_{m_q} = -0.163 (rad^{-1}) \tag{10.4}$$

In Figure 10.9 the velocity contours over the second oscillation period are shown with a time span of 0.2 seconds carried out for the turbulent case.

Within the contours all the main element of the flow structure around a blunt body are present:

- the shock wave ahead of the capsule

- the Prandtl-Mayer expansion

- the recirculating region
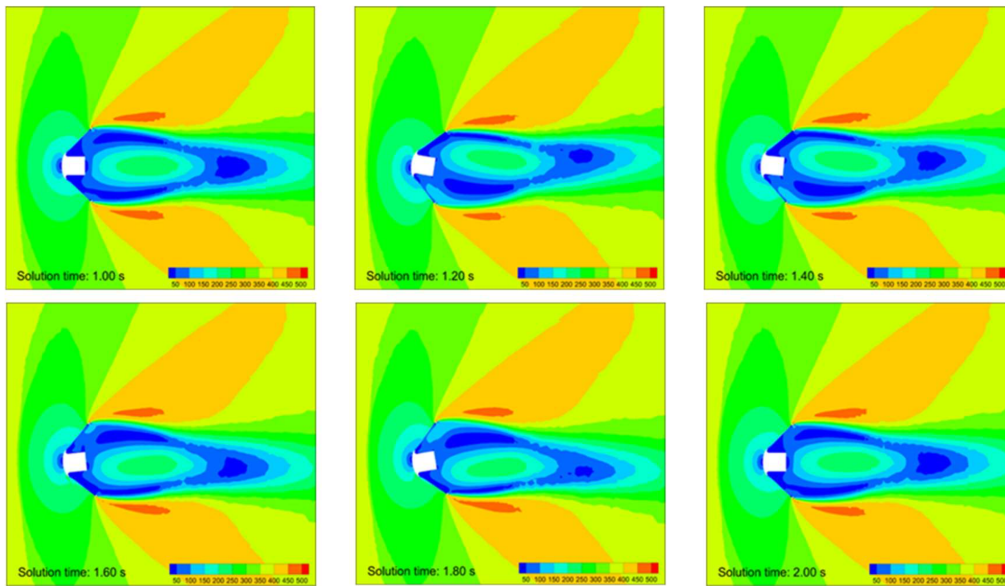
FIGURE 10.9: Velocity contours of the second period oscillation. Mach 1.2 turbulent case, A = 10 deg

- the recompression shock

- the neck of the wake

Moreover, it can be immediately seen that the wake flow has been captured better in comparison to the inviscid case shown in Figure 10.7.

It must be pointed out that the wake follows the motion of the capsule and, in this motion, it has been observed a phase delay of the pressures before and after the capsule. This phenomenon is probably the main responsible of the hysteresis effect as can be confirmed by the study of Teramoto et al. [140].

The results of all the remaining simulations performed are summarized for brevity in Table 10.4 and are shown in Figure 10.10 as a function of pitch amplitude and in Figure 10.11 as a function of Mach number.

The figures highlights the dynamic stability trend of the capsule. As can be seen, the oscillation amplitude has a considerable effect on the damping sum, as well as the Mach number.

Mach	Amplitude	$C_{m_{\dot{\alpha}}} + C_{m_q}$	Behavior
1.2	2	0.627	Unstable
	5	0.059	Unstable
	10	-0.163	Stable
0.3	2	-0.116	Stable
	5	-0.203	Stable
	10	-0.213	Stable
0.8	2	0.007	Unstable
	5	-0.247	Stable
	10	-0.339	Stable
2	2	0.113	Unstable
	5	-0.366	Stable
	10	-0.618	Stable

TABLE 10.4: Pitch Damping Sum CFD Results
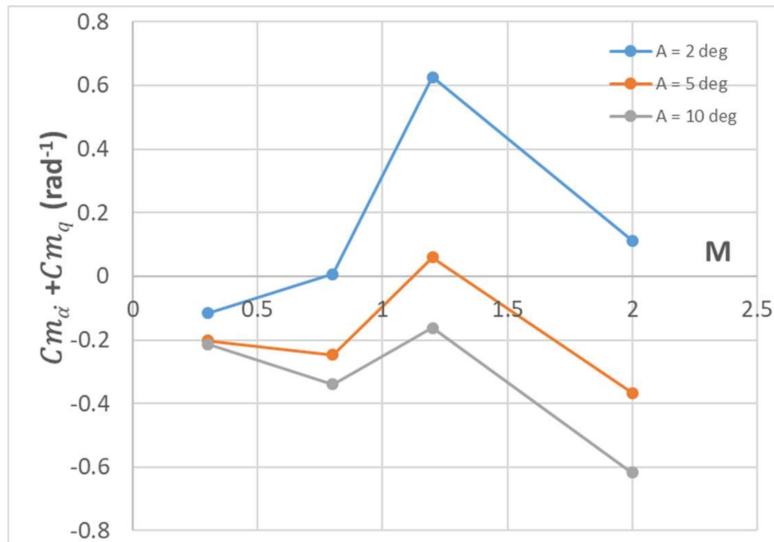
FIGURE 10.10: Damping sum as a function of Mach number at different oscillation amplitudes
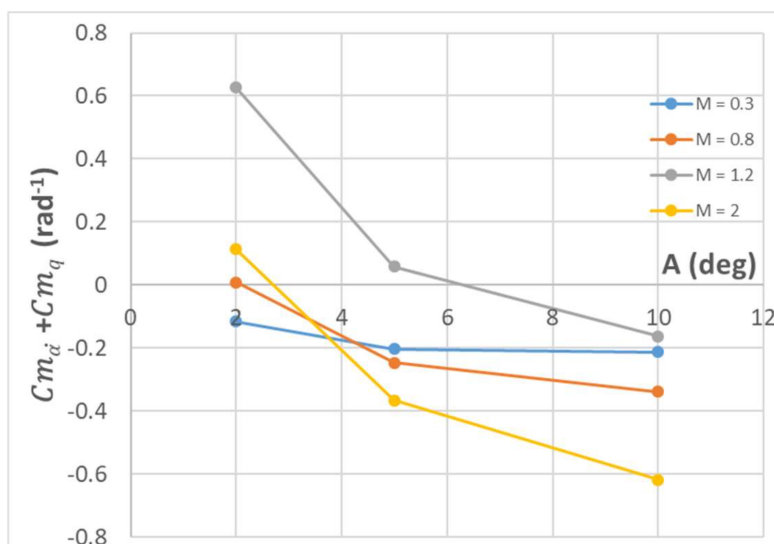
FIGURE 10.11: Damping sum as a function of oscillation amplitudes at different Mach numbers

At low amplitudes, namely 2 deg, the vehicle is unstable at all Mach numbers except for Mach 0.3, where the instability disappears. Increasing the amplitude, the pitch damping sum moves towards negative values leading to a dynamically stable behavior of the capsule.

This behavior is well-expected. Figure 10.12 and Figure 10.13 are taken from [96] and here shown for the sake of comparison.
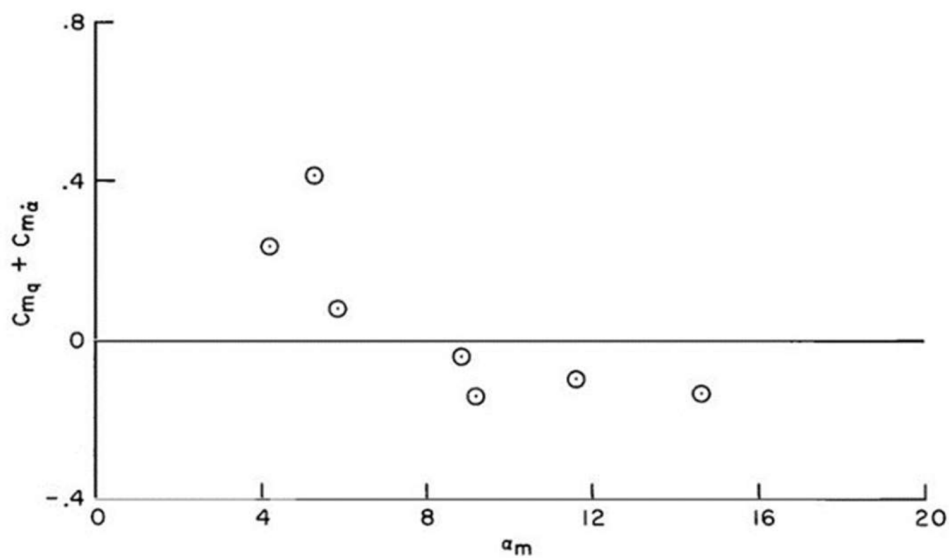
FIGURE 10.12: Pitch amplitude effect on the dynamic stability of
Viking capsule. M = 2.1.

The first shows the effect of the pitch amplitude on the damping sum of the capsule Viking evaluated at Mach number 2.1 (to compare with Figure 10.11). The latter shows the damping sum as a function of Mach number. As can be observed, the behavior results of this work are perfectly in agreement with Viking ones, even though the instabilities are present at higher Mach number for Viking capsule.

In Figure 10.14, referred to Wind Tunnel Forced Oscillation Test of Orion crew module and originally presented in [97] but reported here for comparison, is
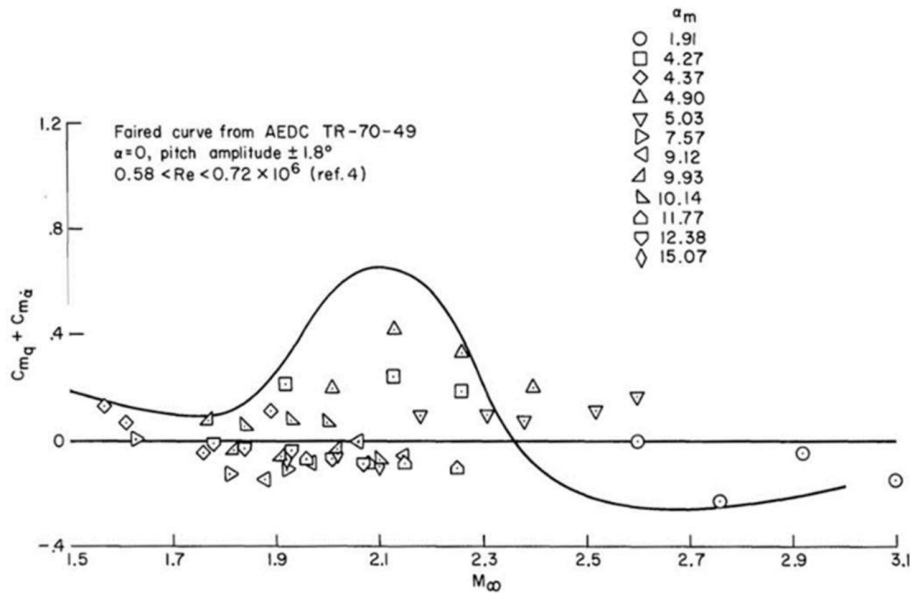
FIGURE 10.13: Variation of the dynamic stability with Mach number
at different oscillation amplitudes of Viking capsule

shown the effect of Mach number, of the sting and of the angle of attack on dynamic stability. In order to make a comparison with the present results, only the effect of Mach number at an angle of attack of 0 deg (α=180 deg corresponds to 0 deg) must be considered. Although in this case Orion capsule is always unstable, there is a peak of instability in the transonic regime.

The same conclusions can be made by looking at the dynamic damping coefficient of Hayabusa capsule shown in Figure 10.15, taken from [95] and here shown for comparison, considering again only the case at 0 angle of attack. Besides, this behavior is well-known in the literature and it is the reason why the effort to study dynamic stability on re-entry capsule is increased over the years.
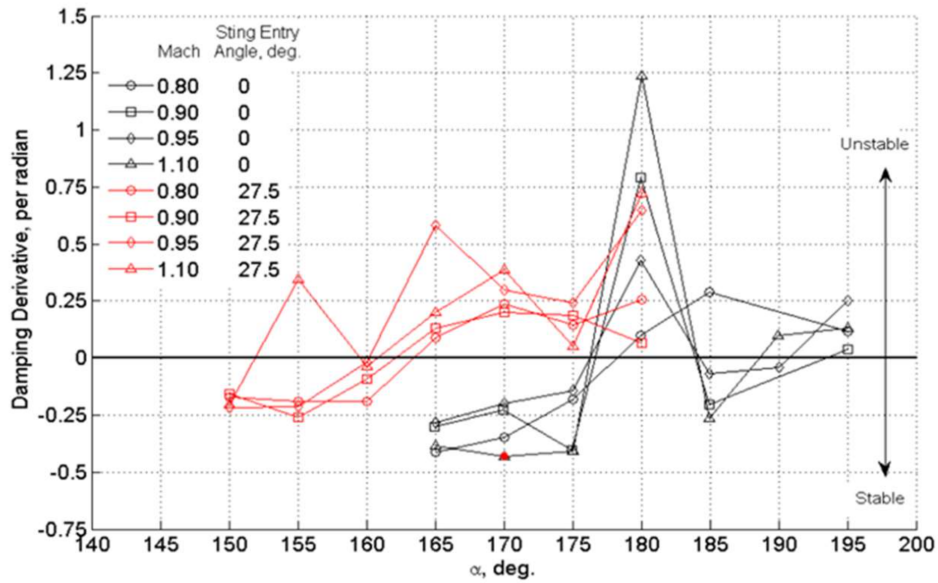
FIGURE 10.14: Orion crew module damping with sting entry angles
of 0 deg and 27.5 deg. α=180 deg corresponds to 0 deg
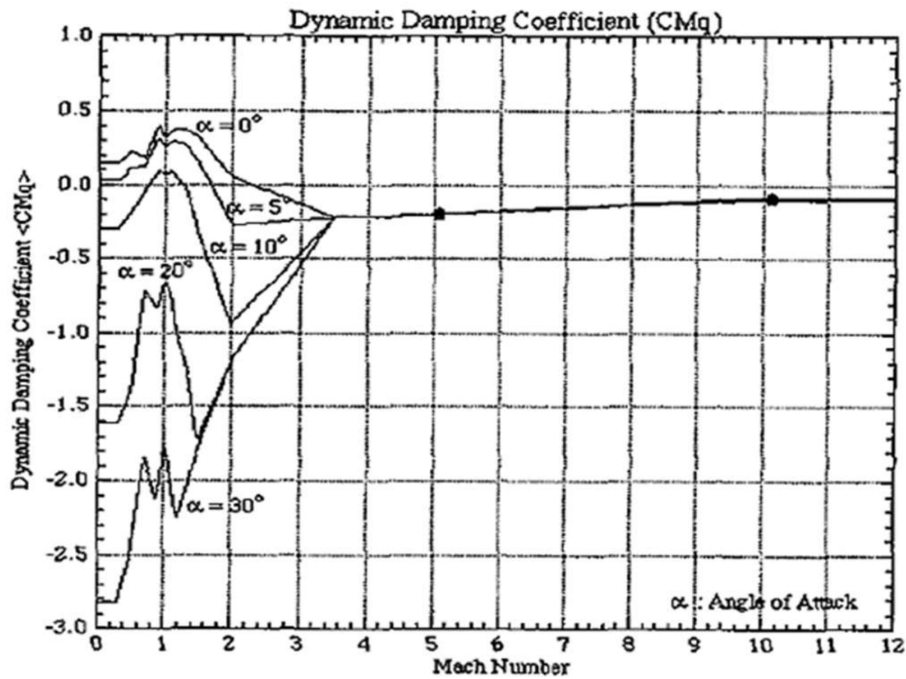
FIGURE 10.15: Dynamic Damping Coefficient vs. Mach Number for
Hayabusa capsule

10.2 Capsule Attitude Analysis

10.2.1 Test Cases

An analysis of the capsule attitude along a sub-orbital re-entry trajectory has been conducted. The objective was to simulate and analyze the oscillating attitude behavior during the re-entry of a 45 degree deployable heat shield capsule with the dumping derivatives, evaluated in the previous section, from the launcher release till landing. For all the analyses an altitude dependent AEDB has been used.

ID	Release Position	Initial Angle of Attack (deg)	Initial Pitch Rate (deg/s)	Initial Roll Rate (deg/s)	Unc.
Case 1A	Separation	180	0	0	No
Case 1B	Separation	180	0	10	
Case 1C	Separation	180	10	0	
Case 1D	Separation	180	10	10	
Case 1E	Separation	180	10	280	
Case 2A	Separation	180	0	0	Yes
Case 2B	Separation	180	0	10	
Case 2C	Separation	180	10	0	
Case 2D	Separation	180	10	10	
Case 2E	Separation	180	10	280	

FIGURE 10.16: Initial attitude conditions at the release

Two batches of several attitude initial conditions have been simulated (see table) in order to assess different possible attitude scenarios during the release in function of the presence of uncertainties. The initial angle of attack is always $180°$ because the capsule is released from the launcher with the nose pointing downward. The high range of variation for the rates are due to the uncertainty of the possible capsule release rate attitudes which is directly related to the uncertainty of the rocket behavior at the moment of the release. In fact in case of a failure of the launcher yo-yo de-spin maneuver the initial roll rate at separation could be

possible as high as 280 deg/sec. The remaining attitude parameters, i.e. initial yaw rate and side slip angle, have been set to 0 for all simulations.

10.2.2 Simulation Results

The results here presented show the demeanor of the Total Angle of Attack (which is the arcsine of the product between the cosine of the angle of attack and the cosine of the sideslip angle, for definition always positive) zoomed on the last 90 km of the trajectory to better show the oscillating behavior in the transonic region.

$$TAoA = atan \left[cos\left(\alpha \right) \cdot cos\left(\beta \right) \right] \tag{10.5}$$

The first batch of cases analyzed was the one with the damping database without uncertainties. The nominal case (Case1D) is the one with an initial pith rate and roll rate of 10 deg/sec at the release.
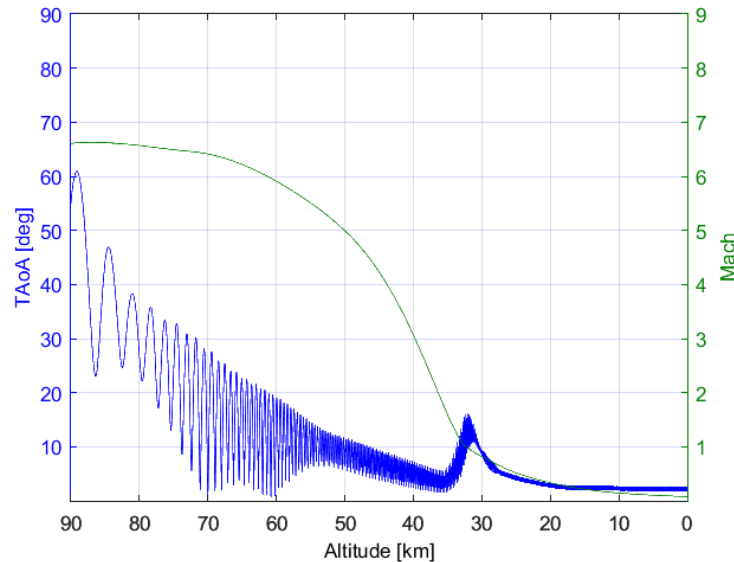
FIGURE 10.17: Total Angle of Attack as a function of Altitude for Case1D

In this case the capsule arrive in low supersonic condition (M=2) with oscilla-
tions of about 5.5 deg. During the transonic there is an increase of this oscillation
that reach a value of 16 deg. After this phase the oscillation are dumped again
and we arrive at landing with oscillation of total angle of attack around 2.5 deg.

In the other first three cases (1A, 1B, and 1C), the value of initial pitch and roll
rate are varied between 0 and 10 deg/sec, and is possible to notice that minimum
difference occurred in the behavior.
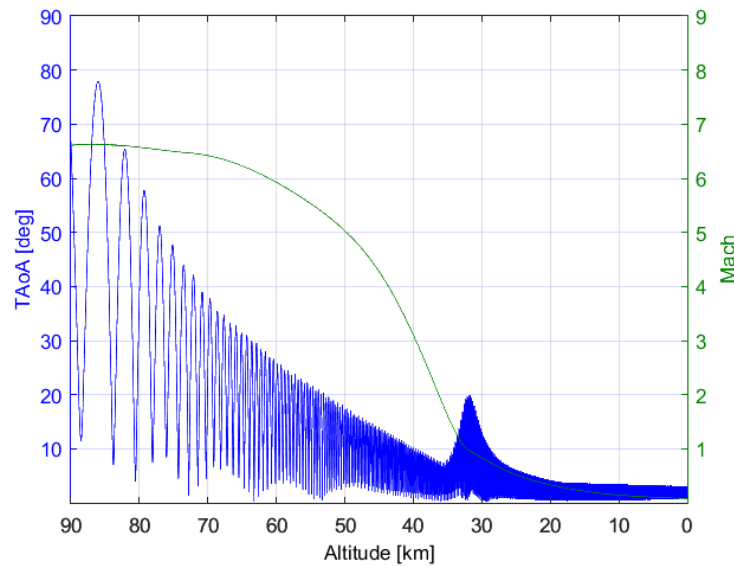
FIGURE 10.18: Total Angle of Attack as a function of Altitude for
Case1A

In all these four cases, the capsule tumbles in high altitudes, and shows a
positive tendency to turn with the front shield facing forward where the altitude
decrease and the dynamic pressure increase. In fact, as the altitude decreases,
higher dynamic pressure causes the damping of the oscillations until low super-
sonic region.

However, when high initial roll rates are assumed (i.e. Case 1E: failure of the
launcher yo-yo de-spin manoeuvre) the gyroscopic stability resulted prevents the
capsule from tumbling and limits the total angle of attack oscillation amplitude
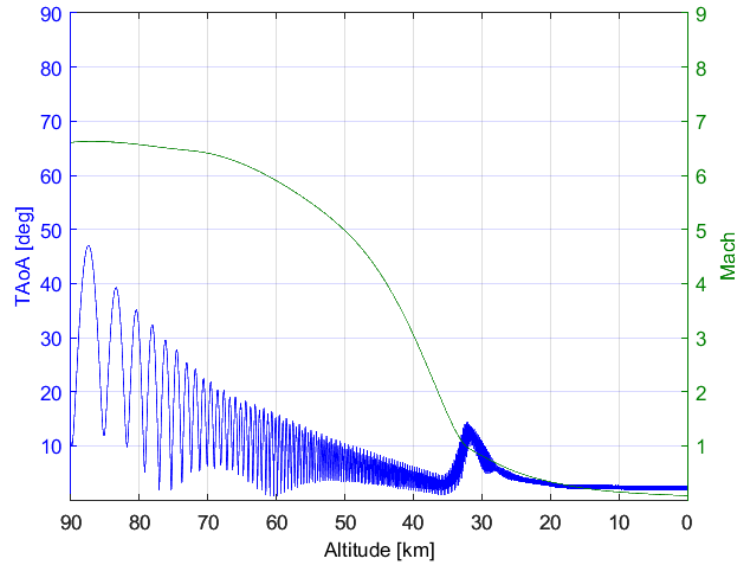
FIGURE 10.19: Total Angle of Attack as a function of Altitude for Case1B
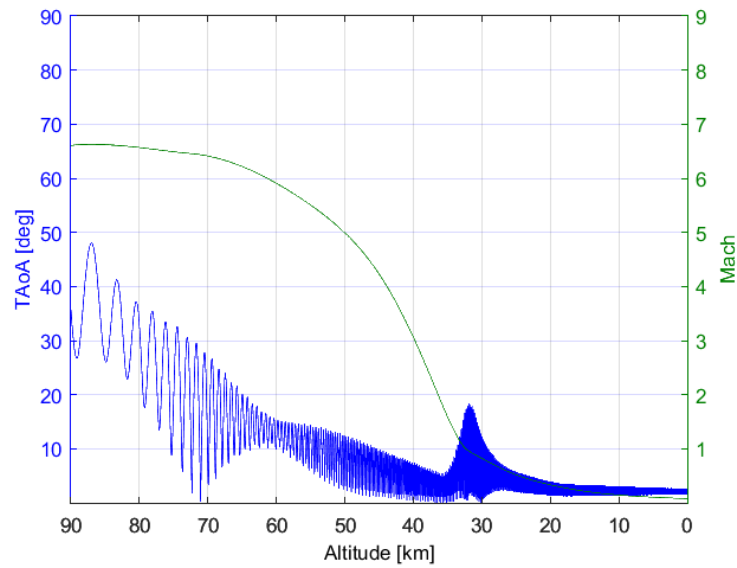
FIGURE 10.20: Total Angle of Attack as a function of Altitude for Case1C

very low. Furthermore, during the transonic region this oscillation reach an angle as high as 9 deg and then are dumped to approximately 2 degrees at landing.
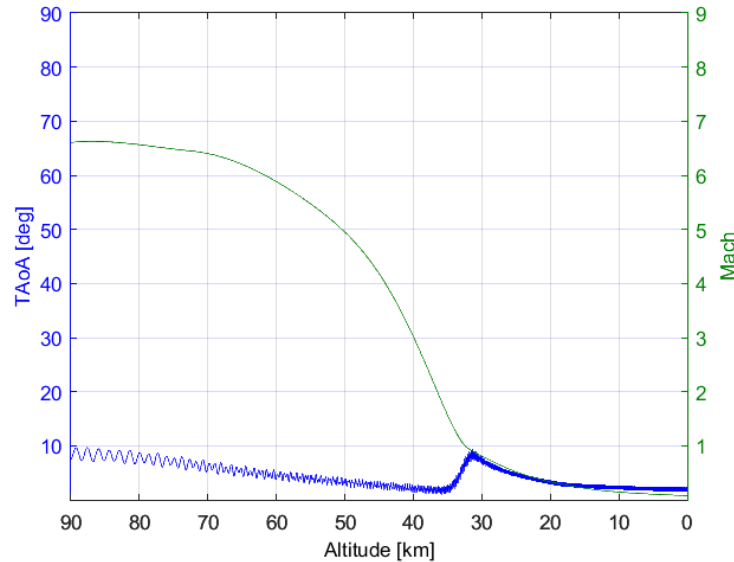
FIGURE 10.21: Total Angle of Attack as a function of Altitude for Case1E

The results show in all the cases the positive tendencies of the capsule to turn with the front shield facing forward and to dump the oscillations to approximately 3 degrees at landing with a peak during transonic of $20°$ in the worst case, i.e. Case 1A. The results show also that the frequency of oscillation for all the cases in the low supersonic and subsonic region are between 1 and 10 Hz.

The second batch of cases analyzed have the same initial conditions of the first five but difference from the presence of uncertainties in the pitch damping derivatives [141].

As is possible to see from the results the general behavior remain the same, but there is an increase of the value of the oscillation amplitude. In this case in fact at low supersonic (M=2) we reach oscillation of around 14 deg, than reach a maximum during transonic around 32 deg in the worst case (2A). Nevertheless at
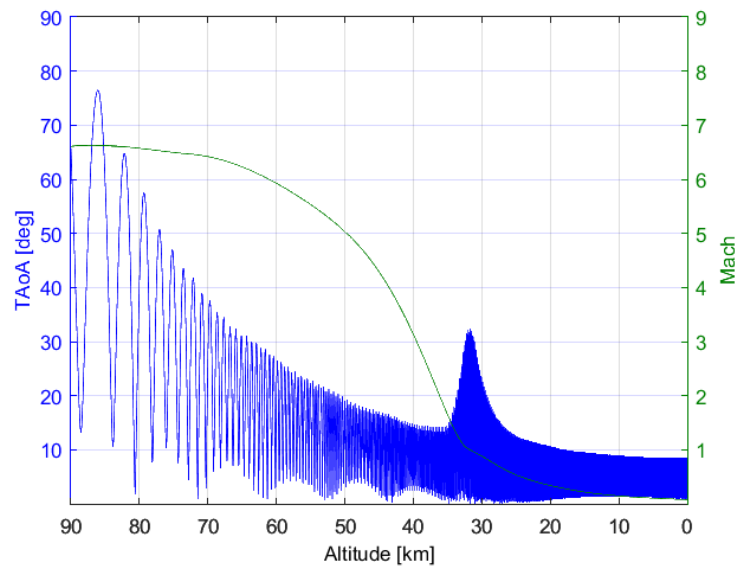
FIGURE 10.22: Total Angle of Attack as a function of Altitude for
Case2A

landing the oscillations are dumping and we reach value equal to the one without uncertainties of around 8 deg.

The results illustrated in the previous plots have been summarized in the following table.

To conclude, is possible to notice how the capsule maintains transonic stability also including a severe level of uncertainties and starting from a tumbling condition.

ID	Initial AoA (deg)	Initial Pitch Rate (deg/s)	Initial Roll Rate (deg/s)	Unc.	TAoA Oscillation @ M = 2 (deg)	TAoA Oscillation @ Transonic (deg)	TAoA Oscillation @ M = 0 (deg)
Case 1A	180	0	0		7	20	3
Case 1B	180	0	10		4.5	15	2.5
Case 1C	180	10	0	No	6	18	2.5
Case 1D	180	10	10		5.5	16	2.5
Case 1E	180	10	280		2	9	2
Case 2A	180	0	0		14	32	8.5
Case 2B	180	0	10		8.5	25	6
Case 2C	180	10	0	Yes	10	32	8.5
Case 2D	180	10	10		11	28	6
Case 2E	180	10	280		3.5	15	5.5

FIGURE 10.23: Summary Result

Chapter 11

Controllability Results

In this chapter are presented the results of studies dedicated to assess the controllability and the performances of the control system and the algorithm proposed in this thesis. In particular a means of controlling a mechanically deployable capsule during the re-entry phase using an aerodynamic control system has been studied and the performance evaluated. Moreover, a new technological solution for re-entering and landing a capsule in a desired location from a low Earth orbit without the use of chemical propulsion has been tested through Monte Carlo analysis.

11.1 Control System Simulation and Performance Evaluation

11.1.1 De-Orbit Burn Uncertainties Analysis

To assess the aerodynamic control system performances proposed in Chapter 6, a reference mission and trajectory have been selected. The chosen mission is a ballistic re-entry from ISS (International Space Station). The initial orbit was chosen considering a Soyuz-like mission profile after separation from ISS (see Figure 11.1). The main orbital parameter considered were:

- Inclination: $i = 51.6°$

- Eccentricity: $e = 0.00038$

- Semi-major axis: $a = 6798 \, km$

The landing site, located in Kazakhstan, was chosen from the nominal landing points for the Soyuz re-entry capsule. The chosen target is defined by the coordinates:

$$\phi_T = 47.06 \, deg \qquad \theta_T = 58.30 \, deg$$
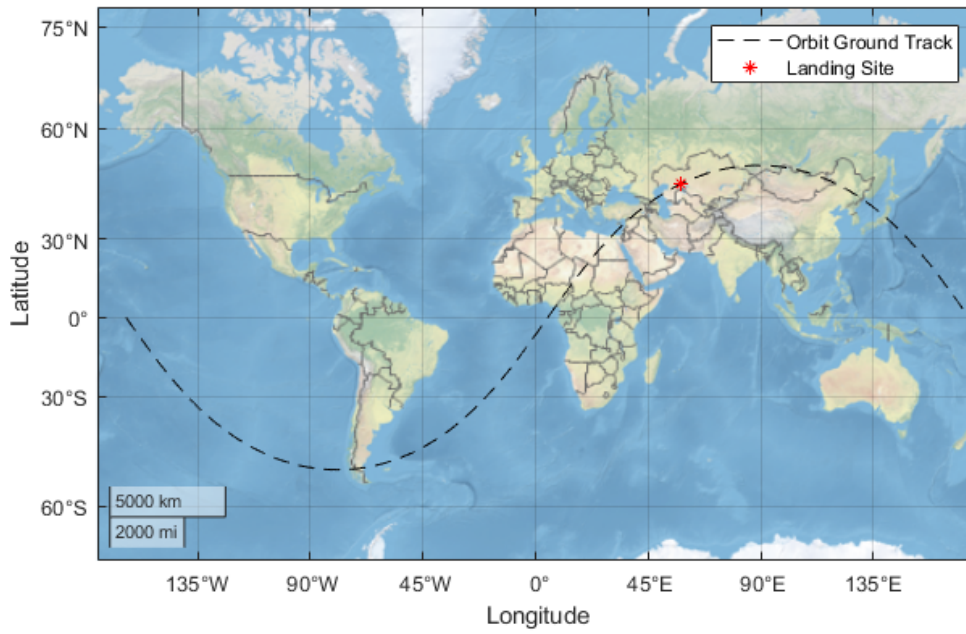
FIGURE 11.1: Mission Orbit Ground Track (in black)
and desired landing site (in red)
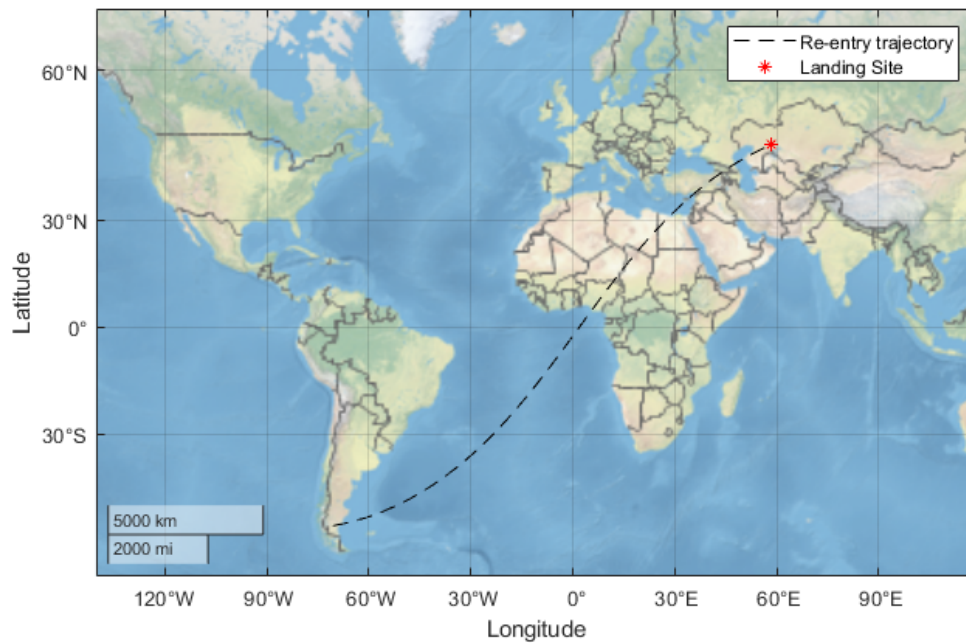
FIGURE 11.2: Re-entry nominal trajectory (in black)
and landing site (in red)

Altitude [m]	422000
Velocity [m/s] (after the de-orbit manoeuvre)	7242.5
Heading [deg]	9.771
Flight Path Angle [deg]	0
Latitude [deg]	-50.3230
Longitude [deg]	-70.5464

TABLE 11.1: Nominal trajectory initial conditions from orbit

FIGURE 11.3: Re-Entry orbit representation, from the De-Orbit Burn
to the landing site

A $\Delta V = 100\,m/s$ de-orbit burn was considered, and the point along the orbit where to perform the de-orbit maneuver in order to reach the landing site was identified iteratively.

The de-orbit maneuver must be performed when the spacecraft is roughly around half an orbit from its landing site, on the southern tip of Argentina (see Figure 11.2). The identified initial conditions for the mission are showed in Table 11.1.

	Simulation Results
Downrange [km]	14637.725
Max Heat Flux [kW/m^2]	334.472
Max Load Factor [g]	7.49
Landing Site Latitude [deg]	47.06
Landing Site Longitude [deg]	58.60

TABLE 11.2: Trajectory Main Elements

The main elements of the trajectory are summarized in Table 11.2 and in Figures 11.4 - 11.8 the evolution along the trajectory of Altitude, Down Range, Velocity, Load factor, Dynamic Pressure, Heat Flux and Mach are shown.
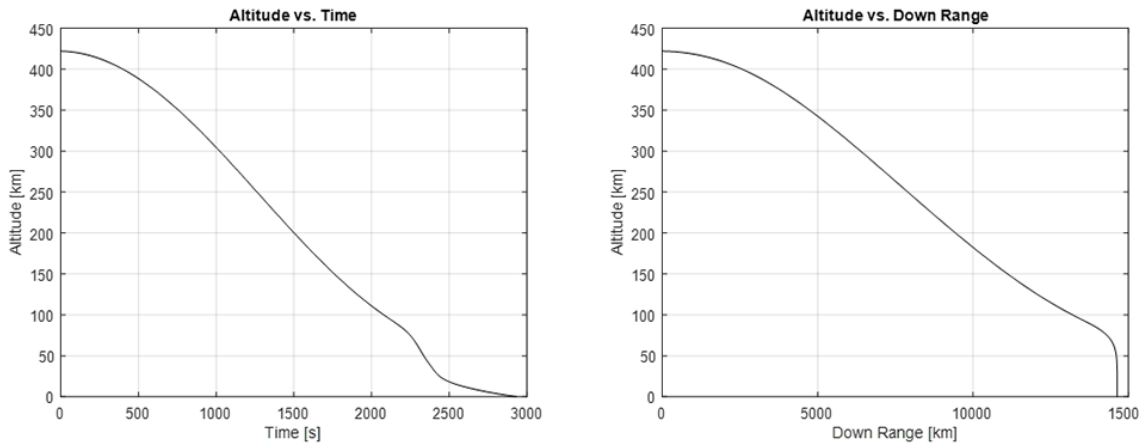
FIGURE 11.4: Altitude vs. Time and Altitude vs. Down Range for the nominal trajectory
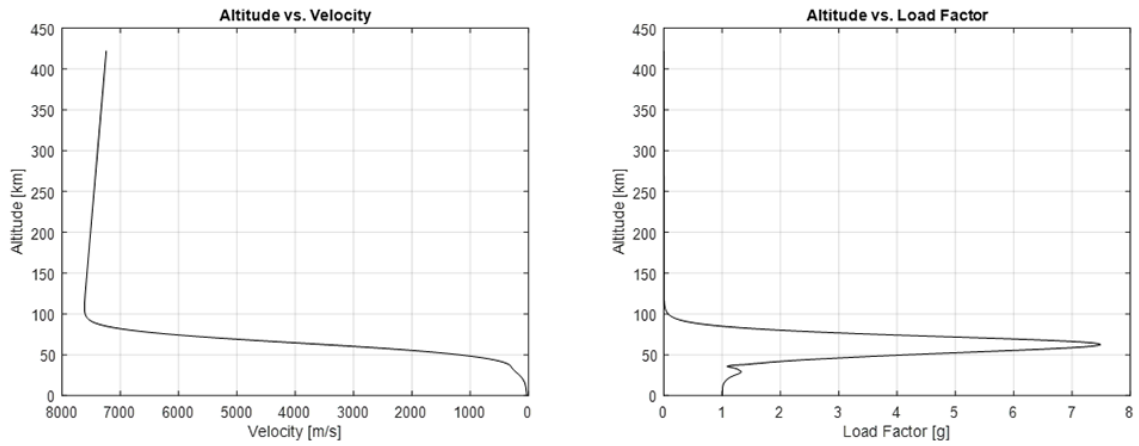
FIGURE 11.5: Altitude vs. Velocity and Altitude vs. Load Factor for
the nominal trajectory
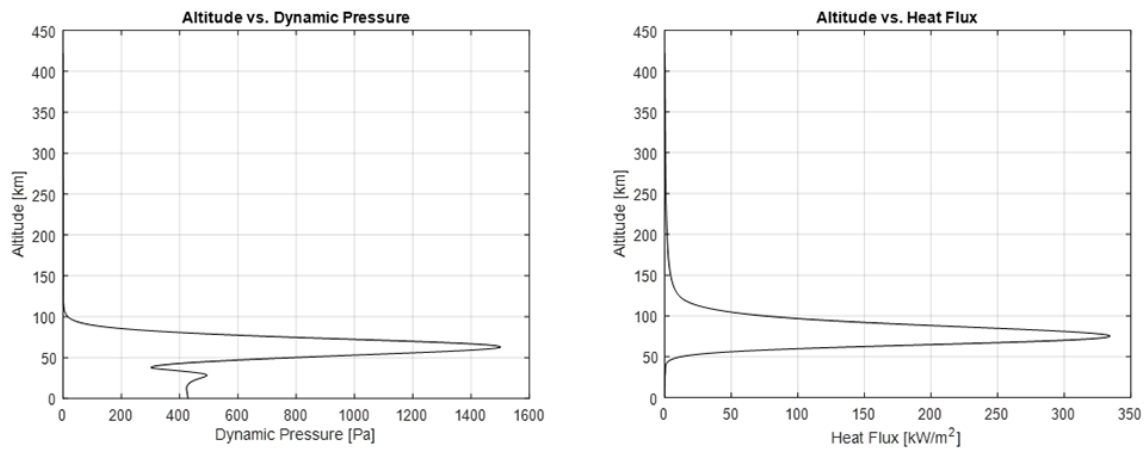
FIGURE 11.6: Altitude vs. Dynamic Pressure and Altitude vs. Heat
Flux for the nominal trajectory
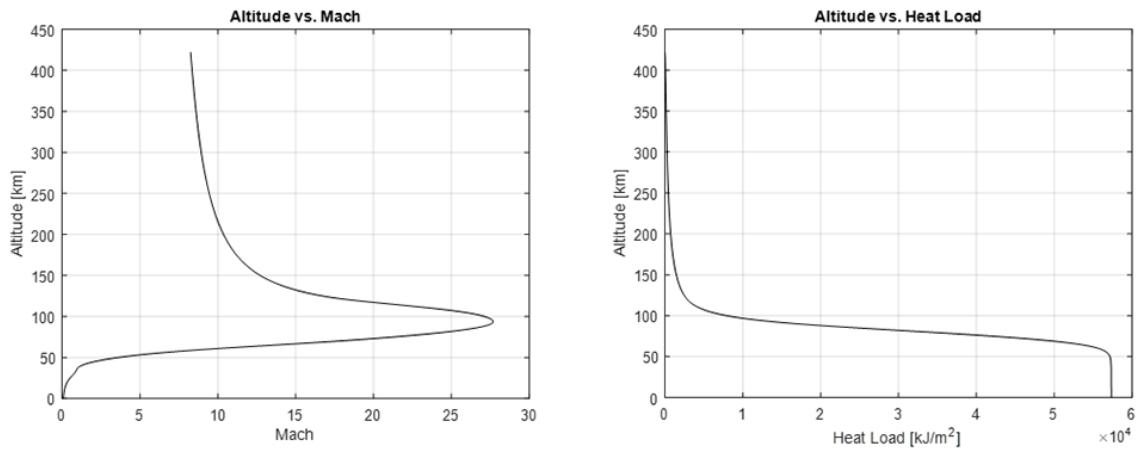
FIGURE 11.7: Altitude vs. Mach and Altitude vs. Heat Load for the nominal trajectory
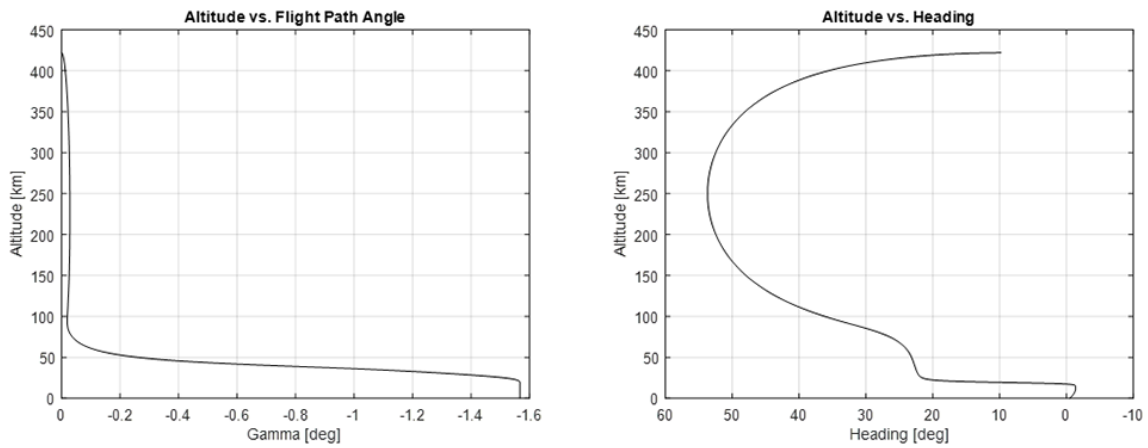
FIGURE 11.8: Altitude vs. Flight Path Angle and Altitude vs. Heading for the nominal trajectory

Due to uncertainties in the de-orbit burn, the capsule will eventually drift from the nominal trajectory, if no control system have been considered. An analysis on the effects of a de-orbit burn error was performed. Dispersions on the landing site were evaluated, as well as effects on the maximum heat flux and maximum load factor.

The consequences of a de-orbit burn error in terms of total ΔV provided were evaluated first. The nominal de-orbit burn considered is 100 m/s and maximum variation of 5 % have been evaluated (Table 11.3) (Figure 11.9).

As can be expected, no large variations in terms of maximum heat flux or maximum load factor can be appreciated. The main effect on a de-orbit burn error is related to downrange displacement.
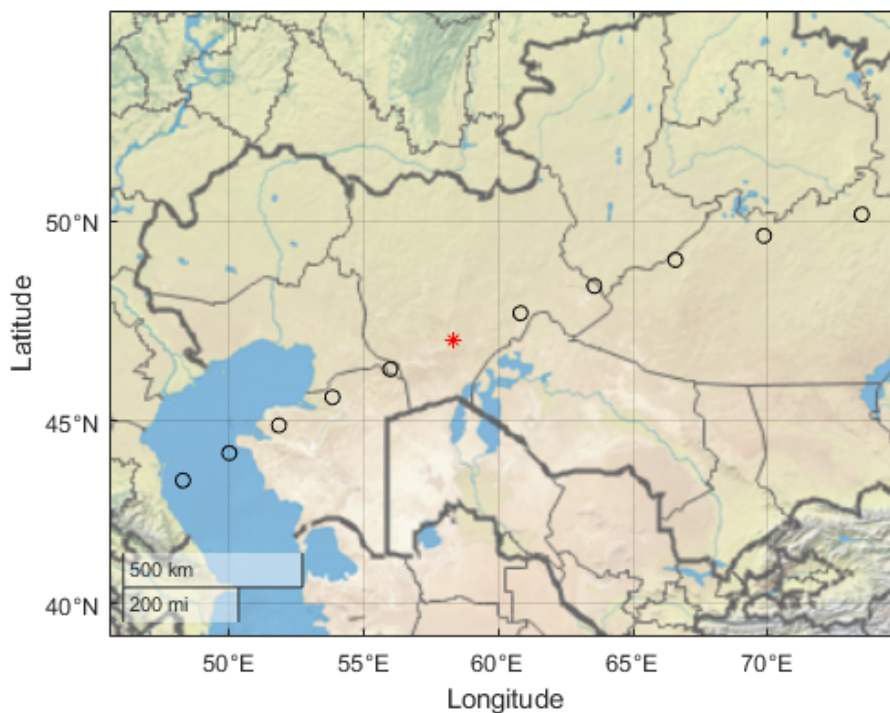
FIGURE 11.9: ΔV De-Orbit burn error landing sites (in black) and
nominal landing site (in red)

ΔV Error	Downrange Displacement [km]	Max Heat Flux [kW/m^2]	Max Load Factor [g]
No Error	0	337.230	7.49
1%	-183.211	331.718	7.50
-1%	195.157	339.979	7.47
2%	-355.215	328.975	7.52
-2%	403.916	342.714	7.46
3%	-518.366	326.260	7.54
-3%	629.020	345.428	7.45
4%	-672.719	323.588	7.56
-4%	871.759	348.117	7.44
5%	-819.521	320.981	7.58
-5%	1136.109	337.230	7.44

TABLE 11.3: ΔV De-Orbit Burn error analysis results

It is worthy to notice that an error of only 2 % on the de-orbit burn (corresponding to an error of 2 *m/s* for a 100 *m/s* ΔV) causes a displacement at landing site approximately of 350 km. For this reason, a correction maneuver after the de-orbit burn could be useful to reduce dispersions.

Similarly, the consequences of de-orbit burn error in terms of delayed or advanced deorbit burn were evaluated too. 1, 2 and 5 seconds early or delayed de-orbit burn effects were evaluated (see Table 11.4 and Figure 11.10).

As can be noticed, this kind of error lead to significantly smaller displacements
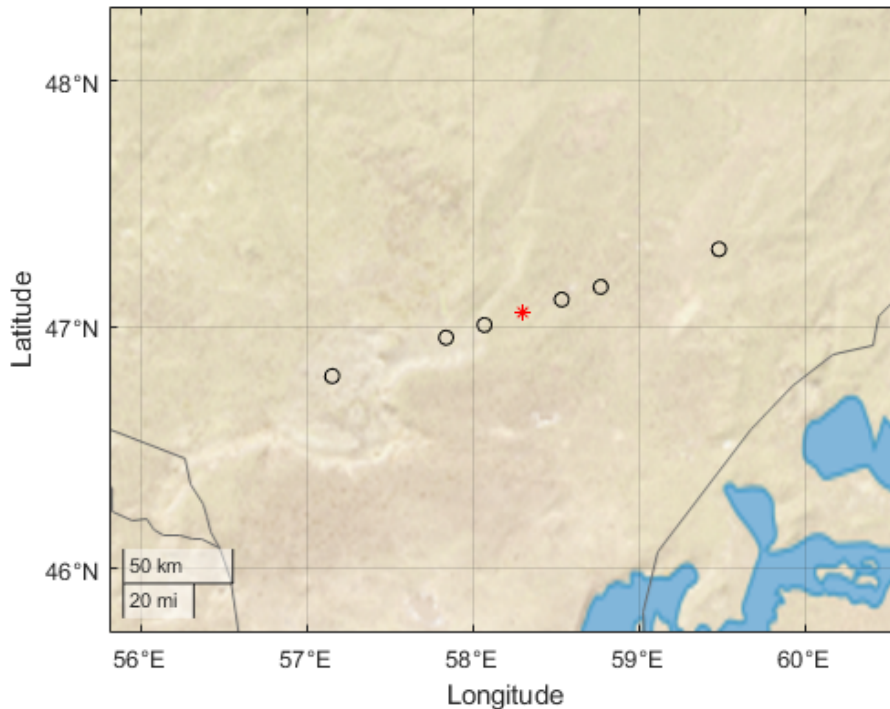
FIGURE 11.10: Δt De-Orbit burn error landing sites (in black) and
nominal landing site (in red)

with respect to an error in terms of ΔV provided.

Moreover, variations in terms of mechanical and thermal loads are negligible.

11.1.2   Landing Dispersion Analysis

During the re-entry phase, many types of uncertainties can affect the re-entry, in addition of the error caused by the de-orbit burn, causing it to deviate even more from the nominal trajectory. The main consequence of all of these uncertainties is landing dispersion, which results in a decrease in the chances of recovery of the capsule and an increase in the risks derived from its landing. A common way to evaluate the effects of these uncertainties on landing dispersions is to perform a

Δt Error	Downrange Displacement [km]	Max Heat Flux [kW/m^2]	Max Load Factor [g]
No Error	0	337.230	7.49
1s	11.766	334.312	7.49
-1s	-11.679	334.633	7.49
2s	23.552	334.151	7.49
-2s	-23.265	334.792	7.49
5s	59.555	333.666	7.48
-5s	-57.520	335.268	7.49

TABLE 11.4: Δt De-Orbit Burn error analysis results

Monte Carlo analysis.

Monte Carlo simulation is a statistical analysis tool, used to model the results of a process and their probabilities, consequently to the identification of random values for the considered uncertainties.

A Monte Carlo simulation can be described with three steps:

1. Sampling of input random variables

2. Numerical simulation

3. Results analysis
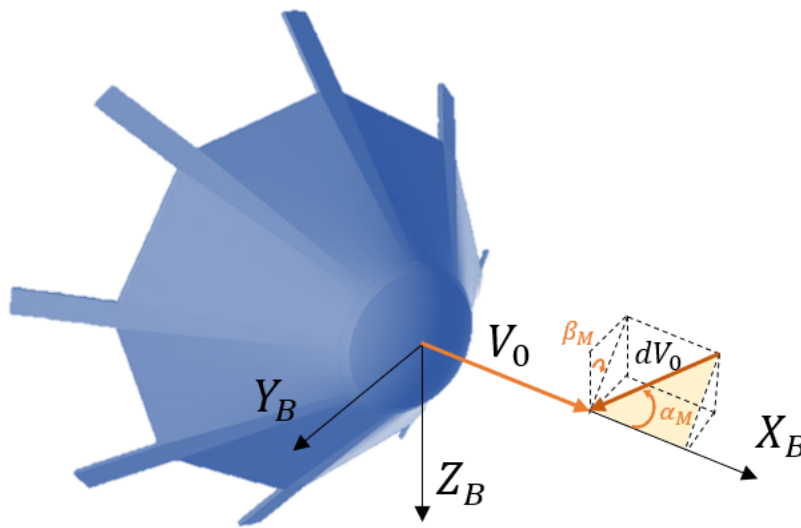
FIGURE 11.11: De-Orbit Burn misalignment

Uniform Distribution	Nominal Value	Min - Max
α_M [deg]	0	0; 5
β_M [deg]	0	0; 360
ΔV [m/s]	100	-1; +1
Gaussian Distribution	**Nominal Value**	3σ
m [kg]	48.04	± 1
C_D, C_L, C_Y	/	$\pm 10\%$
ρ [kg/m^3]	/	$\pm 10\%$

TABLE 11.5: Monte Carlo analysis uncertainties
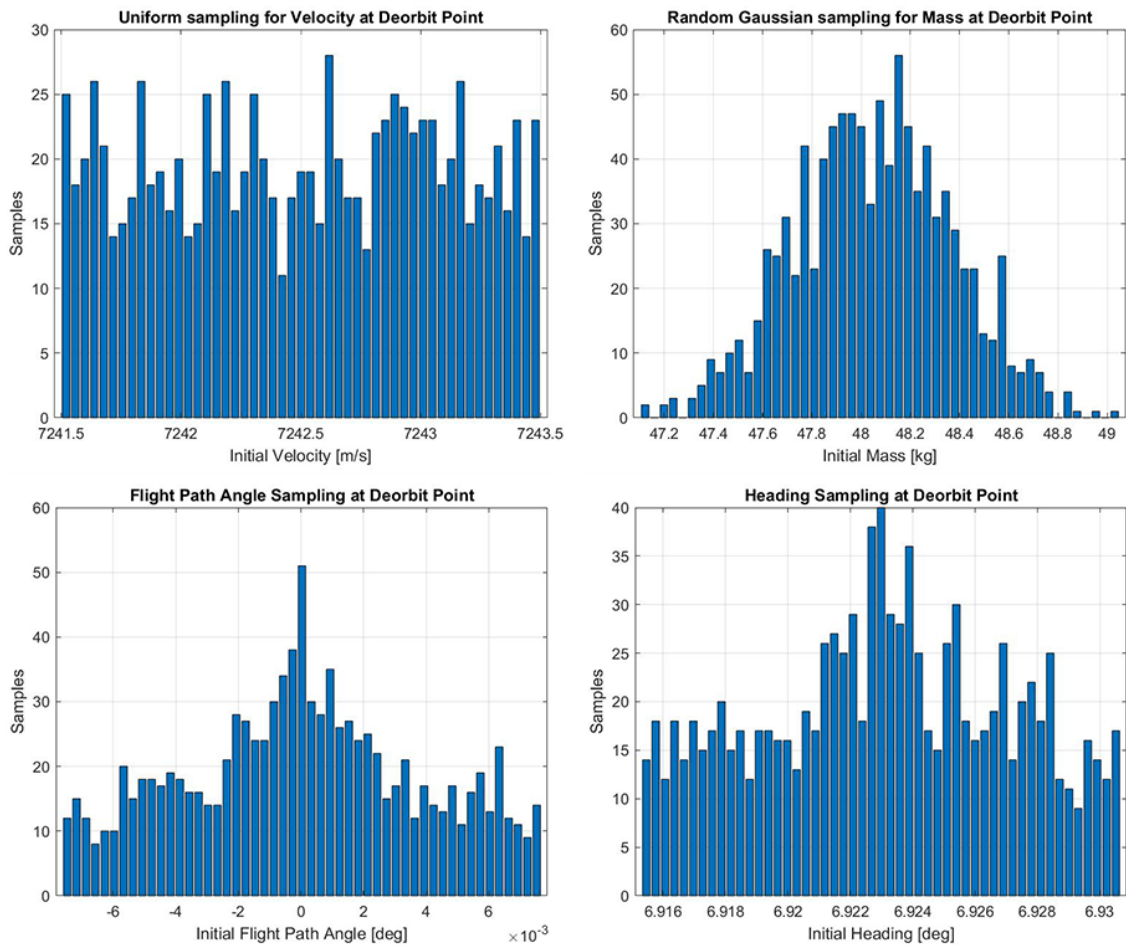
FIGURE 11.12: Uncertainties sampling related to a De-Orbit burn misalignment error

As regards the problem in examination, both environmental and vehicle-related uncertainties have been considered for the ballistic re-entry.

A normal distribution has been considered for air density, aerodynamic coefficients and for the spacecraft's mass uncertainties as found in literature [76]. A uniform distribution has been instead considered to be more conservative for the error in terms of ΔV provided and for the de-orbit burn direction misalignment uncertainties, as showed in Figure 11.11.

As regards the thruster misalignment, two angles have been identified in order to evaluate the de-orbit burn direction. Assuming the spacecraft's body axes are

aligned with the wind axes, and being V_0 the spacecraft's initial velocity, and dV_0 the ΔV module, α_M is the angle between the two velocity vectors and β_M is the angle between the dV_0 projection in the $Y_B - Z_B$ plane and the Z_B axis.

Assuming a uniform distribution for these two angles, flight path angle and heading angle have been derived through geometrical considerations.

Random distributions have been generated for all the variables, based on their average value and 3σ standard deviation for what concerns Gaussian distributions, and on the basis of maximum and minimum values for what concerns uniform distributions. All the distributions consist of 1000 samples.

These values are represented in Table 11.5 while the generated distributions are represented in Figure 11.12.

1000 preliminary simulations have been conducted based on the previously defined distributions, from the de-orbit to the entry interface at 120 km. Thus, state parameters have been evaluated at the entry interface, defined through the nominal entry point coordinates, and saved in order to perform the actual Monte Carlo simulations from this point to the Earth's surface.

Initial conditions evaluated at the entry point are represented in the Figure 11.13 and Figure 11.14.

The results of the Monte Carlo simulation are represented in Figure 11.15, Figure 11.16 and Table 11.6.

As can be noticed, due to the considered uncertainties, landing dispersions vary from 250 km short (landing before flying over the target) to over 250 km long (landing after flying over the target) during a ballistic re-entry.

It is also really interesting to see at the great variations in terms of downrange, load factor and heat flux showed in the cumulative plots in Figures 11.17 - 11.19.
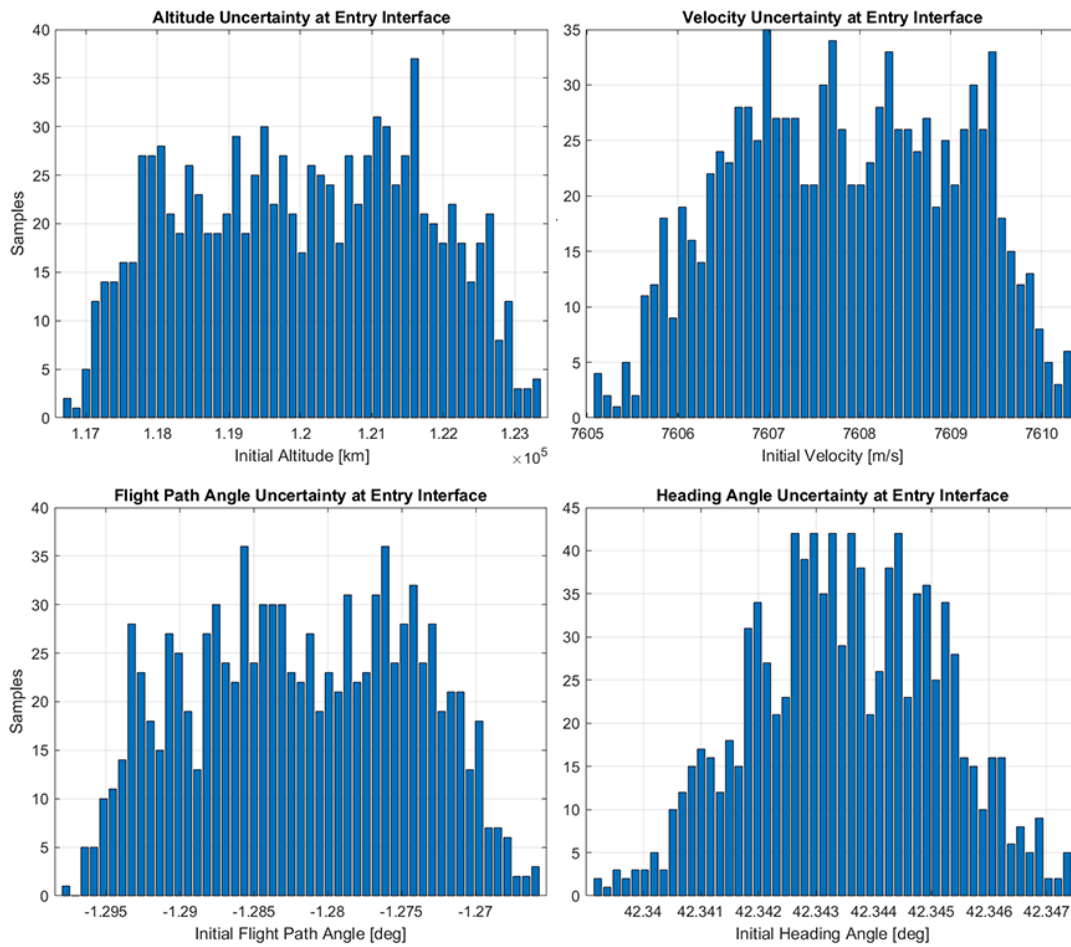
FIGURE 11.13: Uncertainties values at the Entry Interface
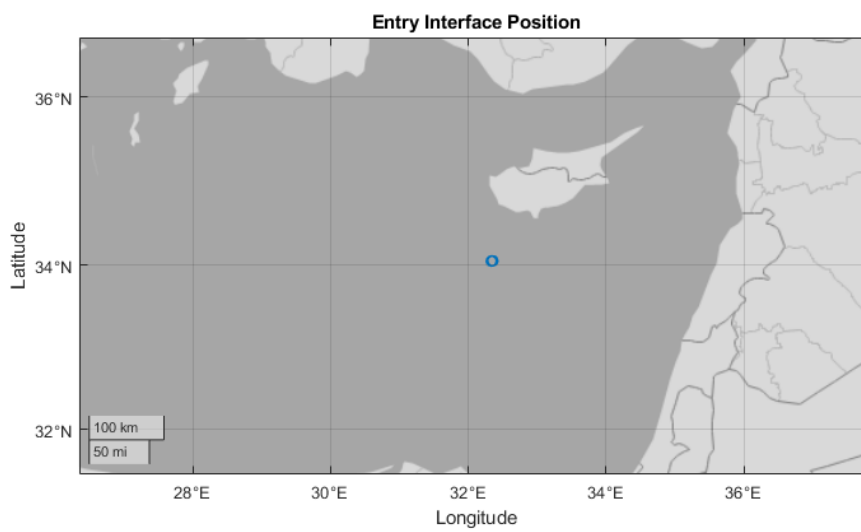
FIGURE 11.14: Entry Interface Position
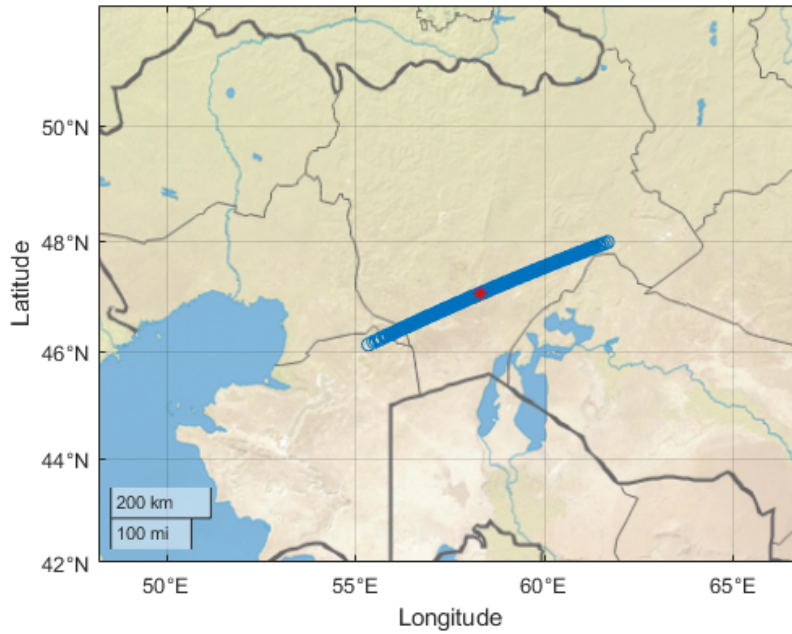
FIGURE 11.15: Monte Carlo Simulation Landing Dispersion Points
for an Uncontrolled Trajectory
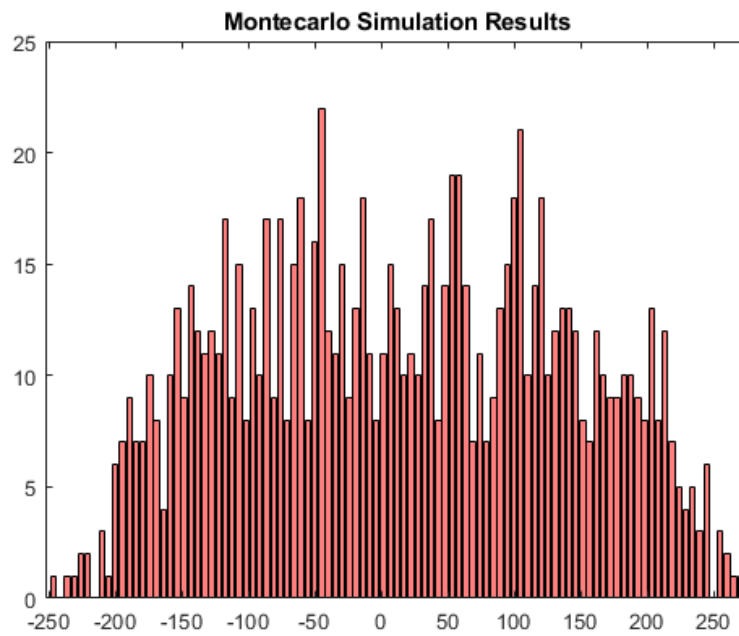
FIGURE 11.16: Landing Dispersion Distributions in [km] for an Un-
controlled Trajectory

Distance from Target	Ballistic Re-entry
Mean [km]	20
Standard Deviation [km]	120

TABLE 11.6: Monte Carlo Simulation Results
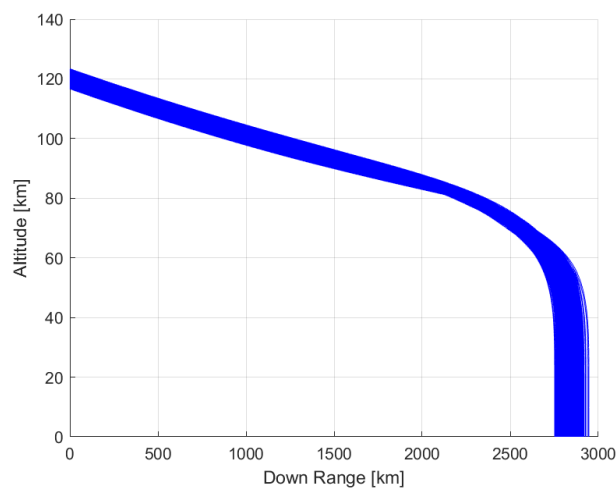
FIGURE 11.17: Cumulative Plot of Altitude vs. Down Range for the Monte Carlo Simulation
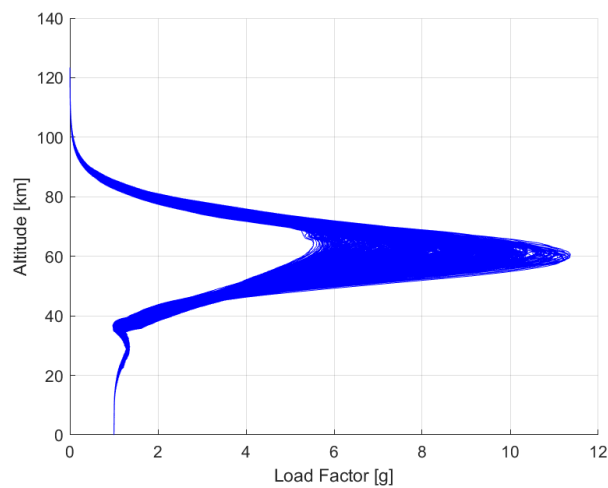
FIGURE 11.18: Cumulative Plot of Altitude vs. Load Factor for the Monte Carlo Simulation
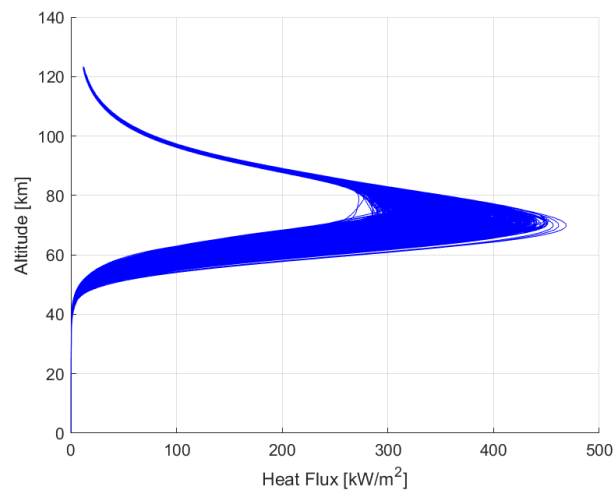
FIGURE 11.19: Cumulative Plot of Altitude vs. Heat Flux for the
Monte Carlo Simulation

11.1.3 Case Specific Simulation Results

Starting from the nominal trajectory, presented at the beginning of this chapter, different analysis were conducted in order to evaluate the performances of the control system in guiding the spacecraft toward the target in presence of some error.

Two simulations were done, concerning two off-nominal conditions:

- The case 1 regards an off-nominal condition where the capsule lands around 100 km before the target

- The case 2 regards an off-nominal condition where the capsule lands around 100 km after the target

The analysis were conducted evaluating the state parameters value at the Entry Interface, since at 120 km the atmosphere is sufficiently dense for the aerodynamic control to be effective. The Initial Conditions at the Entry Interface, derived from the previously introduced re-entry trajectory from ISS, are resumed in Table 11.7.

Two auxiliary variables have been introduced in order to characterize the non-nominal trajectories. As shown in Figure 11.8 they are the distances X_D and Y_D, which are the downrange and the cross range of the trajectory respectively.

In order to determine these two distances, the initial great circle must be defined first. It is the intersection of the Earth and a plane that passes through its centre and is defined by the EI(θ_0, ϕ_0) point and the capsule initial heading ψ_0. The cross range is the perpendicular distance from the target to the initial great circle measured on the Earth surface. Downrange is the distance along the initial great circle from the initial point to the one at which cross range is measured.

 Case 1 The first considered case displacements on the initial condition are resumed in Table 11.9, with the values for the downrange ad the cross range. The

Altitude [m]	120000
Velocity [m/s]	7607.889
Heading [deg]	42.340
Flight Path Angle [deg]	-1.281
Latitude [deg]	34.056
Longitude [deg]	32.353

TABLE 11.7: Nominal initial conditions at the Entry Interface
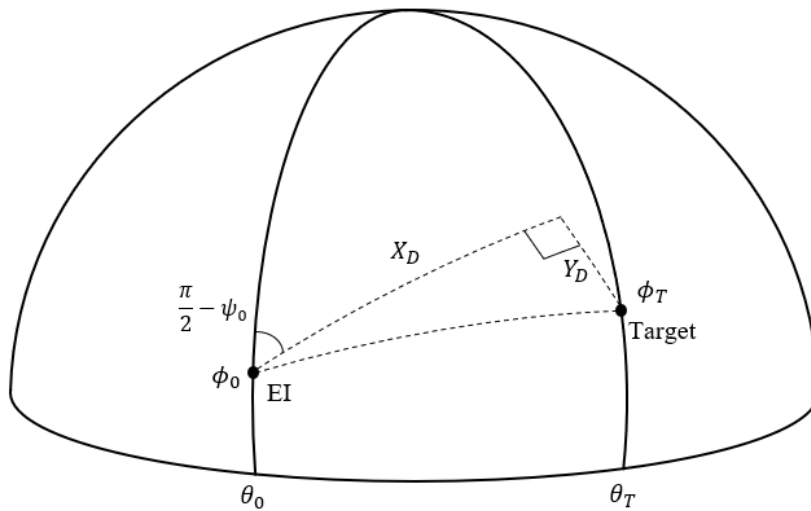
TABLE 11.8: Downrange and cross range definition

simulated trajectories are represented in Figure 11.20. The simulation main results are reported in Table 11.10, while a zoomed view of the landing sites is represented in Figure 11.21. It can be noticed how the displacement at landing site can be reduced to one quarter using the control system.

In the Figures 11.22 - 11.25 the values of Velocity, Altitude, Flight Path Angle and Range-to-go with respect to the time are shown. It can be noticed how the controller follows the reference state with respect to the uncontrolled case.
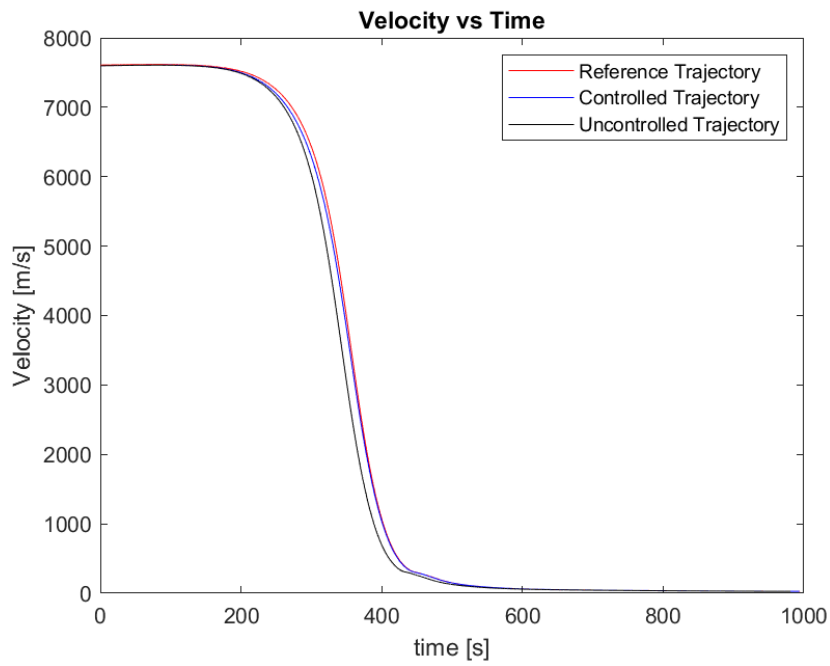
FIGURE 11.22: Velocity vs. Time for the reference, controlled and uncontrolled trajectories
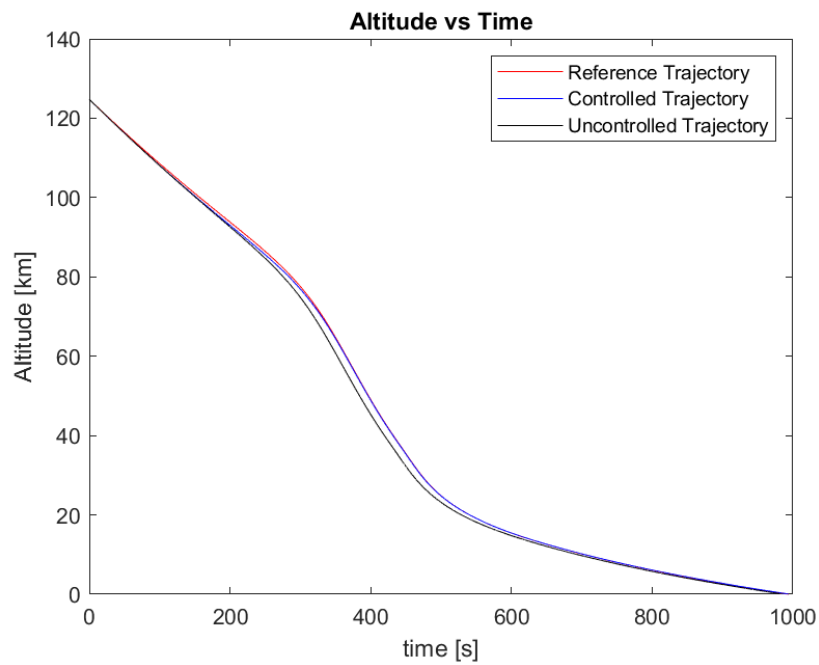
FIGURE 11.23: Altitude vs. Time for the reference, controlled and uncontrolled trajectories
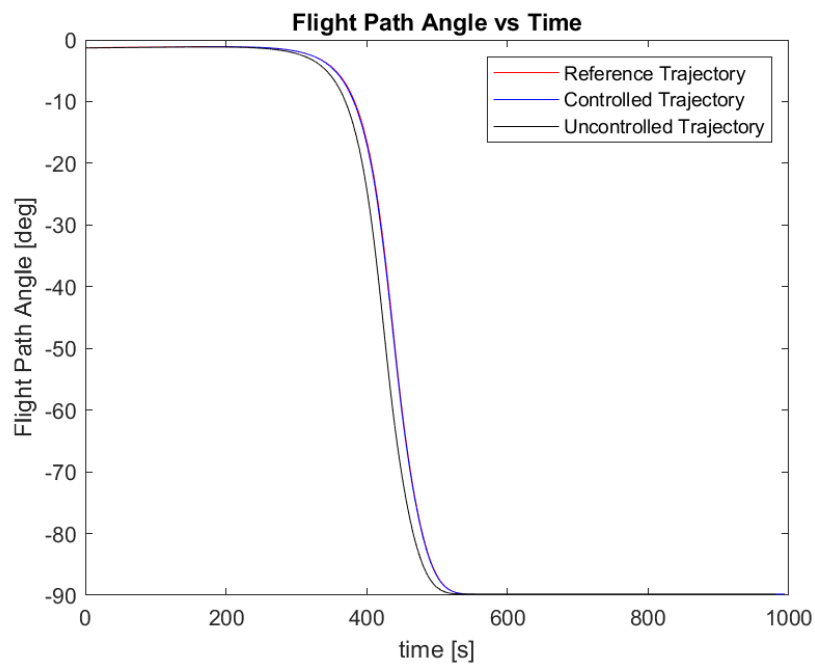
FIGURE 11.24: Flight Path Angle vs. Time for the reference, controlled and uncontrolled trajectories
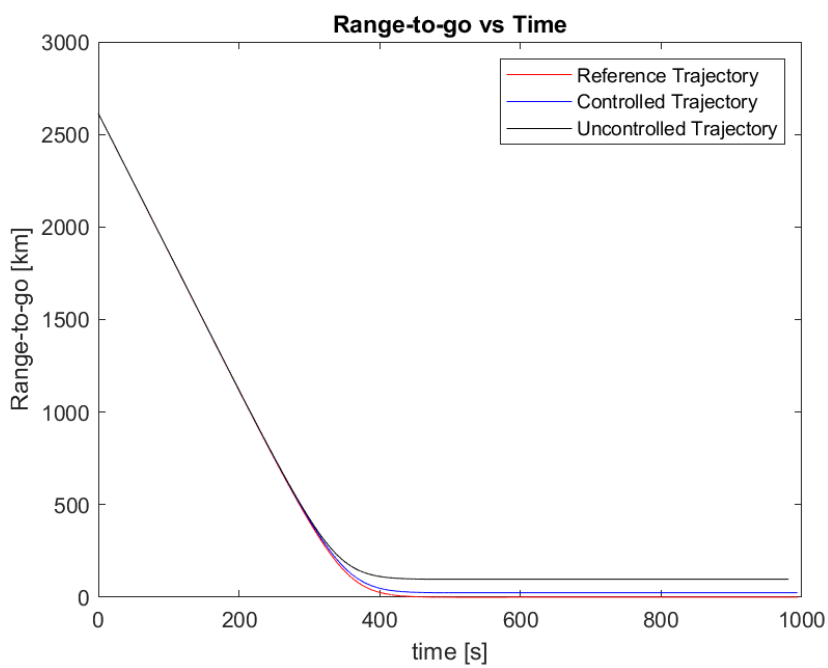
FIGURE 11.25: Range-to-go vs. Time for the reference, controlled and uncontrolled trajectories

Velocity Error [m/s]	-10
Heading Error [deg]	-0.2
Flight Path Angle Error [deg]	-0.03
X_D **[km]**	2613
Y_D **[km]**	36

TABLE 11.9: Displacement of the initial condition for the falling short trajectory
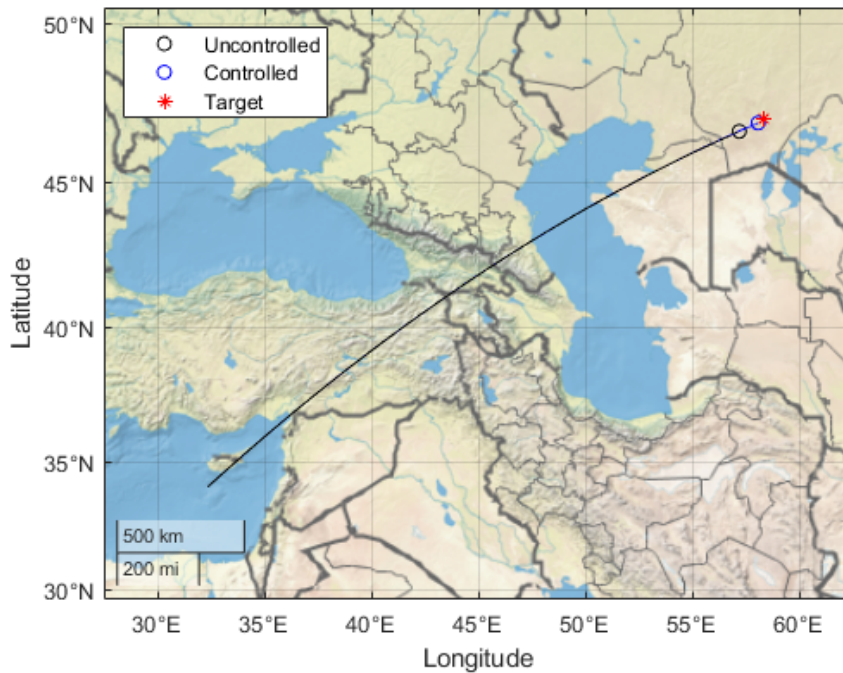
FIGURE 11.20: Uncontrolled (in black) and Controlled (in blue) trajectories for the falling short case

It can be interesting to analyse the control law for the trajectory, shown in Figure 11.26. The controller only works during about the first half of the trajectory, until the Flight Path Angle is larger than 85° and the capsule is in free fall.

The control law is piecewise linear both for α and β, roughly during the first 100

	Distance from Target [km]
Uncontrolled	100
Controlled	23

TABLE 11.10: Simulation Results for the falling short case
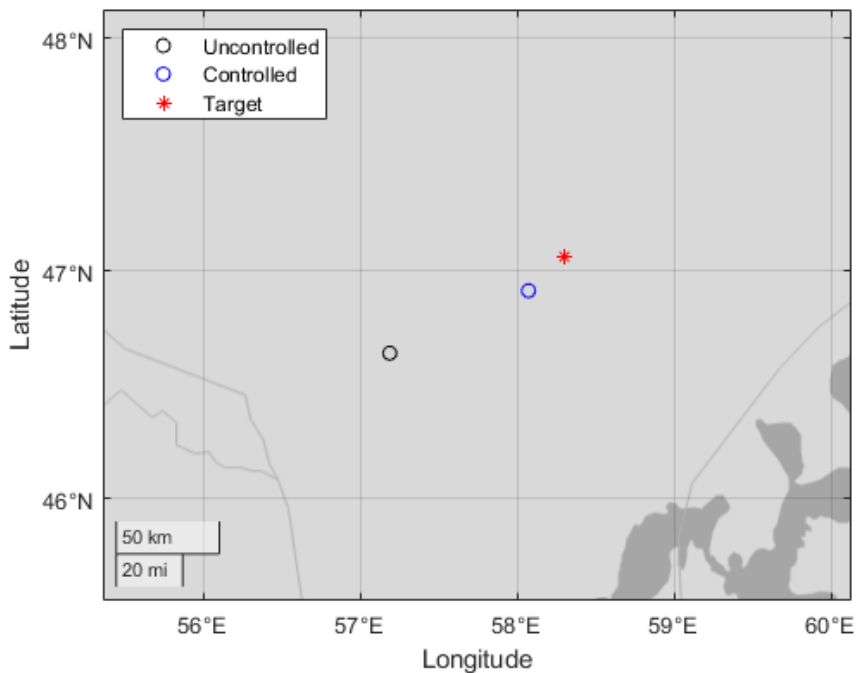
FIGURE 11.21: Landing sites for the falling short case

seconds of the simulation and is linear for the rest of the simulation. The first part indicates the controller saturation.

Analyzing Figure 11.27, where the control laws for α and β are shown separately, it can be clearly noticed how for the first part of the trajectory the controller is in saturation, following the logic presented in Chapter 6.3.2. The piecewise linear behaviour is justified by the change in the Mach number (which is increasing in the first part of the trajectory) and by the saturation logic linking the couple of values of α and β.
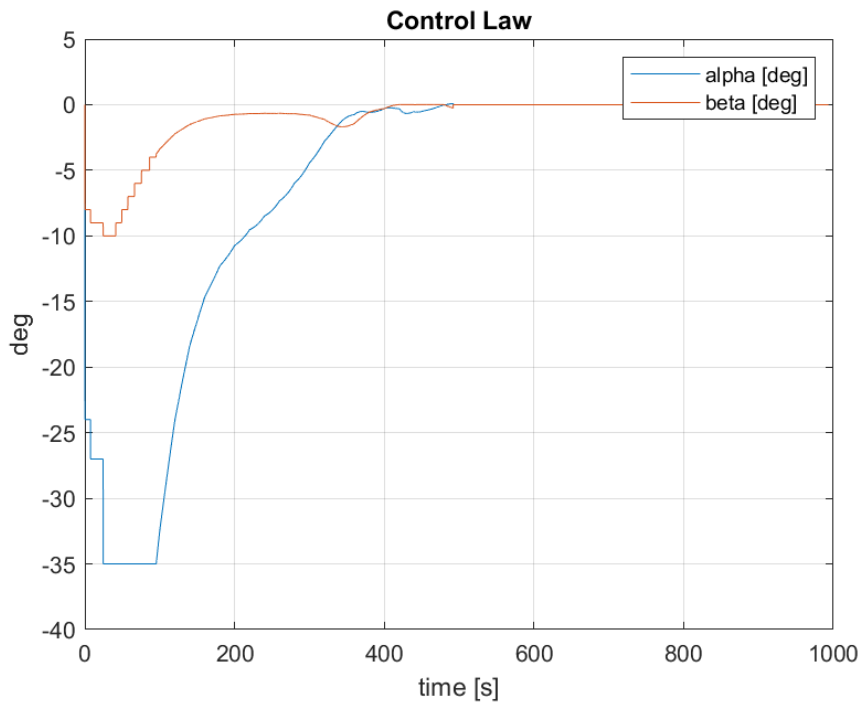
FIGURE 11.26: Control law for the falling short case

Once out of saturation, the control law becomes linear and approaches zero since the state error tends to zero too, as shown in the previous figures.

The sign of the commanded angles can be discussed too. According to the sign convention, previously presented in Figure 6.4, a negative α value is related to a positive C_L value and this is justified by the fact that the capsule is falling short and the trajectory must be corrected with a positive lift in order to decrease the displacement at landing site.

Similarly, a negative β value is related to a negative C_Y value, which generates a force pointing toward the left side of the capsule, correcting the error on the heading angle.

Every attitude condition is associated to a set of deflections for the eight flaps, according to the minimum drag optimization logic introduced in Chapter 6.3.2. In Figure 11.28 the deflection history for every flap is represented and the flaps
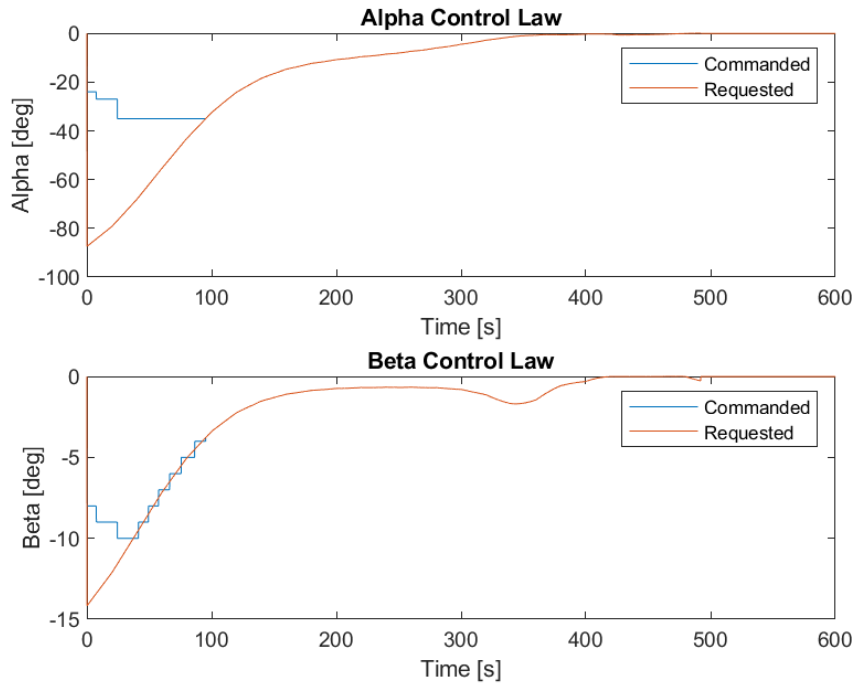
FIGURE 11.27: Control law for α and β, showing commanded and
requested angle values

are enumerated clockwise starting from the upper one on the Z_B axis (see Figure
6.5).

Flaps 4, 5 and 6 deflection brings a negative α angle contribution, while flaps 2, 3
and 4 bring a negative β angle contribution. In fact, it can be noticed that flaps 4,
5 and 6 are saturated for the first part of the control law, as well as flaps 3 and 4.

Some actuators, as flap 3 and 5, just produce contribution for the lateral and for
vertical control respectively. Instead, the flaps which are not disposed along the
body axis, produce contribution for both the control angles. The resulting deflec-
tion histories are given by the balance of all the contributions.

Flap 5 is the main contributor in α, which is the more demanding control action,
while the β contribution is given by flap 3 and by the balancing of the other flaps.

Flaps 1, 2, 7 and 8 are always kept folded inward, in idle position, since their ac-
tion is not required for the commanded attitude and this way the produced drag
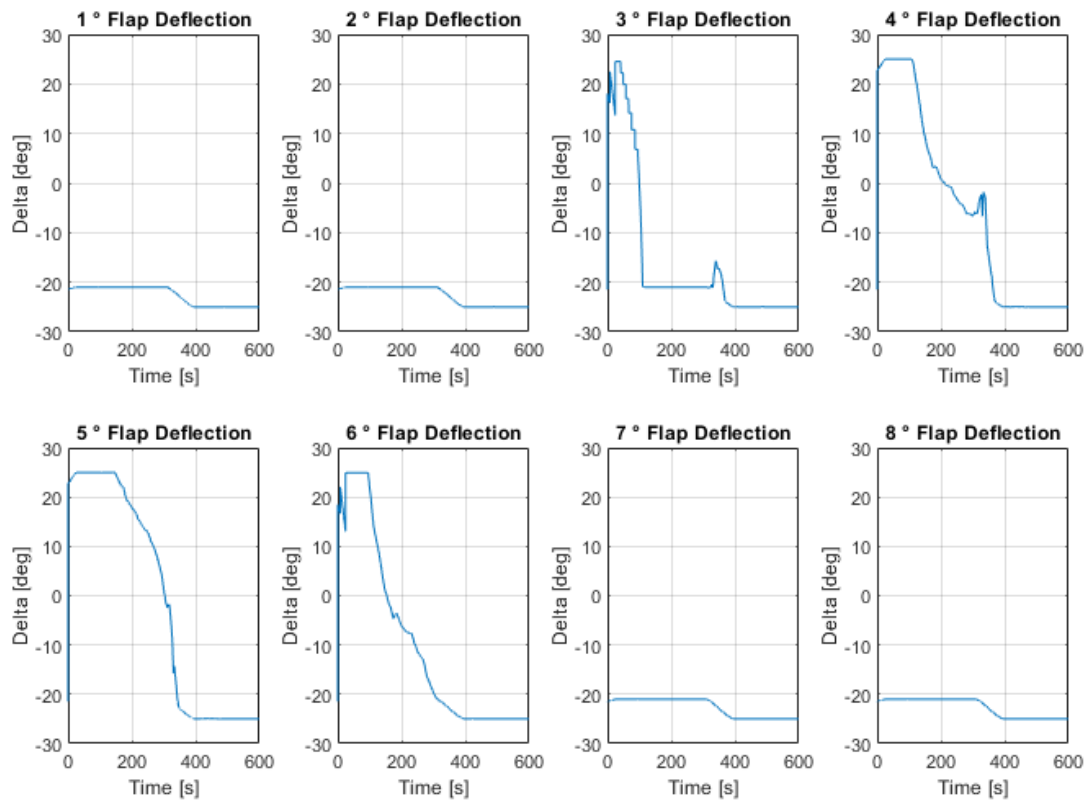
FIGURE 11.28: Control law for α and β, showing commanded and requested angle values

is minimized.

Velocity Error [m/s]	10
Heading Error [deg]	0.2
Flight Path Angle Error [deg]	0.03
X_D **[km]**	2613
Y_D **[km]**	52

TABLE 11.11: Displacement of the initial condition for the falling long trajectory
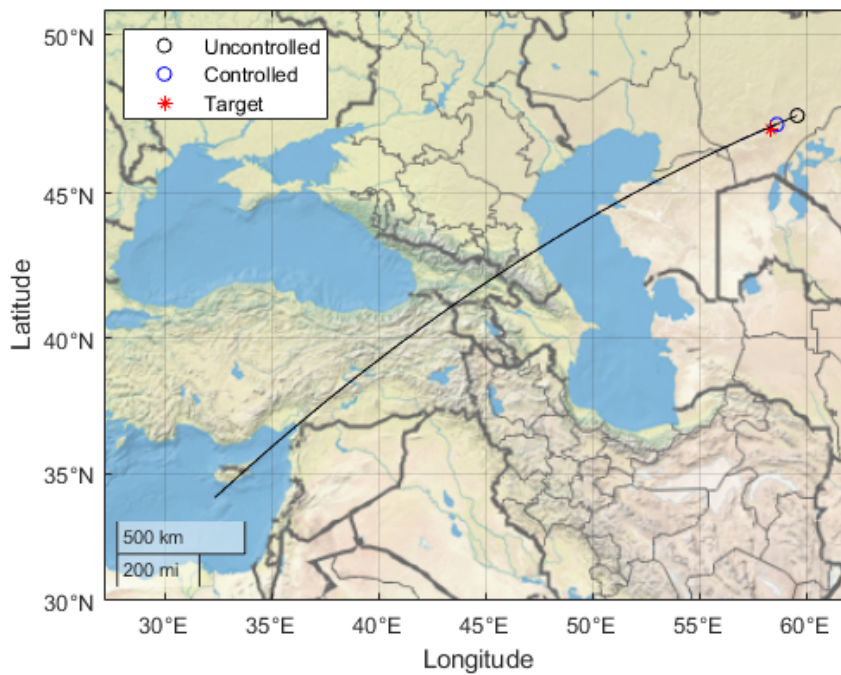
FIGURE 11.29: Uncontrolled (in black) and Controlled (in blue) trajectories for the falling long case

	Distance from Target [km]
Uncontrolled	110
Controlled	29

TABLE 11.12: Simulation Results for the falling long case
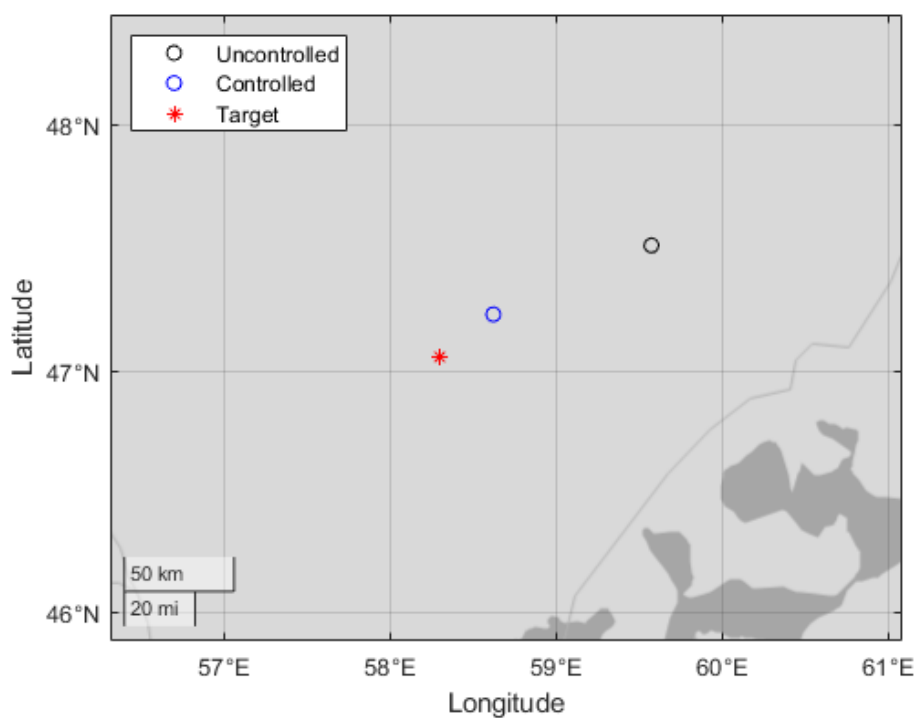
FIGURE 11.30: Landing sites for the falling long case

Case 2 The displacements for the initial conditions of the second considered case are resumed in Table 11.11. The controlled and the uncontrolled trajectories are represented in 11.29. The simulation main results are resumed in 11.12, while a zoomed view of the landing sites is represented in 11.30. As for the previous case, the displacement is roughly reduced to one quarter through the action of the control system. In the Figures 11.31 - 11.34 the values of Velocity, Altitude, Flight Path Angle and Range-to-go with respect to the time are shown. The reference
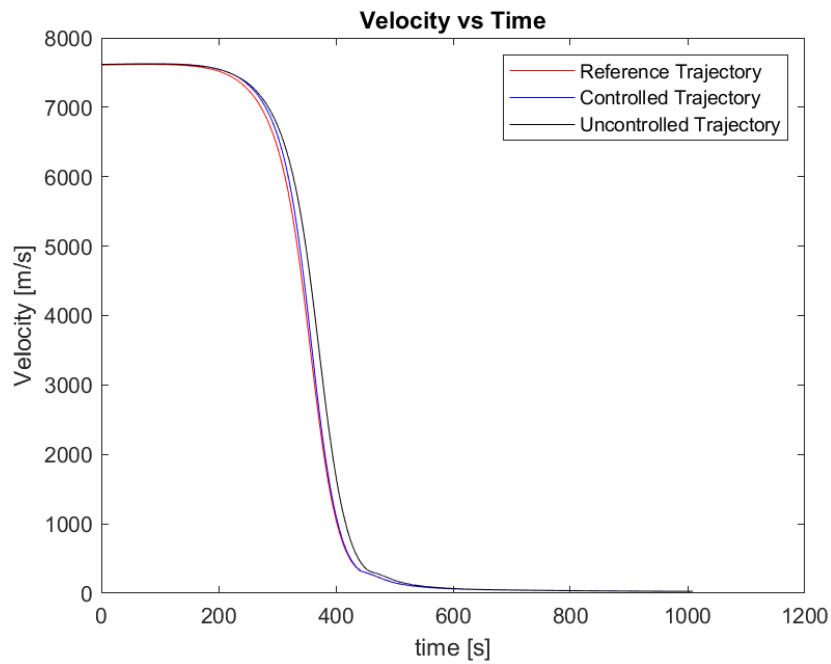
FIGURE 11.31: Velocity vs. Time for the reference, controlled and
uncontrolled trajectories
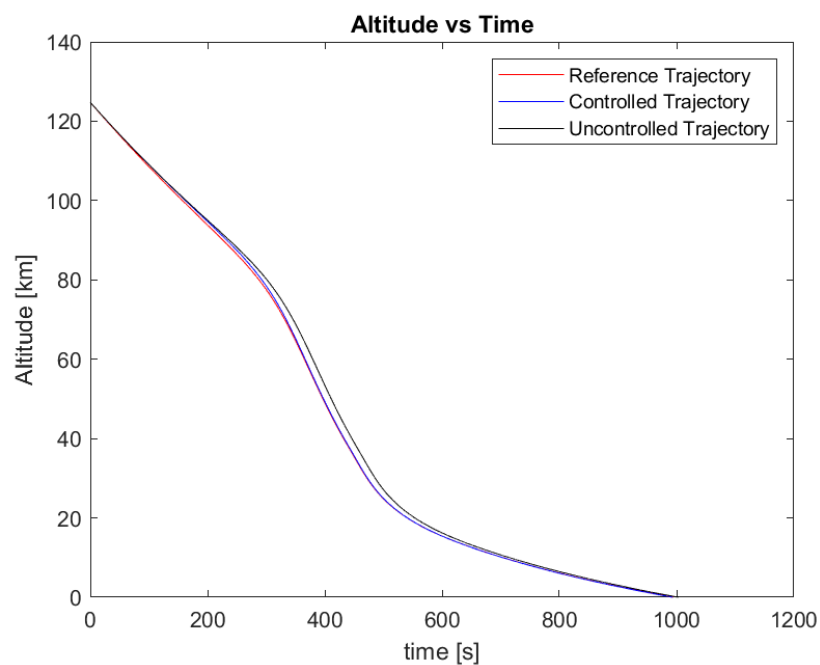
FIGURE 11.32: Altitude vs. Time for the reference, controlled and
uncontrolled trajectories
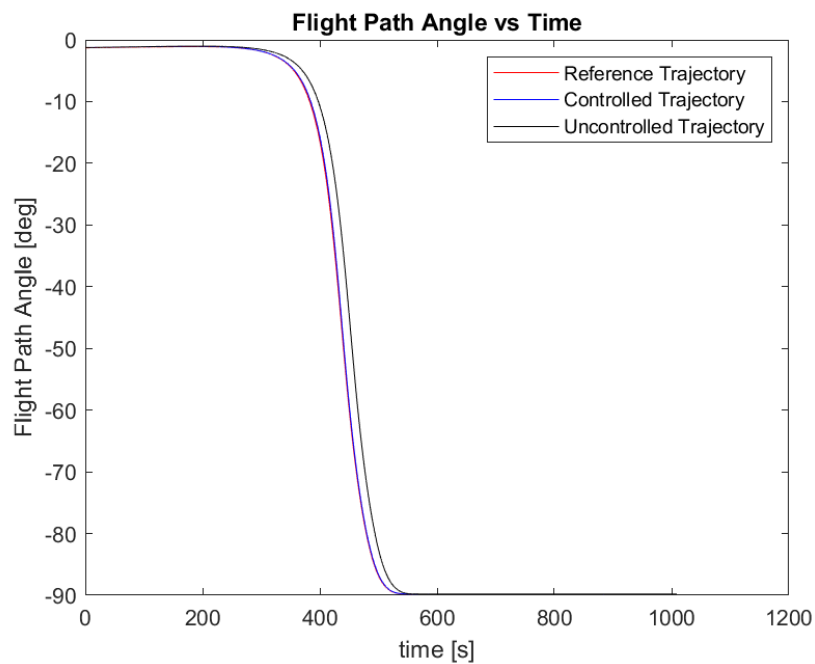
FIGURE 11.33: Flight Path Angle vs. Time for the reference, controlled and uncontrolled trajectories
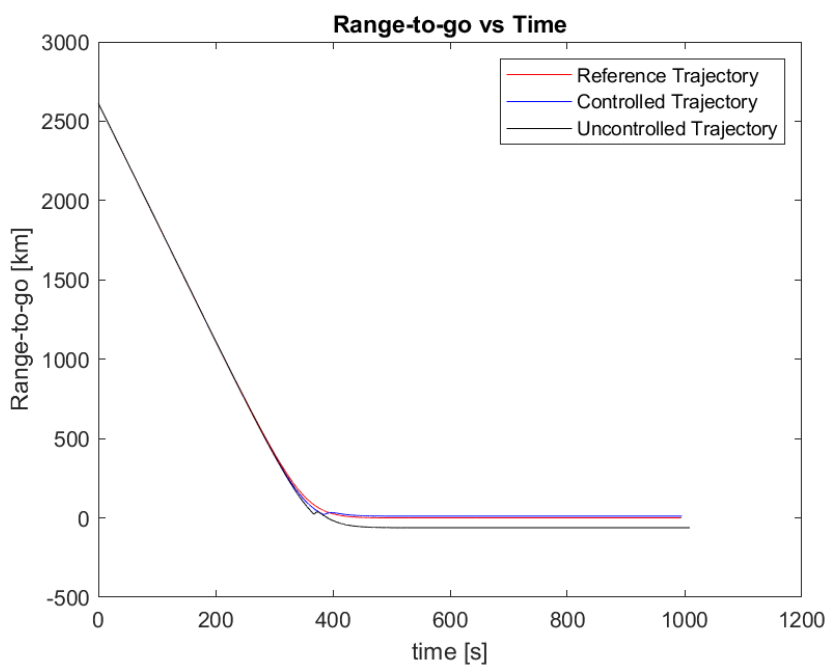
FIGURE 11.34: Range-to-go vs. Time for the reference, controlled and uncontrolled trajectories
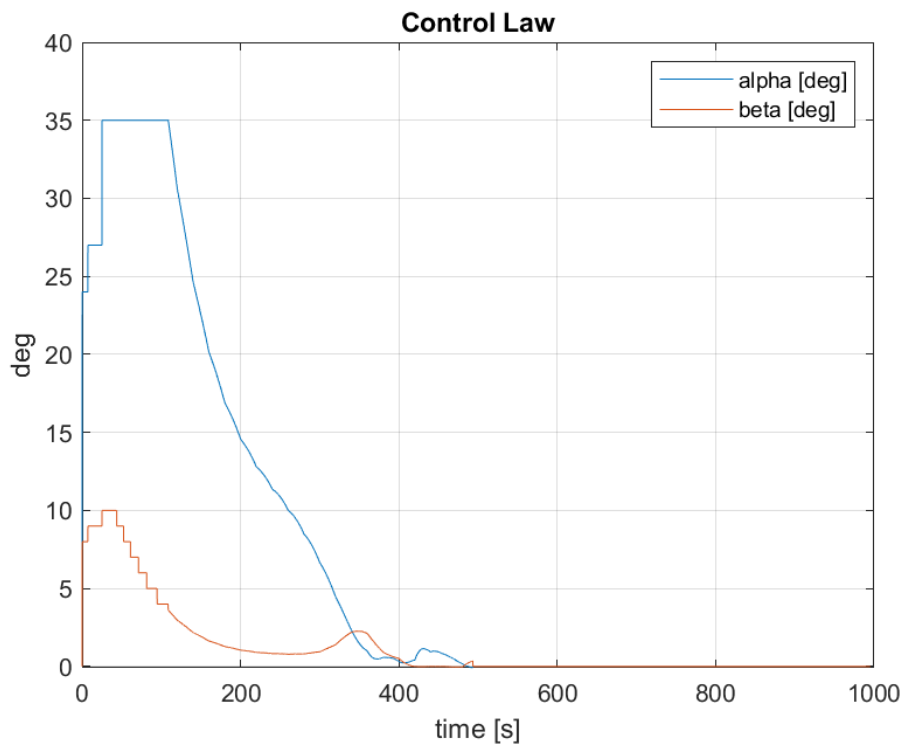
FIGURE 11.35: Control law for the falling long case

state is followed by the controller and the error on the state is greatly reduced with respect to the uncontrolled state.

The control law of the controlled trajectory is shown in Figure 11.35. As for the first case, the controller works only for the first half of the trajectory, until the capsule is in free fall.

The first part of the control law is piecewise linear, both for α and β, since the error on the state is large and the controller is saturated. Once out of saturation the control laws become linear and tends to zero with the state error. The saturation, and the difference between the commanded and the requested attitude angles for the first part of the simulation, is clearly showed in 11.36.

It can be noticed how, differently than the previous case, positive values for α and β are commanded this time, and it is compatible with the introduced sign
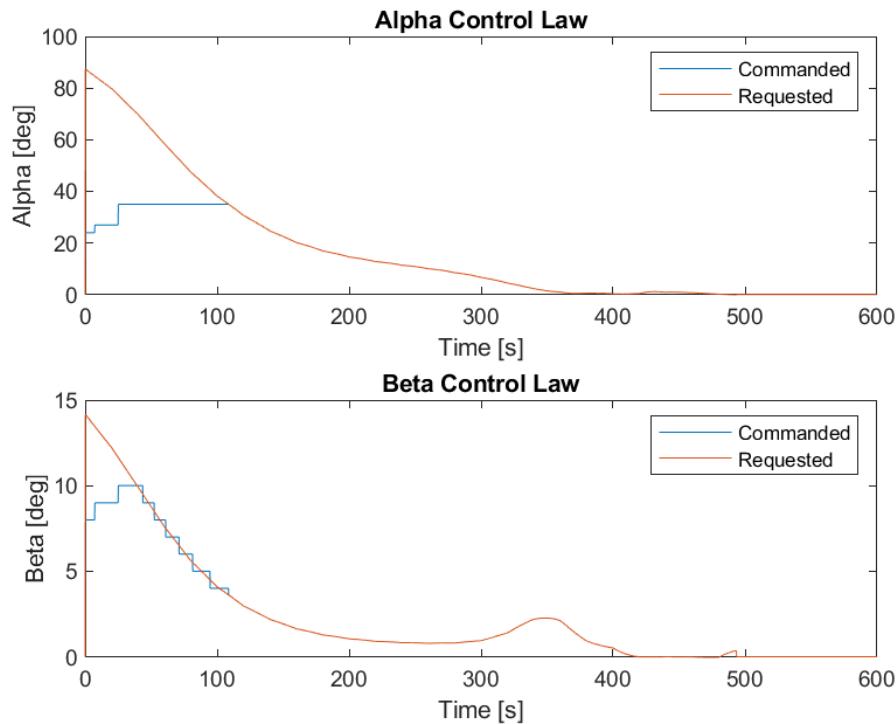
FIGURE 11.36: Control law for α and β, showing commanded and requested angle values

convention. In fact, a positive α value is related to a negative C_L value, which produces a negative lift, necessary in order to correct the trajectory since the capsule is falling long.

Analogously, a positive value for β is related to a positive C_Y values, which generates a force pointing toward the right side of the capsule, correcting the error on the heading angle.

In Figure 11.37 the deflection history for every flap is shown. Flaps 1, 2 and 8 produce positive α contributions, while flaps 6, 7 and 8 produce positive β contributions. However, flap 2 produces negative β contributions too, as flap 6 produces negative α contributions too.

As can be noticed, flaps 1, 2, 7 and 8 are saturated for the first part of the trajectory and decrease differently depending on the requests of the controller. A spike
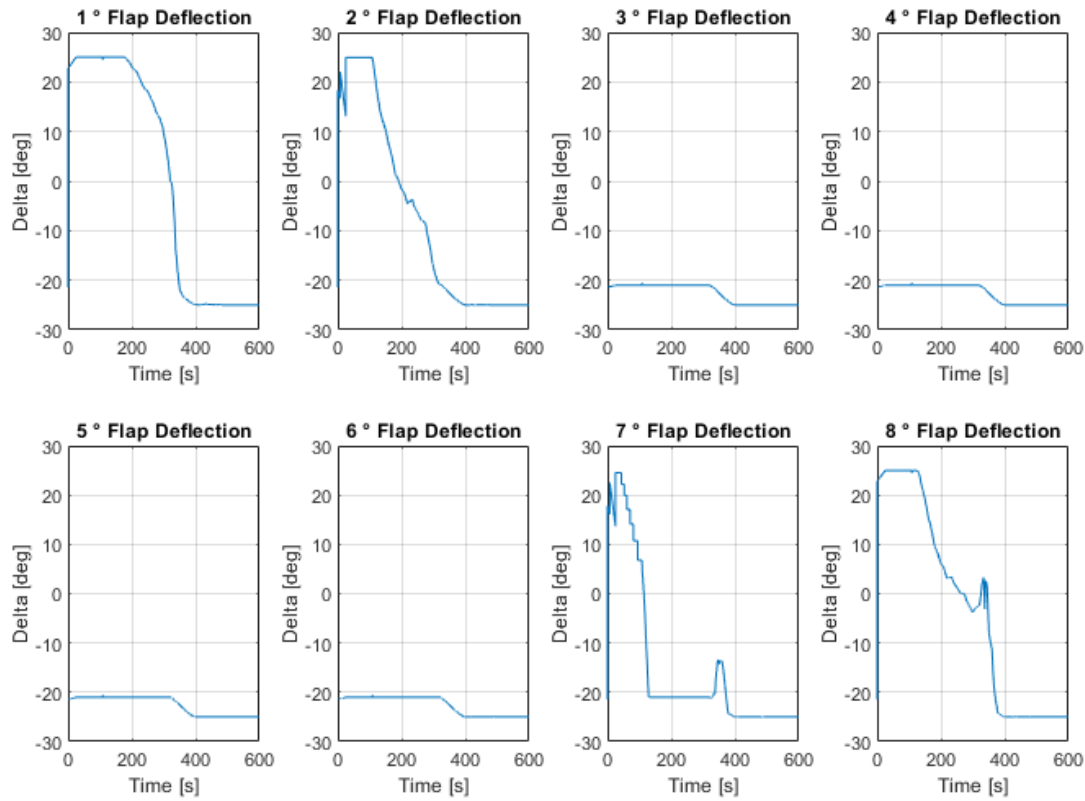
FIGURE 11.37: Control law for α and β, showing commanded and
requested angle values

for flaps 7 and 8 can be noticed between 300 and 400 seconds, in relation with the
request in β from the controller.

Flaps 3, 4, 5 and 6 are not used for this case off-nominal conditions.

11.1.4 Control System Performances

With reference to the Monte Carlo Analysis presented at the beginning of this
chapter, for which a misalignment and an error in magnitude for the de-orbit
burn was considered, another simulation was run in order to evaluate the perfor-
mances of the controller action.

In Figure 11.38 are represented the landing sites for the uncontrolled and for the

controlled case, with respect to the desired target. It can be noticed how the use of the controller system reduces the dispersions around the desired target.

Analysis main results are presented in Table 11.13 and Figure 11.39. It is shown how standard deviation of the displacement is reduced almost to one quarter.

A second Monte Carlo simulation have been run with more severe uncertainties values found in literature. These values are resumed in Table 11.14. A Gaussian distribution was generated for each considered parameter. More critical values for Flight Path Angle and Heading uncertainties have been set, with respect to most of the literature references (which are usually between $0.05°$ and $0.1°$) in order to evaluate the controller performance in worse cases. The uncertainties for the other values are compatible with literature references [142] [143]. In Figure
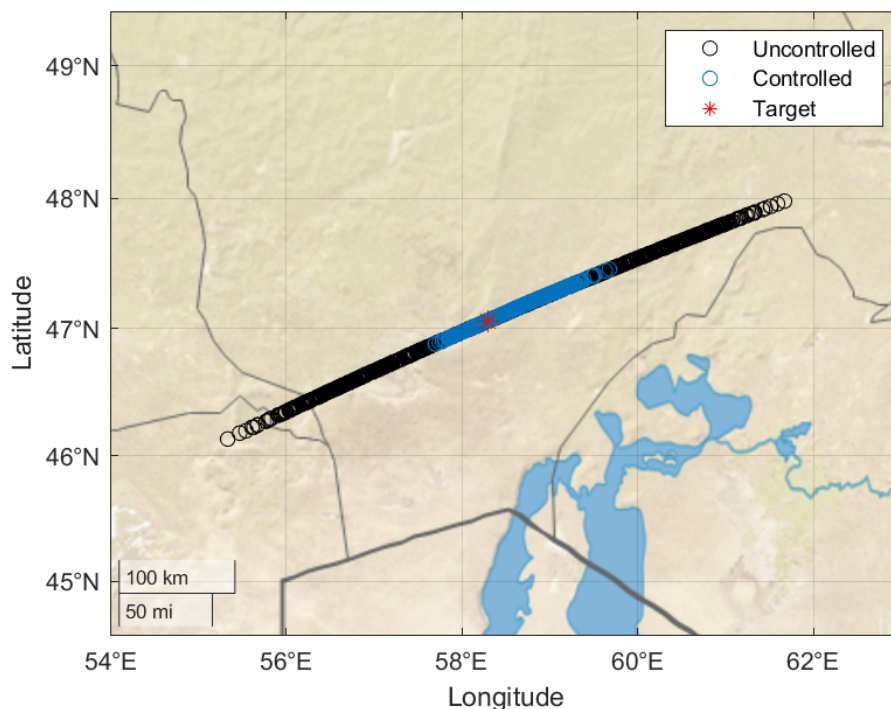
FIGURE 11.38: First Monte Carlo Analysis landing sites: uncontrolled (in black), controlled (in blue) and target (in red)

	Uncontrolled	Controlled
Mean [km]	16	11
Standard Deviation [km]	121	35

TABLE 11.13: First Monte Carlo analysis main results
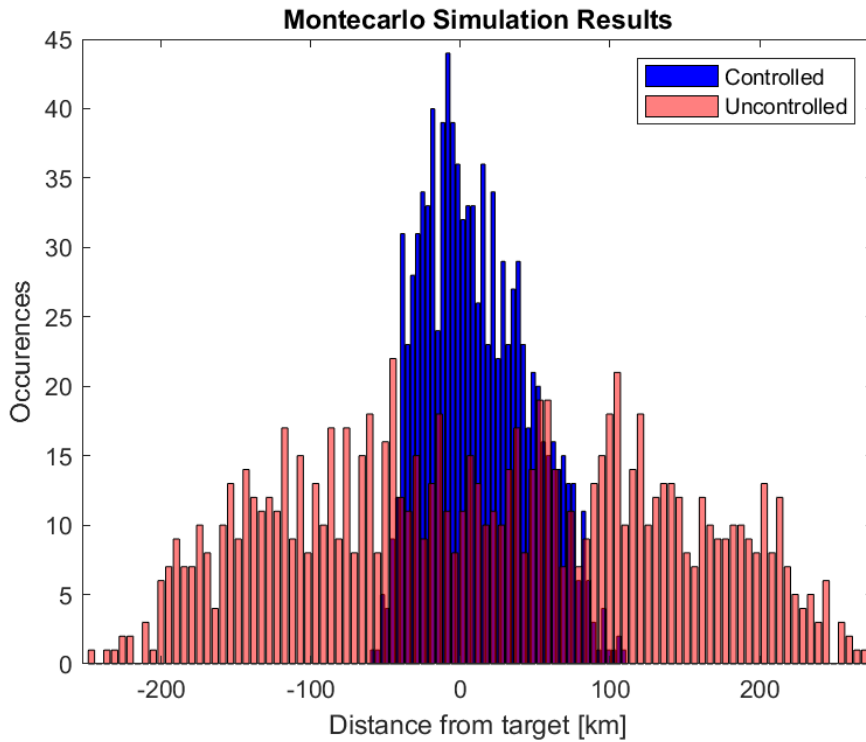
FIGURE 11.39: First Monte Carlo landing dispersions

11.15 are represented the landing sites for the uncontrolled and for the controlled case, with respect to the desired target. Analysis main results are presented in Table 11.16 and Figure 11.40. It is shown how standard deviation of the dispersion at landing site is greatly reduced.

Gaussian Distribution	Nominal Value	$3 - \sigma$ Variance
V [m/s]	7607.889	10
h [m]	120000	500
γ [deg]	-1.281	0.3
ψ [deg]	42.340	0.3
m [kg]	48.04	1
C_D, C_L, C_Y	/	10 %
ρ [kg/m^3]	/	10 %

TABLE 11.14: Second Monte Carlo uncertainties
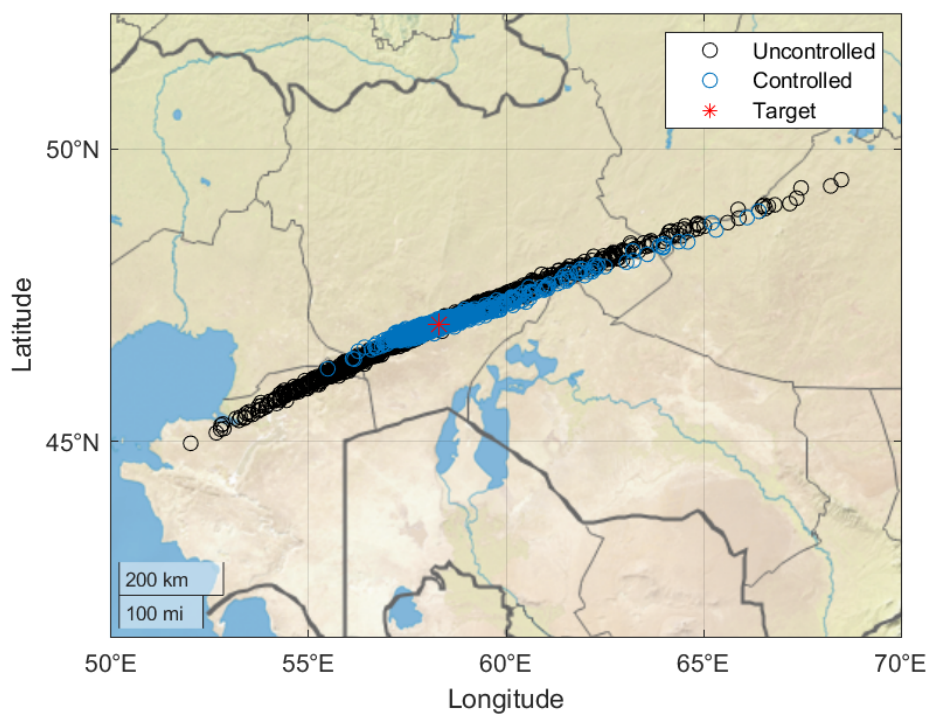
TABLE 11.15: First Monte Carlo Analysis landing sites:
uncontrolled (in black), controlled (in blue) and target (in red)

	Uncontrolled	Controlled
Mean [km]	12	5
Standard Deviation [km]	215	90

TABLE 11.16: Second Monte Carlo analysis main results
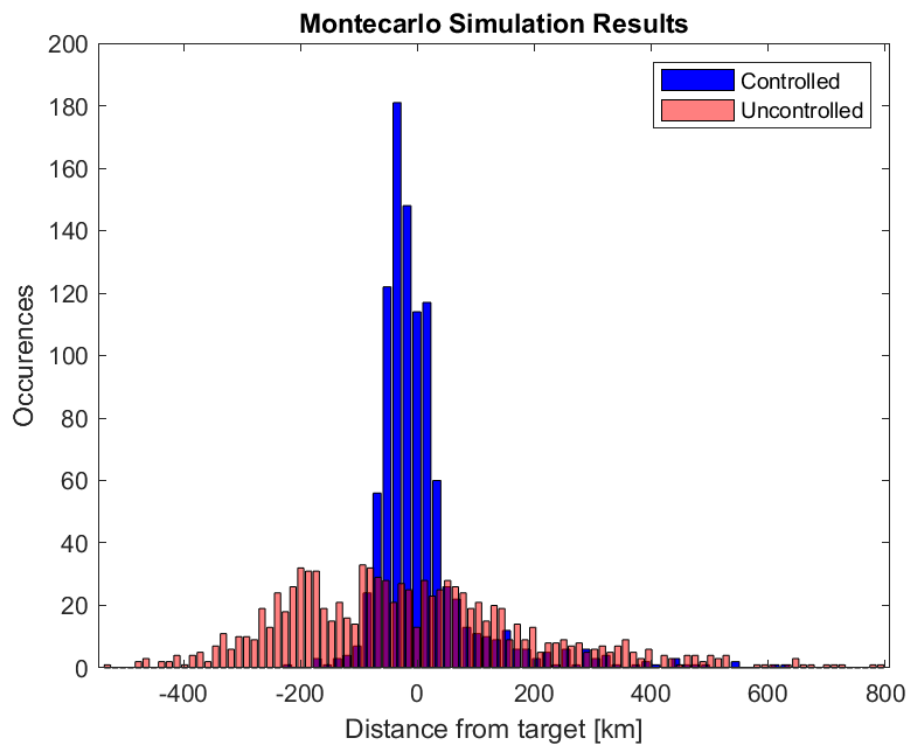
FIGURE 11.40: Second Monte Carlo landing dispersions

11.2 Ground Targeting Simulation and Performance Evaluation

In this section, the results of Monte Carlo analysis conducted to verify the performances of the guidance and control algorithms for ground targeting are presented. The reference mission scenario is the same presented in the previous section, with the only difference that the micro satellite will not use chemical propulsion for de-orbiting. It will use an heat shield that can be repeatedly deployed and retracted on-orbit to provide drag modulation and orbital maneuvering capabilities and small movable flaps used to control the lift/drag ratio and the direction of the lift vector for maneuvering during the re-entry.

11.2.1 Guidance Algorithm Performance

Five hundred Monte Carlo simulations of the guidance generation algorithm, presented in Sec. 6.2.1 , were conducted to verify the ability to calculate an achievable drag profile and corresponding trajectory that if followed, will allow the spacecraft to re-enter in a desired location. The initial conditions and epoch were randomly chosen for each run. The initial epoch of each simulation was randomly selected from within an eleven year period corresponding to a complete solar activity cycle that could affect the density and hence the time of decay of the satellite. All guidance tracking simulations were run assuming that the maximum C_b achievable by the spacecraft was a factor of 1.5 greater than the maximum allowable guidance C_b and the minimum achievable C_b was a factor of 1.5 less than the smallest allowable guidance C_b. This ensured that there would always be a sufficient Cb margin to correct for the simulated drag uncertainties and any tracking errors would be a result of suboptimal controller performance

rather than a complete saturation of the actuator. In Figure 11.41, a map with the landing locations of the simulated trajectories is shown.
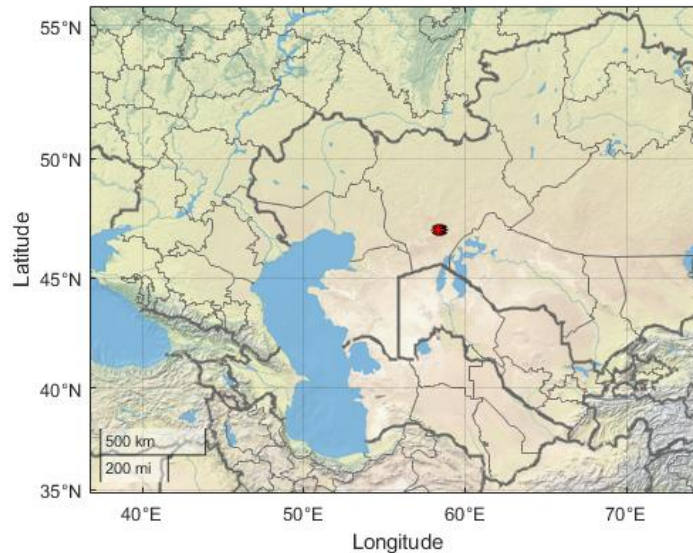
FIGURE 11.41: Guidance Algorithm Performance: Dispersion on Ground

Note that in one hundred percent of the cases the error is below 20 km and in 73.2% of the cases the error is below 10 km (Figure 11.42). The average error is 7.146 km and the standard deviation is 4.05.

The overall mission duration varied between fifty and three hundred days (see Figure 11.43) depending on the simulation epoch. This is because density can vary by up to two orders of magnitude at a given location within the eleven year solar activity cycle.

For all the guidance trajectories generated, the drag device is generally only actuated during the last ten to twenty days of the mission (see Figure 11.44). Prior to this, the satellite is in its maximum drag configuration to decay as fast as possible. For this reason, if an initial ΔV could be provided at the release from ISS, or a bigger drag device could be installed on the satellite, the overall mission time could be under one month for each epoch scenario.
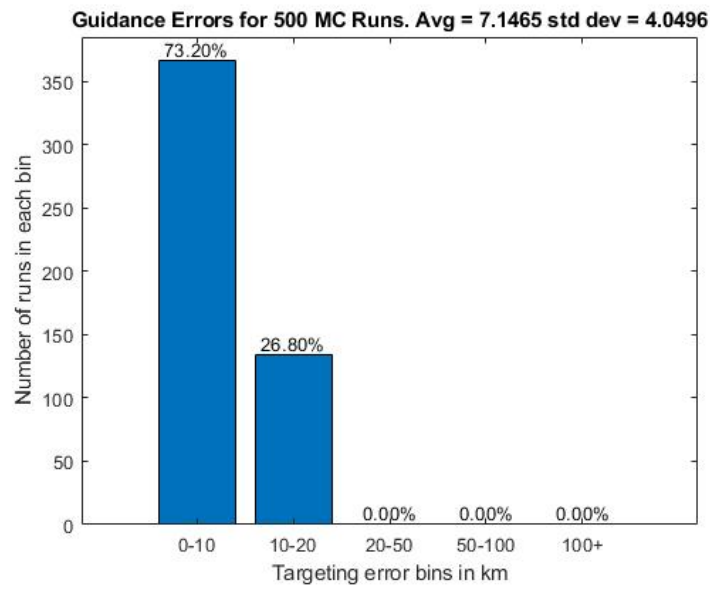
FIGURE 11.42: Guidance Algorithm Performance: Guidance Errors
for 500 MC Runs
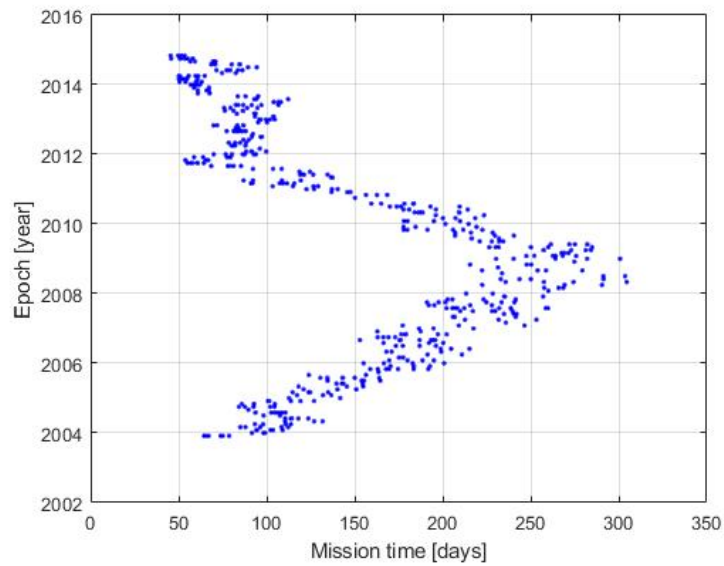
FIGURE 11.43: Guidance Algorithm Performance: Overall Mission
Time
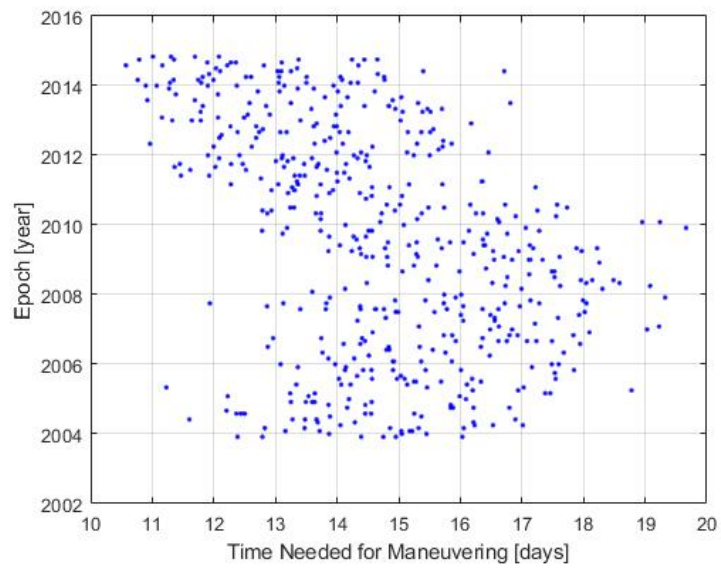
FIGURE 11.44: Guidance Algorithm Performance: Time Needed for
Maneuvering

11.2.2 Tracker Performance with Deployable Heat Shield Device

Another set of five hundred Monte Carlo simulations were conducted to verify the ability to track a drag profile and corresponding trajectory that if followed, using only the modulation od the heat shield device down to the de-orbit point.

Assuming that 240 seconds are required to fully deploy or retract the drag device, the actuator run time was below 0.3% of the total mission time in each simulated scenario (see Figure 11.45).
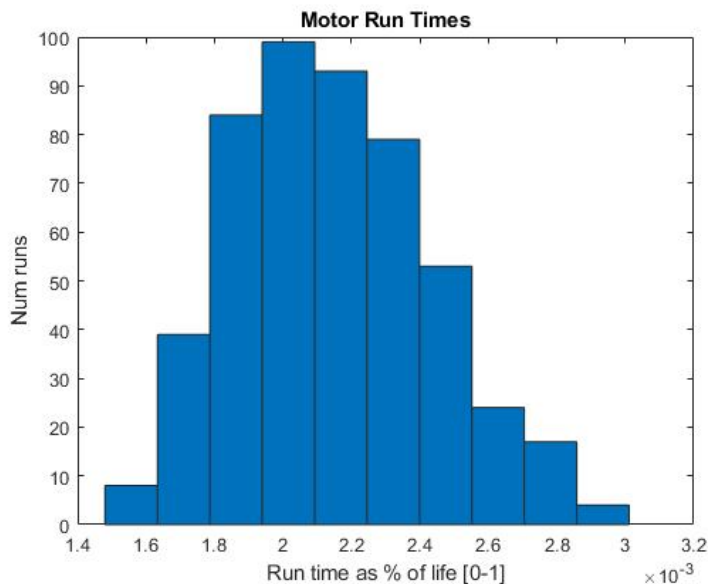
FIGURE 11.45: Tracking Algorithm Performance: Motor Run Times during Orbital Phase

In Figure 11.46 a map with the landing location dispersion is shown assuming that no control is applied after the de-orbit point. As better shown in Figures 11.47 and 11.48, in 99.6% of the cases the error is below 150 km and in 66.6% of the cases the error is below 50 km. The average error is 42.148 km and the standard deviation is 31.314 km.
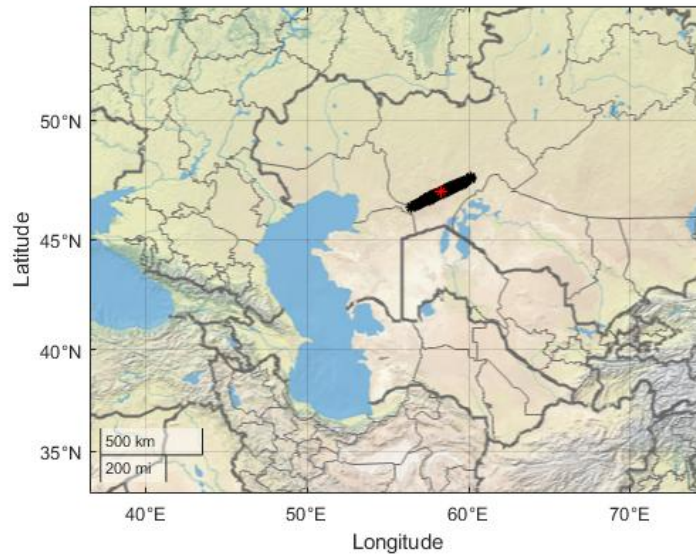
FIGURE 11.46: Tracking Algorithm Performance: Dispersion on Ground
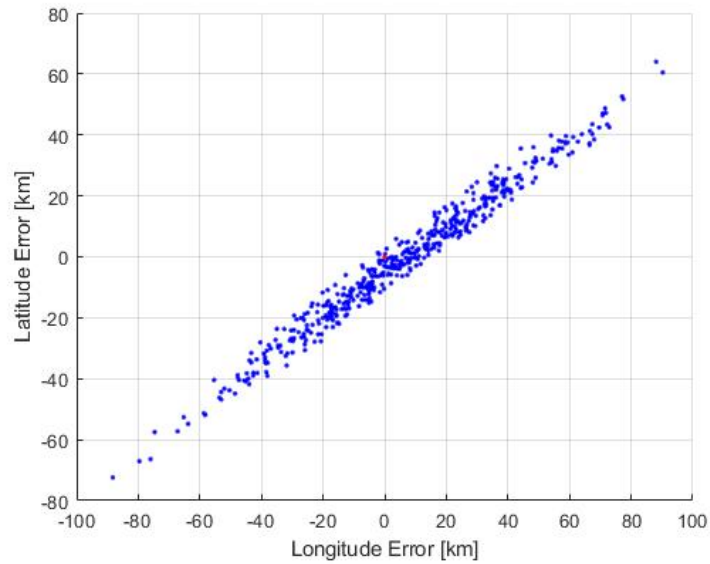
FIGURE 11.47: Tracking Algorithm Performance: Latitude and Longitude Errors on Ground
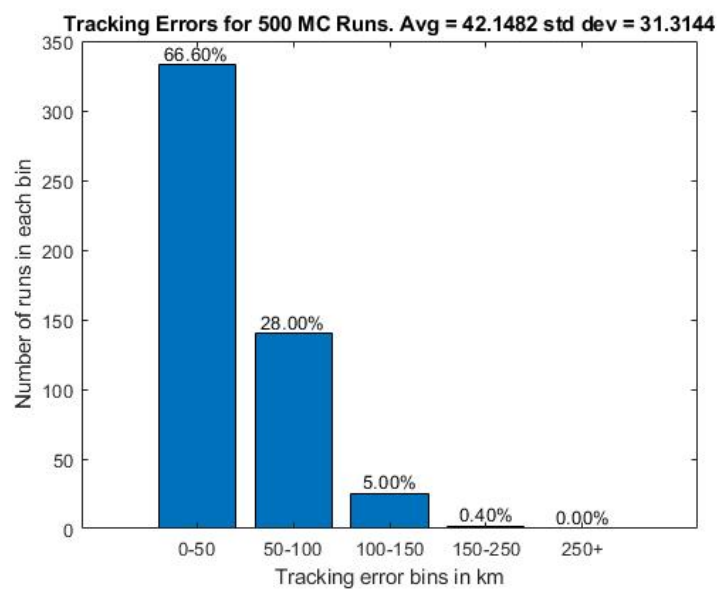
FIGURE 11.48: Tracking Algorithm Performance: Tracking Errors on
Ground for 500 MC Runs

11.2.3 Tracker Performance with Deployable Heat Shield Device and Flaps Actuators

In this section, a last set of five hundred Monte Carlo simulations were conducted to analyze the ability of the system to track the reference trajectory using the modulation of the heat shield aperture down to 100 km and small movable flaps to control the last part of the trajectory below 100 km.

In Figure 11.49 a map with the relative dispersion on the ground is shown assuming continuous guidance trajectory tracking. Significantly smaller errors in the landing location are achievable with this approach. Figure 11.50 shows the latitudinal and longitudinal components of the final position error. As shown in Figure 11.51, in 99.2% of the cases the error is below 50 km and in 72.6% of the cases the error is below 20 km. The average error is 15.537 km and the standard deviation is 10.797.
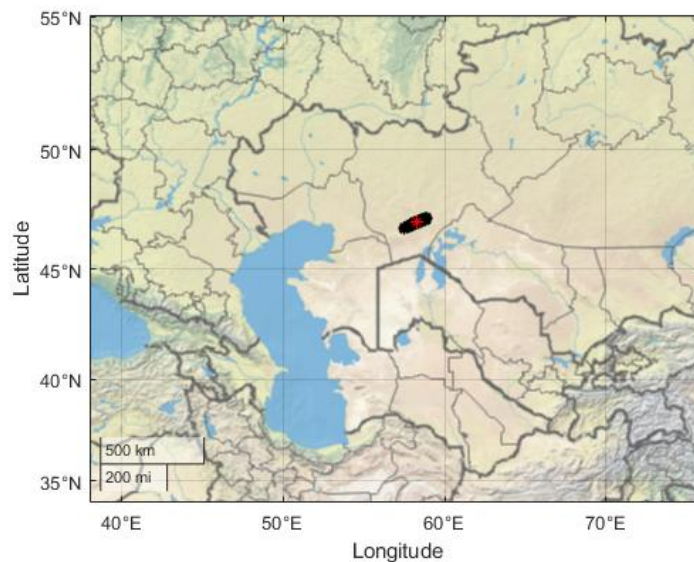
FIGURE 11.49: Tracking Algorithm Performance using flaps: Dispersion on Ground
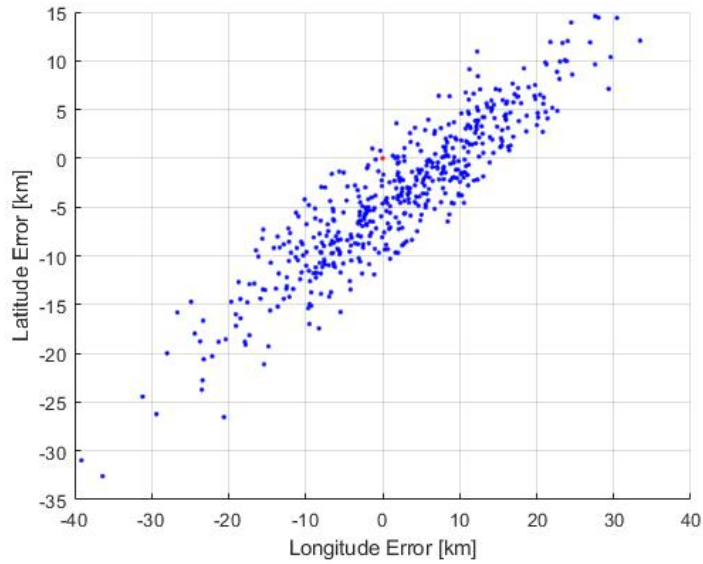
FIGURE 11.50: Tracking Algorithm Performance using flaps: Latitude and Longitude Errors on Ground
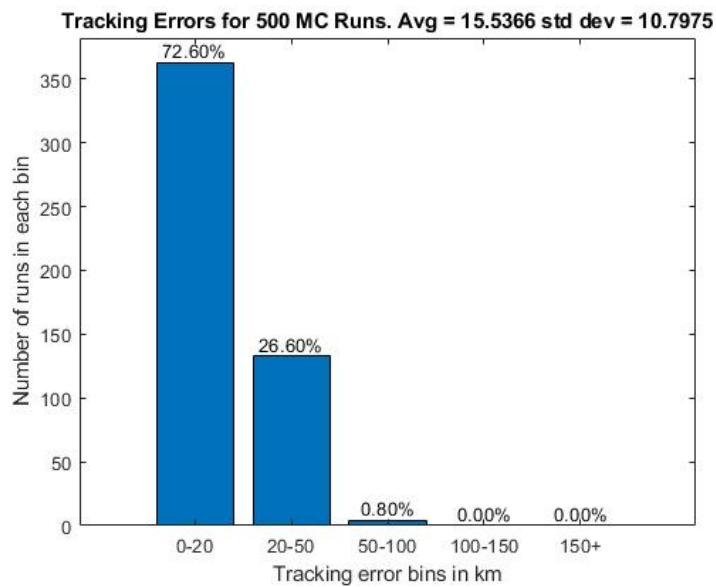
FIGURE 11.51: Tracking Algorithm Performance using flaps: Tracking Errors on Ground for 500 MC Runs

11.2.4   Summary Results

In this chapter a means of targeting a desired landing location for a low Earth orbit spacecraft by modulating the aerodynamic forces the spacecraft experiences have been studied and the results presented. Monte Carlo simulations were conducted to verify the performance and robustness of the ground targeting algorithms. In each of the 500 tested cases, a guidance trajectory and corresponding drag profile were generated from the initial conditions to the desired landing location. In all cases, the guidance landing error was less than 20 km. The tracking of each guidance trajectory was then simulated using realistic sinusoidally varying drag errors during the orbital phase and aerodynamic force errors during the re-entry phase characterized by a fixed offset plus a Gaussian random variable. This represents uncertainties of 10% in the density, vehicle mass, and aerodynamic coefficients during the re-entry. In all cases, the position error at the de-orbit point was less than 2 km. The average position error on the ground was 42.2 km with 99.6% of errors less than 150 km with no control beyond the de-orbit point. The average error was 15.5 km with 99.2% of errors below 50 km when the re-entry control flaps were used. Future work will further investigate the performance and robustness of these algorithms in the face of sensor noise and actuator delays during the re-entry phase.

Ultimately, this work demonstrates that the landing of a spacecraft in a desired recovery location is indeed feasible using exclusively aerodynamic forces. The algorithms are sufficiently robust for a flight mission and are capable of maintaining the nominal satellite trajectory in the face of uncertainties in the aerodynamic model.

Part V

Conclusions

Chapter 12

Conclusions

The work herein was performed to advance the state of the art in deployable heat shield capsule with a 45° sphere-cone geometry in collaboration with the Italian Aerospace Research Centre, the European Space Agency and the University of Florida.

The first contribution of this work regards the design activity of a new mechanically deployable heat shield capsule for an ESA mission. In particular the activities included the design of the mission with a focus on trajectory analysis; the population of an aerodynamic database for the characterization of the capsule; a contribution to the definition of a flight and ground demonstrators architecture, with a specific focus on the assessment of the deployable mechanisms and the multi-layer thermal protection; and the design and execution of a Plasma Wind Tunnel test to demonstrate the capability of the proposed capsule to survive the re-entry environment.

A second contribution has been the study of the problem of dynamic stability. In particular aero-thermodynamic analysis have been conducted to characterize the dynamic response in the supersonic, transonic and subsonic regime of a capsule with a 45° sphere-cone geometry by applying the forced-oscillation method through Computational Fluid Dynamics. The output of these analysis have been used in a six degree of freedom simulator to verify the dynamic stability of a 45°

sphere-cone geometry capsule during a sub-orbital re-entry trajectory. The results show in all the cases the positive tendencies of the capsule to turn with the front shield facing forward during the re-entry starting from a tumbling condition and to effectively dump the oscillations after the transonic regime.

The last contribution of this work has been dedicated to the assessment of the controllability of these systems to reach a desired landing site in the case of re-entry from space, with the focus on landing dispersion minimization.

In particular a means of controlling a mechanically deployable capsule during the re-entry phase using an aerodynamic control system has been proposed. The proposed system, consisting of eight aerodynamic flaps, is able to change the natural trim of the capsule through the flaps independent deflection, in order to produce enough lift and side force to ensure the capsule maneuverability during the re-entry trajectory.

Moreover, a new technological solution for re-entering and landing a capsule in a desired location from a low Earth orbit without the use of chemical propulsion has been studied and proposed in collaboration with University of Florida. Aerodynamic drag modulations, using the heat shield as a drag device, are utilized to guide the capsule to the desired re-entry location. A guidance and control algorithm have been proposed and tested through Monte Carlo analysis demonstrating that the landing in a desired recovery location is indeed feasible using exclusively aerodynamic forces. The algorithms are sufficiently robust for a flight mission and are capable of maintaining the nominal satellite trajectory in the face of uncertainties in the aerodynamic model.

Appendix A

Conferences and Publications

The main studies perform during the thesis period, and detailed in part in this report, were submitted and presented at several international congresses and had led to the following publications:

Article in international peer-reviewed journal

- **A. Fedele**, S. Mungiguerra, "Aerodynamics and Flight Mechanics Activities for a Suborbital Flight Test of a Deployable Heat Shield Capsule" Acta Astronautica volume 151 (2018) 324–333.
  https://doi.org/10.1016/j.actaastro.2018.05.044

- **A. Fedele**, G. Guidotti, G. Rufolo, G. Malucchi, A. Denaro, F. Massobrio, S. Dussy, S. Mancuso, G. Tumino, "The Space Rider Programme: End User's Needs and Payload Applications Survey as Driver for Mission and System Definition". Acta Astronautica (2018).
  https://doi.org/10.1016/j.actaastro.2018.08.042.

- **A. Fedele**, R. Gardi, G. Pezzella, "Aerothermodynamics and Thermal design for on-ground and in-flight testing of a deployable heat shield capsule". Submitted to CEAS Space Journal.

- **A. Fedele**, S. Carannante, M. Grassi, R. Savino, "Aerodynamic Control System for a Deployable Re-Entry Capsule". Selected for Acta Astronautica Special Issue on ICSSA2020.

Papers in international conferences with proceedings

- **A. Fedele**, S. Omar, S. Cantoni, R. Savino, R. Bevilacqua, "Precise Re-Entry and Landing of Propellantless Low Earth Orbit Spacecraft". Proceedings of the 2nd IAA Conference on Space Situational Awareness (ICSSA), Washington DC (United States).

- **A. Fedele**, S. Carannante, M. Grassi, R. Savino, "Aerodynamic Control System for a Deployable Re-Entry Capsule". Proceedings of the 2nd IAA Conference on Space Situational Awareness (ICSSA), Washington DC (United States).

- **A. Fedele**, R. Gardi, P. Vernillo, E. Trifoni, C. Purpura, A. Martucci, G. Ceglia, F. De Filippis, F. Punzo, R. Savino, P. Dell'Aversana, L. Gramiccia, L. Ferracina, "Mini Irene Project: Ground Demonstrator Plasma Wind Tunnel Testing". Proceedings of the 70th International Astronautical Congress, 21-25 October 2019, Washington DC (United States).

- S. Ianelli, M. Albano, M. Di Clemente, A. Gabrielli, S. Cantoni, M. De Stefano Fumo, R. Votta, **A. Fedele**, R. Gardi, M. Cardi, F. Corradino, F. Carrai, F. Carubia, "Iperdrone Roadmap for new On Orbit Services performed by Space Drones". Proceedings of the 70th International Astronautical Congress, 21-25 October 2019, Washington DC (United States).

- P. Vernillo, **A. Fedele**, R. Gardi, F. Punzo, R. Savino, P. Dell'Aversana, L. Gramiccia, L. Ferracina, "Mini Irene Flight Experiment – Stepwise Qualification Approach of a Deployable and Flexible Heat Shield for an Orbital Re-Entry Mission". Proceedings of the International Conference on Flight vehicles, Aerothermodynamics and Re-entry Missions and Engineering (FAR 2019), 30 September - 03 October 2019, Monopoli (Italia).

- D. Bonetti, G. De Zaiacomo, I. Dietlein, B. Esser, G. Guidotti, **A. Fedele**, J. Verant, Y. Prevereaud, G. Gambacciani, G. Bimbi, G. Governale, N. Viola, "European Flexible Heat Shields: Advanced TPS Desing and Tests for Future In-Orbit Demonstration". Proceedings of the International Conference on Flight vehicles, Aerothermodynamics and Re-entry Missions and Engineering (FAR 2019), 30 September - 03 October 2019, Monopoli (Italia).

- S. Ianelli, M. Albano, M. Di Clemente, A. Gabrielli, S. Cantoni, M. De Stefano Fumo, R. Votta, **A. Fedele**, R. Gardi, M. Cardi, F. Corradino, F. Carrai, F. Carubia, A. Brunello, E. Lorenzini, D. Zuin, S. La Luna, M. Valli, A. Zamprotta, F. Punzo, "On Orbit and Re-Entry Services performed by Space Drones". Proceedings of the International Conference on Flight vehicles, Aerothermodynamics and Re-entry Missions and Engineering (FAR 2019), 30 September - 03 October 2019, Monopoli (Italia).

- A. Zamprotta, **A. Fedele**, S. Mungiguerra, R. Savino, "Study on Aerodynamic Stability of a Deployable Aerobraking Re-entry Capsule". Proceedings of the 8th European Conference for Aeronautics and Space Sciences (EUCASS 2019), 01-04 July 2019, Madrid (Spain).

- P. Nigido, M. Grassi, R. Votta, **A. Fedele**, "A Design Trajectory Strategy for Phobos Small Satellite Mission". Proceedings of the iCubeSat 2019, the 8th Interplanetary CubeSat Workshop, 28-29 May 2019, Milano (Italy).

- R. Gardi, **A. Fedele**, G. Pezzella, P. Vernillo, R. Savino, S. Mungiguerra, P. Dell'Aversana, L. Gramiccia, K. Henriksson, J. Smith, J. Longo, "Mini-Irene: Design of a Deployable Heat Shield Capsule for a Sounding Rocket Flight Experiment". Proceedings of the 68th International Astronautical Congress, 25-29 September 2017, Adelaide (Australia).

- **A. Fedele**, G. Guidotti, G. Rufolo, G. Malucchi, A. Denaro, F. Massobrio, S. Dussy, S. Mancuso, G. Tumino, "The Space Rider Programme: End User's Needs and Payload Applications Survey as Driver for Mission and System Definition". Proceedings of the 68th International Astronautical Congress, 25-29 September 2017, Adelaide (Australia).

- R. Gardi, P.Vernillo, **A. Fedele**, G. Pezzella, R. Savino, P. Dell'Aversana, L. Gramiccia, G. D'aniello, R. Aurigemma, N. Cimminiello, F. Punzo, G. Florin, R. Molina, "Mini Irene - Deployable Heat Shield for Suborbital Flight Test". Proceedings of the XXIV Italian Association of Aeronautics and Astronautics International Conference, 18-22 September 2017, Palermo – Enna, Italy.

- P. Vernillo, **A. Fedele**, R. Gardi, R. Savino, F. Punzo, F. Gunnar, R. Molina, "Mini-Irene: The First European Flight Experiment of a Deployable Heat Shield". Proceedings of the 23rd ESA Symposium on European Rocket and Balloon Programmes and Related Research, 11-15 June 2017, Visby (Sweden).

Bibliography

[1]   D. L. Akin, "The parashield entry vehicle concept: Basic theory and flight test developments", 4th Annual AIAA/Utah State University Conference on Small Satellites - Proceedings. Vol. 1 (A91-27376 10-18). Logan UT Utah State University 1990 11 p., 1990.

[2]   D. Akin, "Applications of ultra-low ballistic coefficient entry vehicles to existing and future space missions", in *SpaceOps 2010 Conference Delivering on the Dream Hosted by NASA Marshall Space Flight Center and Organized by AIAA*, 2010, p. 1928.

[3]   M. Wiegand and H. J. Königsmann, "A small re-entry capsule - brem-sat 2", Tech. Rep., 1996.

[4]   S. Wilde and S. Walther, "Inflatable reentry and descent technology (irdt) - further developments", 2001.

[5]   "Inflatable reentry and descent technology (irdt) factsheet", Tech. Rep., 2005.

[6]   P. Reynier and D. Evans, "Post-flight analysis of inflatable reentry and descent technology blackout during earth re-entry", *Journal of Spacecraft and Rockets*, vol. 46, 4 Jul. 2009.

[7]   L Marraffa, D Kassing, P Baglioni, D Wilde, S Walther, K Pitchkhadze, and V Finchenko, "Inflatable re-entry technologies: Flight demonstration and future prospects", *ESA bulletin*, pp. 78–85, 2000.

[8]   D. Wilde, S. Walther, K. Pitchadze, S. Alexsaschkin, D. Vennemann, and
      L. Marraffa, "Flight test and iss application of the inflatable reentry and
      descent technology (irdt)", *Acta Astronautica*, vol. 51, no. 1-9, pp. 83–88,
      2002.

[9]   L Marraffa, D Boutamine, S Langlois, C Reimers, C Feichtinger, T. Wal-
      loschek, P Kyr, and S Alexashkin, "Irdt 2r mission, first results", in *Pro-
      ceedings 5th European Workshop on Thermal Protection Systems and Hot Struc-
      tures, Noordwijk*, 2006.

[10] L Marraffa, F Mazoue, P. Reynier, and C Reimers, "Some aerothermody-
      namic aspects of esa entry probes", *Chinese Journal of Aeronautics*, vol. 19,
      no. 2, pp. 126–133, 2006.

[11] S. Hughes, R. Dillman, B. Starr, R. Stephan, M. Lindell, C. Player, and F
      Cheatwood, "Inflatable re-entry vehicle experiment (irve) design overview",
      in *18th AIAA Aerodynamic Decelerator Systems Technology Conference and
      Seminar*, 2005, p. 1636.

[12] M. Lindell, S. Hughes, M. Dixon, and C. Willey, "Structural analysis and
      testing of the inflatable re-entry vehicle experiment (irve)", in *47th AIAA
      Structures, Structural Dynamics, and Materials Conference*, 2006, p. 1699.

[13] R. A. Dillman, "Flight performance of the inflatable reentry vehicle exper-
      iment ii", Tech. Rep., 2010.

[14] D. Bose, M. Toniolo, S. O'Keefe, F Cheatwood, S. Hughes, and R. Dill-
      man, "Impact of vehicle flexibility on irve-ii flight dynamics", in *21st AIAA
      Aerodynamic Decelerator Systems Technology Conference and Seminar*, 2011,
      p. 2571.

[15] D. Litton, D. Bose, F Cheatwood, S. Hughes, H. Wright, M. Lindell, S.
      Derry, and A. Olds, "Inflatable re-entry vehicle experiment (irve)-4 overview",

in *21st AIAA Aerodynamic Decelerator Systems Technology Conference and Seminar*, 2011, p. 2580.

[16] S. Hughes, F Cheatwood, R. Dillman, A. Calomino, H. Wright, J. DelCorso, and A. Calomino, "Hypersonic inflatable aerodynamic decelerator (hiad) technology development overview", in *21st AIAA Aerodynamic Decelerator Systems Technology Conference and Seminar*, 2011, p. 2524.

[17] J. Del Corso, F Cheatwood, W. Bruce, S. Hughes, and A. Calomino, "Advanced high-temperature flexible tps for inflatable aerodynamic decelerators", in *21st AIAA Aerodynamic Decelerator Systems Technology Conference and Seminar*, 2011, p. 2510.

[18] S. Hughes, F Cheatwood, R. Dillman, A. Calomino, H. Wright, J. DelCorso, and A. Calomino, "Hypersonic inflatable aerodynamic decelerator (hiad) technology development overview", in *21st AIAA Aerodynamic Decelerator Systems Technology Conference and Seminar*, 2011, p. 2524.

[19] R. A. Beck, S. White, J. Arnold, W. Fan, M. Stackpoole, P. Agrawal, and S. Coughlin, "Overview of initial development of flexible ablators for hypersonic inflatable aerodynamic decelerators", in *21st AIAA Aerodynamic Decelerator Systems Technology Conference and Seminar*, 2011, p. 2511.

[20] H. Wright, A. Cutright, J. Corliss, W. Bruce, D. Trombetta, A. Mazaheri, M. Coleman, A. Olds, and S. Hancock, "Heart flight test overview", in *9th International Planetary Probe Workshop, Toulouse, France*, 2012.

[21] A. Cassell, G. Swanson, R Johnson, S. Hughes, and F Cheatwood, "Overview of hypersonic inflatable aerodynamic decelerator large article ground test campaign", in *21st AIAA Aerodynamic Decelerator Systems Technology Conference and Seminar*, 2011, p. 2569.

[22] A. Cassell, G. T. Swanson, B. Quach, L. K. Kushner, J. D. Brown, C. D. Kazemba, C. Kruger, R. K. Johnson, S. J. Hughes, J. Littell, *et al.*, "Design and execution of the hypersonic inflatable aerodynamic decelerator large-article wind tunnel experiment", in *AIAA Aerodynamic Decelerator Systems (ADS) Conference*, 2013, p. 1304.

[23] C. D. Kazemba, K. Tran, B. Quach, L. K. Kushner, A. Cassell, L. Li, R. Braun, J. Littell, J. Van Norman, R. K. Johnson, *et al.*, "Determination of the deformed structural shape of hiads from photogrammetric wind tunnel data", in *AIAA Aerodynamic Decelerator Systems (ADS) Conference*, 2013, p. 1286.

[24] B. D. Goldman and E. Dowell, "Flutter analysis of the thermal protection layer on the nasa hiad", in *AIAA Aerodynamic Decelerator Systems (ADS) Conference*, 2013, p. 1254.

[25] J. S. Green and R. Lindberg, "Morphing hypersonic inflatable aerodynamic decelerator", in *AIAA Aerodynamic Decelerator Systems (ADS) Conference*, 2013, p. 1256.

[26] L. Kushner and J. Littell, "Photogrammetry of a hypersonic inflatable aerodynamic decelerator", in *AIAA Aerodynamic Decelerator Systems (ADS) Conference*, 2013, p. 1284.

[27] G. Swanson and A. Cassell, "Structural strap tension measurements of a 6 meter hypersonic inflatable aerodynamic decelerator under static and dynamic loading", in *AIAA Aerodynamic Decelerator Systems (ADS) Conference*, 2013, p. 1287.

[28] D. Bose and R. Winski, "The hypersonic inflatable aerodynamic decelerator (hiad) mission applications study", in *AIAA Aerodynamic Decelerator Systems (ADS) Conference*, 2013, p. 1389.

[29] B. Harper and R. D. Braun, "Asymmetrically stacked tori hypersonic inflatable aerodynamic decelerator design study for mars entry", in *AIAA Atmospheric Flight Mechanics Conference*, 2014, p. 1095.

[30] J. DiNonno, F. Cheatwood, S. Hughes, M. Ragab, R. Dillman, R. Bodkin, C. Zumwalt, and R. Johnson, "Hiad on ula (hula) orbital reentry flight experiment concept", 2016.

[31] N. Skolnik, H. Kamezawa, L. Li, G. A. Rossman, B. Sforzo, and R. D. Braun, "Design of a novel hypersonic inflatable aerodynamic decelerator for mars entry, descent, and landing", in *AIAA Atmospheric Flight Mechanics Conference*, 2017, p. 0469.

[32] R. Dillman, J. DiNonno, R. Bodkin, S. Hughes, F. Cheatwood, H Blakeley, R. Akamine, and A Bowes, "Planned orbital flight test of a 6 m hiad", in *Presentation, International Planetary Probe Workshop*, 2018.

[33] G. Swanson, B. Smith, R. Akamine, R. Bodkin, N. Cheatwood, A. R. Parker, S. Hughes, D. Gaddy, and A. Parker, "The hiad orbital flight demonstration instrumentation suite", 2018.

[34] R. Dillman, "Flight performance of the inflatable reentry vehicle experiment 3", Tech. Rep., 2013.

[35] D. Jurewicz, G. Brown, B. Gilles, A. Taylor, R. Sinclair, B. Tutt, D. Lichodziejewski, C. Kelley, and S. Hughes, "Design and development of inflatable aeroshell structure for irve-3", in *21st AIAA Aerodynamic Decelerator Systems Technology Conference and Seminar*, 2011, p. 2522.

[36] A. D. Olds and R. E. Beck, "Irve-3 post-flight reconstruction", in *AIAA Aerodynamic Decelerator Systems (ADS) Conference*, 2013, p. 1390.

[37]   Y. Takahashi, "Aerodynamic heating around flare-type membrane inflat-
        able vehicle in suborbital reentry demonstration flight", *Journal of Space-
        craft and Rockets*, vol. 52, 6 Jul. 2015.

[38]   E Sato, "Flight experiment of capsule-type vehicle with membrane aeroshell
        by means of large scientific balloon", in *24th International Symposium on
        Space Technology and Science, Miyazaki, 2004*, 2004.

[39]   K. Yamada, Y. Kimura, D. Akita, T. Abe, K. Suzuki, O. Imamura, M. Koyama,
        and A. K. Hayashi, "Study on low-ballistic-coefficient atmospheric-entry
        technology using flexible aeroshell", *Transactions of the Japan Society for
        Aeronautical and Space Sciences*, vol. 7, no. ists26, Pg_1–Pg_7, 2009.

[40]   K. Yamada, T. Abe, K. Suzuki, N. Honma, Y. Nagata, M. Koyama, D. Abe,
        Y. Kimura, A. K. Hayashi, H. Makino, *et al.*, "Deployment and drop test
        for inflatable aeroshell for atmospheric entry capsule with using large sci-
        entific balloon", in *38th COSPAR Scientific Assembly*, vol. 38, 2010, p. 12.

[41]   K. Yamada, T. Abe, K. Suzuki, N. Honma, M. Koyama, Y. Nagata, D. Abe,
        Y. Kimura, A. K. Hayashi, D. Akita, *et al.*, "Deployment and flight test
        of inflatable membrane aeroshell using large scientific balloon", in *21st
        AIAA aerodynamic decelerator systems technology conference and seminar*, 2011,
        p. 2579.

[42]   K. Yamada, T. Abe, K. Suzuki, O. Imamura, and D. Akita, "Reentry demon-
        stration plan of flare-type membrane aeroshell for atmospheric entry vehi-
        cle using a sounding rocket", in *21st AIAA Aerodynamic Decelerator Systems
        Technology Conference and Seminar*, 2011, p. 2521.

[43]   Y. Nagata, K. Yamada, T. Abe, and K. Suzuki, "Attitude dynamics for flare-
        type membrane aeroshell capsule in reentry flight experiment", in *AIAA
        Aerodynamic Decelerator Systems (ADS) Conference*, 2013, p. 1285.

[44] K. Yamada, K Suzuki, O Imamura, D Akita, Y Nagata, Y Shoji, Y Taka-hashi, Y Watanabe, and T Abe, "Development of re-entry nano-satellite with gossamer aeroshell and gps", *Iridium Deployed from ISS, 30th ISTS, 34th IEPC and 6th NSAT*, 2015.

[45] K Yamada, T Moriyoshi, K Matsumaru, H Kanemaru, T Araya, K Suzuki, O Imamura, D Akita, Y Nagata, Y Shoji, *et al.*, "Re-entry nano-satellite with gossamer aeroshell and gps/iridium deployed from iss", in *Joint Conference: 31st ISTS (International Symposium on Space Technology and Science), 26th ISSFD (International Symposium on Space Flight Dynamics), and 8th NSAT (Nano-Satellite Symposium)*, 2017, pp. 3–9.

[46] Y. Takahashi and K. Yamada, "Aerodynamic heating of inflatable aeroshell in orbital reentry", *Acta Astronautica*, vol. 152, pp. 437–448, 2018.

[47] D. Bonetti and et al., "European flexible heat shields: Advanced tps design and tests for future in-orbit demonstration (efesto)", FAR, 2019.

[48] E. Venkatapathy, K. Hamm, I. Fernandez, J. Arnold, D. Kinney, B. Laub, A. Makino, M. McGuire, K. Peterson, D. Prabhu, *et al.*, "Adaptive deployable entry and placement technology (adept): A feasibility study for human missions to mars", in *21st AIAA Aerodynamic Decelerator Systems Technology Conference and Seminar*, 2011, p. 2608.

[49] E. Venkatapathy, P Wercinski, and D Prabhu, "Mechanically-deployed hypersonic decelerator and conformal ablator technologies for mars missions", 2012.

[50] B. Smith and B. Yount, "Progress in payload separation risk mitigation for a deployable venus heat shield", in *AIAA Aerodynamic Decelerator Systems (ADS) Conference*, 2013, p. 1284.

[51] J. O. Arnold, Y.-K. Chen, D. K. Prabhu, M. Bittner, E. Venkatapathy, *et al.*, "Arcjet testing of woven carbon cloth for use on adaptive deployable entry placement technology", 2013.

[52] B. Yount and D. Prabhu, "Structures and mechanisms design concepts for adaptive deployable entry placement technology", in *AIAA Aerodynamic Decelerator Systems (ADS) Conference*, 2013, p. 1369.

[53] J. Arnold and K. Peterson, "Thermal and structural performance of woven carbon cloth for adaptive deployable entry and placement technology", in *AIAA Aerodynamic Decelerator Systems (ADS) Conference*, 2013, p. 1370.

[54] V. Gidzak and G. Candler, "Wake-fabric interactions in adept-vital", in *AIAA Aerodynamic Decelerator Systems (ADS) Conference*, 2013, p. 1370.

[55] P. Wercinski, "Adaptable deployable entry and placement technology (adept) for cubesat delivery to mars surface", 2014.

[56] B. Smith and S Dutta, "Free flight ground testing of adept in advance of the sounding rocket one flight experiment", 2017.

[57] D. K. Litton, D. K. Prabhu, and B. Smith, "Stability of a mechanically deployed aerodynamic decelerator", in *AIAA Atmospheric Flight Mechanics (AFM) Conference*, 2013, p. 4602.

[58] A. Cassell and et al., "Adaptive deployable entry placement technology (adept) sounding rocket flight test", FAR, 2019.

[59] S. Dutta and J. Green, "Flight mechanics modeling and post-flight analysis of adept sr-1", in *AIAA Aviation 2019 Forum*, 2019, p. 2900.

[60] E. Bassano, R. Savino, and et al., "Irene - italian re-entry nacelle for microgravity experiments", IAC, 2011.

[61] R. Savino, R. Aurigemma, P. Dell'Aversana, L. Gramiccia, J. Longo, L. Marraffa, F. Punzo, and L. Scolamiero, "European sounding rocket experiment on hypersonic deployable re-entry demonstrator", in *Proceedings of 8th European Symposium on Aerothermodynamics for Space Vehicles*, 2015.

[62] R Gardi, A Fedele, G Pezzella, P Vernillo, R Savino, S Mungiguerra, P Dell'Aversana, L Gramiccia, K Henriksson, and J Smith, "Mini-irene: Design of deployable heat shield capsule for a sounding rocket flight experiment", in *68th International Astronautical Congress*, 2017.

[63] P Vernillo, A Fedele, R Gardi, R Savino, F Punzo, F Gunnar, and R Molina, "Mini-irene: The first european flight experiment of a deployable heat shield", in *23rd ESA Symposium on European Rocket and Balloon Programmes and Related Research*, 2017.

[64] R Gardi, P Vernillo, A Fedele, G Pezzella, R Savino, P Dell'Aversana, L Gramiccia, G D'Aniello, R Aurigemma, N Cimminiello, *et al.*, "Mini irene - deployable heat shield for suborbital flight test", in *XXIV International Conference of Italian Association of Aeronautics and Astronautics AIDAA*, 2017.

[65] P Vernillo, A Fedele, R Gardi, R Savino, F Punzo, P Dell'Aversana, L Gramiccia, and L Ferracina, "Mini irene flight experiment – stepwise qualification approach of a deployable and flexible heat shield for an orbital re-entry mission", FAR, 2019.

[66] A. Zamprotta, A. Fedele, and et al., "Study on aerodynamic stability of a deployable aerobraking re-entry capsule", EUCASS 2019, 2019.

[67] A. Fedele, R. Gardi, P Vernillo, and et al., "Mini irene project: Ground demonstrator plasma wind tunnel testing", in *70th International Astronautical Congress*, 2019.

[68]   A. Fedele and S. Mungiguerra, "Aerodynamics and flight mechanics activities for a suborbital flight test of a deployable heat shield capsule", *Acta Astronautica*, vol. 151, pp. 324–333, 2018.

[69]   R Savino and V Carandente, "Aerothermodynamic and feasibility study of a deployable aerobraking re-entry capsule", *Fluid Dynamics and Material Processing*, vol. 8, no. 4, pp. 453–477, 2012.

[70]   R. Fortezza, R. Savino, and G. Russo, "Mistral (air-launcheable micro-satellite with reentry capability) a small spacecraft to carry out several missions in leo", IAC, 2013.

[71]   V Carandente, R Savino, V D'Oriano, and R Fortezza, "Deployable aerobraking earth entry systems for recoverable microgravity experiments", in *Proceedings of the 65th International Astronautical Congress, Toronto, Canada*, 2014.

[72]   S Pagano and R Savino, "Adjustable aerobraking heat shield for satellites deployment and recovery", in *Proceedings of the World Congress on Engineering*, vol. 2, 2017, pp. 5–7.

[73]   S. Mungiguerra, G. Zuppardi, and R. Savino, "Rarefied aerodynamics of a deployable re-entry capsule", *Aerospace Science and Technology*, vol. 69, pp. 395–403, 2017.

[74]   S Mungiguerra, G Zuppardi, L. S. Cuomo, and R Savino, "Effects of solar panels on aerodynamics of a small satellite with deployable aero-brake", *Acta Astronautica*, vol. 151, pp. 456–466, 2018.

[75]   V. Carandente, R. Savino, V. D'Oriano, and R. Fortezza, "A study on earth re-entry capsules with deployable aerobrakes for recoverable microgravity experiments", *Microgravity Science and Technology*, vol. 27, no. 3, pp. 181–191, 2015.

[76] V. Carandente, "Aerothermodynamic and mission analyses of deployable aerobraking earth re-entry systems",

[77] V Carandente, G Elia, and R Savino, "Conceptual design of de-orbit and re-entry modules for standard cubesats", in *Proceedings of the 2nd IAA Conference on University Satellite Missions and Cubesat Work-shop, Rome, February*, 2013, pp. 4–7.

[78] V. Carandente and R. Savino, "New concepts of deployable de-orbit and re-entry systems for cubesat miniaturized satellites", *Recent Patents on Engineering*, vol. 8, no. 1, pp. 2–12, 2014.

[79] S. Ianelli, M. Albano, and et al., "Iperdrone roadmap for new on orbit services performed by space drones", 70th International Astronautical Congress, 2019.

[80] S. Ianelli and et al., "On orbit and re-entry services performed by space drones", FAR, 2019.

[81] *Re-entry from Space* Jan. 1961.

[82] "Guidance and navigation for entry vehicles", Tech. Rep., 1968.

[83] Z. Anatoly. (2019). Here is how soyuz returns to earth, [Online]. Available: http://www.russianspaceweb.com/soyuz-landing.html (visited on 08/09/2019).

[84] R. Morth, "Reentry guidance for apollo", Tech. Rep., 1966.

[85] P. Lu, "Comparison of fully numerical predictor-corrector and apollo skip guidance algorithms", *Journal of the Astronautical Sciences*, 2012.

[86] I. Bogner, "Description of apollo entry guidance", Tech. Rep., 2007.

[87] M. A. Tigges, B. D. Bihari, and et al., "Orion capsule handling qualities for atmospheric entry", AIAA Guidance, Navigation, and Control Conference, 2011.

[88] Z. R. Putnam, M. D. Neave, and G. H. Barton, "Predguid entry guidance for orion return from low earth orbit", IEEAC paper1571, 2009.

[89] V. Carandente, G. Zuppardi, and R. Savino, "Aerothermodynamic and stability analyses of a deployable re-entry capsule", *Acta Astronautica*, vol. 93, pp. 291–303, 2014.

[90] G. Zuppardi, R. Savino, and G. Mongelluzzo, "Aero-thermodynamic analysis of a low ballistic coefficient deployable capsule in earth re-entry", *Acta Astronautica*, 2016.

[91] L. E. Ericcson and J. P. Reding, "Re-entry capsule dynamics", *Journal of Spacecraft and Rockets*, vol. 8, 1971.

[92] S. Dobre, C. Berner, M. Albisser, F. Saada, E. Clopeau, L. Ferracina, and L. Marraffa, "Marcopolo-r erc dynamic stability characterization - open range free flight tests", 8th European Symposium on Aero-thermodynamics for Space Vehicles, 2015.

[93] B. H. Beam and C. E. et Hedstrom, "The damping in pitch of bluff bodies of revolution at mach numbers from 2.5 to 3.5", NASA Technical Memorandum, 1959.

[94] D. A. Buell and N. S. Johnson, "An experimental and analytical investigation of the dynamics of two blunt bodies at subsonic speeds", NASA Technical Memorandum, 1959.

[95] K. Hiraki, Y. Inatani, N. Ishii, T. Nakajima, and M. Hinada, "Dynamic stability of muses-c capsule", 21st International Symposium on Space Technology, 1998.

[96] B. L. Uselton, T. O. Shadow, and A. C Mansfield, "Damping-in-pitch derivatives of 120-and 140-degree blunted cones at mach numbers from 0.6 through 3", AEDC-TR-7049, 1970.

[97] D. B. Owens and V. V. Aubuchon, "Overview of orion crew module and launch abort vehicle dynamic stability", 29th AIAA Applied Aerodynamics Conference, 2011.

[98] J. Hergert, J. Brock, E. Stern, M. C. Wilder, and D. W. Bogdanoff, "Free-flight trajectory simulation of the adept sounding rocket test using us3d", in *35th AIAA Applied Aerodynamics Conference*, 2017, p. 4462.

[99] C. H. Whitlock and P. M. Siemers, "Parameters influencing dynamic stability characteristics of viking-type entry configurations at mach 1.76", *Journal of Spacecraft and Rockets*, vol. 9, 1972.

[100] 3M, *Nextel Ceramic Textiles Technical Notebook*.

[101] D. A. Vallado and D. Finkleman, "A Critical Assessment of Satellite Drag and Atmospheric Density Modeling", *Acta Astronautica*, vol. 95, pp. 141–165, Feb. 2014, ISSN: 0094-5765. DOI: 10.1016/j.actaastro.2013.10.005. [Online]. Available: http://www.sciencedirect.com/science/article/pii/S0094576513003755 (visited on 05/12/2016).

[102] Analytical Graphics Inc, *Systems Toolkit*, Exton, PA, 2017.

[103] O. Montenbruck and E. Gill, *Satellite Orbits*, 1st ed. Springer Berlin Heidelberg, 2005, ISBN: 978-3-540-67280-7.

[104] M. M. Madden, "Gravity Modeling for Variable Fidelity Environments", in *AIAA Modeling and Simulation Technologies Conference and Exhibit*, 2006, p. 6730. [Online]. Available: http://arc.aiaa.org/doi/pdf/10.2514/6.2006-6730 (visited on 04/15/2016).

[105] N. Pavlis, S. Holmes, S. Kenyon, and J. Factor, *An Earth Gravitation Model to Degree 2160: EGM2008*, Vienna, Austria, Apr. 2008.

[106] D. Vallado, *Fundamentals of Astrodynamics and Applications*, 4th ed. Hawthorne, CA: Microcosm Press, 2013.

[107]   D King-Hele, "Decrease In Upper Atmosphere Rotation Rates", *Letters to Nature*, 1971. [Online]. Available: `http://www.nature.com/nature/journal/v233/n5318/pdf/233325a0.pdf` (visited on 06/10/2016).

[108]   S. R. Omar and J. M. Wersinger, "Satellite Formation Control using Differential Drag", in *Proceedings of 53rd AIAA Aerospace Sciences Meeting*, Kissimmee, FL: American Institute of Aeronautics and Astronautics, Jan. 2014. DOI: `10.2514/6.2015-0002`. [Online]. Available: `http://arc.aiaa.org/doi/abs/10.2514/6.2015-0002` (visited on 03/20/2016).

[109]   MathWorks, *MathWorks atmosnrlmsise00 Documentation*, 2016. [Online]. Available: `http://www.mathworks.com/help/aerotbx/ug/atmosnrlmsise00.html`.

[110]   NASA Goddard Space Flight Center, *OMNIWeb*, 2017. [Online]. Available: `http://omniweb.gsfc.nasa.gov`.

[111]   National Oceanic and Atmospheric Administration, *USAF 45-Day Ap and F10.7cm Flux Forecast*, 2017. [Online]. Available: `http://www.swpc.noaa.gov/products/usaf-45-day-ap-and-f107cm-flux-forecast`.

[112]   F. Marcos, B. Bowman, and R. Sheehan, "Accuracy of Earth's Thermospheric Neutral Density Models", in *Proceedings of the AIAA/AAS Astrodynamics Specialist Conference*, Keystone, CO, Aug. 2006. [Online]. Available: `http://arc.aiaa.org/doi/pdf/10.2514/6.2006-6167` (visited on 07/17/2016).

[113]   MathWorks, *Solve nonstiff differential equations — variable order method - MATLAB ode113*, 2017. [Online]. Available: `https://www.mathworks.com/help/matlab/ref/ode113.html` (visited on 03/23/2017).

[114]   M. E. Tauber, "A review of high speed convective, heat transfer computation methods", Tech. Rep., 1989.

[115] W. L. Hankey, *Re-entry Aerodynamics*. AIAA Educational Series, AIAA Inc, 1988.

[116] J. J. Bertin, *Hypersonic Aerothermodynamics*. AIAA Education Series, 1994.

[117] G. Pezzella, P. Catalano, and A. Bourgoing, "Computational flowfield analysis of a sample return capsule", in *18th AIAA/3AF international space planes and hypersonic systems and technologies conference*, 2012, p. 5818.

[118] A. S. Potturi and O. Peroomiany, "Dynamic stability analysis of the orion crew module through computational fluid dynamics", 46th AIAA Fluid Dynamics Conference, 2016.

[119] S. Paris and O. Karatekin, "Experimental determination of the dynamic derivatives of a reentry capsule in transonic supersonic regime", 8th International Planetary Probe Workshop, 2011.

[120] O. Karatekin, "Aerodynamics of a planetary entry capsule at low speeds", VKI PhD report, 2002.

[121] F. J. Regan and S. M. Anandakrishnan, *Dynamics of Atmospheric Re-Entry*. AIAA Educational Series, AIAA Inc., 1993.

[122] A. Steltzner, D. Kipp, A. Chen, D. Burkhart, C. Guernsey, G. Mendeck, R. Mitcheltree, R. Powell, T. Rivellini, M. Martin, and D. Way, "Mars science laboratory entry, descent, and landing system", in *IEEE Aerospace Conference*, IEEE, 2006. DOI: 10.1109/aero.2006.1655796.

[123] G. Emanuel, *Gasdynamics: theory and applications*. American Institute of Aeronautics and Astronautics, 1986.

[124] A. Fedele, S. Omar, S. Cantoni, R. Savino, and R. Bevilacqua, "Precise re-entry and landing of propellantless low earth orbit spacecraft", 2nd IAA Conference on Space Situational Awareness, 2020.

[125] S. Omar and R. Bevilacqua, "Guidance, navigation, and control solutions for spacecraft re-entry point targeting using aerodynamic drag", *Acta Astronautica*, vol. 155, pp. 389–405, Feb. 2019, ISSN: 0094-5765. DOI: `10.1016/j.actaastro.2018.10.016`. [Online]. Available: `http://www.sciencedirect.com/science/article/pii/S00945765183002893` (visited on 09/05/2019).

[126] S. R. Omar, R. Bevilacqua, D. Guglielmo, L. Fineberg, J. Treptow, S. Clark, and Y. Johnson, "Spacecraft Deorbit Point Targeting Using Aerodynamic Drag", en, *Journal of Guidance, Control, and Dynamics*, vol. 40, no. 10, pp. 1–7, May 2017, ISSN: 0731-5090, 1533-3884. DOI: `10.2514/1.G002612`. [Online]. Available: `https://arc.aiaa.org/doi/10.2514/1.G002612` (visited on 06/17/2017).

[127] S. R. Omar and R. Bevilacqua, "Hardware and GNC solutions for controlled spacecraft re-entry using aerodynamic drag", *Acta Astronautica*, vol. 159, pp. 49–64, Jun. 2019, ISSN: 0094-5765. DOI: `10.1016/j.actaastro.2019.03.051`. [Online]. Available: `http://www.sciencedirect.com/science/article/pii/S0094576519300359` (visited on 04/20/2019).

[128] H. Curtis, *Orbital Mechanics for Engineering Students*, 2nd ed. Burlington, MA: Elsevier, 2009.

[129] S. A. Schweighart and R. J. Sedwick, "High-Fidelity Linearized J Model for Satellite Formation Flight", *Journal of Guidance, Control, and Dynamics*, vol. 25, no. 6, pp. 1073–1080, 2002, ISSN: 0731-5090. DOI: `10.2514/2.4986`. [Online]. Available: `http://dx.doi.org/10.2514/2.4986` (visited on 03/26/2017).

[130] G. Franklin, J. Powell, and A. Emami-Naeini, *Feedback Control of Dynamic Systems*, 4th ed. Upper Saddle River, NJ: Prentice Hall, 2002, ISBN: 0-13-032393-4.

[131] S. N. D'Souza and N. Sarigul-Klijn, "Survey of planetary entry guidance algorithms", *Progress in Aerospace Sciences*, vol. 68, pp. 64–74, 2014.

[132] *Linear Optimal Control for Reentry Flight* 1994.

[133] A. Cavallo and F. Ferrara, "Atmospheric re-entry control for low lift/drag vehicles", *Journal of Guidance and Dynamics*, vol. 19, pp. 47–53, 1 1996.

[134] A. Fedele, S. Carannante, M. Grassi, and R. Savino, "Aerodynamic control system for a deployable re-entry capsule", 2nd IAA Conference on Space Situational Awareness, 2020.

[135] R. A. Mitcheltree, J. N. Moss, F. M. Cheatwood, F. A. Greene, and R. D. Braun, "Aerodynamics of the mars microprobe entry vehicles", *Journal of Spacecraft and Rockets*, vol. 36, 1999.

[136] C. Park, "Review of chemical kinetic problems of future nasa missions. i - earth entries", *Journal of Thermophysics and Heat Transfer*, vol. 7, 1993.

[137] M. Tauber, "A review of high-speed, convective, heat-transfer computation methods", NASA Technical Report, 1989.

[138] M. Iacovazzo, *Aerodynamic analysis of a low-ballistic coefficient deployable re-entry capsule*. Master Thesis, 2013.

[139] MathWorks, *MathWorks filtering and smoothing data Documentation*, 2019. [Online]. Available: `https://it.mathworks.com/help/curvefit/smoothing-data.html`.

[140] S. Teramoto, K. Fujii, and K. Hiraki, "Numerical analysis of dynamic stability of a reentry capsule at transonic speeds", *AIAA Journal*, vol. 39, 2001.

[141] "Marco polo re-entry capsule dynamic stability characterization: Abstract and summary report", ESA/ESTEC Contract Nr. 4000107482/12/NL/CBi, 2014.

[142] P. N. Desai and F. McNeil Cheatwood, "Entry dispersion analysis for the genesis sample return capsule", *Journal of Spacecraft and Rockets*, vol. 38, pp. 345–350, 2001.

[143] P. Desai and et al., "Entry, descent, and landing operations analysis for the stardust re-entry capsule", AIAA/AAS Astrodynamics Specialist Conference and Exibit, 2006.